Université de Lille

N° d'ordre :

THÈSE DE DOCTORAT

DE L'UNIVERSITÉ DE LILLE

réalisée au sein de

École doctorale n°632 : Sciences de l'Ingénierie et des Systèmes – ENGYS

Laboratoire de Génie Civil et Géo-Environnement – LGCgE ULR4515

Modélisation multi-échelle du comportement mécanique en grandes déformations de systèmes polymères

Multiscale modeling of the large-strain mechanical behavior of polymer systems

Thèse soutenue publiquement le 14/12/2022, par

Zhu YAN

pour obtenir le grade de

DOCTEUR en Mécanique, génie mécanique, génie civil de L'UNIVERSITE DE LILLE

Devant le jury composé de :

LEFEBVRE Jean-Marc, Université de Lille	Directeur de Recherche CNRS (Émérite)	Président
KAMALI-BERNARD Siham, INSA Rennes	MCF-HDR	Rapporteur
ESTEVEZ Rafael, Université de Grenoble Alpes	Professeur	Rapporteur
GILABERT VILLEGAS Francisco Antonio, Ghent University (UGent) (Belgium)	Professeur	Examinateur
ZAIRI Fahmi, Université de Lille	Professeur	Direction de thèse
ZAOUI Ali, Université de Lille	Professeur	Direction de thèse
BOUIBES Amine, INSA Toulouse	MCF	Invité
LIU Xiaobing, Xihua University (China)	Professeur	Invité

Laboratoire de Génie Civil et géo-Environnement

Abstract

Polymers are important raw materials in the actual industrial production due to their peculiar properties. They offer a lot of new extraordinary opportunities in a wide range of engineering applications including 3D printing, waste-water treatment, civil engineering, biomedical engineering, actuators and energy storage. The present PhD dissertation deals with the multiscale modeling of the mechanical behavior of polymer systems using the molecular-level description via molecular dynamics and the continuum-level mechanics.

In a first part of the thesis, molecular dynamics simulations are employed to study the physical and mechanical properties of polyethylene (PE) and carbon-black filled vulcanized *cis*-polyisoprene (*cis*-PI) systems. We first show the determinant role of the structural composition (i.e. length and number of chains) and temperature on the crystallinity in PE systems obtained by two general measurement methods (bond orientation and global order parameters). We especially highlight the strong influence of the latter factors on the biaxial large-strain stress-strain response till failure, the orientation crystallization provoking a significant directional effect. We then point out that the branch chain composition has a great effect on the shape memory capacities of branched PE systems. Finally, the vulcanization and nanofiller reinforcement mechanisms in *cis*-PI are investigated at the nanoscale. Besides, we quantify the mechanical response upon stretching-retraction loading sequences and the related nonlinear and inelastic features are studied. The interactions between fullerenes and *cis*-PI atoms and the aggregation configuration of *cis*-PI atoms around fullerenes are analyzed in details by introducing local number density and potential mean force through radial distribution function.

In a second part of the present thesis, we address the problem of the continuum-based representation of various polymer systems, including PE, polyvinylidene fluoride (PVDF) and entangled *cis*-PI systems. We first develop a multi-scale model for strain-induced morphological anisotropy in semi-crystalline PE formulated within a continuum-based micromechanical framework. The crystallographic shear in the crystalline lamellae and the molecular alignment/relaxation of the amorphous phase are two underlying inelastic processes integrated in the constitutive representation. The cavitation damage accumulation related to the progressive nucleation and anisotropic growth of nano-sized cavities in the amorphous phase is

also integrated. The coupling between the different phases is performed by means of a multi-scale homogenization-based approach in which the interfacial interaction is considered. The model output is compared to tensile experimental observations of PE containing a broad range of crystallinities obtained under monotonic and oligo-cyclic tensile loading sequences upon large-strain plastic deformation. We also examine the damage behavior upon stretching and stretching-retraction-recovery sequences at different strain rates and temperatures. We then enrich the continuum-based model to semi-crystalline PVDF by connecting the macroscopic response to strain-induced $\alpha \rightarrow \beta$ phase transition. Some fundamental parameters taken from molecular dynamics simulations are transferred to the continuum scale. By completing the scale bridging method by the identification of the other model parameters, the model outputs are found in good agreement with the existing tensile experiments of a PVDF upon large-strain plastic deformation. Finally, we examine the biaxial capacities of a hyperelastic constitutive model thanks to molecular dynamics data of entangled *cis*-PI systems obtained for different deformation modes.

Keywords: Polymer systems; Molecular dynamics; Continuum mechanics; Mechanical properties; Interface; Strain-induced mechanisms.

Résumé

La présente thèse de doctorat porte sur la modélisation multi-échelle du comportement mécanique de systèmes polymères en utilisant la description au niveau moléculaire via la dynamique moléculaire et à l'échelle du continuum via la mécanique des milieux continus.

Dans une première partie, des simulations de dynamique moléculaire sont utilisées pour étudier les propriétés physiques et mécaniques de systèmes en polyéthylène (PE) et en *cis*-polyisoprène (*cis*-PI) vulcanisés et renforcés en noir de carbone. Nous montrons d'abord le rôle déterminant de la composition structurelle (c'est-à-dire la longueur et le nombre de chaînes) et de la température sur la cristallinité de systèmes en PE, obtenue par deux méthodes de mesure générales (à savoir les paramètres d'orientation des liaisons et d'ordre global). Nous mettons particulièrement en évidence la forte influence de ces derniers facteurs sur la réponse mécanique biaxiale en grandes déformations et ce, jusqu'à la rupture, la cristallisation de l'orientation provoquant un effet directionnel significatif. Nous montrons ensuite que la composition de la chaîne de ramification a un effet important sur les capacités de mémoire de forme des systèmes en PE ramifiés. Enfin, les mécanismes de vulcanisation et de renforcement par des nanocharges dans le *cis*-PI sont étudiés à l'échelle nanométrique. En outre, nous quantifions la réponse mécanique lors de séquences d'étirement-rétraction et les caractéristiques non linéaires et inélastiques associées sont étudiées. Les interactions entre les fullerènes et les atomes de *cis*-PI et la configuration d'agrégation des atomes de *cis*-PI autour des fullerènes sont analysées en détail en introduisant la densité de nombre local et la force moyenne potentielle par le biais de la fonction de distribution radiale.

Dans une deuxième partie, nous abordons le problème de la représentation constitutive de divers systèmes polymères, notamment le PE, le polyfluorure de vinylidène (PVDF) et le *cis*-PI enchevêtrés. Nous développons d'abord un modèle multi-échelle pour représenter l'anisotropie morphologique induite par la déformation dans le PE semi-cristallin, formulé dans un cadre micromécanique. Le cisaillement cristallographique dans les lamelles cristallines et l'alignement/relaxation moléculaire de la phase amorphe sont deux processus inélastiques sous-jacents intégrés dans la représentation constitutive. L'accumulation de l'endommagement par cavitation liée à la nucléation progressive et à la croissance anisotrope de cavités de taille

nanométrique dans la phase amorphe est également intégrée. Le couplage entre les différentes phases est effectué au moyen d'une approche basée sur l'homogénéisation multi-échelle dans laquelle l'interaction interfaciale est prise en compte. Les résultats du modèle sont comparés aux observations expérimentales en traction de PE contenant une large gamme de cristallinités, obtenues sous des séquences de chargement en traction monotones et oligo-cycliques lors de grandes déformations plastiques. Nous examinons également le comportement endommageable lors de séquences d'étirement et d'étirement-rétraction-récupération à différentes vitesses de déformation et températures. Nous enrichissons ensuite le modèle constitutif à l'application du PVDF semi-cristallin en reliant la réponse macroscopique à la transition de phase $\alpha \rightarrow \beta$ induite par la déformation. Certains paramètres fondamentaux issus de simulations de dynamique moléculaire sont transférés à l'échelle du continuum. En complétant la méthode de transfert d'échelle par l'identification des autres paramètres du modèle, les résultats de ce dernier sont trouvés en bon accord avec les expériences de traction existantes d'un PVDF lors d'une grande déformation plastique. Enfin, nous examinons les capacités biaxiales d'un modèle constitutif hyperélastique grâce aux données de dynamique moléculaire de systèmes *cis*-PI enchevêtrés obtenues pour différents modes de déformation.

Mots clés : Systèmes polymères ; Dynamique moléculaire ; Mécanique des milieux continus ; Propriétés mécaniques; Interface ; Mécanismes de déformation.

Acknowledgements

As I write this section, it marks the end of my PhD and I look back on the past four years with a flood of emotions. I would like to thank my teachers, family and friends who have been with me all along the way, and whose presence has been an important benchmark in this beautiful landscape, which will remain in my memory.

First of all, I would like to thank my tutors, Prof. Fahmi ZAIRI and Prof. Ali ZAOUI. Four years ago, I was fortunate enough to be admitted to the LGCgE, and I have always benefited from their advice and guidance. I have been deeply influenced by your calm and light-hearted attitude, your open and selfless mind, your rigorous and meticulous style of governance, and your profound and broad knowledge vision. I would like to express my sincere gratitude to the professors who have given so much of themselves to the successful completion of my thesis.

Then, I would like to thank my parents, your valuable and selfless contribution is the prerequisite and foundation for my successful completion of my studies. In the future, I will keep striving to go beyond and repay you with practical actions! I would also like to thank my sister and brother-in-law for taking care of our parents and making me worry-free during this period of time when I was studying in a foreign country. And of course, my sweet little nephew, uncle loves you.

Next, I would like to thank my wife for being there without complaint and for walking with me through thick and thin during our toughest times. I love three things in this world. Sun, moon and you. Sun for morning, moon for night, and you forever.

Most of all, I want to thank my son for giving me the world with your arrival. You will soon be one year old and I wish you a happy and healthy life.

I would also like to thank all my colleagues in the laboratory, especially Dr. Qiang GUO, for your help and inspiration on my life and research.

Finally, I would like to thank all the experts and professors who took time out of their busy schedules to review and comment on this paper.

Zhu YAN

Contents

General introduction

Polymer systems have a large range of applications, in sectors like oil industry, automobile, aeronautic, robotic, biomechanics, 3D printing, waste-water treatment, civil engineering, actuators and energy storage, in which they may be subjected to large strains under in-service or manufacturing process. These materials present an extremely large variety of molecular architectures and structural factors (length and number of chains, crystallinity, vulcanization, nanofiller reinforcement…) that leads to an extremely large variety of mechanical responses from the plastic response characteristics of thermoplastics to the nonlinear elastic response characteristics of elastomers. Besides, the external mechanical loading conditions (strain rate, temperature, non-monotonicity, multiaxiality…) affect significantly both the deformation mechanisms (molecular orientation, cavitation damage, phase transformation…) and the large-strain mechanical behavior. As a meaningful prerequisite of advanced applications of polymer systems, predictive multiscale modeling is needed. This PhD dissertation deals with the multiscale modeling of the large-strain mechanical behavior of polymer systems using the molecular-level description via molecular dynamics and the continuum-level mechanics. Various polymers are investigated in the present work namely, semi-crystalline polyethylene (PE), semi-crystalline polyvinylidene fluoride (PVDF) and carbon-black filled vulcanized *cis*-polyisoprene (*cis*-PI).

The first part of this PhD dissertation containing Chapters I, II and III is exclusively related to molecular dynamics simulations that are employed to study the physical and mechanical properties of PE and *cis*-PI systems. In *Chapter I,* the atomistic approach is employed to study the crystallinity and mechanical properties of PE systems. The influence of the structural composition (i.e. length and number of chains) and temperature on the crystallinity in PE systems is firstly reported by means of two general measurement methods, namely bond orientation parameter and global order parameter. For the different designed PE systems, the large-strain stress-strain response till failure is then examined under different conditions in terms of mechanical loading modes and stretching temperatures. We especially highlight the strong influence of the structural composition and loading conditions on the biaxial large-strain

stress-strain response till failure, the orientation crystallization provoking a significant directional effect. In *Chapter 2*, through the molecular dynamics simulations, we bring some insights on the influence of branched chain composition and temperature on the large-strain mechanical behavior and the shape memory performance of the same material system. *Chapter 3* is dedicated to carbon-black filled vulcanized *cis*-PI systems. We report the effects of vulcanization and nanofiller reinforcement mechanisms on the physical and mechanical properties of the different designed *cis*-PI systems. The mechanical response is quantified upon stretching-retraction loading sequences and the related nonlinear and inelastic properties are studied. The local interactions at the nanoscale are analyzed in details by introducing local number density and potential mean force through radial distribution function.

In the second part of this PhD dissertation containing Chapters IV to VII we address the problem of the continuum-based representation of various polymer systems, including PE, PVDF and entangled *cis*-PI systems. In *Chapter IV*, we examine the ability of a multi-scale homogenization-based constitutive model to capture the PE large-strain tensile response variation with crystal concentration. The model is applied on a high-density polyethylene with 0.72 crystal content, a low-density polyethylene with 0.3 crystal content and an ultra-low-density polyethylene with 0.15 crystal content. The results of our simulations are criticized by analyzing the model ability to capture a series of experimental observations under monotonic, loading-unloading and oligo-cyclic stretching over a large strain range. The effect of the amorphous phase fraction on the microstructure evolution is finally discussed thanks to the model. In *Chapter V*, the continuum-based model is further developed to consider the cavitation damage effects in the material anisotropy during finite plastic deformation of polyethylene. By this way, a more physically consistent description is formulated in continuum terms to describe the complex coupling existing between microstructure (amorphous and crystalline phases), micromechanical deformation processes including cavitation damage and large-strain flow behavior. The efficiency of the proposed plastic-damage model to capture material response in terms of finite deformation stress-strain behavior and inelastic volumetric strain is critically discussed by comparing simulations to experimental results including strain rate and stretching temperature effects. The effects of crystal plasticity and amorphous cavitation damage on the

macroscopic and internal responses are observed thanks to the model under stretching and stretching-retraction conditions. In *Chapter VI*, we enrich the continuum-based model to render it capable to replicate the mechanical response of PVDF along with the α → β phase transition caused by the straining in the final aim to clarify the connection between the mesostructural evolution and the benefices on the electroactive response. Besides, molecular dynamics simulations are employed to examine the respective mechanical properties of α-PVDF, β-PVDF and amorphous phase. The elastic constants of the distinguishing phases and the onset of α → β phase transition, when α-PVDF is drawn, are then used as direct inputs into the continuum-based model. The intermolecular constants of the amorphous phase are also obtained thanks to molecular dynamics data. The other parameters of the continuum-based model are determined using the stress-strain experimental data of a PVDF deformed over a large-strain range. The effect of the progressive variation in the mesostructural properties caused by the straining on the piezoelectric properties is finally observed. In Chapter VII, we address the problem of the multiscale prediction of the multiaxial hyperelastic behavior of rubbers. We attempt to verify the predictive ability of a hyperelastic constitutive model based on the theoretical framework of continuum mechanics while connecting the continuum-level mechanics to the molecular-level description by means of molecular dynamics method.

A general conclusion closes this PhD dissertation with the main results obtained.

Chapter I

Crystallization and Mechanical Behavior of Semi-Crystalline Polyethylene

Chapter I. Crystallization and mechanical behavior of semi-crystalline polyethylene[1]

Abstract

Molecular dynamics simulations are employed to study the crystallinity and mechanical properties of multi-chain polyethylene systems. Results show that structural composition (length and number of chains) and temperature lead to different crystallinity, which are obtained by using two general measurement methods, namely chain orientation and global order. The semi-crystalline polyethylene systems are deformed under various mechanical loading modes and at different temperatures representing different polymer states. The stretching temperature and structural composition have a strong influence on the mechanical properties, including elastic modulus, yield stress and inelastic mechanisms. The orientation crystallization caused by the heat treatment stage induces a significant direction effect on the different parts of the large-strain stress-strain response. Besides, the competition of the two main inelastic deformation mechanisms, namely shear yielding and cavitation damage, are revealed during the course of stretching.

Keywords: Semi-crystalline polyethylene; Crystallinity; Mechanical properties; Molecular dynamics.

[1] This chapter is based on the following paper: Yan, Z., Zaoui, A., Zaïri, F., 2021. Crystallization and mechanical behavior of semi-crystalline polyethylene. Physica Scripta 96, 125729.

I.1. Introduction

Due to their peculiar properties, polyethylene became important raw materials in the actual industrial production and offer many new extraordinary opportunities in a wide range of engineering applications including 3D printing, wastewater treatment, biomedical engineering, actuators and energy storage.

As a meaningful prerequisite of advanced applications of polyethylene, the formulation of continuum-based constitutive models is needed (van Dommelen et al., 2003; Ayoub et al., 2010, 2011; Abdul-Hameed et al., 2014; Jiang et al., 2019). In the most sophisticated developments, they are developed within a multiscale framework using statistical mechanics and an adequate transition scale scheme. A representative example is the introduction of the crystallization micro-mechanism at the chain-scale and the prediction of its effect on the response at the macroscale (Guo et al., 2018, 2020). A rigorous constitutive representation of polyethylene requires the most physically realistic introduction of the structural and loading parameters that govern the macroscopic response. A deeper understanding of the separate and synergistic effects of key parameters is still crucially needed to propose physically based models avoiding (or at least limiting) the arbitrary inclusion of heuristic model constants and providing accurate information for the polyethylene design.

In the meantime, even if the qualitative understanding of the deformation mechanisms in polyethylene is substantial (Schrauwen et al., 2004a, 2004b; Hong et al., 2004; Addiego et al., 2006; Pawlak et al., 2007; Bartczak et al., 2010; Cheng et al., 2010; Xiong et al., 2018), the assessment of their effects on the macroscopic response is difficult to quantify. Number of experiments have been devoted to the study of the relationship between structure and properties in polyethylene. For instance, small angle X-ray diffraction, small-angle neutron scattering, and proton magnetic resonance have been used to characterize the structure. Ayoub et al. (2010) and Schrauwen et al. (2004a) have realized tensile experiments on polyethylene and analyzed the four typical regimes before fracture of the large-strain stress-strain curves (elastic deformation, yield strength and strain-softening in the small-strain domain and strain-hardening in the moderate/large-strain domain), and further explored the crystallinity and crystal region. The

influence of lamellar thickness and orientation of crystalline regions on the mechanical behavior of polyethylene was analyzed by Hong et al. (2004), Cheng et al. (2010) and Xiong et al. (2018). They investigated the influence of structural factors such as crystal region, amorphous region, crystallinity, molecular weight and entanglement on the different strain regimes of the macroscopic response.

Due to the objective limitations of the current experimental techniques, it is nonetheless difficult to highlight the separate effects of the structural features on the macroscopic response, to measure the material properties at the molecular level and to quantify the various deformation mechanisms that may take place at different scales, at any location in the loaded specimen and at any time upon the mechanical loading. With the continuous improvement of computer level, molecular simulation has become an indispensable tool for studying the properties of complex material systems by including structural parameters and interactions at relevant scales. Indeed, nowadays such a method is a powerful tool to study local interactions and structure properties relationship of polymers from the nanoscale to the macroscale (Brown et al., 1991; Zhang et al., 2001; Simoes et al., 2004; Li et al., 2006; Makke et al., 2009; Hossain et al., 2010; Sanmartin et al., 2012; Anoukou et al., 2013, 2015; Liao et al., 2018; Hagita et al., 2018, 2019). Li et al. (2006) used the Monte Carlo (MC) method to explore the uniaxial stretching of polyethylene under glassy state at different strain rates and temperatures. The simulation results were highly consistent with those obtained from experiment. Makke et al. (2009) carried out uniaxial and multiaxial tensile simulations on polymers under glassy and rubbery states at different strain rates by the MC method and obtained stress-strain behavior in agreement with experiment. This article discusses the effects of different loading methods on the properties of non-homogeneous glassy and rubbery polymers, including the boundary conditions of loading and the direction of loading, but does not specifically analyze the structural composition of the non-homogeneous polymers. Simoes et al. (2004) also used the MC method to simulate the tensile deformation of amorphous polymers and investigated the mechanical properties and the deformation mechanisms upon the tensile process. Brown and Clarke (1991) qualitatively obtained the deformation behavior of polyethylene-like amorphous polymers in uniaxial tensile simulations at higher strain rates than experimental ones. Hossain et al. (2010) adopted united-atom (UA)

method to model the amorphous polyethylene system in the simulation in order to investigate the deformation mechanisms and the influence of temperature, chain number and chain length on the tensile deformation. They found that the elastic deformation and yielding phases are primarily inter-molecular chain interactions, while the strain-reinforced phase is primarily intra-molecular interaction. Hagita et al. (2018) used the Molecular Dynamics (MD) approach to investigate the evolution of single polyethylene molecular structure with eight different force fields under quenching processes. They found that different force fields caused different degrees of chain folding, resulting in different degrees of crystallinity. Hagita et al. (2019) studied the crystallization properties of polyethylene with different molecular structures, namely linear and ring polymers. They found that the linear polyethylene has a slower crystallization rate than cyclic polyethylene. Zhang et al. (2001) and Sanmartin et al. (2012) studied the effect of side chains on the crystallization of single-chain polyethylene. Their results showed that both crystallization temperature and crystallization parameters decrease as the number of branches increases, which corresponds to the conclusion obtained from experiment. Liao et al. (2018) studied the influence of composition of chain branching (Methyl-, Ethyl- and Butyl-groups) on the mechanical properties of branched and linear polyethylene.

In this chapter, MD simulation is employed to study crystallization and mechanical properties of various semi-crystalline polyethylene systems. The large-strain stress-strain response is examined under different conditions in terms of mechanical loading modes and stretching temperatures. This chapter attempts to analyze the inelastic deformation mechanism of multi-chain semi-crystalline polyethylene using the concept of strain decomposition to investigate the relationship between shear strain and cavitation damage in inelastic deformation.

I.2. Computational details

Using the explicit atom model for polymer simulations requires large number of atoms, complex force fields and small time-step that should be about 1/10 of the vibrational period of the C-H bond (the smallest vibrational period in most organics). This means such simulations require high performing computer and long simulation time, which is suitable for studying the intramolecular interactions of effects. However, the aim of our work is to study the interactions

between each linear chain molecules, including slipping, unentanglement, de-crosslinking etc., and therefore the united atom model is more suitable for this study. In the united atom model, each Methyl-, Ethyl- and Butyl-groups (i.e. the CH, CH_2, CH_3 monomer) will be considered as a single bead (Fig. I.1). By this way, united-atom model requires only one-third of atoms in the explicit atom model. In addition, there is only one kind of bead, which results in fewer interaction between beads and therefore does not need smaller time steps and different integration schemes such as in the explicit atom model, and therefore shorter computational time (Chen et al., 2006).

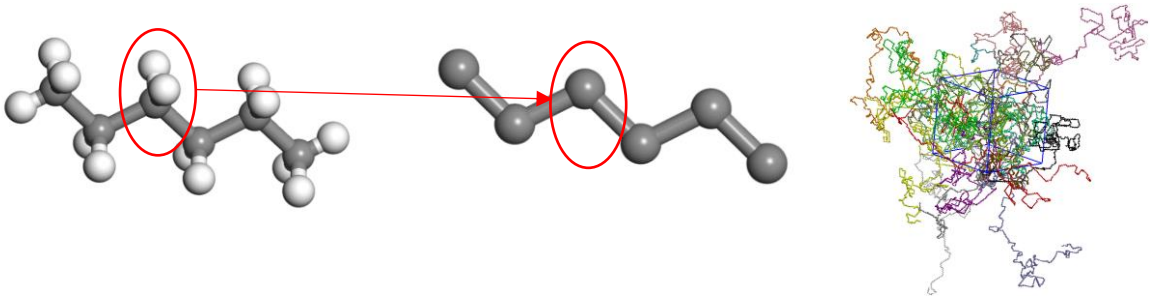

Fig. I.1. Polyethylene models: (a) Explicit-atom and united-atom models, (b) multi-chain molecular structure.

Table I.1. Specific parameters of the three initial structures.

Structure ID	Chain length	Number of chains	Number of total beads
Structure 1	1000	20	20000
Structure 1-i		80	80000
Structure 1-ii		160	160000
Structure 2	1000/100	10/100	20000
Structure 2-i		80/800	160000
Structure 3	100	200	20000
Structure 3-i		800	80000
Structure 3-ii		1600	160000

The MC self-avoiding random walks is employed here to create the different initial structures. During the chain generation process, a face-centered cubic (FCC) lattice superimposed on the simulation cell is used, with nearest neighbor distance of 1.53 Å (Binder et al., 1995; Shepherd, 2006; Hossain et al., 2010; Vu-Bac et al., 2014). In this work, we create eight structures with different number and length of chain to describe the effect of structural composition on the material properties, as shown in Table I.1. The simulation cell is orthogonal and the initial length

is determined based on a representative density of 0.95 g/cm^3 for high-density polyethylene (HDPE). A snapshot of the initial state of the polyethylene molecular structure is provided in Fig. I.1 taking the Structure 1 as an illustrative example.

The DREIDING force field (Mayo et al., 1990) was used in this chapter. This force field has four components: bond stretching, bond angle bending, bond angle torsion and non-bonded interaction, which can be expressed as:

$$E_{val} = E_{bond} + E_{angle} + E_{dihedral} + E_{nb} \quad \text{(I.1)}$$

The energy expressions and parameters for each component are displayed in Table I.2.

Table I.2. Functional form of force field and potential parameters used for MD calculations.

Interaction	Form	Parameters
Bond Length	$E_{bond} = \frac{1}{2}K_b(r - r_0)^2$	$K_\mathrm{b} = 700\,\mathrm{kcal/mol}, r_0 = 1.53\text{Å}$
Bond Angle	$E_{angle} = \frac{1}{2}K_\theta(\theta - \theta_0)^2$	$K_\theta = 100\,\mathrm{kcal/mol/rad^2}, \theta_0 = 109.1°$
Dihedral Angle	$E_{dihedral} = \sum_{i=0}^{4} C_i(\cos\phi)^i$	$C_0 = 1, C_1 = -3, C_2 = 0, C_3 = 4, C_4 = 0$ (kcal/mol) with $1-4$ LJ interaction
Non-bonded	$E_{non-bond} = 4\varepsilon\left[\left(\frac{\sigma}{r}\right)^{12} - \left(\frac{\sigma}{r}\right)^{6}\right], \mathrm{r} \le r_c$	$\sigma = 3.6239\text{Å}, \varepsilon = 0.1984\,\mathrm{kcal/mol}$

The large-scale molecular dynamics code LAMMPS was used. Before deforming the simulation cells, we carry out energy minimization of the initial structure, followed immediately by structural relaxation step. The minimize step relaxes any high-energy configurations that crested during the MC self-avoiding random walks. The simulation cells are subjected to a five-stage relaxation process as shown in Table I.3. The Nosé-Hoover Thermostat and Barostats were applied to control temperature and pressure. This simulation uses periodic boundary conditions. Periodic boundary conditions lead to greater stresses, but we study the overall trend of the different structures, so their effects can be ignored. The energy evolution is constantly monitored throughout the relaxation process to ensure that the simulation cells remain in equilibrium at the end of each stage, as shown in Fig. I.2. In order to see the degree of crystallization of each simulation cell, we analyse chain orientation and global order of simulation cell.

Table I.3. Parameter setting for five steps during the relaxation.

Process		Ensemble	Temperature (K)	Time step (fs)	Steps	Time (ns)
	Warm	NVT	0-500	1	1000000	1
	1	NVT	500	1	15000000	15
Relaxation	2	NPT (aniso)*	500	0.5	20000000	10
	3	NPT (aniso)*	500-$T_{desired}$	0.5	14000000	7
	4	NPT (aniso)*	$T_{desired}$	0.5	24000000	12

* During relaxation step, the pressure in X, Y and Z directions was kept constant at 1 atm, but independently.

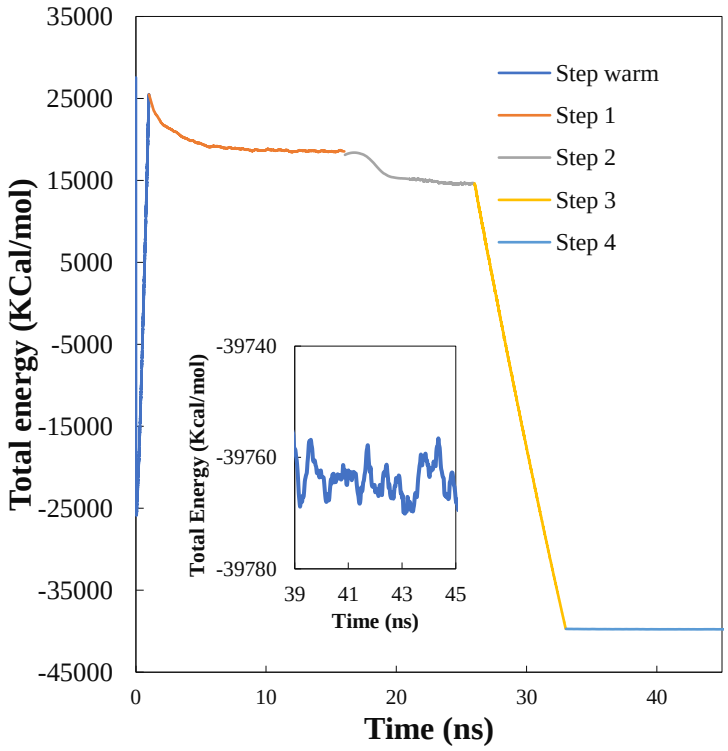

Fig. I.2. Total energy evolution during the relaxation step (end temperature is 100 K).

i) Chain orientation χ_n, χ_l

Here, the length of the *trans*-segment is the number of consecutive trans-bonds with dihedral angles $|\varphi| < \pi/3$; which is referred to as "stem length" in the polymer-crystallization field (Fujiwara et al., 1997, 2001). Two crystallization parameters, namely $n_{i,trans}$ and $l_{i,trans}$, are used in this chapter: $n_{i,trans}$ is the number of the trans-segments in which the monomer i is involved in the formation of the trans-segment, and takes a value ranged from 0 to 4 (Fig. I.3), and $l_{i,trans}$ is the length of the trans-segments whose formation involves the monomer i. In general, the crystallinity χ is determined as the number of crystalline atoms divided by the total number of atoms. In this work, the value of χ can be estimated if we deem that an atom

crystallizes when $n_{i,trans}$ = 4 and $l_{i,trans}$ > 7.

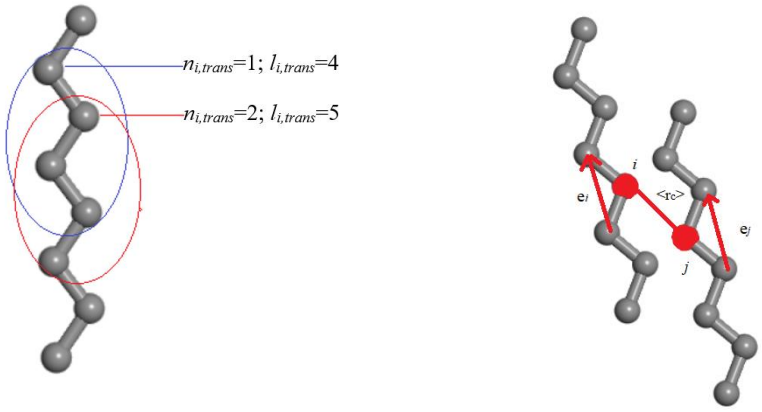

(a) (b)

Fig. I.3. Schematic images depicting the judgment of crystalline: (a) Chain orientation and (b) global order.

ii) Global order (r_c, $P_{2,i}$)

The Hermans orientation factor was used to compute the order parameter, which is used to determine the global crystallinity parameters, as follows (Fujiwara et al., 1997, 2001; Yi et al., 2001; Lavine et al., 2003; Kim et al., 2014; Nicholson et al., 2016; Hagita et al., 2019):

$$P_{2,i} = \frac{3}{2}\langle (e_i \cdot e_j)^2 \rangle - \frac{1}{2} \quad \text{(I.2)}$$

Here, *i* and *j* index different atoms, all atoms *j* within a cutoff distance r_c of atom *i* are included in the set for calculating the average value, where σ is the van der Waals diameter (Fig. I.3). The atom *i* with $P_{2,i} > P_{2,th}$ are designated as crystalline. In addition, two crystal beads that are within a distance r_{th} are considered to be in the same nucleus. Values of (r_c, $P_{2,th}$) of (2.5σ, 0.40) and (1.5σ, 0.52) are adopted to calculate crystallinity of each atom (Yi et al., 2001; Nicholson et al., 2016).

I.3. Results and discussion

I.3.1. Glass transition temperature

The glass transition temperature T_g is a fundamental physical feature of polymers. At temperatures below T_g, the material is in a rigid "glassy state". When the temperature is higher than T_g, the amorphous molecular chains begin to move, and the material becomes rubber-like

in its softness and flexibility. In the present work, T_g was determined according to the change in the slope of the specific volume-temperature curve (Takeuchi et al., 1991; Han et al., 1994; Gee et al., 1998; Capaldi et al., 2004). The system was equilibrated at 500 K followed by quenching from 500 K to 100 K at a rate of 100 K/ns. Fig. I.4 shows the specific volume-temperature curves for different systems. First, a linear fit is performed at both ends of the curve to obtain two linear fit lines. Thus, the temperature at the intersection of these two first points is defined as T_g. The obtained values are in agreement with previous theoretical studies (Takeuchi et al., 1991; Han et al., 1994; Gee et al., 1998; Capaldi et al., 2004a, 2004b), as well as typical experimental values(Gaur et al., 1980; Brandrup et al., 1999; Jiang et al., 2019). The systems will be deformed at four temperatures: 100 K that falls into the glassy state, 250 K and 300 K that are within the transition temperature range (between glassy and rubbery states) and, 400 K that falls into the rubbery state.

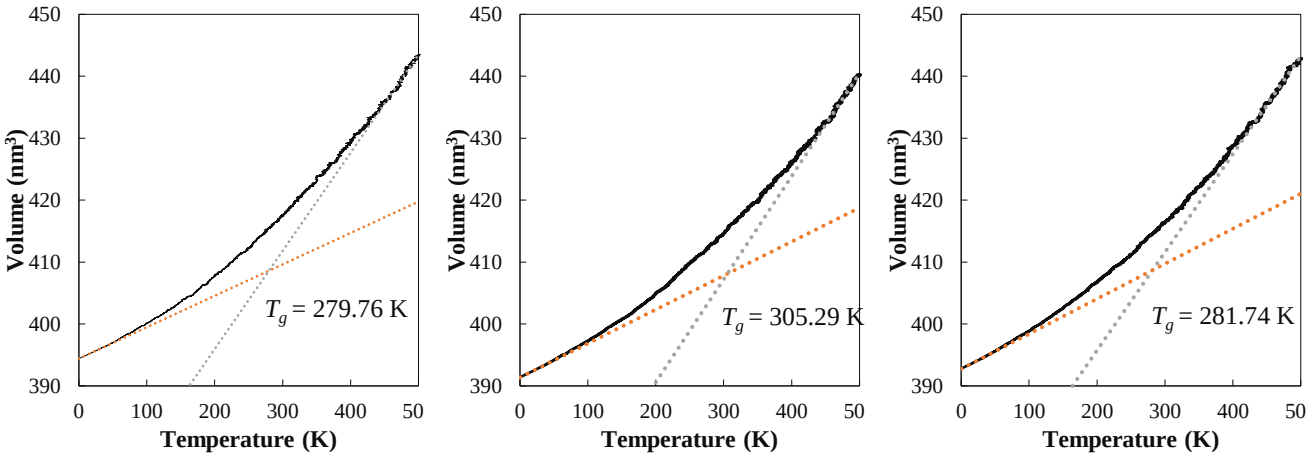

Fig. I.4. Volume evolution as a function of temperature used to extract the glass transition temperature: (a) Structure 1, (b) Structure 2 and (c) Structure 3.

I.3.2. Structure configuration

The simulation cell of Structure 1 for the final equilibrium state at a temperature of 100 K is shown in Fig. I.5(a), where we can clearly distinguish the amorphous domains from the crystallized domains. The crystallinity at the equilibrium state of different structures was analyzed using the local crystallinity parameters χ_n, χ_l and the global orientation parameters (r_c, $P_{2,i}$) introduced above and a summary is provided in Figs. I.5(b), I.5(c) and I.5(d).

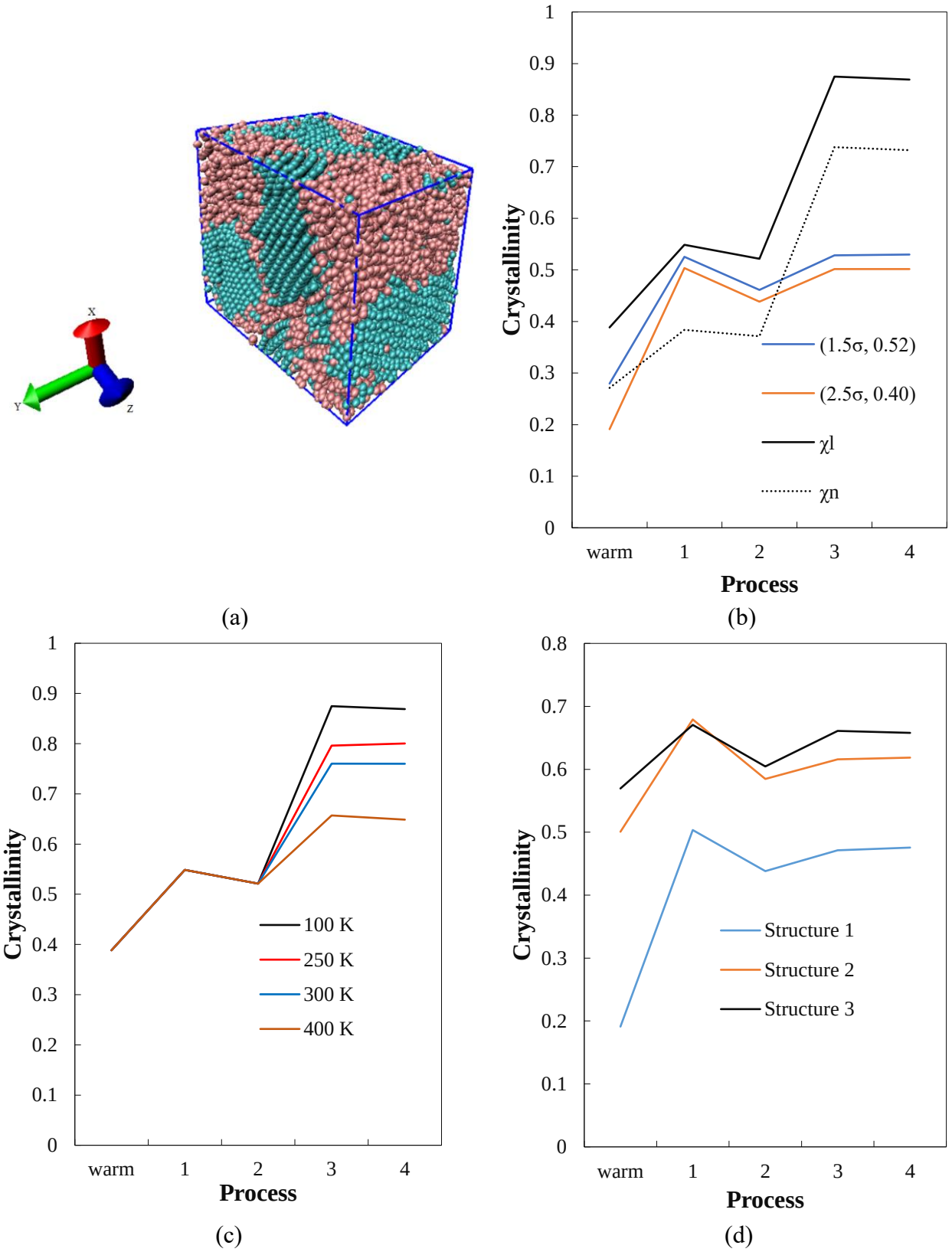

Fig. I.5. Crystallinity: (a) Structure 1 at the equilibrium state (amorphous domains are labeled in brown color and crystalline domains are labelled in green color), (b) evaluation based on different parameters, (c) effect of temperature and (d) effect of structural composition.

Fig. I.5(b) shows the crystallinity of structure 1 at 100 K with four parameters. Local crystallinity parameters χ_n, χ_l have the same curve shape, but there is a difference of about 14% between them. Global crystallinity parameters have also a similar behavior, with a slighter difference of about 1% between the two curves. For all crystallinity parameters, it is clear that only in step 2, the crystallinity parameters are slightly reduced. Compared with the final global crystallinity parameter, final local crystallinity parameters is obviously weak.

Polymer crystallization is a kinetically limited process. Fig. I.5(c) shows the local crystallinity parameters of Structure 1. Fig. I.5(c) highlights how the temperature affects the crystallinity parameters that decreases with increasing temperature. Fig. I.5(d) shows the crystallinity parameter of the three designed structures at 100 K. The final crystallinity parameters for the short length chain is clearly higher than the long length chain. It can be concluded that theshorter chain is easier to crystallize, and the short chain can also promote the crystallization of the long chain.

After equilibrium step, the radial distribution functions (RDFs) of equilibrium structures are shown in Fig. I.6(a). At the initial stage of the RDFs curve of equilibrium structure, three narrow peaks appear at 1.55 Å, representing the bonds between united atoms, 2.45 Å and 3.85 Å, corresponding to the second and third nearest united atoms along the united atom chain. It can be seen that the bond length does not differ depending on whether it is in the crystalline region or not. The area around the peak represents the number of neighbors in the interval. The further the distance, the greater the difference between the curves in these two regions. Perfact crystalline region shows the typical long-range ordered discrete distances in crystals, starting at 4.95 Å and extending to very large distances, with peaks appearing at certain intervals. However, some broader tips appear and g(R) approaches 1, which reflects the curve for the amorphous region. The temperature dependence of RDFs is shown in Fig. I.6(b). It can be clearly seen that at different temperatures, the peaks arise at the same position with different areas. As the temperature increases, the area decreases, which implies a lower degree of stacking.

I.3.3. Mechanical behavior

I.3.3.1. Uniaxial stretching

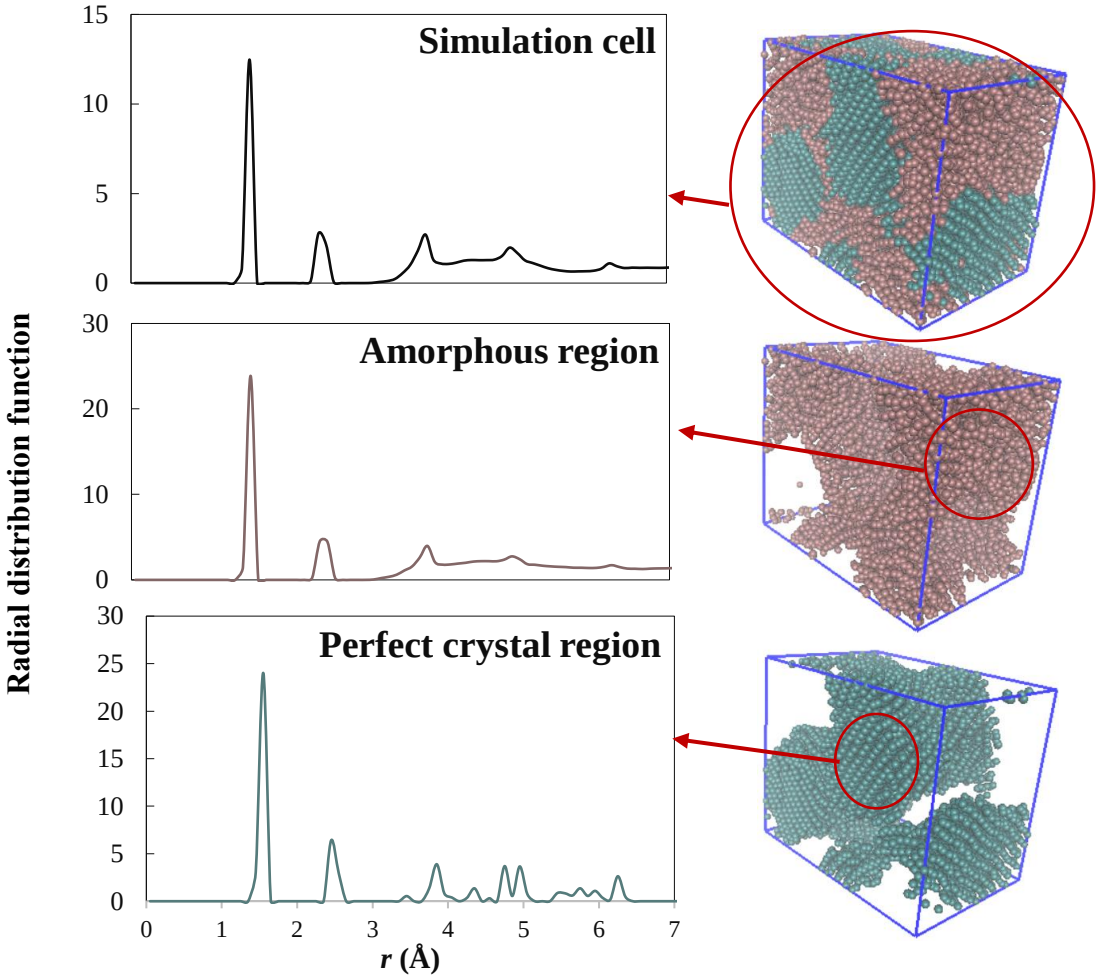

(a)

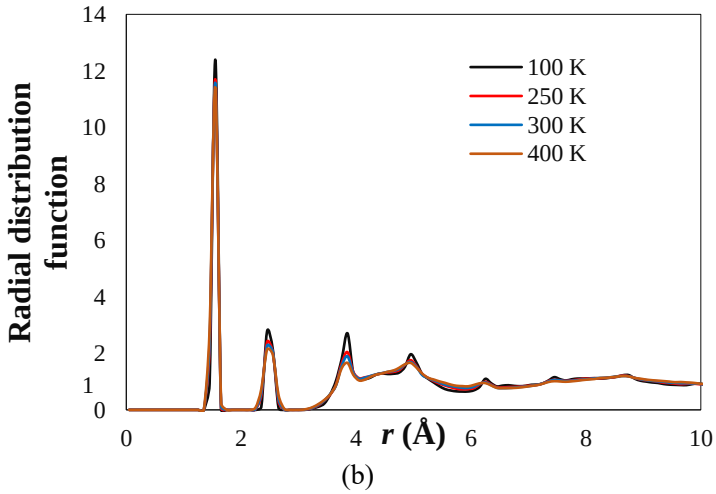

(b)

Fig. I.6. RDF for: (a) the total, amorphous and perfect crystal regions in Structure 1 at 100 K and (b) Structure 1 at different temperatures.

In this section, the simulation cells were stretched at the strain rate of 10^{10} s^{-1}. Fig. I.7(a) shows the uniaxial stress-strain curve of the polyethylene deformed continuously. The illustrative example concerns Structure 1 deformed at 100 K along Y direction. At this stretching temperature, the material system is in the glassy state. The stress-strain curve shows clearly four distinct regimes before failure. It is worth noting that the Y-axis is perpendicular to the crystal plane that is the polyethylene crystallizes in the XZ plane in this case (Fig. I.5(a)). In the first part, the stress increases almost linearly with strain increasing, the slope of the linear part corresponds to the elastic modulus. At the end of the elastic region, the material reaches the yield point. At this time, in addition to the elastic deformation, some plastic deformations also occur. Then, the stress decreases suggesting a strain-softening process after the yield point. Further deformation of polyethylene causes a drastic strain hardening and a final stress drop. In this stage, the stiffness decreases catastrophically and the system can be considered in a failure state. Similar behaviors were obtained in previous works (Yoon et al., 1993; Kremer et al., 2001; Faller et al., 2002; Fukunaga et al., 2002). The macro-response may be connected to the structure evolution with the applied strains.

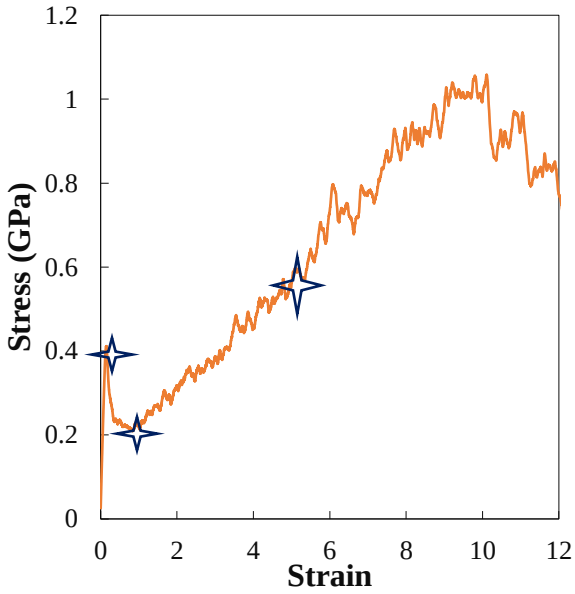

(a)

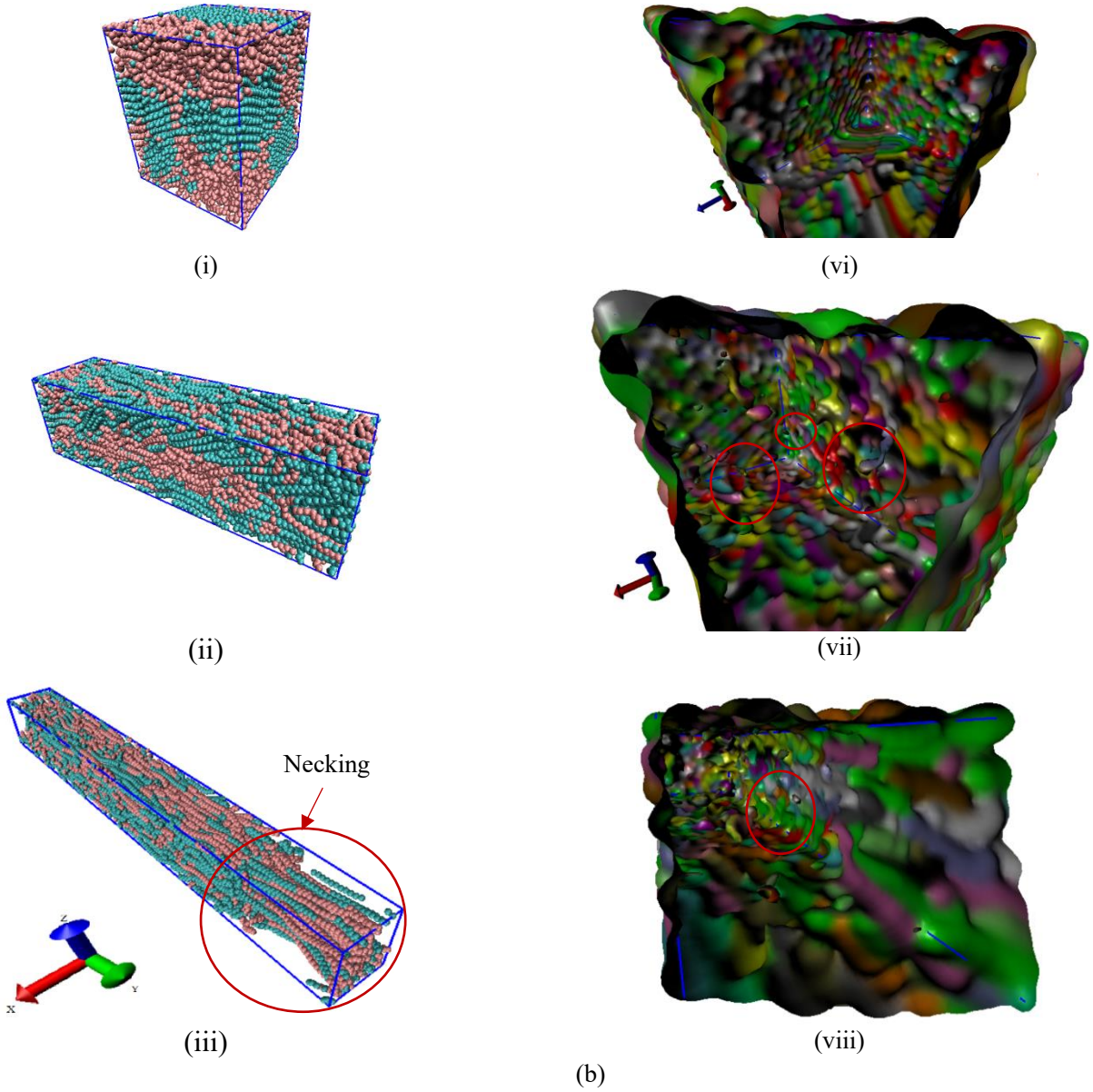

Fig. I.7. (a) Uniaxial stress-strain response of the Structure 1 deformed along Y direction at a stretching temperature of 100 K. (b) External and internal screenshots of the simulated cell at different loading strains, with the external screenshot showing each marble and the internal structure showing the cavitation of the structure.

Fig. I.8 demonstrates the effect of the number and the length of chains on the tensile properties of polyethylene at a temperature of 300 K. Firstly, the more chains there are, the smoother the curve is within the natural stretching rate, but the overall trend is the same, so that the properties of the material can be accurately obtained even with a small number of chains.

Above the natural draw rate, the friction between the beads of the united atom model is altered by the presence of hydrogen atoms due to the united atom model ignoring the presence of

hydrogen atoms, which affects the overall performance when multiple chains create necking and voids (part of the increased volume strain, Fig. I.8), according to Stokes' law, which relates the coefficient of friction to the hydrodynamic radius.

For simulated cells of the same chain length, the larger the system, i.e. the higher the number of chains, the slightly higher the ductility of the cell, which is also reflected in the response to volume strain, where the steep increase in volume strain is delayed, i.e. the necking is delayed For long chain length structure, the material has higher elastic stiffness, yield strength and breaking elongation. Fig. I.8(c) shows an obvious breakpoint for Structure 3 (short length chain). The material with shorter length chain exhibits more mechanical behavior similar to crystals. This proves that when the chains are shorter, the polymer cannot be fully entangled and therefore the stretch ability is smaller.

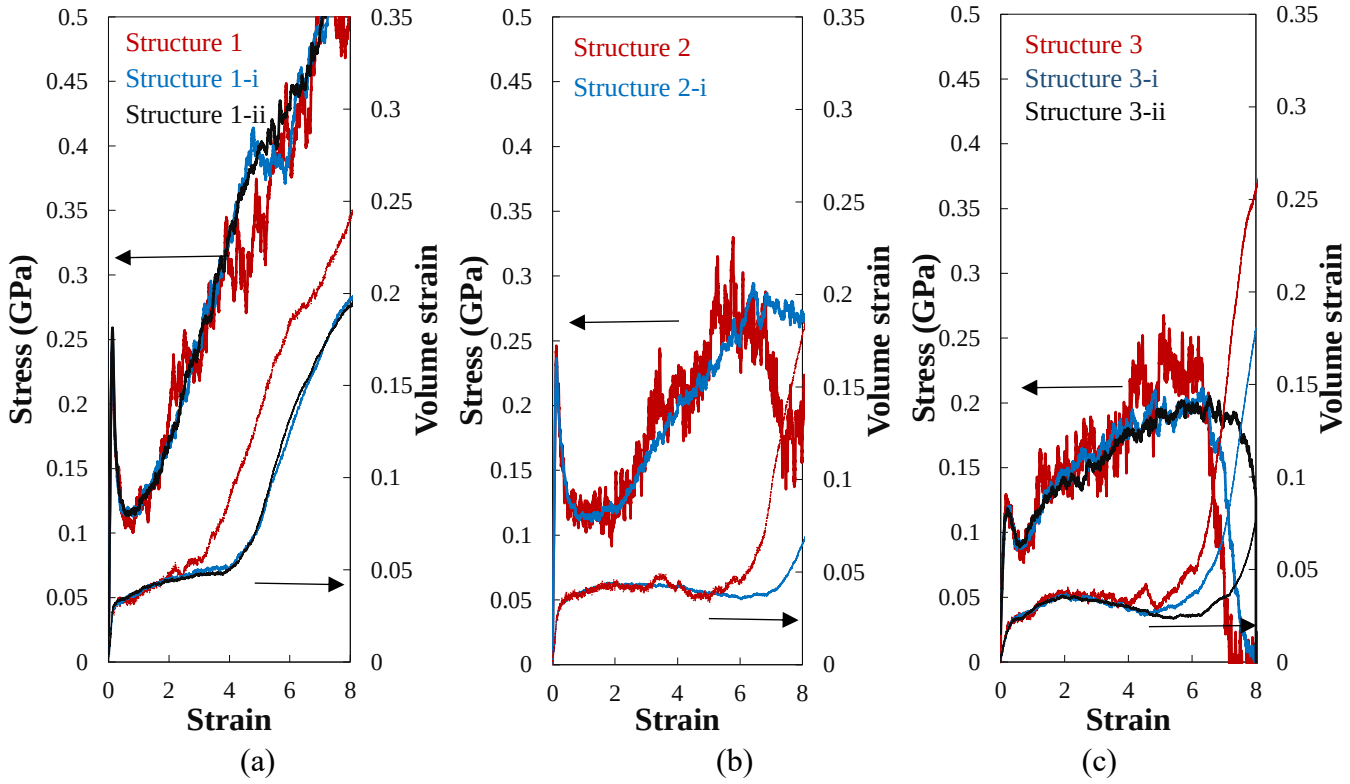

Fig. I.8. Structural composition effect on the uniaxial stress-strain response and volume strain at a stretching temperature of 300 K for different structures.

Fig. I.9 presents the uniaxial stress-strain response of Structure 1 deformed at 100 K along the three directions. A global view at these results indicates that the mechanical response exhibits

a directional effect. At a strain of approximately 0.15, the yield strength along the Y direction is higher than that of the two other stretch directions, which means highest elastic stiffness. Along the X and Z directions, the initial elastic response is followed by a rollover to yield and no strain-softening is observed. This is a result of the crystal orientation. Indeed, because the polymer chains are parallel in the Y-axis, the folded chains are mainly opened instead of slipping when strain occurs.

The inelastic deformation mechanisms can be analyzed during the course of the uniaxial stretching using the strain decomposition concept (Zaïri et al., 2005). The elastic volumetric strain ε_{el}, shearing strain ε_{shear} and cavitation strain ε_{cav}, making up the complete strain, are additively split and plotted in Fig. I.9. This figure allows a distinction to be made between the dilatational mechanisms, giving rise to a volume increase, and the shear yielding, occurring at constant volume.

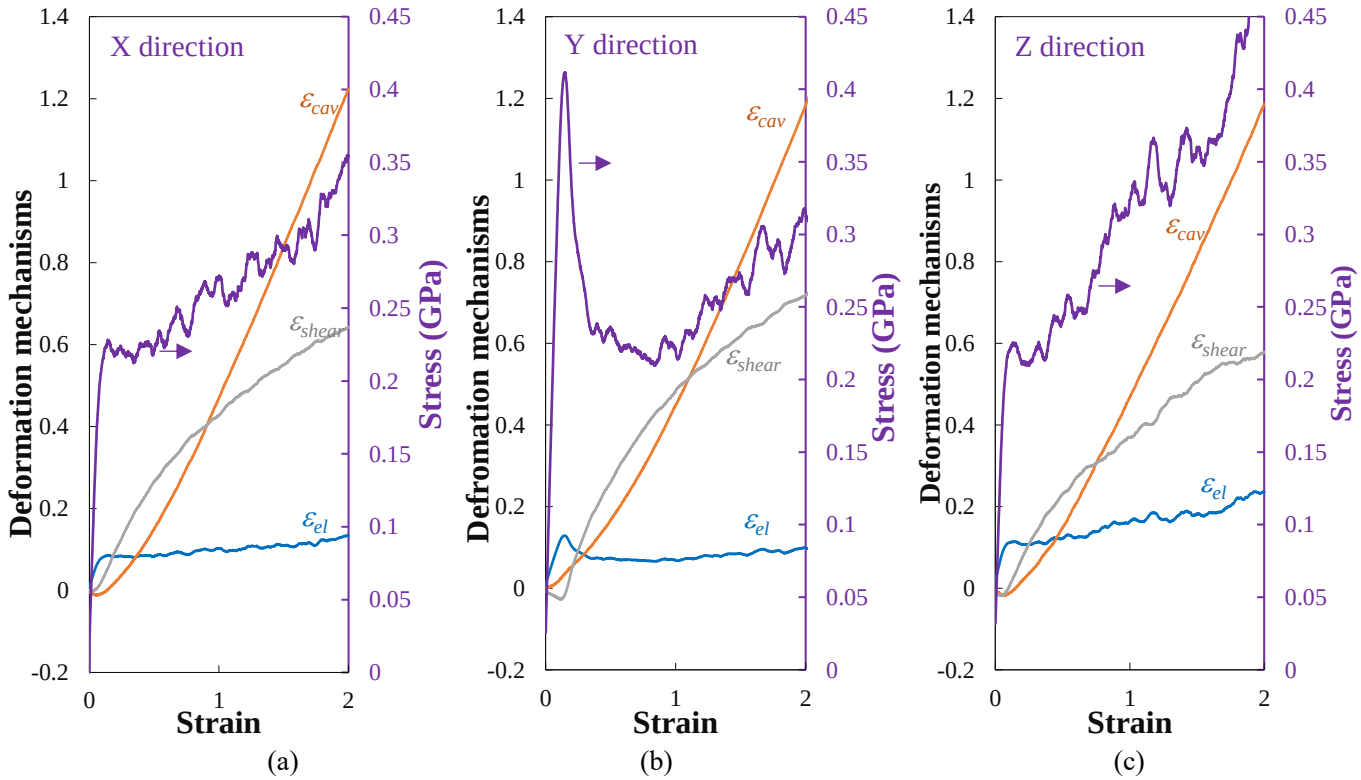

Fig. I.9. Direction effect on the uniaxial stress-strain response along with deformation mechanisms of Structure 1 at a stretching temperature of 100 K: (a) along X direction, (b) along Y direction and (c) along Z direction.

The elastic volumetric strain plays an important role within the small strain region, whereas the

shearing strain is negative. The latter behavior is due to some tiny gaps in the structure that still exist in the equilibrium state. In the initial deformation stage, due to the slippage or opening of the chains, these gaps become smaller. At larger strain region, the shearing strain progressively increases and informs about progressive plasticity/fragmentation mechanisms of the crystalline domains. The cavitation strain takes place as the plastic deformation proceed. This most direct indicator of the progressive voiding mechanism informs about the cavities between crystalline domains that become larger and larger until the final failure (Addiego et al., 2006; Pawlak et al., 2007; Bartczak et al., 2010). The voiding mechanism enters in competition with the shear yielding. The latter is the predominant deformation mechanism after yielding but the cavitation strain takes over the shearing strain at larger strains. The competition between these two inelastic mechanisms is clearly directional dependent. The anisotropic response at the macroscale is therefore related to both the initial anisotropy in crystal orientation and the anisotropic deformation micro-mechanisms.

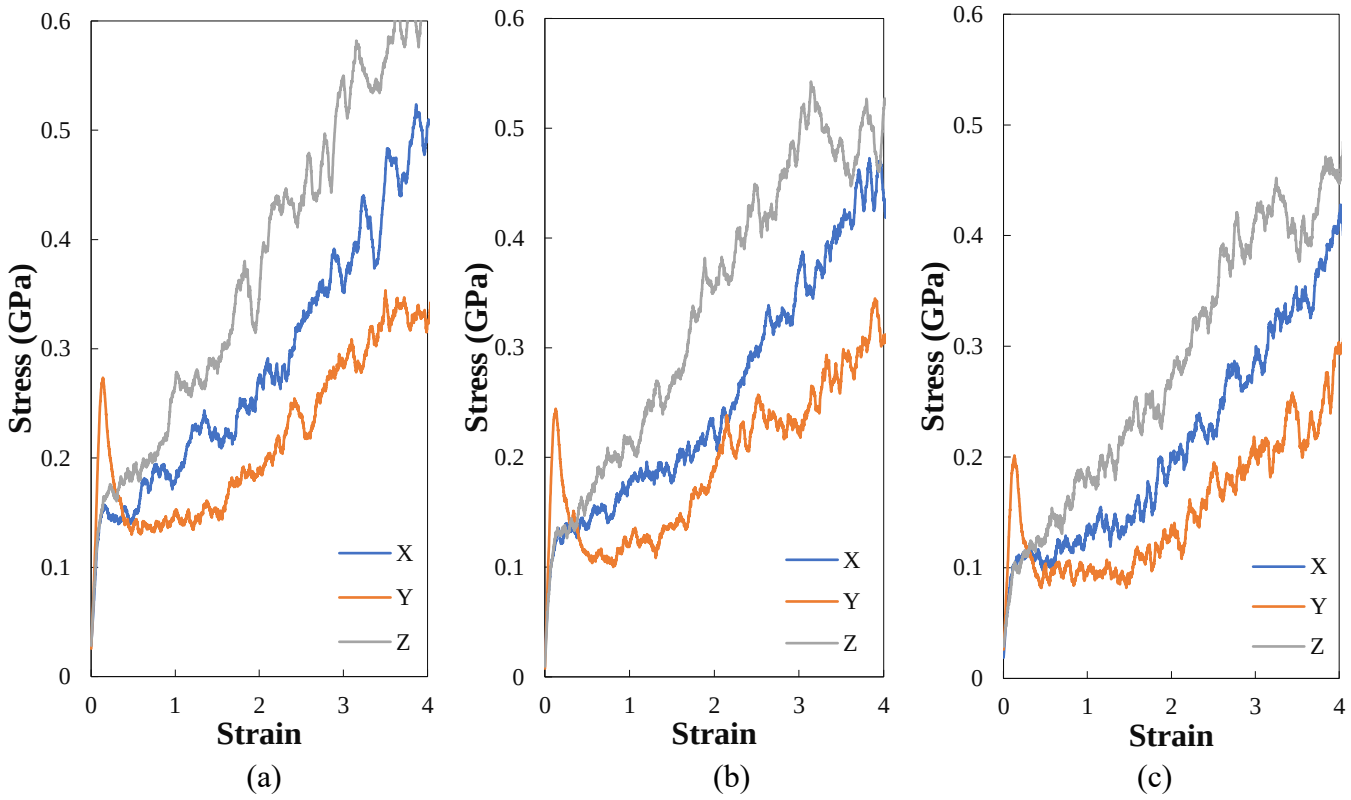

Fig. I.10. Temperature effect on the uniaxial stress-strain response of Structure 1 deformed along different directions: (a) 250 K, (b) 300 K and (c) 400 K.

The effect of the stretching temperature on the uniaxial stress-strain behavior is reported in Fig.

I.10 along with the direction effect. As the temperature increases, we may clearly see a decrease of the elastic stiffness. The Young's modulus of the material is displayed in Fig. I.11, from strain equal to 0.1, which clearly indicates that the Young's modulus decreases when the temperature decreases for the same material. The material shows a very clear anisotropy.

I.3.3.2. Biaxial stretching

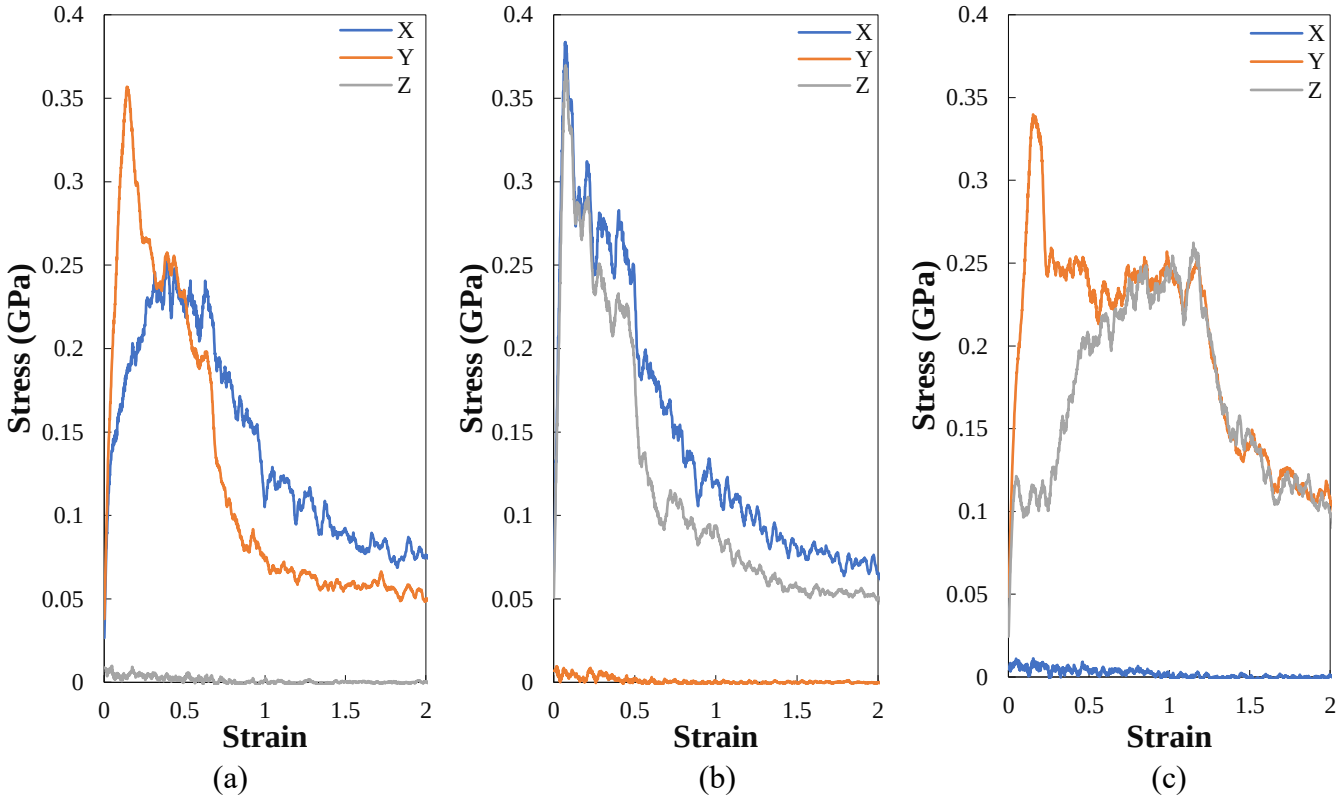

Fig. I.12. Stress-strain response of Structure 2 at a stretching temperature of 100 K: (a) XY equibiaxial stretching, (b) XZ equibiaxial stretching, (c) YZ equibiaxial stretching.

The polyethylene response is known to be sensitive to the mechanical loading mode (Zaïri et al., 2005; Hachour et al., 2014). The equibiaxial stress-strain response is provided in Fig. I.12 and can be compared to the uniaxial stress-strain response in Fig. I.8(b). The illustrative example concerns Structure 2 deformed at 100 K. For the uniaxial stretching, as explained above, the stress-strain curve has four distinct regimes before failure (manifested by the catastrophic stiffness decrease), along with a directional effect due to the crystal orientation. Different loading axis combinations for equibiaxial stretching show a great influence on the anisotropic stress-strain response. The equibiaxial stretchability before reaching the peak stress is significantly lower than that observed under uniaxial loading.

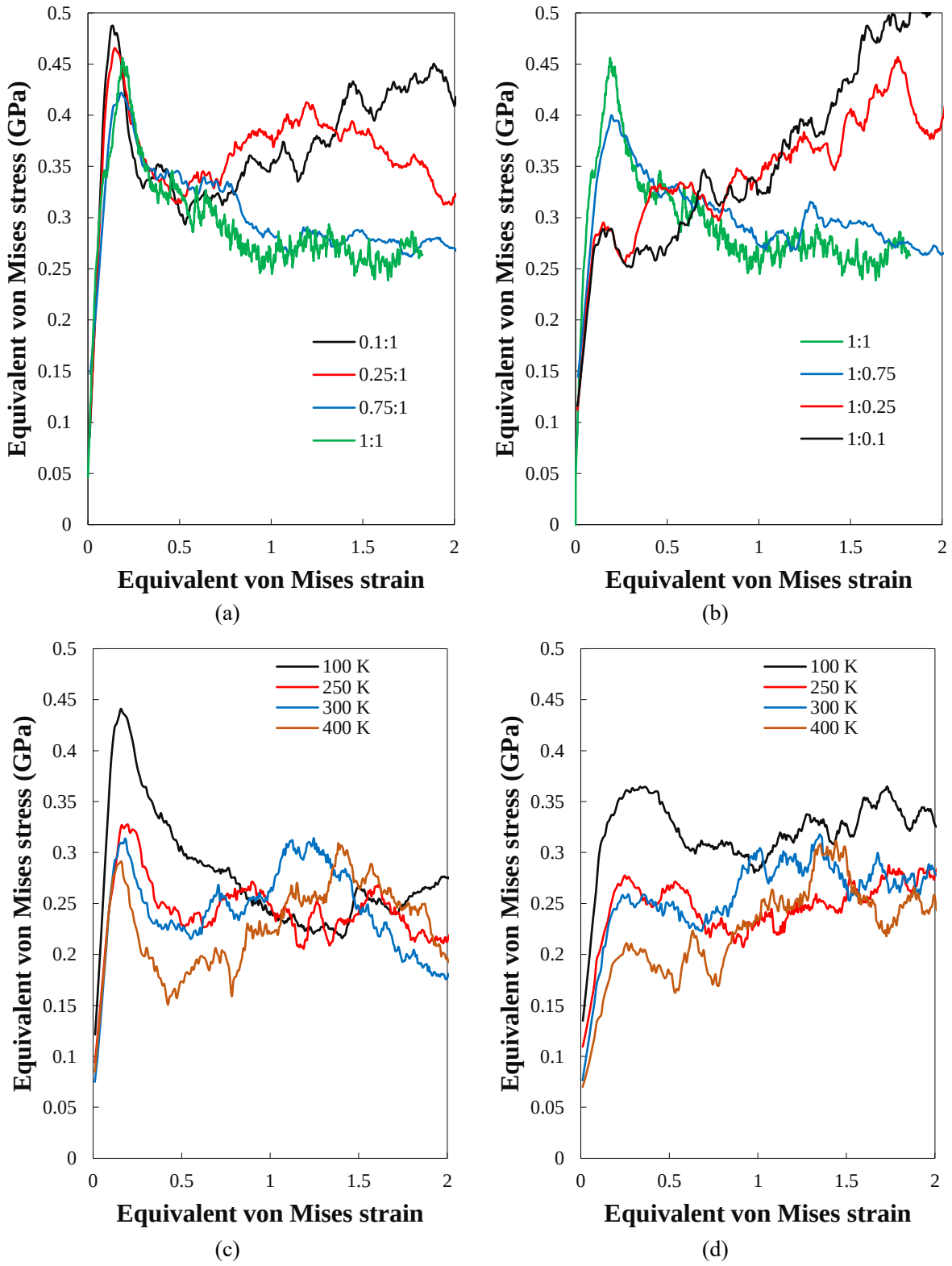

Fig. I.13. Biaxial stress-strain response of Structure 1: (a), (b) different biaxial strain ratios X:Y at a stretching temperature of 100 K, (c) different temperatures for a biaxial strain ratio 0.5:1, (d) different temperatures for a biaxial strain ratio 1:0.5.

For stretching axis combinations, the stress-strain curves of the same axis are also different.

This is the case of the stress-strain along X axis in XY (Fig. I.12(a)) and XZ (Fig. I.12(b)) planes. The elastic stiffness along X direction in XZ stretch axis combinations is much higher than in XY stretch axis combinations. The same phenomenon also occurs in Z axis in YZ (Fig. I.12(b)) and XZ (Fig. I.12(c)).

The response is plotted for different biaxial strain ratios X:Y in Fig. I.13 in terms of equivalent von Mises quantities. A global view at these plots shows that the yield strength and the post-yield response are strongly affected by the biaxial strain ratio. The strain ratios 1:0.1, 1:0.25 and 1:0.5 show a lower yield strength than their counterparts (0.1:1, 0.25:1 and 0.5:1) but a high strain-hardening ability. The temperature has a significant influence on the elastic stiffness and the stress magnitude.

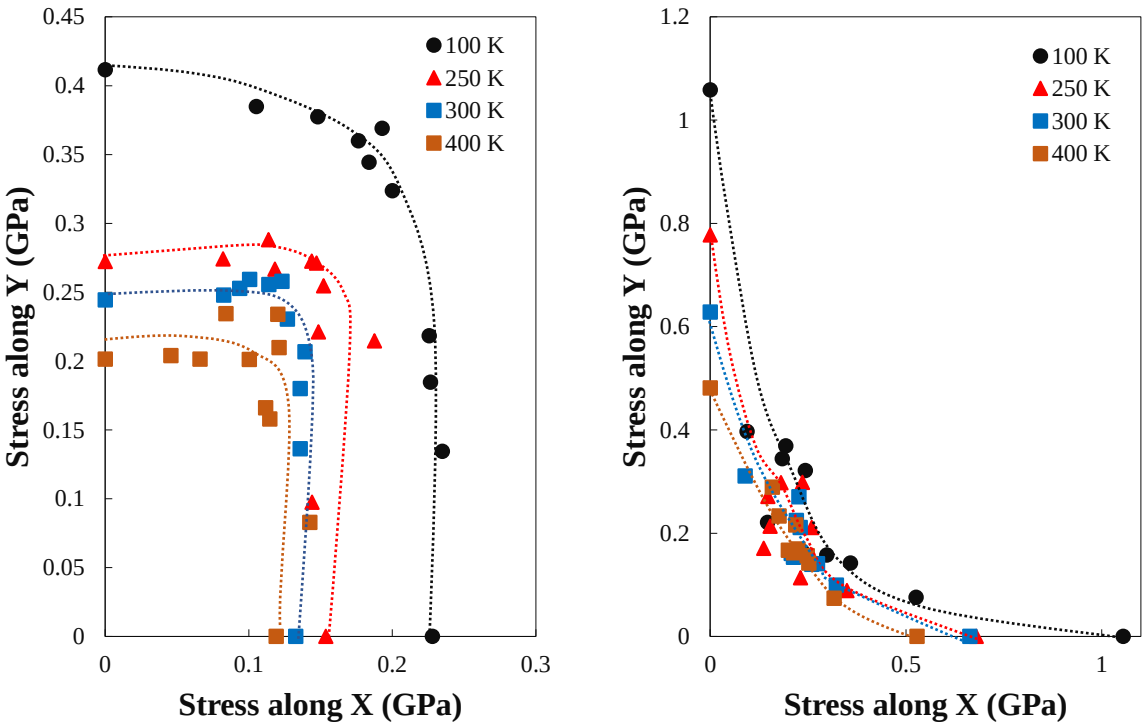

(a) (b)

Fig. I.14. Temperature effect on the biaxial response: (a) yield strength and (b) failure point.

Fig. I.14 reports the stresses at yield and at failure under different biaxial states such that envelopes are obtained. The material failure is identified as the point with the maximum stress. The yield envelope is found concave, whereas the failure envelope is convex. Due to the directional effect, the two envelopes exhibit an asymmetry relative to the main bisectrix. It can

be also observed that the increase in temperature leads to the decrease of the two envelopes.

I.4. Conclusion

MD simulations were carried out to investigate the crystallization of multi-chain polyethylene structures and the mechanical behavior under uniaxial and biaxial stretching loading. The simulations were conducted for different semi-crystalline polyethylene structures under various loading temperatures representing different polymer states (100 K: glassy state, 250 K and 300 K: transition state and 400 K: rubbery state). From the main results, the following conclusions can be drawn:

1) When side lengths change independently, polymer crystallinity in each direction is different. Structure composition and temperature have a great effect on the crystallinity parameters (i.e. crystallinity based on bond orientation and global order parameters). The higher the temperature, the lower the crystallinity of linear polyethylene and the longer the chain length, the lower the crystallinity.

2) The stress-strain curves obtained during the course of the uniaxial stretching show four distinct regimes before failure and the same structure has similar behavior under different stretching temperatures. Structure composition and temperature have a great effect on the different mechanical properties, such as elastic stiffness, plastic flow and failure. Besides, the strain decomposition concept allows to clearly highlight the main deformation mechanisms split into shear yielding and dilatational mechanisms. A directional effect is pointed out both on the uniaxial response and the underlying deformation micro-mechanisms.

3) The biaxial strain ratio has a significant effect on the different mechanical properties, especially the yield strength and the strain-hardening ability. Data are collected to construct yield and failure envelopes under a wide range of biaxial strain ratios and temperatures.

References

Abdul-Hameed, H., Messager, T., Zaïri, F., Naït-Abdelaziz, M., 2014. Large-strain viscoelastic-viscoplastic constitutive modeling of semi-crystalline polymers and model identification by deterministic/evolutionary approach. Computational Materials Science 90, 241-252.

Addiego, F., Dahoun, A., G'Sell, C., Hiver, J. M., 2006. Characterization of volume strain at large deformation under uniaxial tension in high-density polyethylene. Polymer 47(12), 4387-4399.

Anoukou, K., Zaoui, A., Zaïri, F., Naït-Abdelaziz, M., Gloaguen, J. M., 2013. Molecular dynamics study of the polymer clay nanocomposites (PCNs): Elastic constants and basal spacing predictions. Computational Materials Science 77, 417-423.

Anoukou, K., Zaoui, A., Zaïri, F., Naït-Abdelaziz, M., Gloaguen, J. M., 2015. Structural and thermodynamics properties of organo-modified montmorillonite clay. Physica E: Low-dimensional Systems and Nanostructures 65, 56-60.

Ayoub, G., Zaïri, F., Naït-Abdelaziz, M., Gloaguen, J. M., 2010. Modelling large deformation behaviour under loading-unloading of semicrystalline polymers: Application to a high density polyethylene. International Journal of Plasticity 26(3), 329-347.

Ayoub, G., Zaïri, F., Fréderix, C., Gloaguen, J. M., Naït-Abdelaziz, M., Seguela, R., Lefebvre, J. M., 2011. Effects of crystal content on the mechanical behaviour of polyethylene under finite strains: Experiments and constitutive modelling. International Journal of Plasticity 27(4), 492-511.

Bartczak, Z., Galeski, A., 2010. Plasticity of semicrystalline polymers. Macromolecular Symposia 294(1): 67-90.

Binder, K., 1995. Monte Carlo and Molecular Dynamics Simulations in Polymer Science. Oxford University Press, New York.

Brandrup, J., Immergut, E. H., Grulke, E. A., 1998. Polymer Handbook. 4th ed. New York: Wiley Interscience.

Brown, D., Clarke, J. H. R., 1991. Molecular dynamics simulation of an amorphous polymer under tension. 1. Phenomenology. Macromolecules 24(8), 2075-2082.

Capaldi, F. M., Boyce, M. C., Rutledge, G. C., 2004. Molecular response of a glassy polymer to active deformation. Polymer 45(4), 1391-1399.

Chen, C., Depa, P., Sakai, V. G., Maranas, J. K., Lynn, J. W., Peral, I., Copley, J. R., 2006. A comparison of united atom, explicit atom, and coarse-grained simulation models for poly(ethylene oxide). The Journal of Chemical Physics 124(23), 234901.

Cheng, J. J., Alvarado-Contreras, J. A., Polak, M. A., Penlidis, A., 2010. Chain entanglements and mechanical behavior of high-density polyethylene. Journal of Engineering Materials and Technology 132(1), 011016.

Faller, R., Muller-Plathe, F., 2002. Modeling of poly(isoprene) melts on different scales. Polymer 43(2), 621-628.

Fujiwara, S., Sato, T., 1997. Molecular dynamics simulations of structural formation of a single polymer chain: Bond orientational order and conformational defects. The Journal of Chemical Physics 107, 613-622.

Fujiwara, S., Sato, T., 2001. Structure formation of a single polymer chain. I. Growth of trans domains. The Journal of Chemical Physics 114, 6455-6463.

Fukunaga, H., Takimoto, J., Doi, M., 2002. A coarse-graining procedure for flexible polymer chains with bonded and nonbonded interactions. The Journal of Chemical Physics 116(18), 8183-8190.

Gaur, U., Wunderlich, B., 1980. The glass transition temperature of polyethylene. Macromolecules 13(2), 445-446.

Gee, R. H., Boyd, R. H., 1998. The role of the torsional potential in relaxation dynamics: A molecular dynamics study of polyethylene. Computational and Theoretical Polymer Science 8(1-2), 93-98.

Guo, Q., Zaïri, F., Guo, X., 2018. Thermodynamics and mechanics of stretch-induced crystallization in rubbers. Physical Review E 97, 052501.

Guo, Q., Zaïri, F., 2020. A physically-based thermo-mechanical model for stretch-induced crystallizable rubbers: Crystallization thermodynamics and chain-network crystallization anisotropy. International Journal of Plasticity 131, 102724.

Hachour, K., Zaïri, F., Naït-Abdelaziz, M., Gloaguen, J.M., Aberkane, M., Lefebvre, J.M., 2014. Experiments and modeling of high-crystalline polyethylene yielding under different stress states. International Journal of Plasticity 54, 1-18.

Hagita, K., Fujiwara, S., Iwaoka, N., 2018. Structure formation of a quenched single polyethylene chain with different force fields in united atom molecular dynamics simulations. AIP Advances 8, 115108.

Hagita, K., Fujiwara, S., Iwaoka, N., 2019. An accelerated united-atom molecular dynamics simulation on the fast crystallization of ring polyethylene melts. The Journal of Chemical Physics 150, 074901.

Han, J., Gee, R. H., Boyd, R. H., 1994. Glass transition temperatures of polymers from molecular dynamics simulations. Macromolecules 27(26), 7781-7784.

Hong, K., Rastogi, A., Strobl, G., 2004. A model treating tensile deformation of semicrystalline polymers: quasi-static stress- strain relationship and viscous stress determined for a sample of polyethylene. Macromolecules 37(26), 10165-10173.

Hossain, D., Tschopp, M. A., Ward, D. K., Bouvard, J. L., Wang, P., Horstemeyer, M. F., 2010. Molecular dynamics simulations of deformation mechanisms of amorphous polyethylene. Polymer 51(25), 6071-6083.

Jiang, Q., Zaïri, F., Frederix, C., Derrouiche, A., Yan, Z., Qu, Z., Liu, X., Zaïri, F., 2019. Crystallinity dependency of the time-dependent mechanical response of polyethylene: Application in total disc replacement. Journal of Materials Science: Materials in Medicine 30, 46.

Jiang, Q., Zaïri, F., Frederix, C., Yan, Z., Derrouiche, A., Qu, Z., Liu, X., Zaïri, F., 2019. Biomechanical response of a novel intervertebral disc prosthesis using functionally graded polymers: A finite element study. Journal of the Mechanical Behavior of Biomedical Materials 94, 288-297.

Kim, J. M., Locker, R., Rutledge, G. C., 2014. Plastic deformation of semicrystalline polyethylene under extension, compression, and shear using molecular dynamics simulation. Macromolecules 47(7), 2515-2528.

Kremer, K., Muller-Plathe, F., 2001. Multiscale problems in polymer science: Simulation approaches. MRS Bulletin 26(3), 205-210.

Lavine, M. S., Waheed, N., Rutledge, G. C., 2003. Molecular dynamics simulation of orientation and crystallization of polyethylene during uniaxial extension. Polymer 44, 1771-1779.

Li, J., Mulder, T., Vorselaars, B., Lyulin, A. V., Michels, M. A. J.,2006. Monte Carlo simulation of uniaxial tension of an amorphous polyethylene-like polymer glass. Macromolecules 39(22), 7774-7782.

Liao, L., Huang, C. Meng, C.,2018. Study on mechanical properties of polyethylene with chain branching in atomic scale by molecular dynamics simulation. Molecular Simulation 44(12), 1016-1024.

Makke, A., Perez, M., Lame, O., Barrat, J. L., 2009. Mechanical testing of glassy and rubbery polymers in numerical simulations: Role of boundary conditions in tensile stress experiments. The Journal of Chemical Physics 131(1), 014904.

Mayo, S. L., Olafson, B. D., Goddard, W. A., 1990. DREIDING: A generic force field for molecular simulations. The Journal of Chemical Physics 94(26), 8897-8909.

Meijer, H. E. H., 2004. Structure, deformation, and failure of flow-oriented semicrystalline polymers. Macromolecules 37(23), 8618-8633.

Nicholson, D. A., Rutledge, G. C., 2016. Molecular simulation of flow-enhanced nucleation in n-eicosane melts under steady shear and uniaxial extension. The Journal of Chemical Physics 145, 244903.

Pawlak, A., 2007. Cavitation during tensile deformation of high-density polyethylene. Polymer 48(5), 1397-1409.

Sanmartin, S., Ramos, J., Martinez-Salazar, J., 2012. Following the crystallization process of polyethylene single chain by molecular dynamics: The role of lateral chain defects. Macromolecular Symposia 312(1), 97-107.

Schrauwen, B. A. G., Janssen, R. P. M., Govaert, L. E., Meijer, H. E. H., 2004a. Intrinsic deformation behavior of semicrystalline polymers. Macromolecules 37(16), 6069-6078.

Schrauwen, B. A. G., Breemen, L. C. A, Spoelstra, A. B., Govaert, L. E., Peters, G. W. M., Meijer, H. E. H., 2004b. Structure, deformation, and failure of flow-oriented semicrystalline polymers. Macromolecules 37(23): 8618-8633.

Shepherd, J. E., 2006. Multiscale modeling of the deformation of semicrystalline polymers. Ph.D. Thesis at Georgia Institute of Technology.

Simoes, R., Cunha, A. M., Brostow, W., 2004. Molecular deformation mechanisms and mechanical properties of polymers simulated by molecular dynamics. e-Polymers 4(1), 067.

Takeuchi, H, Roe, R. J., 1991. Molecular dynamics simulation of local chain motion in bulk amorphous polymers. II. Dynamics at glass transition. The Journal of Chemical Physics 94, 7458-7465

van Dommelen, J. A. W., Parks, D. M., Boyce, M. C., Brekelmans, W. A. M., Baaijens, F.P.T., 2003. Micromechanical modeling of the elasto-viscoplastic behavior of semi-crystalline polymers. Journal of the Mechanics and Physics of Solids 51(3), 519-541.

Vu-Bac, N., Lahmer, T., Keitel, H., Zhao, J., Zhuang, X., Rabczuk, T., 2014. Stochastic predictions of bulk properties of amorphous polyethylene based on molecular dynamics simulations. Mechanics of Materials 68, 70-84.

Xiong, B., Lame, O., Seguela, R., Men, Y., 2018. Micro/macro-stress relationship and local stress distribution in polyethylene spherulites upon uniaxial stretching in the small strain domain. Polymer 140, 215-224.

Yi, P., Rutledge, G. C., 2001. Molecular simulation of bundle-like crystal nucleation from n-eicosane melts. The Journal of Chemical Physics 135, 024903.

Yoon, D. Y., Smith, G. D., Matsuda, T., 1993. A comparison of a united atom and an explicit atom model in simulations of polymethylene. The Journal of Chemical Physics 98, 10037-10043.

Zaïri, F., Naït-Abdelaziz, M., Woznica, K., Gloaguen, J. M., 2005. Constitutive equations for the viscoplastic-damage behaviour of a rubber-modified polymer. European Journal of Mechanics A/Solids 24(1), 169-182.

Zhang, X., Li, Z., Lu, Z., Sun, C., 2001. Molecular dynamics simulation of the linear low-density polyethylene crystallization. The Journal of Chemical Physics 115, 3916.

Chapter II

Uniaxial Stretching and Shape Memory Behavior of Branched Amorphous Polyethylene from Molecular Dynamics

Chapter II. Uniaxial stretching and shape memory behavior of branched amorphous polyethylene from molecular dynamics[2]

Abstract

The current work investigates the effects of branching and temperature on the mechanical properties and shape memory properties of branched polyethylene. The results show that the mechanical properties of low-density polyethylene are strongly influenced by the length, number and temperature of the branched chains. The lower the temperature, the lower the modulus of elasticity. When the length is longer and the number is smaller, the stress in the hardening phase is higher. For shape memory properties, we found that the fewer and shorter the branched chains, the better the shape memory properties, and the shape memory behavior can promote the repolymerization and crystallization of the structure, which will cause the enhancement of stress hardening.

Keywords: Polyethylene; Mechanical properties; Shape memory; Molecular dynamics.

[2] This chapter is based on the following paper: Yan, Z., Zaoui, A., Zaïri, F., 2022. Uniaxial stretching and shape memory behavior of branched amorphous polyethylene. Chinese Journal of Physics 79, 6-12.

II.1. Introduction

Polyethylene (PE) is becoming increasingly important in industries due to its performant mechanical properties and moldability. In order to expand the versatility of its use, it is important to have comprehensive features and corresponding mechanisms. In fact, different molecular structures result in different properties of polyethylene (Omar et al., 2012; Vicente-Alique et al., 2015).

The different properties of polyethylene are based primarily on density and the degree of molecular branching. When the single chains of polyethylene are linear or approximately linear, as high-density polyethylene (HDPE), the molecules stack and pack well during the crystallization process. When the linear chains are longer, the material is called ultra-high molecular weight polyethylene (UHMWPE) and stacks and packs molecules much better. In contrast, low-density polyethylene (LDPE), such as linear low-density polyethylene (LLDPE) and cross-linked polyethylene (PEX) (Liao et al., 2018), have molecules that are loose and do not stack and pack well, whereas LDPE is tough and flexible. Which is especially important. The effect of these different molecular structures on properties has attracted extensive research interest. Let us note here that the most important is the deformation mechanism of the mechanical properties (Ramachandran et al., 2008; Yan et al., 2021). Many experiments have been devoted to the study of the relationship between structure and properties in polymers, such as small-angle X-ray diffraction, small-angle neutron scattering and proton magnetic resonance.

With the continuous improvement of computer computing power, molecular simulation has become an important tool for studying the characteristics of complex material systems. Brown and Clarke (1991) qualitatively obtained the deformation behavior of polyethylene-like amorphous polymers in uniaxial tensile simulations at higher strain rates than experimental ones. The autohrs previous studies (Yan et al., 2021) adopted united-atom (UA) model to model the semi-crystalline polyethylene system in the simulation in order to investigate the deformation mechanisms and the influence of temperature, chain number and chain length on the deformation mechanisms. They found that the stress-strain curve of polyethylene has four distinct regimes: elastic, yield, softening and hardening. It is also found that the elastic regime

and yield are mainly intermolecular chain interactions, while the strain-hardening state is mainly intramolecular interactions. Liao, Huang and Meng (2018) used molecular dynamics to study the mechanical properties of polyethylene with short branch chain. The results show that the longer length of chain branching induces lower density and higher yield of branched polyethylene. In addition, more branched chains bring higher density and lower yield of branched polyethylene. However, these studies are quite limited. For example, the effect of long branched chains and a large number of branched chains on the properties of polyethylene has not been better studied. There have been many previous studies on shape memory property (Shi et al., 2019, 2020). In Shi's study, the molecule dynamic (MD) simulations were used to characterize the property of shape memory polyurethane (SMPU) and silicon dioxide/shape memory polyurethane (SiO_2/SMPU) composite from the atomistic scale. The shape memory property of polyurethane is largely dependent on molecular self-aggregation and thermal-induced molecular diffusion. They suggested set the melting point of soft segment as the target temperature for bring SMPU to the optimal self-recovery capacity.

The purpose of this study is to investigate the uniaxial tensile deformation and shape memory properties of branched polyethylene in molecular dynamics simulations using UA model. In this chapter, we investigate the stress-strain response of branched polyethylene for different branched chain lengths, number of branched chains and temperatures. The stress-strain behavior of polyethylene deformation and its dependence on strain rate and temperature are investigated and compared with previous theoretical and experimental results. To investigate the shape memory properties of branched polyethylene, we applied temperature-induced shape memory behavior on different structures after stretching at different stretching temperatures and performed uniaxial stretching on the structures after shape memory behavior to compare the mechanical properties before and after shape memory behavior.

II.2. Computational details

II.2.1. Molecular structures of polyethylene chains

In this work, we adopted the UA model to model the branched polyethylene systems. In the UA model, each Methyl-, Ethyl- and Butyl-groups (i.e. the CH, CH_2, CH_3 monomer) (Yi et al., 2001;

Capaldi et al., 2004; David et al., 2016; Yan et al., 2021) will be considered as a single bead (Fig. II.1(a)). By this way, the number of atoms included in the simulation is reduced which will results in fewer interaction between atoms, and consequently the calculation time becomes shorter.

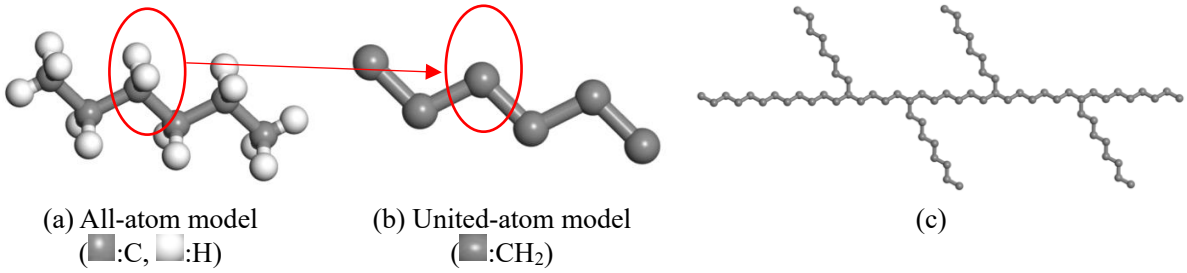

(a) All-atom model (:C, :H) (b) United-atom model (:CH_2) (c)

Fig. II.1. Polyethylene models for: (a) all-atom and (b) United-atom models and (c) single branched polyethylene chain.

The Monte Carlo self-avoiding random walks method is employed here to build the different branched polyethylene structures. During the chain generation process, a face-centered cubic (FCC) lattice superimposed on the simulation cell is used, with nearest neighbor distance of 1.53 Å (Yi et al., 2001; Lavine et al. 2003; Capaldi et al., 2004; Vu-Bac et al., 2014; David et al., 2016; Yan et al., 2021). Three different branched polyethylene molecules will be built to study the influence of the different branched chain lengths, number of branched chains and temperatures on the mechanical properties. The length and unmber of main and branched chain in three structures is given in Table II.1. These include a large number of short branch chains (Structure 1), a small number of short branch chains (Structure 2) and long branched chains (Structure 3).

Table II.1. Three branched polyethylene systems.

	Chain length	Chain number
Main chain	1000	10
Branch structure 1	10	100 (on each chain)
Branch structure 2	10	10 (on each chain)
Branch structure 3	100	10 (on each chain)

II.2.2. Force field

The DREIDING force field (Mayo et al., 1990; Kim et al., 2014; Yuji et al., 2016; Bowman et al., 2019), special for the UA model, was used in this work. This potential describes the energy

compensation for deviations from the equilibrium position as a function of bond expansion and bond angle bending during molecular motion (Kremer et al., 2001; Faller et al., 2002; Fukunaga et al., 2002; Hagita et al., 2019). It also includes related functions that describe the change in energy when a chemical bond is rotated, and the interactions between non-bonded particles. It can be expressed as:

$$E_{val} = E_{bond} + E_{angle} + E_{dihedral} + E_{nb} \quad \text{(II.1)}$$

The functional expression and respective parameters for each part of the force field for the UA model of polyethylene system are listed in Table II.2.

Table II.2. Functional form of force field and potential parameters used for MD calculations.

Interaction	Form	Parameters
Bond Length	$E_{bond} = \frac{1}{2}K_b(r - r_0)^2$	$K_b = 700\,\text{kcal/mol}\,, r_0 = 1.53\text{Å}$
Bond Angle	$E_{angle} = \frac{1}{2}K_\theta(\theta - \theta_0)^2$	$K_\theta = 120\,\text{kcal/mol/rad}^2\,, \theta_0 = 109.3°$
Dihedral Angle	$E_{dihedral} = \sum_{i=0}^{4} C_i(\cos\phi)^i$	$C_0 = 1.736, C_1 = -4.49,$ $C_2 = 0.776, C_{3=}6.99\,, C_{4=}0$ (kcal/mol)
Non-bonded	$E_{non-bond} = 4\varepsilon\left[\left(\frac{\sigma}{r}\right)^{12} - \left(\frac{\sigma}{r}\right)^{6}\right], \text{r} \le r_c$	$\sigma = 4.01\text{Å}, \varepsilon = 0.112\,\text{kcal/mol}$

II.3. Results and discussion

II.3.1. Uniaxial stretching

Table II.3. Parameter setting for four steps during the relaxation.

Process	Ensemble	Temperature (K)	Timestep (fs)	Steps	Time (ns)
1	NVT	500	1	2000000	2
2	NPT (aniso)	500	0.5	2000000	1
3	NPT (aniso)	500-$T_{desired}$	0.5	500000	0.25
4	NPT (aniso)	$T_{desired}$	0.5	3000000	1.5

The large-scale molecular dynamics code LAMMPS was used here to minimize the energy of the initial structure followed by an equilibration sequence before mechanical loading of polyethylene. The minimize relaxes any high energy configurations that crested during the Monte Carlo self-avoiding random walks. The structures after minimize step of each polyethylene model were subjected to a four-stages equilibration for final equilibrium state, as shown in Table II.3. The Nosé-Hoover Thermostat and Barostats were applied to control

temperature and pressure. Periodic boundary conditions were employed in all three directions to approximate bulk-like behavior. In this section, to obtain the mechanical properties of branched low-density polyethylene, we will first perform uniaxial deformation, NPT ensemble was used in this step, that is, in the stretching direction, the polyethylene systems were stretched at the strain rate of 10^{10} s^{-1}, and the face perpendicular to the direction of stretching, free shrinkage.

Table II.4. Parameter setting during the deformation.

Process	Ensemble	Temperature	Time step (fs)	Strain rate
Tensile	NPT	$T_{desired}$	1	10^{10} s^{-1}

The stretch simulations were performed for three different structures for a total of 20000 or 11000 total united atoms. Four temperatures were examined: 100 K, 250 K,300 K and 400 K, as shown in Table II.4. These temperatures were purposely chosen to select a lowest one (100 K), which corresponds to a temperature just below and above the glass transition temperature (250 K and 300 K), and a temperature above the glass transition temperature (400 K).

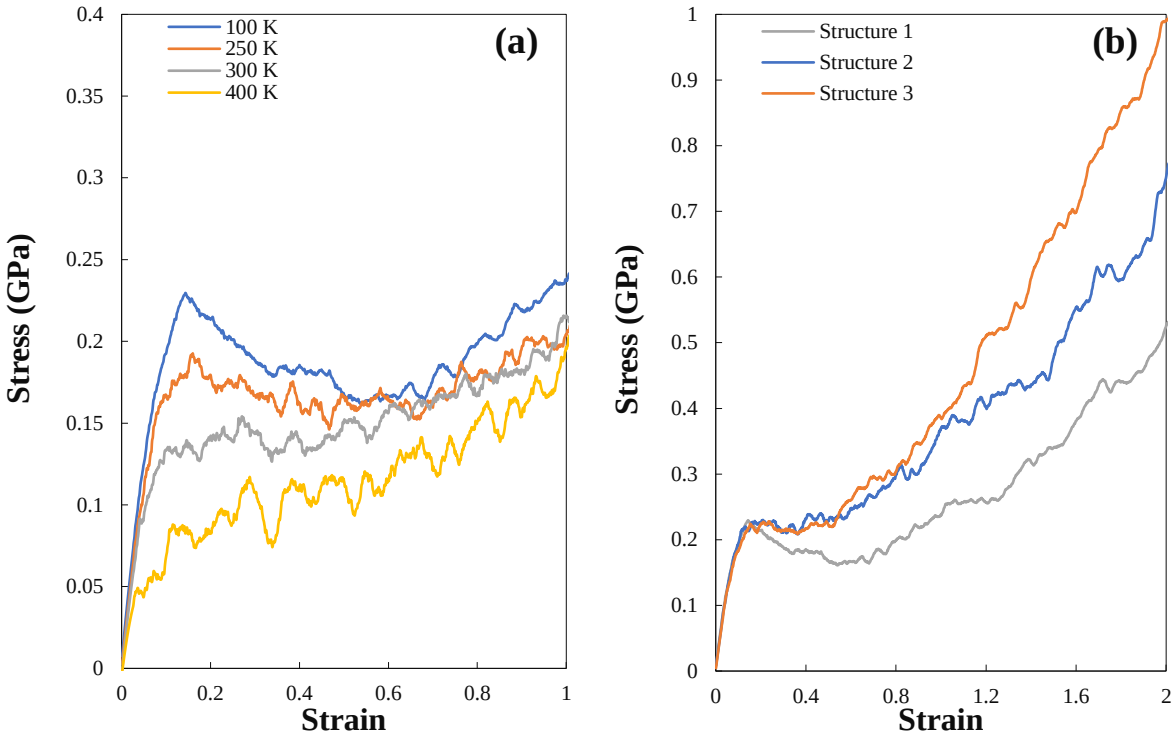

Fig. II.2. Stress-strain variation for: Structure 1 at 100 K (a) and three structures at 100 K (b).

From Fig. II.2 (a), it is clear that temperature has a great influence on the mechanical properties

of branched polyethylene. As the temperature rises, the Young's modulus of the material becomes larger, and the softening is also evident after yielding point.

Table II.5 gives the Young's modulus in the elastic regime. It can be seen that Structure 1 and Structure 2, with the same length and different number of branched chains, have similar Young's modulus within the error range [±5]. Structure 3 has a lower Young's modulus than others, indicating that the elastic modulus decreases when the branched chains are longer, what means that short branch chains promote crystallization of the molecule. Fig. II.2 (b) shows the stress-strain curves of the three structures at a temperature of 100 K. For short branch structures, Structure 1 which contains larger number of branch chains has lower hardening strength than Structure 2, but the resistance to fracture is higher (higher fracture strain). For long branched structures (Structure 3), the hardening strength is stronger than that of short branch chains during the initial hardening phase, but the resistance to fracture is lower and the fracture strain is smaller.

Table II.5. Young's modulus of three structure at 100 K.

Structure	Structure 1	Structure 2	Structure 3
Young's modulus (MPa)	1900	1905	1847

Fig. II.3 displays the stress versus temperature at 10% strain (a) and 200% strain (b) for different structures. For the small strain level (10% strain), we can see that, branched polyethylene with short branch chain (Structure 1) have higher strength than one with long branched chain (Structure 3). This is because the short chain is advantageous to the crystallization of the material, which results in a higher degree of crystallinity. For lager stain level (200 % strain), it is obvious that the longer branch chain can stand greater stretching force due to entanglement of long chain.

II.3.2. Shape memory behavior and results

Smart polymers are materials that can adapt their shape and physical properties by responding to external stimuli. Shape memory polymers (SMPs) can recover their original shape from a temporarily deformed state upon responding to an external stimulus such as temperature, light, chemical, electrical or electromagnetic field.

II.3.2.1. Loading and unloading

In order to make the simulation about the shape memory behavior of branched polyethylene, the material is first stretched until the strain is 100%, and then the stretch is removed. Since this is viscoelastic-plastic material, we know that when the stress returns to zero, the shape of the material will not be completely restored, and the strain that is not restored is inelastic strain, which includes plastic deformation and the resulting voids.

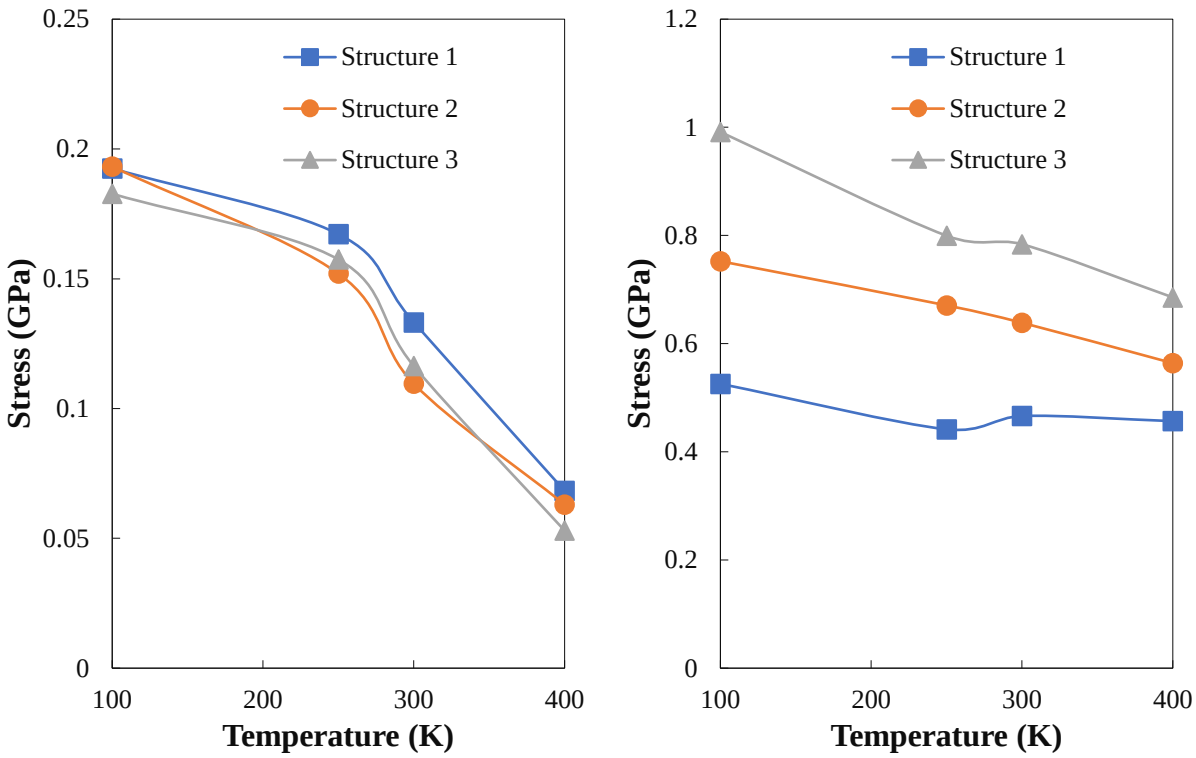

Fig. II.3. Stress versus temperature at 10% strain (a) and 200% strain (b) for different structures.

The stress-strain curves, for loading and unloading, are shown in the Fig. II.4. We may remark that for branched polyethylene materials, when the stress returns to zero, the recovered elastic strain is about 0.2 and the inelastic one is about 0.8, while the inelastic strain for branched polyethylene is less than 0.8.

II.3.2.2. Shape memory behavior

The shape memory of polyethylene was achieved according to four steps after unloading: cooling down, shape fixation, warm up and shape memory, as summarized in Table II.6.

First, the material, after unloading stress, is cooled down to 100 K (low temperature), and stress relaxation is performed at low temperature, then the relaxed structure is warmed up to 450 K (higher than T_g). Finally, shape memory simulation is performed at high temperature.

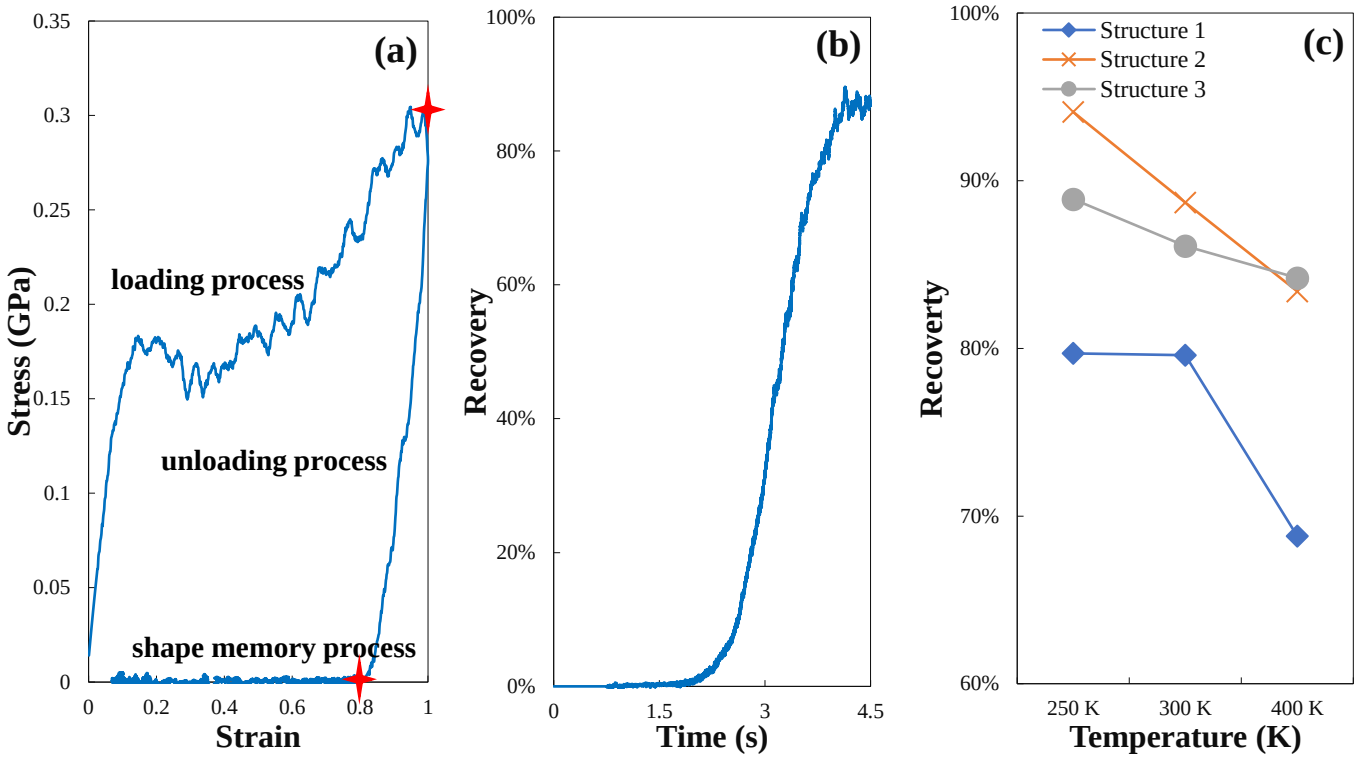

Fig. II.4. Response to shape memory behavior for: Stress-strain variation (a); Recovery rate evolution (b); and Temperature and structure response of recovery rate (c).

Table II.6. Four shape memory steps.

step	Ensemble	Temperature (K)
Cool down	NVT	T $_{deformation}$ → 100 K
Stress relaxes	NPT	100 K
Warm up	NPT	100 K → 450 K
Shape memory	NPT	450 K

Fig. II.4(a) displays the stress evolution of branched polyethylene, which shows that the stress is always maintained at 0 during the shape memory process. The recovery R will be defined as:

$$R = \left(1 - \frac{\varepsilon}{\varepsilon_{max}}\right) \times 100 \quad \text{(II.2)}$$

where ε and ε_{max} are, respectively, the remanent strain stored in the material and its maximum value. The shape memory response is shown in Fig. II.4(c) in which it can be seen that the higher the stretching temperature, the lower the final strain recovery. From Fig. II.4(c), we can see that for the structures with the branched chain of the same length, when the number of

branched chains is larger, the strain recovery is smaller, and the shape memory performance became weaker. Moreover, it is also clear that for the same number of branched chains, when the branched chain length is short, the strain recovery is higher.

II.3.3. Shape memory effect

The evolution of mechanical properties caused by shape memory behavior will be studied in this part. The structures previously obtained will undergo the two-relaxation step presented in Table II.7. This is to obtain the stable structure at different temperatures followed by being stretched at strain rate of 10^{10} s^{-1} and various temperatures.

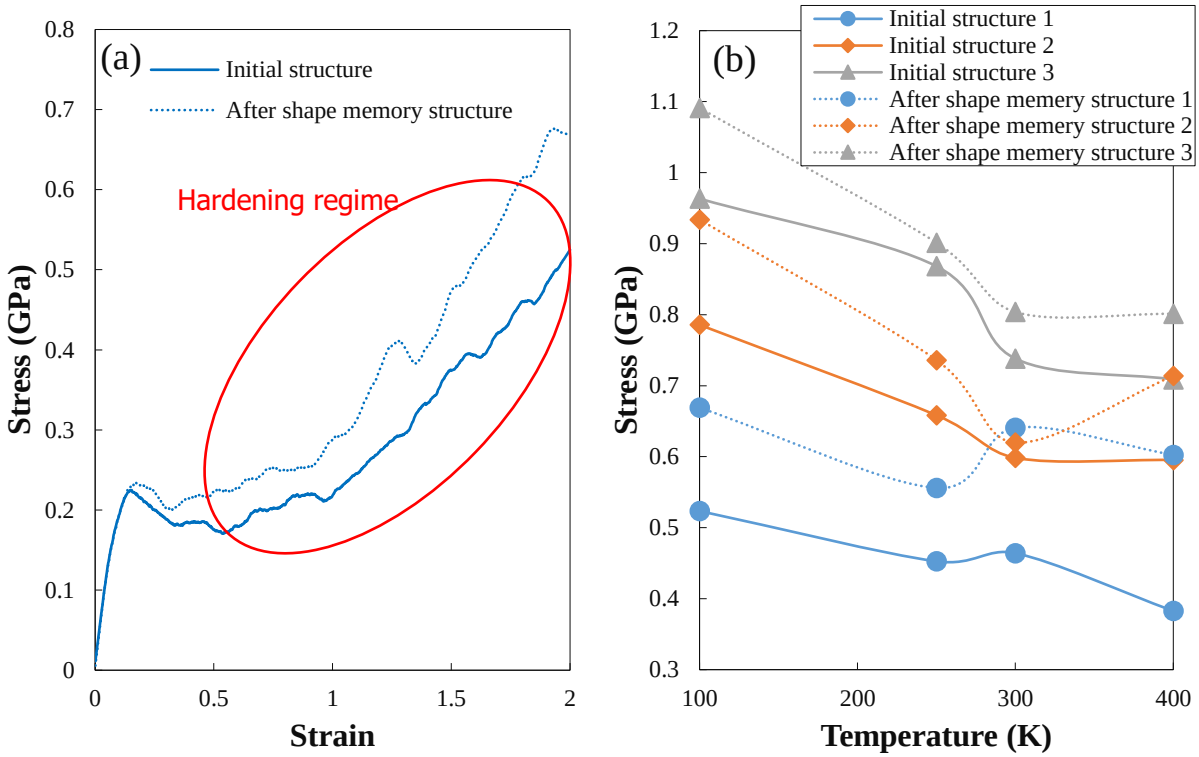

Fig. II.5. Stress-strain relationship at: 100 K for structure 1 (a), and stress versus temperature (b) at 200% strain before and after shape memory.

Table II.7. Parameter setting for four steps during the relaxation.

Process	Ensemble	Temperature (K)	Timestep (fs)	Steps
1	NPT (aniso)	450-$T_{desired}$	0.5	1250 steps/K
2	NPT (aniso)	$T_{desired}$	0.5	3000000

The stress-strain curve of branched polyethylene before and after shape memory behavior at 100 K were shown in Fig. II.5(a) and the stress at 200% strain of different structure for different temperature were shown in Fig. II.5(b). Through the study of the stress-strain curve, we can

find that the shape memory behavior has a greater influence on the mechanical properties of branched chain, especially the hardening regime. It is because the shape memory behavior leads to the re-polymerization and crystallization of the chain, and the the branched chain facilitate the re-polymerization. From Fig. II.5(b), it is evident that the stress hardening is increased for all structures after the shape memory behavior.

II.4. Conclusion

Molecular dynamics simulations were used here in order to study the mechanical properties and shape memory behavior of branched low-density polyethylene in uniaxial stretching. We have found that the stress-strain variations obtained during the progress of uniaxial stretching show four distinct regimes before failure, and the same structure has similar behavior under different temperatures. Structure composition and temperature have a great effect on the different mechanical properties, such as elastic stiffness, plastic flow and failure. Moreover, the response of the memory behavior indicates that the material can restore the original shape well, the lower the temperature, the higher the recovery rate. The material through the shape memory behavior, has better mechanical properties.

References

Bowman, A.L., Mun, S., Nouranian, S., Huddleston, B.D., Gwaltney, S.R., Baskes, M.I., Horstemeyer, M.F., 2019. Free volume and internal structural evolution during creep in model amorphous polyethylene by Molecular Dynamics simulations. Polymer 170, 85-100.

Brown, D., Clarke, J.H.R., 1991. Molecular dynamics simulation of an amorphous polymer under tension. 1. Phenomenology. Macromolecules 24(8), 2075-2082.

Capaldi, F.M., Boyce, M.C., Rutledge, G.C., 2004. Molecular response of a glassy polymer to active deformation. Polymer 45, 1391-1399.

Faller, R., Muller-Plathe, F., 2002. Modeling of poly(isoprene) melts on different scales. Polymer 43(2), 621-628.

Fukunaga, H., Takimoto, J., Doi, M. 2002. A coarse-graining procedure for flexible polymer chains with bonded and nonbonded interactions. The Journal of chemical physics 116(18), 8183-90.

Hagita, K., Fujiwara, S. and Iwaoka, N., 2019. An accelerated united-atom molecular dynamics simulation on the fast crystallization of ring polyethylene melts. The Journal of chemical physics 150, 074901.

Higuchi, Y., and Kubo, M., 2016. Coarse-grained molecular dynamics simulation of the void growth process in the block structure of semicrystalline polymers. Modelling and Simulation in Materials Science and Engineering 24, 055006.

Kim, J.M., Locker, R., Rutledge, G.C., 2014. Plastic deformation of semicrystalline polyethylene under extension, compression, and shear using molecular dynamics simulation. Macromolecules 47, 2515-2528.

Kremer, K. and Müller-Plathe, F., 2001. Multiscale problems in polymer science: simulation approaches. MRS Bulletin 26(3), 205.

Lavine, M.S., Waheed, N., Rutledge, G.C., 2003. Molecular dynamics simulation of orientation and crystallization of polyethylene during uniaxial extension. Polymer 44, 1771-1779.

Liao, L., Huang, C. and Meng, C., 2018. Study on mechanical properties of polyethylene with chain branching in atomic scale by molecular dynamics simulation. Molecular Simulation 44, 1016-1024.

Mayo, S.L., Olafson, B.D., Goddard, W.A., 1990. DREIDING: A generic force field for molecular simulations. The Journal of Chemical Physics 94(26), 8897-8909.

Nicholson, D. A. and Rutledge, G.C., 2016. Molecular simulation of flow-enhanced nucleation in n-eicosane melts under steady shear and uniaxial extension. The Journal of chemical physics 145, 244903.

Omar, M.F., Akil, H.M., Ahmad, Z.A., 2012. Effect of molecular structures on dynamic compression properties of polyethylene. Materials Science and Engineering: A 538, 125-134.

Ramachandran, R., Beaucage, G., Kulkarni, AS., et al., 2008. Persistence length of short-chain branched polyethylene. Macromolecules 41, 9802-9806.

Shi, S., Liu, Q., Xu, T. and Oeser, M., 2019. Study on the effect of transition temperature on shape memory behavior in polyurethane based on molecular dynamics simulation. Materials Research Express 6(11), 115323.

Shi, S., Xu, T., Wang, D. and Oeser, M., 2020. The difference in molecular orientation and interphase structure of SiO2/shape memory polyurethane in original, programmed and recovered states during shape memory process. Polymers 12, 1994.

Vicente-Alique, E., Vega, JF., Robledo, N., et al., 2015. Study of the effect of the molecular architecture of the components on the melt rheological properties of polyethylene blends. Journal of Polymer Researc 22, 1-11.

Vu-Bac, N., Lahmer, T., Keitel, H., Zhao, J., Zhuang, X., Rabczuk, T., 2014. Stochastic predictions of bulk properties of amorphous polyethylene based on molecular dynamics simulations. Mechanics of Materials 68, 70-84.

Yan, Z., Zaoui, A., Zaïri, F., 2021. Crystallization and mechanical behavior of semi-crystalline polyethylene. Physica Scripta 96(1), 125729.

Yi, P., Rutledge, G.C., 2001. Molecular simulation of bundle-like crystal nucleation from n-eicosane melts. The Journal of chemical physics 135, 024903.

Chapter III

Physical and Mechanical Properties of Filled Vulcanized Rubber by Molecular Dynamics Simulations

Chapter III. Physical and mechanical properties of filled vulcanized rubber by molecular dynamics simulations[3]

Abstract

The purpose of this study is to investigate -at nanoscale- *cis*-Polyisoprene(*cis*-PI), the main component of natural rubber. This system is vulcanized by adding elemental sulfur to *cis*-PI and vulcanizing at high temperature to obtain vulcanized rubber. The study is extended to *cis*-PI including different amounts of fullerenes to the vulcanized rubber at high temperature in order to obtain carbon black filled vulcanized rubber. The physical and thermodynamic properties of vulcanized rubber as well as filled vulcanized rubber were studied to shed light on the effects of vulcanization and reinforcement on natural rubber. Besides, the mechanical response was quantified upon stretching-retraction loading sequences and the related nonlinear and inelastic properties were studied. The interaction between fullerenes and *cis*-PI atoms and the aggregation configuration of *cis*-PI atoms around fullerenes were analyzed in details by introducing local number density and potential mean force (PMF) through radial distribution function (RDF).

Keywords: Natural rubber; Vulcanization; Nanofiller; Interface; Configuration; Molecular dynamics.

[3] This chapter is based on the following paper: Yan, Z., Zaoui, A., Zaïri, F.. Physical and mechanical properties of filled vulcanized rubber by molecular dynamics simulations. Under review.

III.1. Introduction

Natural rubber is an elastomeric polymer with high molecular weight and whose main component is *cis*-Polyisoprene (*cis*-PI). It is widely used in industry due to its scalable mechanical properties and low masses (Sheiko et al., 2019). It has nonetheless the disadvantages of low elasticity, low tensile strength and low abrasion resistance, which limit its applications. Therefore, it is important to think about improving its intrinsic properties by proceeding with other methods (Sethulekshmi et al., 2022).

The most popular method to improve the mechanical and thermomechanical properties of natural rubber is to vulcanize it (Akiba et al., 1997; Mark et al., 2013). The process of vulcanization is to heat the rubber and sulfur together to form crosslinks between the single chains of rubber. Considerable experimental studies have been devoted to elaboration and characterization of crosslinked rubbers. To name a few, Zhao et al. (2011), Chaikumpollert et al. (2012), Kashihara et al. (2019) and Kim et al. (2020) used experimental means to study the crosslinking process and the effect of crosslinking on properties and especially the tensile strength. However, only few theoretical studies were developped so far. Note for example continuum-based (Guo et al., 2018) and coarse-grained (Yagyu et al., 2018) models that were developed to predict the tensile strength of crosslinked rubbers.

Another approach enhancing durability and strength consists to add nanofillers into the rubber, the most widely used being carbon black (CB) (Yazdani et al., 2018; Gao et al., 2019; Jian et al., 2019). The structure of CB is composed of CB particles aggregated by van der Waals forces. Therefore, each CB structure is different, depending on the particle size, aggregation size, etc. Among them, the most frequently used materials are fullerenes in zero dimension, carbon nanotubes (CNT) in one dimension, and graphene in two dimensions. Researchers have developed a great interest in studying natural rubber-based nanocomposites containing CB. Various properties of NR composites that can be enhanced by filling the NR matrix with CB, including but not limited to: graphene, CNT or fullerenes (C_{60}). Yazdani et al. (2018) studied the effect of CNT on polyethylene (PE). They found that CNT increases the tensile strength of

LDPE-CNT and HDPE-CNT composites in the studied concentration range lying between 0.79 and 2.63 wt%. Jian and Lau (2019) found that the scale, weight fraction and good dispersion state of the nanofiller of nanocomposites have a great influence on the resistance to time-dependent deformation. In addition, the experiments of Gao et al. (2019) showed that when the pre-treatment temperature is lower than 450 °C, the 300% modulus of rubber increases with the pre-treatment temperature increase; when the pre-treatment temperature is higher than 450 °C, the conclusion is the opposite.

Based on today's advanced computers, there is an increasing interest in using molecular dynamics simulations (MD) to study the properties of complex material systems (Yan et al., 2021). However, so far, only a few previous studies have dealed with MD applied on rubber filled with carbon nanoparticles. Li et al. (2017) used MD to simulate the properties of graphene-filled polymers and found that after adding graphene reinforcements, the Young's modulus of the polymer composites increases by about 150%, the shear modulus increases by 27.6%, and the hardness increases by 27.6%. In addition, the average coefficient of friction and wear rate of the polymer composites were reduced by about 35% and 48%, respectively. In the same context, He et al. (2013), Kwon et al. (2013) and Gong et al. (2016) demonstrated the MD ability to quantitatively predict the thermal conductivity of polymers.

Based on the aforementioned research, this chapter quantitatively studies the effects of vulcanization and nanofiller on the physical and mechanical properties of rubber by means of MD simulation. In addition, the packing on the surface of the filler is also analyzed. For this purpose, natural rubber-CB composites were investigated, where the rubber melt consists of 30 single chains ($C_{170}H_{274}$) containing 34 monomers (C_5H_8), and C_{60}, whose amount is in the range between 0 and 26.42 phr (per hundred rubber). By creating aggregates, we can study the effect of the number of fullerenes on the mechanical and thermodynamic properties of rubber-based materials.

III.2. Structure and potential

The explicit atom model (Kang et al., 2019; Sharma et al., 2020; Zhang et al., 2021) adopted

here for intial *cis*-PI model is generally accepted. The monomer atomic formula is C_5H_8 as shown in Fig. III.1(a). Each *cis*-PI single chain is a polymeric chain consisting of 34 monomers. The thirty chains are then heated and melted to form a *cis*-PI melt (Fig. III.1(b)).

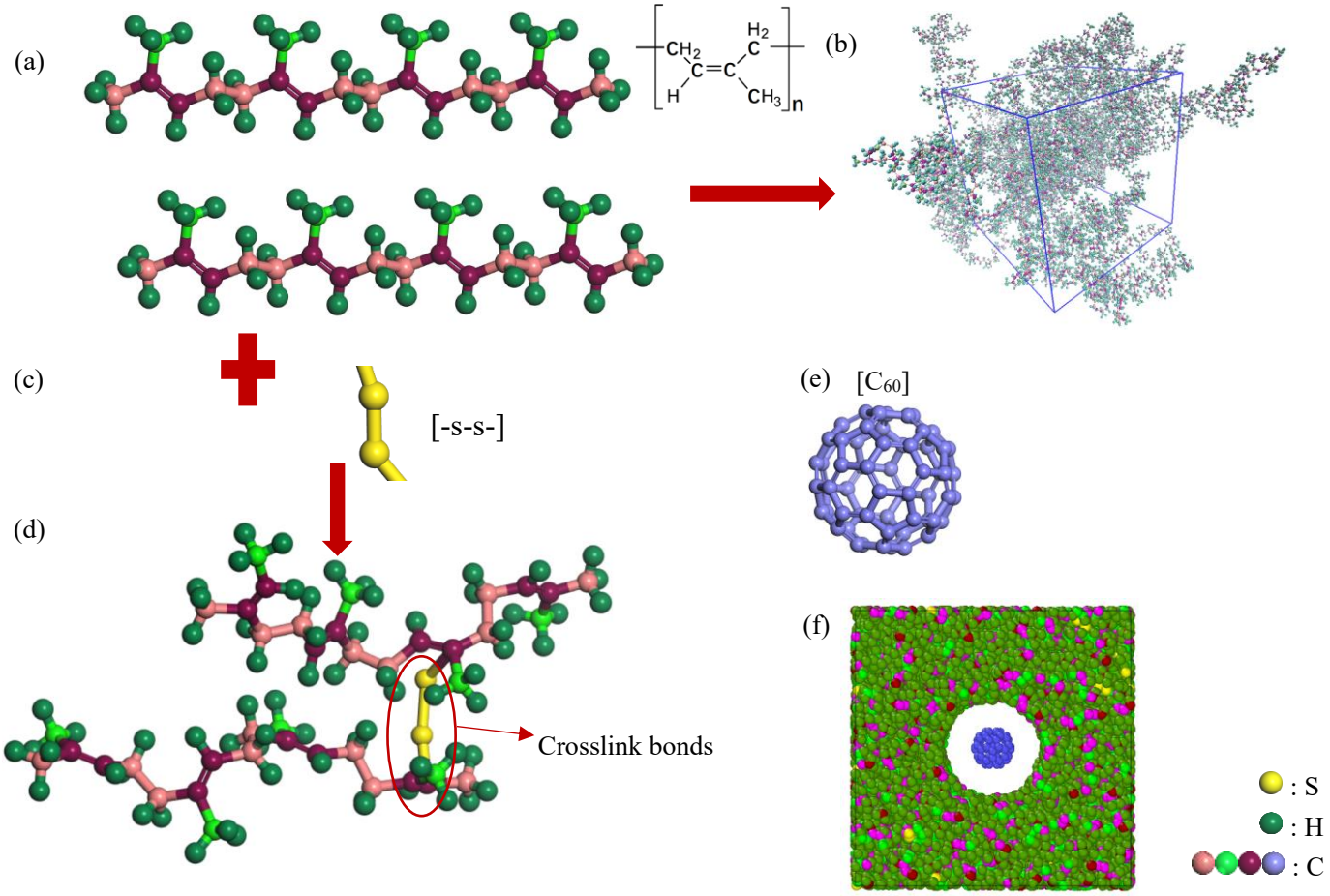

Fig. III.1. Structures used in this study: (a) *cis*-PI chains, (b) natural rubber simulation cell, (c) elemental sulfur, (d) vulcanized natural rubber, (e) fullerene molecules (C_{60}) and (f) filled vulcanized natural rubber.

Here, we adopt the polymer consistent force field (PCFF) (Sun et al., 1994) as the basis of the potential function, which belongs to the consistent force fields family with the same functional form as other members such as CFF91, CFF, and COMPASS. It involves a Lennard-Jones 9-6 potential for the intermolecular and intramolecular dispersion-repulsion interactions. Specific stretching, bending and torsion terms describe 1-2, 1-3 and 1-4 interactions, respectively. Electrostatic charges are determined from pair contributions. In this force field, the carbon atoms in the *cis*-PI can be classified into 3 types according to the way the atoms are grouped,

as indicated by the different colors in Fig. III.1. The parameters of these interactions are described in details in references (Sun et al., 1994; Li et al., 2016) and skipped here for brevity. The total force field is the sum of the bonded force field U_{bonded} and the non-bonded force field $U_{no-bonded}$. The functional form can be illustrated in Eq. (III.1)- Eq.(III.12).

$$U_{no-bonded} = \frac{q_i q_j}{r_{ij}} + \epsilon_{ij}\left[2\left(\frac{{r_{ij}}^0}{r_{ij}}\right)^9 - 3\left(\frac{{r_{ij}}^0}{r_{ij}}\right)^6\right] \quad \text{(III.1)}$$

$$U_{bonded} = U_b + U_\theta + U_\varphi + U_\aleph + U_{b-b'} + U_{b-\theta} + U_{b-\varphi} + U_{\theta-\varphi} + U_{\theta-\theta'} + U_{\theta-\theta-\varphi} \quad \text{(III.2)}$$

U_{bonded}:

$$U_b = k_2(b-b_0)^2 + k_3(b-b_0)^3 + k_4(b-b_0)^4 \quad \text{(III.3)}$$

$$U_\theta = k_2(\theta-\theta_0)^2 + k_3(\theta-\theta_0)^3 + k_4(\theta-\theta_0)^4 \quad \text{(III.4)}$$

$$U_\varphi = k_1(1-\cos\phi) + k_2(1-\cos 2\phi) + k_3(1-\cos 3\phi) \quad \text{(III.5)}$$

$$U_\aleph = k_2\chi^2 \quad \text{(III.6)}$$

$$U_{b-b'} = k(b-b_0)(b'-{b'}_0) \quad \text{(III.7)}$$

$$U_{b-\varphi} = (b-b_0)[k_1\cos\phi + k_2\cos 2\phi + k_3\cos 3\phi] \quad \text{(III.8)}$$

$$U_{\theta-\varphi} = (\theta-\theta_0)[k_1\cos\phi + k_2\cos 2\phi + k_3\cos 3\phi] \quad \text{(III.9)}$$

$$U_{\theta-\theta'} = k(\theta-\theta_0)(\theta'-{\theta'}_0) \quad \text{(III.10)}$$

$$U_{\theta-\theta-\varphi} = k(\theta-\theta_0)(\theta'-{\theta'}_0)\cos\phi \quad \text{(III.11)}$$

$$U_{b-\theta} = k(b-b_0)(\theta-\theta_0) \quad \text{(III.12)}$$

III.3. Simulation details

III.3.1. Vulcanization of natural rubber

To obtain vulcanized rubber, elemental sulfur (-S-S-, as the most common vulcanizing agent) (Fig. III.1(c)) (Engelmann et al., 2017) is added to the *cis*-PI melt and, by heating at 600 K, crosslinking bonds are formed, as shown in Fig. III.1(d). PCFF force field is also applied to C-S bonds, and the sulfur crosslinking bonds are supposed only generated in the C atom of the double bond. In this process, we control the degree of crosslinking of natural rubber by adding different amounts of elemental sulfur. The degree of crosslinking was defined by volume

fraction. The vulcanization degree is displayed in Table III.1, where 0 indicates unvulcanized natural rubber.

Table III.1. Crosslink density.

Crosslink degree (%)
0, 0.3, 1.16, 2.3

III.3.2. Addition of fullerenes

In order to add fullerene (Fig. III.1(e)) to the simulation cell, we first create a certain number of cylindrical indentations in the simulation cell, where 1 indentation is for 1 added fullerene, 3 indentations for 3 added fullerenes, 4 indentations for 8 or 12 added fullerenes, and 9 indentations for 27 added fullerenes, while the diameter of the cylindrical indentation is slightly larger than the diameter of the fullerene. Then, we add a certain amount of fullerene to the simulation cell, as shown in Fig. III.1(f), and in Table III.2. The interaction between the CB atoms and between the CB atoms and the atoms of the rubber are also determined by the PCFF force field. Previous studies (Xiong et al., 2015; Choi et al., 2016; Singh et al., 2018; Jiang et al., 2019; Jian et al., 2020; Liu et al., 2020) have proven that PCFF is well suited for CB-polymer composite systems, and the results they provide are reliable, compared to the theoretical and experimental values. The fraction of nanofillers was defined by nanofiller mass fraction in phr.

Table III.2. Nanofiller amount.

Nanofiller fraction (phr)
0.97, 2.94, 7.83, 11.74, 26.42

III.3.3. Simulation step

The initial rubber-fullerene composites structure will be subjected to a four-stages relaxation step to relax any high-energy configurations. Initially, the simulation run for 2×10^6 timesteps (Δt=0.5 fs) using NVT ensemble at 600 K, then the structure is relaxed for 2×10^6 timesteps (Δt=0.5 fs) using NPT ensemble at 600 K. In this process, the crosslinking reaction is performed in the simulation cell, and in order to obtain a random hinge structure, crosslinking is performed every 100,000 steps until the sulfur is completely crosslinked. When the crosslinking is

completed, the vulcanized structure will continue to relax at 600 K with NPT ensemble. The next relaxation cooled the structure down to the room temperature, 297 K, for 2×10^6 timesteps (Δt=0.5 fs) followed by further relaxation of 2×10^6 timesteps (Δt=0.5 fs) at room temperature.

III.4. Results and discussion

III.4.1. Crosslinking degree dependence

III.4.1.1. Physical and thermal properties

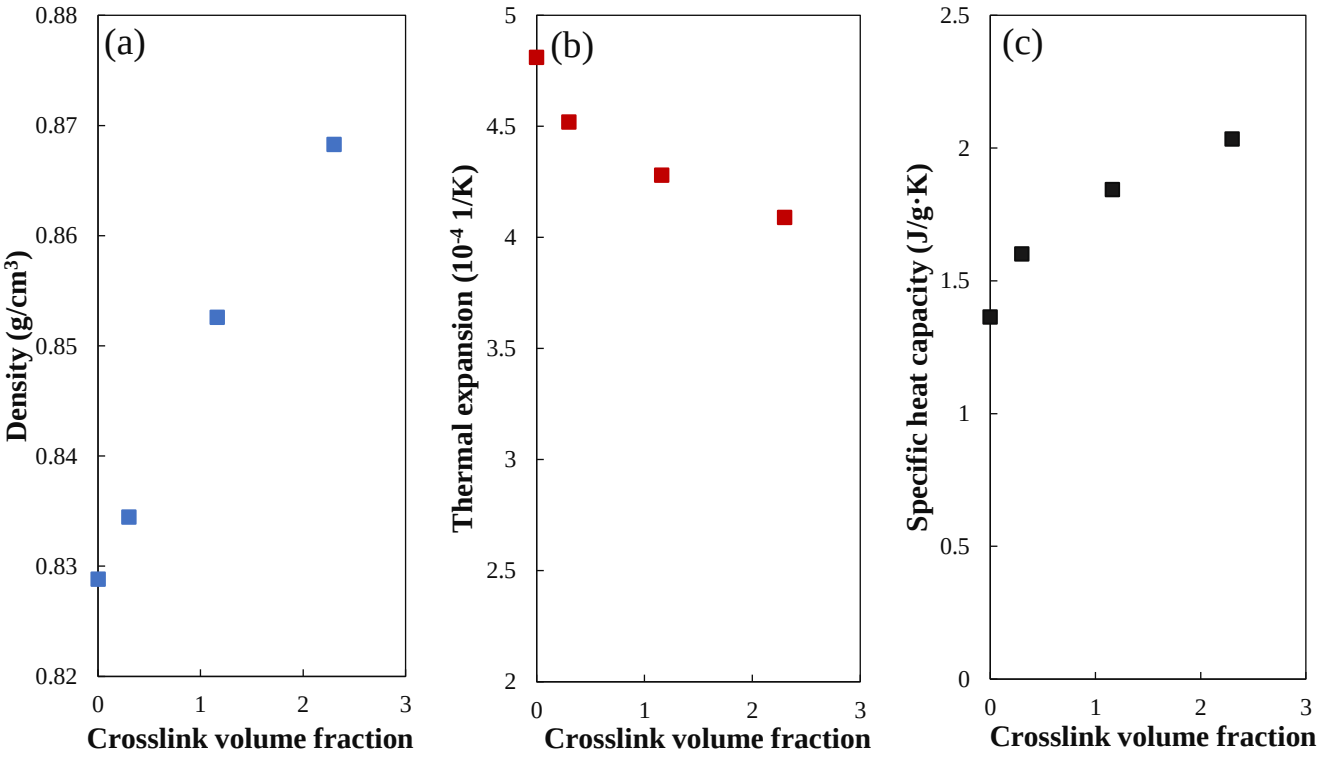

Fig. III.2. Effect of crosslink volume fraction on (a) density, (b) thermal expansion and (c) specific heat capacity.

Fig. III.2 shows the effect of crosslink on the thermal properties of the rubber. Fig. III.2(a) shows that the physical density of vulcanized natural rubber increases almost linearly with the crosslink volume fraction increase. These results coincide with the experimental value of the literature (0.91 g/cm3 (Fujiwara et al.,1997)) and the previous simulation results (0.825 g/cm^3 (Harmandaris et al., 2002), 0.84 g/cm^3 (Pandey et al., 2014), 0.854 g/cm^3 (Khuntawee et al., 2019) and 0.885 g/cm^3 (Sharma et al., 2016)). The coefficient of thermal expansion is defined as the fractional increase in volume per unit rise in temperature: $\alpha_v = \frac{\partial V}{\partial T} \cdot \frac{1}{V}$. It is plotted in Fig.

III.2(b). It can be observed that it decreases with the crosslink volume fraction increase. In the unvulcanized case, the thermal expansion value is found to be 4.81×10^{-4} K^{-1}, which is quite close to experimental values of the literature (5.97×10^{-4} K^{-1} (Kawahara et al., 1999) and 6.1×10^{-4} K^{-1} (Mark et al., 2007)). The specific heat capacity is calculated by $C_v = \frac{dE_{total}}{NKT^2}$, in which E_{total} is the total energy, N is the number of atoms, K is the Boltzmann constant and T is the temperature. In this work, the C_v value was found to be in the range between 1.36 $J\cdot g^{-1}\cdot K^{-1}$ and 2.3 $J\cdot g^{-1}\cdot K^{-1}$ and increases with increasing the crosslink volume fraction, as shown in Fig. III.2(c). These findings are in good agreement with experimental data (1.87 $J\cdot g^{-1}\cdot K^{-1}$ (Sapkota et al., 2011)), and preceding simulation result (1.75 $J\cdot g^{-1}\cdot K^{-1}$ (Mandal et al., 2014)).

III.4.1.2. Mechanical properties

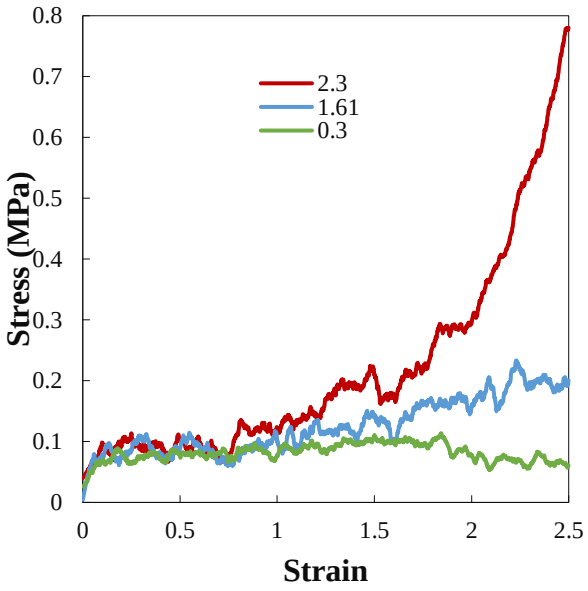

Fig. III.3. Stress-strain curves of simulated units with different crosslinking degrees upon stretching process.

In this part, we study the mechanical response of the system under a stretching at a strain rate of 10^{10} s^{-1}. All stress and strain quantities are defined in their true form: Cauchy stress vs. Hencky strain. Note that due to the small size of the simulated cell, there are fluctuations in the stress-strain curve, a phenomenon that exists in many studies (Yazdani et al., 2018; Payal et al., 2019; Zhang et al., 2021). The Savitzky-Golay filter (Larive et al., 2013) was used to reduce the magnitude of the fluctuations and finally to obtain the trend of the stress. Fig. III.3 shows

the stress evolution as a function of the strain. Firstly, it can be observed that the stress-strain response presents a yield event characteristic of thermoplastic-type materials although natural rubber is an elastomeric medium. Actually, its special structure (crosslinking, long chains, etc.) renders the simulation at molecular level not accurate regarding their mechanical properties till today (Sen et al., 2005; Sapkota et al., 2011; Larive et al., 2013; Mandal et al., 2014). Secondly, the crosslinking influence is not significant below a strain of 1 and the three curves are superimposed. Using the Neo-Hookean law to fit the elastomer response, C_1 is displayed in Table III.3. It can be seen that the difference is very small. When the strain is greater than 1, crosslinked bonds come into play and strain-hardening occurs.

Table III.3. C_1 for different crosslink degrees.

Crosslink degree	0.3	1.61	2.3
C_1*	32.367	33.6514	39.5154

* The Neo-Hookean model is the simplest form among polynomial models. Its strain energy density function is presented as: $W = C_1(I_1 - 3)$ with I_1 the first strain invariant.

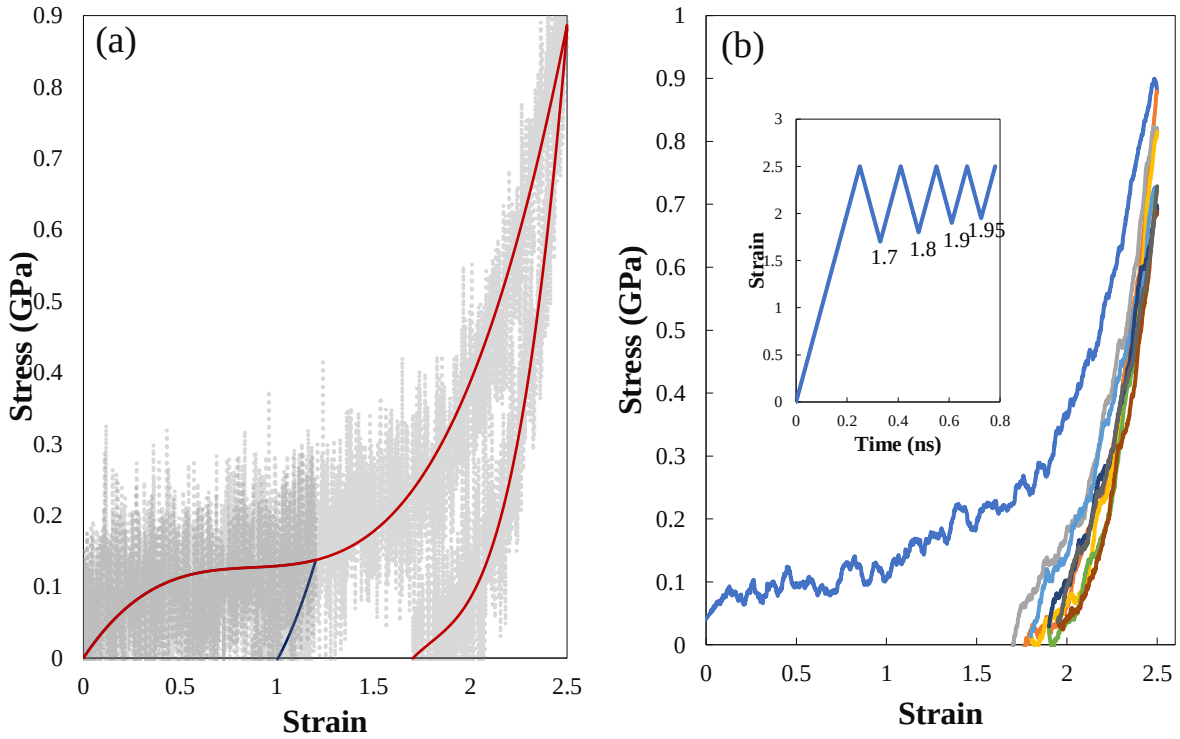

Fig. III.4. Stress-strain curves of simulation cell upon (a) stretching-retraction and (b) cyclic loading sequences.

The response upon stretching-retraction process is shown in Fig. III.4 for the rubber system

with the highest crosslinkage. The strain is ramped to a pre-determined level at a constant rate and then ramped down to zero-stress at the same absolute rate. Fig. III.4(a) shows the mechanical response at two different maximum strain levels. At the end of the retraction, the strain amount retained in the rubber system increases with the applied strain level. During stretching-retraction cycles, a set of phenomena are displayed by the rubber system as shown in Fig. III.4(b) including hysteresis loop, stress-softening and remanent strain at zero-stress. The data are extracted and displayed in Fig. III.5. As also observed experimentally (Guo et al., 2018), both loop area (along with the related dissipated energy) and stress-softening decrease with the cycle number while remanent strain increases.

III.4.2. Nanofiller fraction dependence

III.4.2.1. Macroscopic and thermal properties

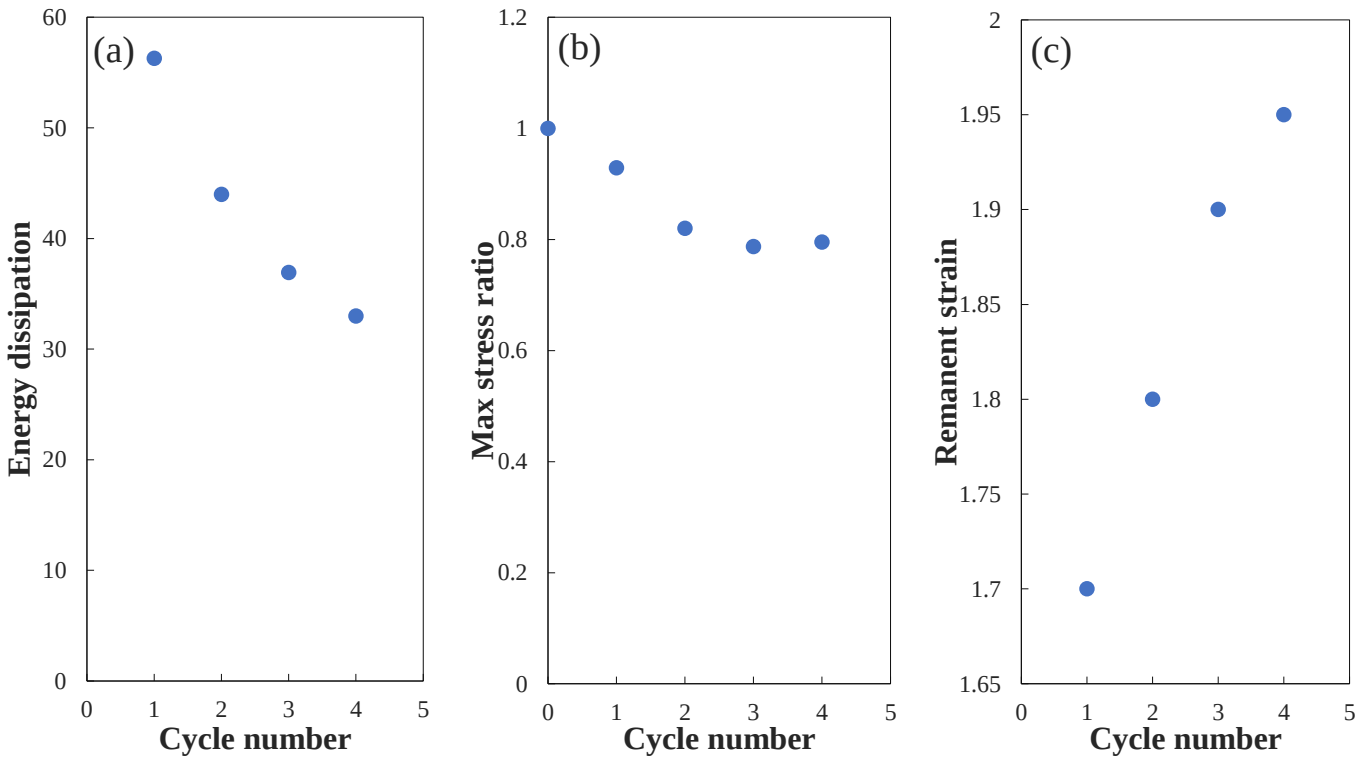

Fig. III.5. (a) Dissipated energy, (b) stress-softening and (c) remanent strain upon stretching-retraction cycles.

In this part, we check the properties of natural rubber-fullerene composites. The simulation cells were merged with C_{60} with a number of 1, 3, 8, 12 and 27 corresponding to filler concentrations

of 0.97, 2.94, 7.83, 11.74, 26.42 phr, respectively. Fig. III.6 shows the initial configurations of the *cis*-PI-C_{60} composite with C_{60} components ranging from 0 phr to 26.42 phr, respectively. The atoms of the *cis*-PI matrix material have been reduced to better show the initial position of C_{60} in the simulation cell and do not represent the true size of the individual atoms. It is ensured that C_{60} does not overlap with other atoms by creating a cylindrical cavity as shown in Fig. III.1(f). Considering that the boundary conditions are periodic, we equate the three sides of the original simulation cell accordingly (2.94 phr: 3×3×3; 7.83 phr: 2×2×2; 11.74 phr: 2×2×3; 26.42 phr: 3×3×3) as shown in Fig. III.6, with the corresponding C_{60} located at the centre of each small square. The special one being 2.94 phr, since it contains only three C_{60} moleculars, in order to maximize the initial distance of C_{60}. C_{60} is placed as displayed in Fig. III.6(c).

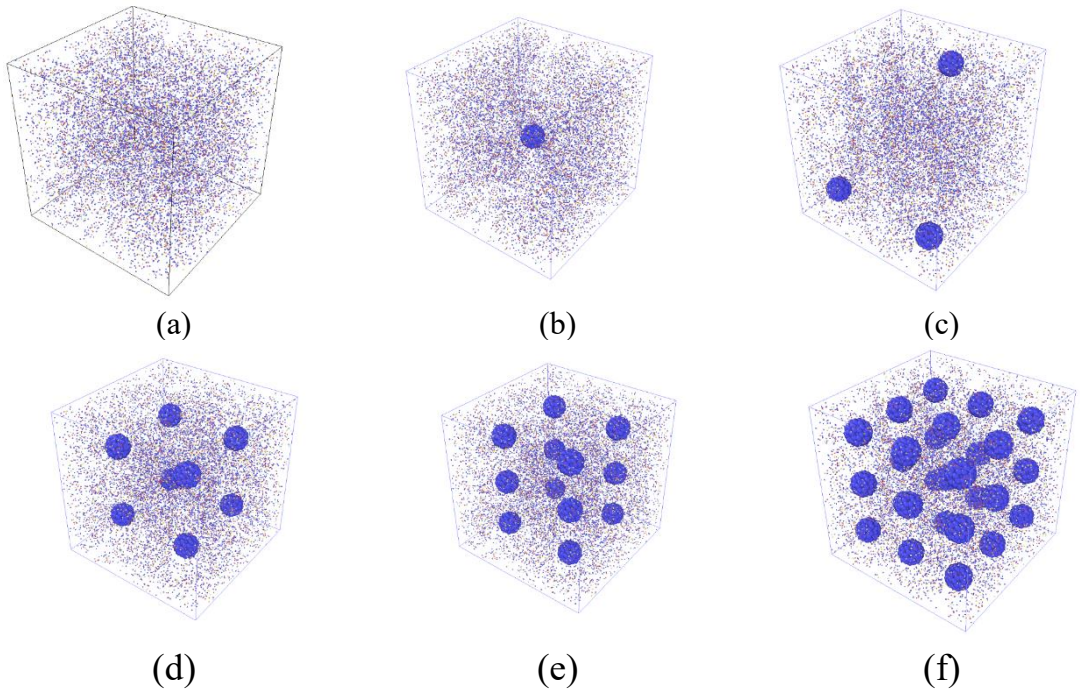

Fig. III.6. Initial structure of the *cis*-PI-C_{60} composite with C_{60} components: (a) 0, (b) 0.97 phr, (c) 2.94 phr, (d) 7.83 phr, (e) 11.74 phr, (f) 26.42 phr.

Fig. III.7 shows the effect of nanofillers fraction on the macroscopic and thermal properties. For C_{60} less than 5 phr, the filler has essentially no effect on the density; while at greater than 5 phr, the density increases, similar to the results of a previous study (Jian et al., 2019). However, the coefficient of thermal expansion is more complicated, which should be caused by the aggregation of the filler in the simulation cell. Specific heat capacity, on the other hand, is the

opposite of density, which varies greatly in small quantities and does not increase excessively when the amount of filler becomes larger. All simulation results in this section match previous studies (Fujiwara et al., 1997; Kawahara et al., 1999; Harmandaris et al., 2002; Mark et al., 2007; Sapkota et al., 2011; Mandal et al., 2014; Pandey et al., 2014; Sharma et al., 2016; Khuntawee et al., 2019), where the experimental data are presented in Section III.4.1.

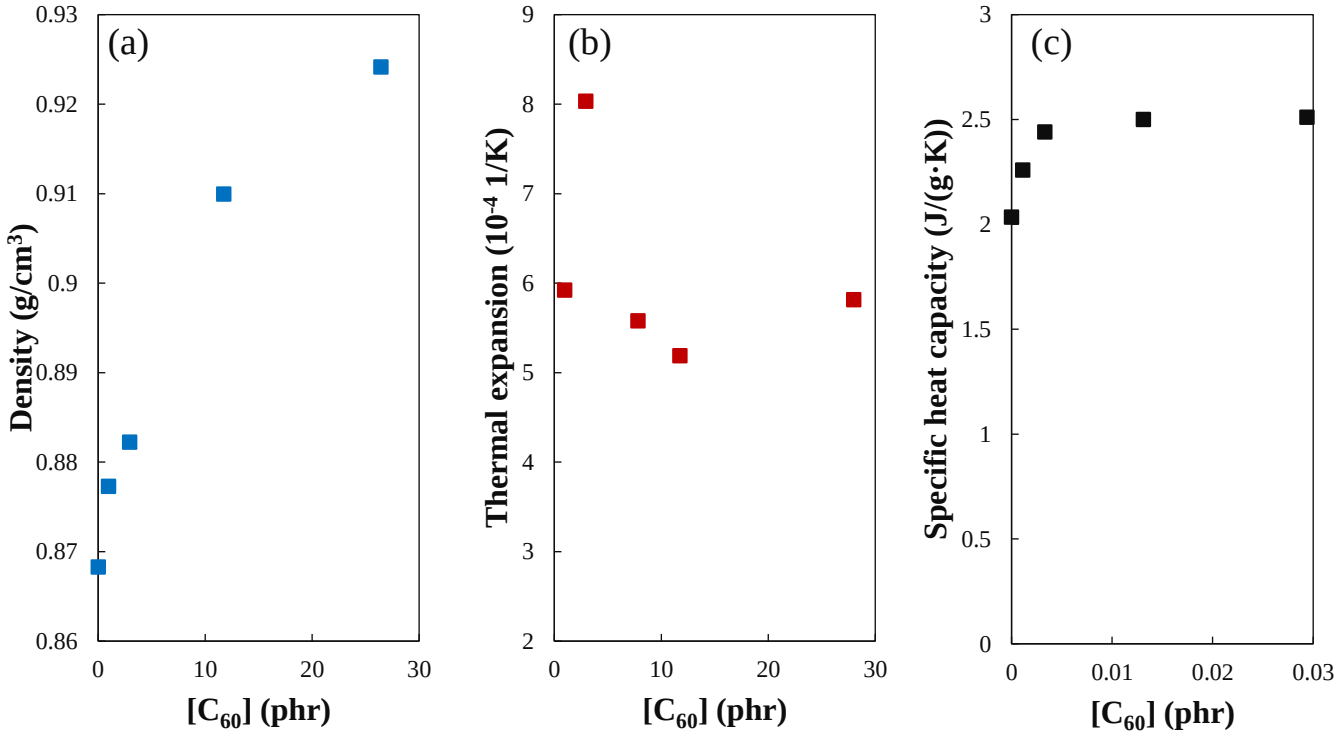

Fig. III.7. Effect of C60 amount on (a) density, (b) thermal expansion and (c) specific heat capacity.

III.4.2.2. Configuration of the interface

To explain the nanofiller-induced changes on the macroscopic properties of natural rubber, we analyse the interactions between fullerenes and *cis*-PI at different concentrations and the interfacial build-up due to the attraction, and the nanofiller aggregation due to the mutual attraction between fullerenes. The pair distribution functions (C_{60}-*cis*-PI, C_{60}-H(*cis*-PI), C_{60}-C(*cis*-PI), C_{60}-S(*cis*-PI), C_{60}-C_{60}) were calculated and local number density (ρ_{local}) and potential mean forces (PMF) were obtained using the following equations:

$$\rho_{local} = \rho \cdot g(r) \quad \text{(III.13)}$$

$$\mathrm{PMF} = -KT\ln\big(g(r)\big) \tag{III.14}$$

where $\rho = N/V$ is the number density in which N is the total number of the atoms in system and V is the volume of the system; K is the Boltzmann constant; T is the temperature.

C_{60} is involved in the calculations, the centre of mass of C_{60} is used for all calculations, as shown in Fig. III.8. The local aggregation density in the *cis*-PI chains around fullerenes can be used to study the probabilistic configuration of polymers around fullerenes. The peak values of PMF were used to justify preferences of C_{60} molecules for aggregation and *cis*-PI chain adsorption (Khuntawee et al., 2019).

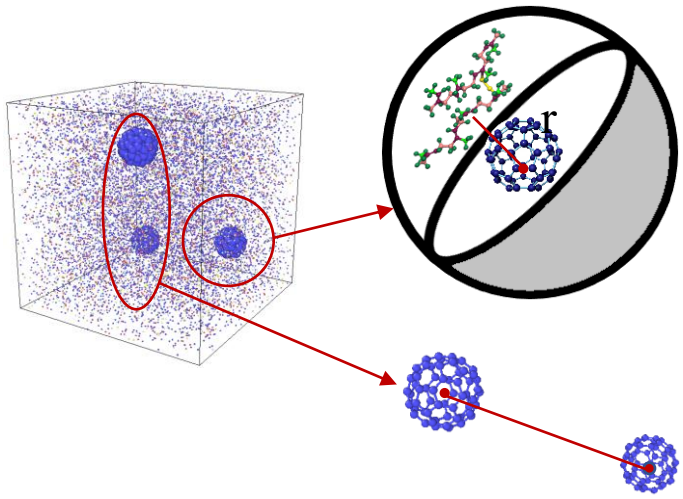

Fig. III.8. A schematic diagram describing the distance between the center of mass of the C60 molecule and the explicit atoms of *cis*-PI.

The local number density of *cis*-PI around fullerenes can be used to study the probabilistic configuration of polymers around fullerenes. Fig. III.9 shows the local density of the elements of crosslinked rubber and the crosslinked rubber as a whole around the filler in a rubber-C_{60} composite with 1 phr. From Eq. (III.13), we can derive the global number density as 0.0356 Å(C), 0.0573 Å(H), 0.00089 Å(S) and 0.0938 Å(*cis*-PI), their colour is marked by the dotted line of the color bar in Fig. III.9.

In the centre of the contour there is a schematic of a fullerene, where the interior of the fullerene and the surface immediately adjacent to the fullerene are pure white, which is an indication that within this range no stacking of the atoms occurs and shows that neither the initial position of

cis-PI and C_{60} nor the position of the equilibrium state overlap. First, since there is very little sulphur relative to pure *cis*-PI, the blank region is larger in diameter, i.e. the sulphur atoms are further away from C_{60}. Comparing the density clouds of C_{60}-C(*cis*-PI) and C_{60}-H(*cis*-PI), firstly, the internal gap radius of carbon is significantly larger than that of H, indicating that around C_{60}, hydrogen atoms are closer to the C_{60} surface than carbon atoms, and the local density of hydrogen atoms is larger than that of carbon atoms at the corresponding positions, similar to the relationship between the global densities of the two atoms, and it is evident that for both C and H, the largest aggregation of *cis*-PI atoms is not at the the surface closest to C_{60} (6.25 Å for C and 5.75Å for H far from the mass center of C_{60}), but in the second layer, i.e. (7.25 Å for C and 6.75 Å for H far from the mass center of C_{60}). The local number density of *cis*-PI around C_{60} is obtained by summing the number densities of the different atoms.

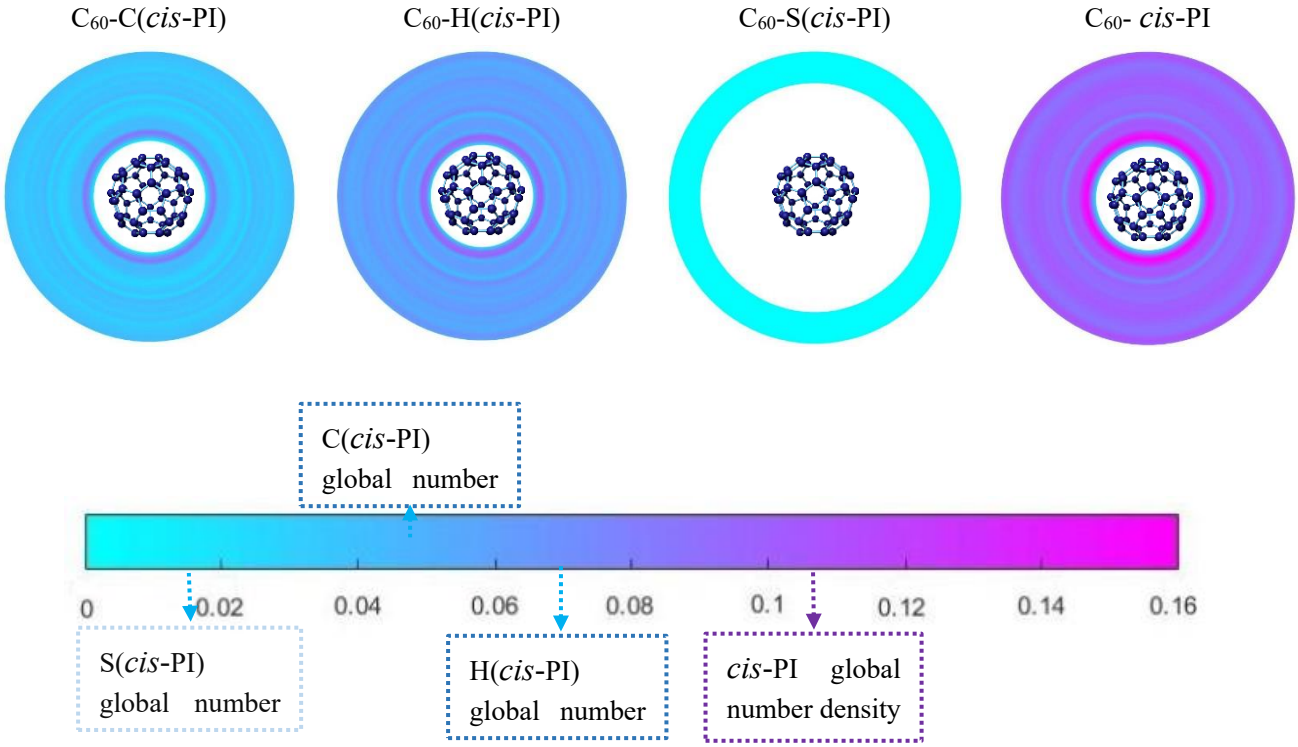

Fig. III.9. Local number density contour map of *cis*-PI around C60 interface for *cis*-PI-C60 composite at 1 phr.

The local number density, PMF and RDF of different composite are shown in Fig. III.10. When the C_{60} fraction is between 0.97 phr and 11.74 phr, the first peak of the local density is gradually reduced as can be seen in Fig. III.10(a) but is still roughly 1.5 times the global density. However,

the plateau period is enhanced, i.e. the resulting pile thickness widens, but all converge to the global density as the distance increases. In contrast, when the C_{60} fraction is 26.42 phr, there is no plateau period, because when the C_{60} fraction is larger, some fillers are closer together, as in Fig. III.10(c), where the first peak of 26.42 phr is 9.75 Å, i.e. the surface distance between two C_{60} is 2.25 Å. At this point, the closer C_{60} form a cluster. And as can be seen from the RDF, when the fraction is 26.42 phr, the rdf exhibits an amorphous state, different from the small content. The first minimum of the PMF is the minimum of the curve in Fig. III.10(b), i.e. the attraction between C_{60} and *cis*-PI is more attractive than the attraction between *cis*-PI.

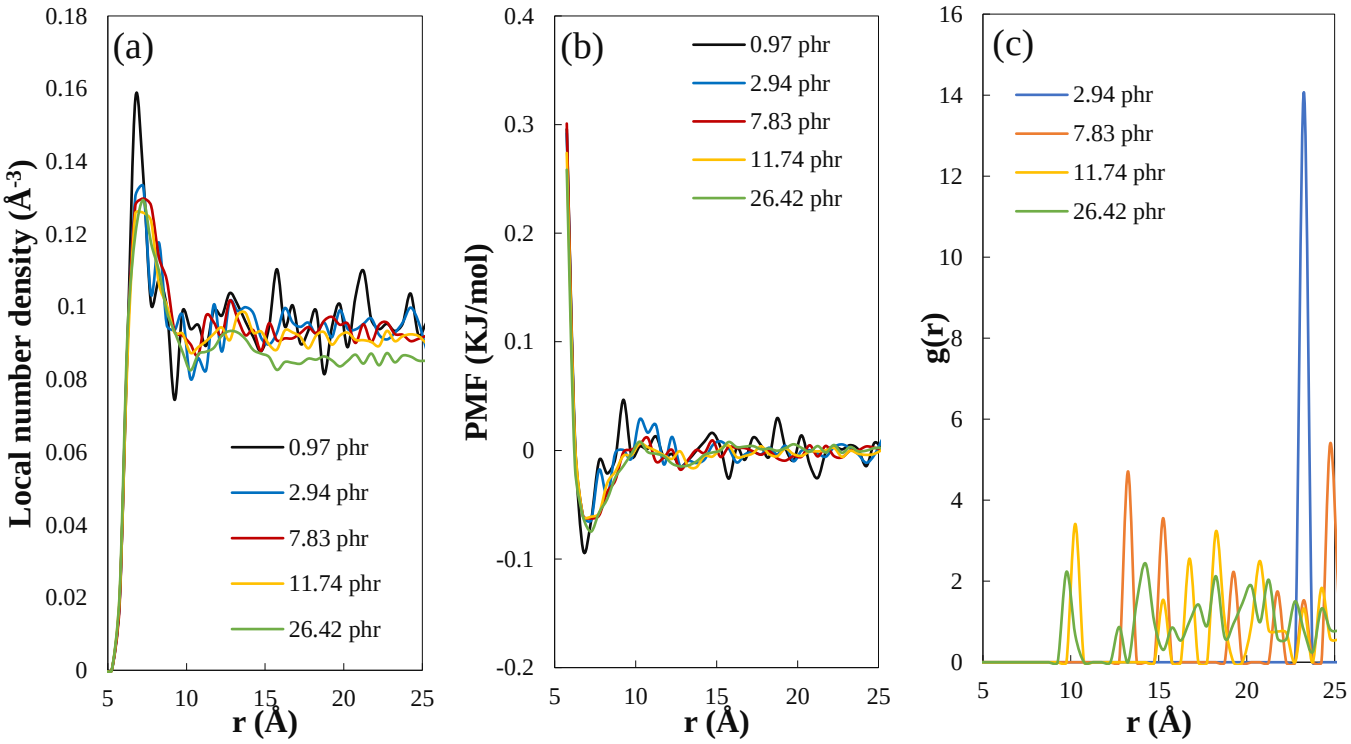

Fig. III.10. (a) Local number density and (b) PMF of C_{60}-*cis*-PI composite in different proportions, (c) PMF between the fullerenes as a function of the distance between the fullerenes.

III.4.2.3. Mechanical properties

The simulation unit is then uniaxially stretched and unloaded with a strain rate of 10^9 s^{-1} and 10^{10} s^{-1}. Stress-strain curves are shown in Fig. III.11. By calculating the slope of the initial elastic phase of the stress-strain curve in Fig. III.11, we obtained the initial modulus of natural

rubber. The initial moduli of natural rubber were obtained as 478.7 MPa for crosslink degree=0.3, 899.2 MPa for crosslink degree=1.16 and 1332.8 MPa for crosslink degree=2.3 at a strain rate of 10^{10} s^{-1}, and 252.2 MPa for crosslink degree=0.3, 458.3 MPa for crosslink degree=1.16 and 699.5 MPa for crosslink degree=2.3 at a strain rate of 10^{9} s^{-1}. A linearized Eyring-like model (Pavlov et al., 2016) was used to derive the moduli at experimental dimensions, as shown in Fig. III.11(c). We can find that the calculated results then converge to the previous study (Ogden et al., 1997), and the value of the elastic modulus is larger when the filler concentration is more important.

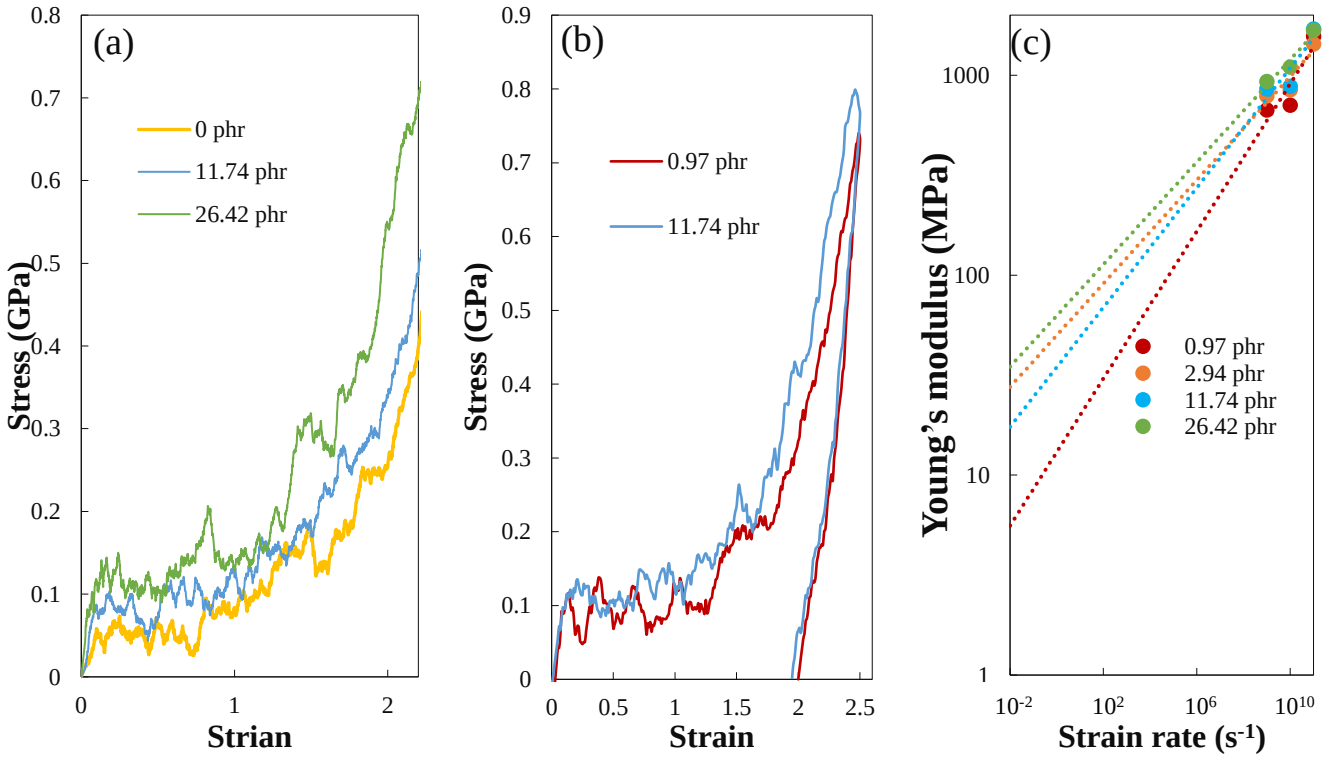

Fig. III.11. Stress-strain curves (a) upon stretching and (b) stretching-retraction loading sequences and (c) Young's modulus.

Table III.4. C_1 for different nanofiller fractions.

Nanofiller fraction	0	11.74	26.42
C_1	39.5154	44.6596	58.2745

When the strain is less than one, there is a clear difference between the three curves. We have used Neo-Hookean fitting stress-strain curves, and C_1 is given in Table III.4. The difference is greater than 30%, indicating that the nanofillers can improve the initial elastic properties of the material, and the slope of the stress is basically similar at this time in the large strain stage, so

it indicates that crosslinking will control the strain-hardening. During unloading, as the C_{60} content increases, the more strain is recovered.

III.5. Conclusion

The object of this study is the main component of natural rubber, *cis*-polyisoprene(*cis*-PI), which is vulcanized by adding element sulphur to *cis*-PI and vulcanizing at high temperatures to obtain vulcanized rubber, and then adding different amounts of fullerenes (C_{60}) to the vulcanized rubber at high temperatures to obtain CB filled vulcanised rubber. The macroscopic physical and thermodynamic properties of vulcanized rubber and CB filled vulcanised rubber were studied to obtain the effect of vulcanisation and nanofiller on natural rubber. The higher the degree of vulcanization, the formation of a network between the molecular chains, resulting in higher density, lower thermal expansion and higher specific heat capacity. Vulcanization therefore also leads to an increased ability of the rubber to withstand stress at large strains. Fillers, on the other hand, have the same effect on density and specific heat capacity as vulcanization, but there is no clear trend towards an effect on the coefficient of thermal expansion. The filler also leads to an increase in the constant parameter (C_1) of the rubber at small strains, about 30% and an increase in the recovery strain. The attraction of fullerenes to *cis*-PI atoms and the aggregation configuration of *cis*-PI atoms around fullerenes were analysed by radial distribution function (RDF), introducing local number density and potential mean force (PMF).

References

Akiba, M., Hashim, A.S., 1997. Vulcanization and crosslinking in elastomers. Progress in Polymer Science 22, 475-521.

Chaikumpollert, O., Yamamoto, Y., Suchiva, K., Kawahara, S., 2012. Mechanical properties and cross-linking structure of cross-linked natural rubber. Polymer Journal 44, 772-777.

Choi, J., Shin, H., Cho, M., 2016. A multiscale mechanical model for the effective interphase of SWNT/epoxy nanocomposite. Polymer 89, 159-171.

Engelmann, S., Meyer, J., Hentschke, R., 2017. Computer simulation of thermal conductivity in vulcanized polyisoprene at variable strain and temperature. Physical Review B 96, 054110.

Fujiwara, S., Sato, T., 1997. Molecular dynamics simulations of structural formation of a single polymer chain: bond-orientational order and conformational defects. The Journal of Chemical Physics 107, 613-622.

Gao, M., Zheng, F., Xu, J., Zhang, S., Bhosale, S.S., Gu, J., Hong, R., 2019. Surface modification of nano-sized carbon black for reinforcement of rubber. Nanotechnolology Reviews 8, 405-414.

Gong, F., Duong, H.M., Papavassiliou, D.V., 2016. Mesoscopic modeling of heat transfer in carbon nanotube multiphase polymer composites. AIP Conference Proceedings 1790, 150001.

Guo, Q., Zaïri, F., Guo, X., 2018. A thermo-viscoelastic-damage constitutive model for cyclically loaded rubbers. Part I: model formulation and numerical examples. International Journal of Plasticity 101, 106-124.

Guo, Q., Zaïri, F., Guo, X., 2018. A thermo-viscoelastic-damage constitutive model for cyclically loaded rubbers. Part II: experimental studies and parameter identification. International Journal of Plasticity 101, 58-73.

Harmandaris, V.A., Doxastakis, M., Mavrantzas, V.G., Theodorou, D.N., 2002. Detailed molecular dynamics simulation of the self-diffusion of n-alkane and cis-1,4 polyisoprene oligomer melts. The Journal of Chemical Physics 116, 436-446.

He, Y., Tang, Y., 2013, Thermal conductivity of carbon nanotube/natural rubber composite from molecular dynamics simulations. Journal of Theoretical and Computational Chemistry 12, 1350011.

Jian, W., Lau, D., 2019. Creep performance of CNT-based nanocomposites: a parametric study. Carbon 153, 745-756.

Jian, W., Lau, D., 2020. Understanding the effect of functionalization in CNT-epoxy nanocomposite from molecular level. Composites Science and Technology 191, 108076.

Kang, Y., Zhou, D., Wu, Q., Duan, F., Yao, R., Cai, K., 2019. Fully atomistic molecular dynamics computation of physico-mechanical properties of PB, PS, and SBS. Nanomaterials 9, 1088.

Kashihara, Y., Okada, S., Urahama, Y., Hikasa, S., Makuta, S., Fujiwara, K., Fujii, S., Nakamura, Y., 2019. Effects of the degree of crosslinking and test rate on the tensile properties of a crosslinked polyacrylic pressure-sensitive adhesive and vulcanized rubber. Journal of Applied Polymer Science 136, 47272.

Kawahara, S., Kakubo, T., Suzuki, M., Tanaka, Y., 1999. Thermal properties and crystallization behavior of highly deproteinized natural rubber. Rubber Chemistry and Technology 72, 174-180.

Khuntawee, W., Sutthibutpong, T., Phongphanphanee, S., Karttunen, M., Wong-ekkabut, J., 2019. Molecular dynamics study of natural rubber-fullerene composites: connecting microscopic properties to macroscopic behavior. Physical Chemistry Chemical Physics 21, 19403-19413.

Kim, D.Y., Park, J.W., Lee, D.Y., Seo, K.H., 2020. Correlation between the crosslink characteristics and mechanical properties of natural rubber compound via accelerators and reinforcement. Polymers 12, 2020.

Kwon, S.Y., Kwon, I.M., Kim, Y.G., Lee, S., Seo, Y.S., 2013. A large increase in the thermal conductivity of carbon nanotube/polymer composites produced by percolation phenomena. Carbon 55, 285-290.

Larive, C.K., Sweedler, J.V., 2013. Celebrating the 75th anniversary of the ACS division of analytical chemistry: a special collection of the most highly cited analytical chemistry papers published between 1938 and 2012. Analytical Chemistry 85, 4201-4202.

Li, Y., Wang, S., Wang, Q., 2017. A molecular dynamics simulation study on enhancement of mechanical and tribological properties of polymer composites by introduction of graphene. Carbon 111, 538-545.

Li, X., Murthy N.S., Becker, M.L., Latour, R.A., 2016. Multiscale approach for the construction of equilibrated all-atom models of a poly(ethylene glycol)-based hydrogel. Biointerphases 11, 021002.

Liu, L., Zhang, Z., Gou, X., 2020. Thermal conductivity of aligned CNT-polyethylene nanocomposites and correlation with the interfacial thermal resistance. Polymer Composites 41, 3787-3797.

Mandal, A., Pan, S., Mukherjee, S., Saha, A.K., Thomas, S., Sengupta, A., 2014. Variations in specific heat and microstructure in natural rubber filled with different fillers as studied by differential scanning calorimetry. Journal of Polymer and Biopolymer Physics Chemistry 2, 25-28.

Mark, J.E. (Ed), 2007. Physical Properties of Polymers Handbook. Second Edition. Springer.

Mark, J.E., Erman, B., Roland, C.M. (Fourth eds.), 2013. The Science and Technology of Rubber. Academic Press.

Ogden, R.W., 1997. Non-linear Elastic Deformations. New York: Dover Publication.

Pandey, Y.N., Brayton, A., Burkhart, C., Papakonstantopoulos, G.J., Doxastakis, M., 2014. Multiscale modeling of polyisoprene on graphite. The Journal of Chemical Physics 140, 054908.

Pavlov, A.S., Khalatur, P.G., 2016. Filler reinforcement in cross-linked elastomer nanocomposites: insights from fully atomistic molecular dynamics simulation. Soft Matter 12, 5402-5419.

Payal, R.S., Fujimoto, K., Jang, C., Shinoda, W., Takei, Y., Shima, H., Tsunoda, K., Okazaki, S., 2019. Molecular mechanism of material deformation and failure in butadiene rubber:

insight from all-atom molecular dynamics simulation using a bond breaking potential model. Polymer 170, 113-119.

Sapkota, J., 2011. Influence of clay modification on curing kinetics of natural rubber nanocomposites. Master of Science Thesis, Tampere University of Technology, Finland.

Sen, S., Kumar, S.K., Keblinski, P., 2005. Viscoelastic properties of polymer melts from equilibrium molecular dynamics simulations, Macromolecules 38, 650-653.

Sethulekshmi, A.S., Jayan, J.S., Saritha, A., Joseph, K., 2022. Recent developments in natural rubber nanocomposites containing graphene derivatives and its hybrids. Industrial Crops & Products 177, 114529.

Sharma, P., Roy, S., Karimi-Varzaneh, H.A., 2016. Validation of force fields of rubber through glass-transition temperature calculation by microsecond atomic-scale molecular dynamics simulation. The Journal of Physical Chemistry B, 2016, 120, 1367-1379.

Sharma, P., Roy, S., 2020. Glass transition temperature of polybutadiene and polyisoprene from high temperature segmental relaxation correlation using molecular dynamics. Soft Materials, 18, 290-296.

Sheiko, S.S., Dobrynin, A.V., 2019. Architectural code for rubber elasticity: from supersoft to superfirm materials. Macromolecules 52, 7531-7546.

Singh, A., Kumar, D., 2018. Effect of temperature on elastic properties of CNT-polyethylene nanocomposite and its interface using MD simulations. Journal of Molecular Modeling 24, 178.

Sun, H., Mumby, S.J., Maple, J.R., Hagler, A.T., 1994. An ab initio CFF93 all-atom force field for polycarbonates. Journal of the American Chemical Society 116, 2978-2987.

Xiong, Q.L., Meguid, S.A., 2015. Atomistic investigation of the interfacial mechanical characteristics of carbon nanotube reinforced epoxy composite. European Polymer Journal 69, 1-15.

Yagyu, H., 2015. Coarse-grained molecular dynamics simulation of the effects of strain rate on tensile stress of crosslinked rubber. Soft Materials 13, 263-270.

Yan, Z., Zaoui, A., Zaïri, F., 2021. Crystallization and mechanical behavior of semi-crystalline polyethylene. Physica Scripta 96, 125729.

Yazdani, H., Ghasemi, H., Wallace, C., Hatami, K., 2018. Mechanical properties of carbon nanotube-filled polyethylene composites: a molecular dynamics simulation study. Polymer Composites 40, 1850-1861.

Zhang, Z., Wang, Y., Liu, P., Chen, T., Hou, G., Xu, L., Wang, X., Hu, Z., Liu, J., Zhang, L., 2021. Quantitatively predicting the mechanical behavior of elastomers via fully atomistic molecular dynamics simulation. Polymer 223, 123704.

Zhao, F., Bi, W., Zhao, S., 2011. Influence of crosslink density on mechanical properties of natural rubber vulcanizates. Journal of Macromolecular Science, Part B: Physics 50, 1460-1469.

Chapter IV

Continuum-Based Modeling Large-Strain Plastic Deformation of Semi-Crystalline Polyethylene Systems: Implication of Texturing and Amorphicity

Chapter IV. Continuum-based modeling large-strain plastic deformation of semi-crystalline polyethylene systems: Implication of texturing and amorphicity[4]

Abstract

The present contribution examines the ability of a constitutive model to capture polyethylene response variation with crystallinity. The model considers the elastic-viscoplastic crystal deformation and anisotropy due to the crystallographic texturing along with the amorphous chains network elastic-viscoplastic-viscohyperelastic deformation. The coupling between the two phases is performed by means of a multi-scale homogenizationbased approach in which the interfacial interaction is considered. The model is applied on semi-crystalline polyethylene systems containing a broad range of crystallinities. Both monotonic and oligo-cyclic tensile loading sequences are considered upon large-strain plastic deformation. The model is found able to correctly capture the gradual transition of the rate-dependent monotonic response from a thermoplastic-like behavior at high crystallinity to a nearly elastomeric-like behavior at low crystallinity. The model abilities to capture cyclically loaded polyethylene systems are critically discussed. The influential and decisive role of the amorphous chains network alignment/relaxation on the cyclic stretching is emphasized by analyzing local stresses and stretches.

Keywords: Semi-crystalline polyethylene; Crystallographic texturing; Amorphicity; Oligo-cyclic loading; Viscoplastic-viscohyperelastic modeling.

[4] This chapter is based on the following paper: Yan, Z., Guo, Q., Zaïri, F., Zaoui, A., Jiang, Q., Liu, X., 2021. Continuum-based modeling large-strain plastic deformation of semi-crystalline polyethylene systems: Implication of texturing and amorphicity. Mechanics of Materials 162, 104060.

IV.1. Introduction

Semi-crystalline polyethylene systems have a large range of applications, in sectors like oil industry, automobile, aeronautic, robotic, biomechanics and civil engineering, in which they may be subjected to large strains under in-service or manufacturing process. These materials present an extremely large variety of molecular architectures with a crystallinity index ranged from about seventy percent down to a few percent only, passing the morphology from well-organized crystalline lamellae to discrete crystalline lamellae randomly dispersed within an amorphous matrix (Peacock, 2000). The broad morphology range leads basically to an extremely large variety of responses from the plastic response characteristics of thermoplastics to the nonlinear elastic response characteristics of elastomers (Ayoub et al., 2011; Abdul-Hameed et al., 2014) with a profound influence of the amorphous and crystalline features such as density of stress transmitters in the amorphous layers and crystal dimensions (Hillmansen et al., 2000; Argon et al., 2005; Kazmierczak et al., 2005; Bartczak and Galeski, 2010). The development of continuum-based models is a prerequisite for designing and performance predicting polyethylene-based products whether in the form of fibers, films or massive parts.

Modeling response of semi-crystalline polyethylene systems is to relate to their complex organization hierarchy from the nano-sized lamellar structure to the macroscopic scale. Purely phenomenological approaches using theories such as viscoelasticity (Zhang and Moore, 1997) or viscoplasticity (Drozdov and Gupta, 2003; Colak and Dusunceli, 2006; Zaïri et al., 2006; Khan and Krempl, 2006; Ben Hadj Hamouda et al., 2007; Dusunceli and Colak, 2008; Drozdov et al., 2013) have the advantage of simplicity. Nonetheless, these models provide only a mathematical description of the different aspects of the material response, generally under low-strain and without obvious connection to the actual microstructure and its deformation-induced evolution. Over the years, continuum-based models have been developed with the concern to introduce microstructural specificities as precisely as possible in the aim to provide a deep understanding of the separate and synergic effects of key microstructural parameters governing the macroscopic response. The link with the microstructure strongly depends on the approach used for the constitutive representation and the observation scale from which the model starts.

In the most physically consistent models, the microstructure approximation of semi-crystalline polymer systems is generally based on composite-type representations.

Following the pioneering work of Haward and Thackray (1968), continuum-based models have been proposed to constitutively describe the large-strain material behavior of semi-crystalline polymers by the combination of resistances representing intermolecular and molecular network micro-mechanisms (Ayoub et al., 2010, 2011; Abdul-Hameed et al., 2014; Makki et al., 2017; Sepiani et al., 2018; Chen et al., 2019; Deplancke et al., 2019; Qi et al., 2019; Bernard et al., 2020). The latter micro-mechanism describes the resistance to deformation of the amorphous molecular structure to simulate the molecular orientation/relaxation process during the strain-hardening stage of the stress-strain response (Boyce et al., 2000). In the above-cited models, a simple averaging homogenization is used and only for the intermolecular resistance which does not allow to represent the crystallinity effect on the deformation-induced orientation. The active interaction between crystalline and amorphous domains is a first-order factor which requires to be taken into account using more sophisticated micromechanics-based approaches. For instance, micromechanics-based models using the Eshelby inclusion theory were proposed through the matrix-inclusion constitutive representation of the semi-crystalline polymer system (Bédoui et al., 2006; Gueguen et al., 2010; Anoukou et al., 2014; Hachour et al., 2014). These models were restricted to the elastic stiffness and yield strength predictions, and more recently extended to the small-strain post-yielding behavior (Mesbah et al., 2021). Multi-scale homogenization-based constitutive models have been also developed by considering at the mesoscopic scale an aggregate of two-phase layered composite inclusions consisting in parallel crystalline lamellae and amorphous layers. Using this concept, the elastic-viscoplastic deformation behavior of high-density polyethylene was predicted at small strain levels (Nikolov and Doghri, 2000; Nikolov et al., 2002) and moderate strain levels by simulating the texture evolution (Lee et al., 1993a, 1993b; van Dommelen et al., 2003; Agoras and Ponte Castaneda, 2012; Uchida and Tada, 2013; Mirkhalaf et al., 2019). The models are generally identified using loading modes in which the crystal plasticity is a first-order phenomenon, such as compression, channel die compression and shear. While the local events involved in yielding due to tensile straining are not connected with clear crystal shearing but with the phenomena occurring in the amorphous phase and the

relation to crystal thickness is not expected, rather to crystallinity degree, read amorphicity (Seguela et al., 1998a, 1998b; Bartczak and Kozanecki, 2005; Bartczak and Galeski, 2010; Rozanski and Galeski, 2013). The latter is an influential and decisive parameter in tensile yielding, the strength and consistency of the amorphous phase being thus first-order factors (Mesbah et al., 2021).

The aim of the present chapter is to examine the ability of a multi-scale homogenization-based constitutive model to capture the polyethylene large-strain tensile response variation with crystal concentration. The model is applied on a high-density polyethylene with 0.72 crystal content, a low-density polyethylene with 0.3 crystal content and an ultralow-density polyethylene with 0.15 crystal content. The results of our simulations are criticized by analyzing the model ability to capture a series of experimental observations under monotonic, loadingunloading and oligo-cyclic stretching over a large strain range. The effect of the amorphous phase fraction on the microstructure evolution is finally discussed thanks to the model.

The present chapter is organized as follows. Section IV.2 presents the fully three-dimensional continuum-based constitutive theory. The model-experiments comparisons are presented and discussed in Section IV.3. Concluding remarks are finally given in Section IV.4.

The following notation is used throughout the text. Tensors and vectors are denoted by normal boldfaced letters and italicized boldfaced letters, respectively, while scalars and individual components of vectors and tensors are denoted by normal italicized letters. The superposed dot designates the time derivative. The superscript T indicates the transpose quantity.

IV.2. Model presentation

IV.2.1. Constitutive representation

The organization hierarchy of the semi-crystalline polyethylene structure depends on the amorphicity. As illustrated in Fig. IV.1, decreasing the crystallinity leads to a morphology transition from micro-sized interconnecting spherulites to individually crystalline lamellae randomly dispersed in the rubbery amorphous matrix. According to the microstructure

approximation based on a composite-type description, the morphology may be regarded as a percolated crystalline matrix at high crystallinity and a rubbery matrix at low crystallinity. A constitutive representation unifying these views is illustrated in Fig. IV.2.

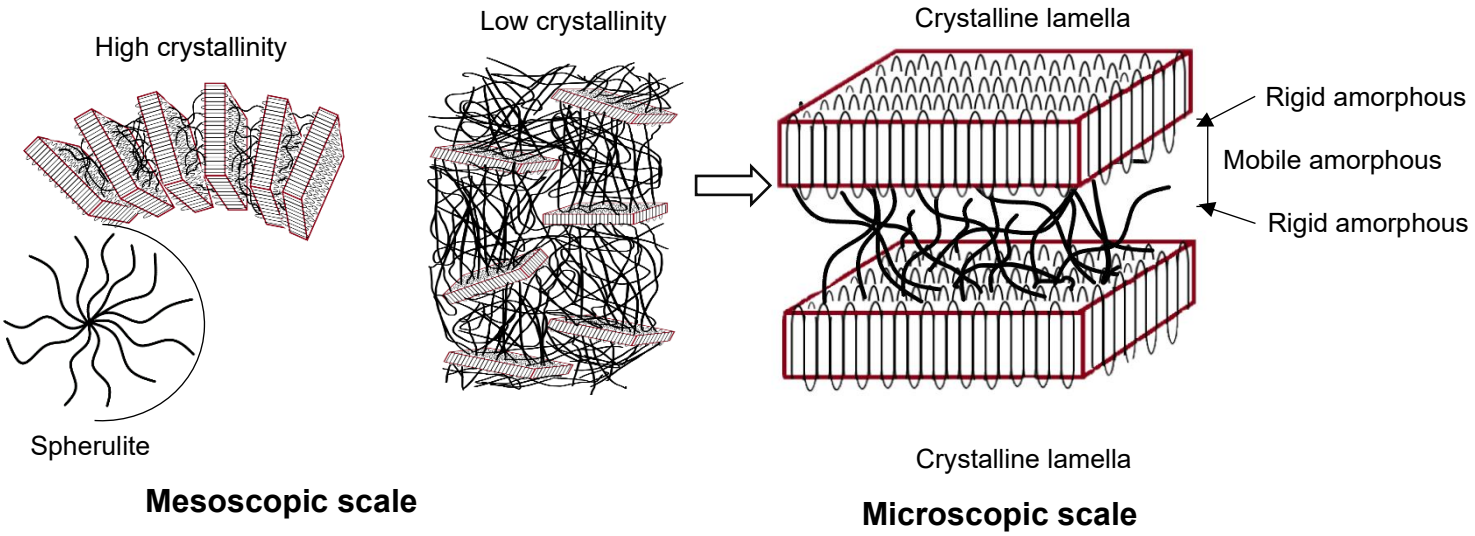

Fig. IV.1. Two-scale view of the semi-crystalline structure; At the mesoscopic scale, the crystalline lamellae may be arranged in highly regular stacking to form spherulitic morphology for high-crystalline media or they may be randomly distributed in the amorphous matrix for low-crystalline media; Both phases are coupled in a complex manner.

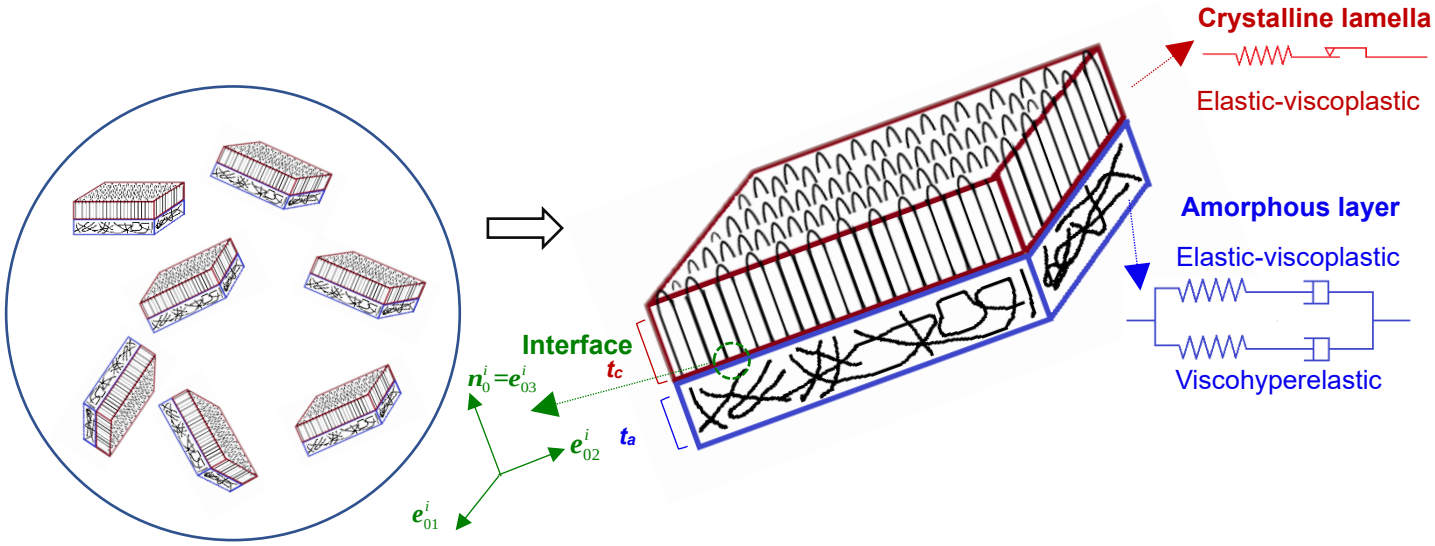

Fig. IV.2. Constitutive representation considering the semi-crystalline medium as an aggregate of randomly distributed two-phase layered composite inclusions. Each inclusion is constituted by a stiff crystalline lamella with an internal elasti-viscoplastic stress and a rubbery amorphous layer with an internal stress including elastic-viscoplastic intermolecular and viscohyperelastic network stresses.

At the mesoscopic scale, the representative volume element of the heterogeneous material is

seen as a mixture of crystalline and amorphous domains organized as an aggregate of two-phase layered composite inclusions which are randomly oriented, the macroscopic response being obtained by the averaging homogenization. The relative thickness of the two layers determines the crystal concentrations, which allows to consider high-to-low crystalline structures. Both crystalline lamella and amorphous layer are homogeneous and continuous media. The crystalline lamella consists of regularly ordered chains resulting in an orthorhombic structure with a high elastic modulus in the chain direction while the amorphous layer consists of randomly oriented entangled chains and is thus supposed to be an isotropic medium.

IV.2.2. Constitutive equations

In what follows, the three-dimensional constitutive equations are described for the different physical sources governing the macro-response. The model satisfies the continuum mechanics rules within the large inelastic deformation kinematics. In the latter framework, the deformation gradient tensor $\mathbf{F} = \nabla \boldsymbol{x}(\boldsymbol{X}, t)$ is introduced to map a material point from its initial position $\boldsymbol{X}$ in the reference configuration to its actual position $\boldsymbol{x}$ in the deformed configuration. The inelastic deformation mechanisms within each phase are considered to be distinct and are described using the multiplicative decomposition concept of the deformation. The introduction of an intermediate configuration during a spontaneous elastic unloading allows the multiplicative deformation decomposition into elastic and inelastic parts: $\mathbf{F} = \mathbf{F}^{e}\mathbf{F}^{in}$ in which the elastic and inelastic components are depicted by superscripts *e* and *in*, respectively. The two tensors can be further decomposed into stretch (right $\mathbf{U}$ or left $\mathbf{V}$) and rotation $\mathbf{R}$ movements using the polar decomposition: $\mathbf{F}^{e} = \mathbf{R}^{e}\mathbf{U}^{e} = \mathbf{V}^{e}\mathbf{R}^{e}$ and $\mathbf{F}^{in} = \mathbf{R}^{in}\mathbf{U}^{in} = \mathbf{V}^{in}\mathbf{R}^{in}$. The subscripts *c* and *a* are used to differentiate the crystalline and amorphous phases, respectively.

IV.2.2.1. Elastic-viscoplastic-viscohyperelastic polyethylene amorphous network

We assume that the behavior of the amorphous domain is the sum of an elastic-viscoplastic resistance that accounts for intermolecular interactions and a viscohyperelastic resistance that accounts for molecular network stretching and orientation process, the two physically distinct sources acting in parallel. The amorphous Cauchy stress tensor $\boldsymbol{\sigma}_a$ is thus split into

intermolecular stress $\boldsymbol{\sigma}_{a\_\text{inter}}$ and network stress $\boldsymbol{\sigma}_{a\_\text{net}}$:

$$\boldsymbol{\sigma}_a = \boldsymbol{\sigma}_{a\_\text{inter}} + \boldsymbol{\sigma}_{a\_\text{net}} \tag{IV.1}$$

From the rheological point of view, the intermolecular resistance is represented by an elastic spring in series with a viscous dashpot (Fig. IV.2). The intermolecular Cauchy stress $\boldsymbol{\sigma}_{a\_\text{inter}}$ is constitutively coordinated with the corresponding strain by the following relationship:

$$\boldsymbol{\sigma}_{a\_\text{inter}} = \frac{1}{J_{a\_\text{inter}}} \mathbf{K}_a \ln\left(\mathbf{V}^e_{a\_\text{inter}}\right) \tag{IV.2}$$

where $J_{a\_\text{inter}} = \det \mathbf{F}^e_{a\_\text{inter}}$ is the elastic intermolecular volume change, $\ln\left(\mathbf{V}^e_{a\_\text{inter}}\right)$ is the Hencky elastic strain and $\mathbf{K}_a$ is the fourth-order elastic stiffness tensor of the isotropic amorphous layers given by:

$$\left[K_{a\_ij}\right]_{6\times 6} = \begin{bmatrix} \lambda+2\mu & \lambda & \lambda & 0 & 0 & 0 \\ \lambda & \lambda+2\mu & \lambda & 0 & 0 & 0 \\ \lambda & \lambda & \lambda+2\mu & 0 & 0 & 0 \\ 0 & 0 & 0 & 2\mu & 0 & 0 \\ 0 & 0 & 0 & 0 & 2\mu & 0 \\ 0 & 0 & 0 & 0 & 0 & 2\mu \end{bmatrix} \tag{IV.3}$$

in which λ and μ are the amorphous Lame's constants.

From the rheological point of view, the molecular network resistance is constituted by a nonlinear spring in series with a viscous dashpot (Fig. IV.2). The molecular network Cauchy stress $\boldsymbol{\sigma}_{a\_\text{net}}$ is given by the Arruda and Boyce (1993) eight-chain model of rubber elasticity introducing the extensibility limit of amorphous chains as a deformation measure:

$$\boldsymbol{\sigma}_{a\_\text{net}} = \frac{1}{J_{a\_\text{net}}} \frac{C_h}{3} \frac{\sqrt{N}}{\lambda^e_{a\_\text{net}}} \mathcal{L}^{-1}\left(\frac{\lambda^e_{a\_\text{net}}}{\sqrt{N}}\right)\left(\mathbf{B}^e_{a\_\text{net}} - \lambda^{e^2}_{a\_\text{net}} \mathbf{I}\right) \tag{IV.4}$$

where two relevant molecular network properties are introduced: the amorphous network hardening modulus $C_h = n_c k\theta$ (in which n_c is the average density of amorphous chains per unit volume, k is the Boltzmann's constant and θ is the absolute temperature) and the average number of molecular units N between entanglements (similar to average length of amorphous chains). The term $\mathbf{I}$ is the identity tensor, $J_{a\_\text{net}} = \det \mathbf{F}^e_{a\_\text{net}}$ is the elastic network volume

change, $\lambda^{e}_{a\_\text{inter}}$ is the elastic stretch on each chain in the amorphous layers:

$$\lambda^{e}_{a\_\text{net}} = \left[\frac{1}{3}\text{trace}\left(\mathbf{B}^{e}_{a\_\text{net}}\right)\right]^{1/2} \tag{IV.5}$$

in which $\mathbf{B}^{e}_{a\_\text{net}} = J^{-2/3}_{a\_\text{net}}\mathbf{F}^{e}_{a\_\text{net}}\mathbf{F}^{e^T}_{a\_\text{net}}$ is the isochoric elastic left Cauchy-Green tensor and $\mathcal{L}^{-1}$ is the inverse Langevin function $\mathcal{L}(x) = \coth(x) - 1/x$ which can be treated by a Padé approximation: $\mathcal{L}^{-1}(x) \approx x\left(3-x^2\right)/\left(1-x^2\right)$.

The time derivative of the deformation gradient tensor writes $\dot{\mathbf{F}}_a = \mathbf{L}_a\mathbf{F}_a$ where $\mathbf{L}_a$ is the gradient tensor of the spatial velocity described by: $\mathbf{L}_a = \mathbf{L}^{e}_a + \mathbf{L}^{in}_a$ where $\mathbf{L}^{e}_a = \dot{\mathbf{F}}^{e}_a\mathbf{F}^{e^{-1}}_a$ is the elastic spatial velocity gradient tensor and $\mathbf{L}^{in}_a = \mathbf{F}^{e}_a\dot{\mathbf{F}}^{in}_a\mathbf{F}^{in^{-1}}_a\mathbf{F}^{e^{-1}}_a$ is the inelastic spatial velocity gradient tensor. The tensor $\mathbf{L}_a = \mathbf{D}_a + \mathbf{W}_a$ may be further additively decomposed into a symmetric part $\mathbf{D}_a = \left(\mathbf{L}_a + \mathbf{L}^{T}_a\right)/2$ (stretching rate tensor) and a skew-symmetric part $\mathbf{W}_a = \left(\mathbf{L}_a - \mathbf{L}^{T}_a\right)/2$ (spin tensor). The Taylor assumption is used such that the deformation gradients in the intermolecular and network resistances are equal: $\mathbf{F}_{a\_\text{inter}} = \mathbf{F}_{a\_\text{net}}$. The cavitation damage associated with progressive nucleation and growth of cavities in the amorphous layers (Zaïri et al., 2011; Mesbah et al., 2021) is neglected and the amorphous inelastic deformation is assumed to be isovolumetric, i.e. $\det\mathbf{F}^{in}_{a\_\text{inter}} = \det\mathbf{F}^{in}_{a\_\text{net}} = 1$. By choosing the inelastic flow irrotational, i.e. $\mathbf{W}^{in}_{a\_\text{inter}} = \mathbf{W}^{in}_{a\_\text{net}} = \mathbf{0}$, the evolution equations of the amorphous inelastic deformation gradients, $\mathbf{F}^{in}_{a\_\text{inter}}$ and $\mathbf{F}^{in}_{a\_\text{net}}$, are given by:

$$\dot{\mathbf{F}}^{in}_{a\_\text{inter}} = \mathbf{F}^{e^{-1}}_{a\_\text{inter}}\mathbf{D}^{in}_{a\_\text{inter}}\mathbf{F}^{e}_{a\_\text{inter}}\mathbf{F}^{in}_{a\_\text{inter}} \text{ and } \dot{\mathbf{F}}^{in}_{a\_\text{net}} = \mathbf{F}^{e^{-1}}_{a\_\text{net}}\mathbf{D}^{in}_{a\_\text{net}}\mathbf{F}^{e}_{a\_\text{net}}\mathbf{F}^{in}_{a\_\text{net}} \tag{IV.6}$$

The amorphous elastic deformation gradients are then extracted from the multiplicative deformation decomposition: $\mathbf{F}^{e}_{a\_\text{inter}} = \mathbf{F}_{a\_\text{inter}}\mathbf{F}^{in^{-1}}_{a\_\text{inter}}$ and $\mathbf{F}^{e}_{a\_\text{net}} = \mathbf{F}_{a\_\text{net}}\mathbf{F}^{in^{-1}}_{a\_\text{net}}$. The amorphous inelastic strain rate tensors, $\mathbf{D}^{in}_{a\_\text{inter}}$ and $\mathbf{D}^{in}_{a\_\text{net}}$, are given by the following flow rules:

$$\mathbf{D}^{in}_{a\_\text{inter}} = \dot{\gamma}_{a\_\text{inter}}\frac{\boldsymbol{\sigma}'_{a\_\text{inter}}}{\sqrt{2}\left\|\boldsymbol{\sigma}_{a\_\text{inter}}\right\|} \text{ and } \mathbf{D}^{in}_{a\_\text{net}} = \dot{\gamma}_{a\_\text{net}}\frac{\boldsymbol{\sigma}'_{a\_\text{net}}}{\sqrt{2}\left\|\boldsymbol{\sigma}_{a\_\text{net}}\right\|} \tag{IV.7}$$

where $\left\|\boldsymbol{\sigma}_{a\_\text{inter}}\right\| = \left(\boldsymbol{\sigma}'_{a\_\text{inter}}\boldsymbol{\sigma}'_{a\_\text{inter}}/2\right)^{1/2}$ and $\left\|\boldsymbol{\sigma}_{a\_\text{net}}\right\| = \left(\boldsymbol{\sigma}'_{a\_\text{net}}\boldsymbol{\sigma}'_{a\_\text{net}}/2\right)^{1/2}$ are the effective shear

stresses, $\boldsymbol{\sigma}'_{a\_\text{inter}}$ and $\boldsymbol{\sigma}'_{a\_\text{net}}$ are the deviatoric parts and, $\dot{\gamma}_{a\_\text{inter}}$ and $\dot{\gamma}_{a\_\text{net}}$ are the amorphous intermolecular and network shear strain rates, respectively, given by (Boyce et al., 2000):

$$\dot{\gamma}_{a\_\text{inter}}=\dot{\gamma}_{a,0}\exp\left[-\frac{\Delta G}{k\theta}\left(1-\frac{\left\|\boldsymbol{\sigma}_{a\_\text{inter}}\right\|}{s}\right)\right] \text{ and } \dot{\gamma}_{a\_\text{net}}=C_v\left(\frac{1}{\lambda_{a\_\text{net}}^{in}-1}\right)\left\|\boldsymbol{\sigma}_{a\_\text{net}}\right\| \tag{IV.8}$$

The left formula of Eq. (IV.8) captures barriers to molecular chain segment rotation in the amorphous layers. The term $\dot{\gamma}_{a,0}$ is the pre-exponential factor, ΔG is the activation energy (which must be overcome for inelasticity begins), S is the shear strength controlling the amorphous chain segment rotation:

$$\dot{s}=\frac{\kappa^n s_0^n}{n}s^{1-n}\dot{\gamma}_{a\_\text{inter}} \tag{IV.9}$$

where s_0 is the initial shear strength, n is the intermolecular hardening coefficient and κ is a factor introduced to take into account the crystal-dependency of concentration of stress transmitters in the amorphous layers.

The right formula of Eq. (IV.8) captures molecular relaxation process in the amorphous layers. The term $\lambda_{a\_\text{net}}^{in}$ must be slightly higher than one at the beginning of the loading process to avoid singularity and ensure stability of the numerical algorithm. It is given by:

$$\lambda_{a\_\text{net}}^{in}=\left[\frac{1}{3}\text{trace}\left(\mathbf{B}_{a\_\text{net}}^{in}\right)\right]^{1/2}+\varsigma \tag{IV.10}$$

in which $\mathbf{B}_{a\_\text{net}}^{in}=\mathbf{F}_{a\_\text{net}}^{in}\mathbf{F}_{a\_\text{net}}^{in^T}$ is the inelastic left Cauchy-Green tensor and $\varsigma=0.01$ is the added perturbation coefficient ensuring numerical stability.

The term C_v in Eq. (IV.8) is the amorphous network viscosity coefficient given by:

$$C_v=D\exp\left(-\frac{Q}{R\theta}\right) \tag{IV.11}$$

in which D and Q are two molecular relaxation parameters and R is the universal gas constant.

IV.2.2.2. Elastic-viscoplastic polyethylene crystals

The contribution of the polyethylene crystals may be represented by an elastic spring in series with a viscoplastic dashpot capturing barriers to crystallographic shear in the crystalline phase

(Fig. IV.2). The crystalline stress tensor $\boldsymbol{\tau}_c$ is constitutively coordinated with the strain as:

$$\boldsymbol{\tau}_c = \mathbf{K}_c : \mathbf{E}_c^e \text{ with } \boldsymbol{\tau}_c = J_c \mathbf{F}_c^{e^{-1}} \boldsymbol{\sigma}_c \mathbf{F}_c^{e^{-T}} \tag{IV.12}$$

where $J_c = \det \mathbf{F}_c^e$ is the elastic volume change, $\boldsymbol{\sigma}_c$ is the crystalline Cauchy stress tensor, $\mathbf{E}_c^e = \left(\mathbf{F}_c^{e^T} \mathbf{F}_c^e - \mathbf{I}\right)/2$ is the Green-Lagrange strain tensor and $\mathbf{K}_c$ denotes the anisotropic fourth-order elastic stiffness tensor of the orthorhombic crystalline phase of polyethylene taken from the literature (Tashiro et al., 1978):

$$\left[K_{c\_ij}\right]_{6\times 6} = \begin{bmatrix} 7.99 & 3.28 & 1.13 & 0 & 0 & 0 \\ 3.28 & 9.92 & 2.14 & 0 & 0 & 0 \\ 1.13 & 2.14 & 315.92 & 0 & 0 & 0 \\ 0 & 0 & 0 & 3.62 & 0 & 0 \\ 0 & 0 & 0 & 0 & 1.62 & 0 \\ 0 & 0 & 0 & 0 & 0 & 3.19 \end{bmatrix} \text{ [GPa]} \tag{IV.13}$$

The plastic deformation of polyethylene crystals occurs by crystallographic slip that is captured by the following relation to account for the N_s distinct slip systems:

$$\mathbf{L}_c^{in} = \sum_{\alpha=1}^{N_s} \dot{\gamma}_c^\alpha \mathbf{R}^\alpha, \ \mathbf{R}^\alpha = \frac{1}{2}\left(\boldsymbol{n}^\alpha \otimes \boldsymbol{m}^\alpha + \boldsymbol{m}^\alpha \otimes \boldsymbol{n}^\alpha\right) \tag{IV.14}$$

where $\mathbf{R}^\alpha$ is the nonsymmetric Schmid tensor with $\boldsymbol{n}^\alpha$ and $\boldsymbol{m}^\alpha$ are the "slip plane" normal vector and the "slip direction" vector in this plane, respectively, and $\dot{\gamma}_c^\alpha$ is the crystalline shear strain rate constitutively coordinated to the resolved shear stress $\tau^\alpha = \boldsymbol{\tau}_c : \mathbf{R}^\alpha$ via a power law:

$$\dot{\gamma}_c^\alpha = \dot{\gamma}_{c,0} \text{sign}\left(\tau^\alpha\right) \left| \frac{\tau^\alpha}{g^\alpha} \right|^{1/m} \tag{IV.15}$$

where $\dot{\gamma}_{c,0}$ is a reference strain rate, m is the strain rate sensitivity parameter and g^α is the shear strength of the slip system α listed in Table IV.1. The term $\text{sign}\left(x\right)$ is the signum function defined as:

$$\text{sign}\left(x\right) = \begin{cases} -1 & x < 0 \\ 0 & x = 0 \\ 1 & x > 1 \end{cases} \tag{IV.16}$$

The crystalline inelastic deformation gradient $\mathbf{F}_c^{in}$ at time $t_{n+1} = t_n + \Delta t$ is calculated

incrementally using the previous one at time t_n (van Dommelen et al., 2003):

$$\mathbf{F}_c^{in}\left(t_{n+1}\right)=\mathbf{F}_{c\_inc}^{in}\mathbf{F}_c^{in}\left(t_n\right) \tag{IV.17}$$

in which $\mathbf{F}_{c\_inc}^{in}$ is the incremental inelastic deformation gradient for the time increment Δt which can be treated by a Padé approximation:

$$\mathbf{F}_{c\_inc}^{in}\approx\left(\mathbf{I}-\mathbf{L}_c^{in}\Delta t/2\right)^{-1}\left(\mathbf{I}+\mathbf{L}_c^{in}\Delta t/2\right) \tag{IV.18}$$

The crystalline elastic deformation gradient is then extracted from the multiplicative deformation decomposition: $\mathbf{F}_c^e=\mathbf{F}_c\mathbf{F}_c^{in^{-1}}$.

The definition of the mechanical coupling of the crystalline lamella with its corresponding amorphous layer remains unchanged from that initially proposed by Lee et al. (1993a, 1993b) and van Dommelen et al. (2003). Therefore, only a summary of the concept is addressed in the next subsection since the details can be found in the paper abovementioned.

Table IV.1 Slip systems and associated shear strength (Lee et al., 1993a).

Slip system	g^α (MPa)
(100)[001]	8
(010)[001]	20
{110}[001]	20
(100)[010]	13.3
(010)[100]	20
{110}<1$\bar{1}$0>	17.6

IV.2.3. Volume-averaging

The mechanical coupling between the deformation modes in amorphous and crystalline domains is obtained using as ensemble-volume averaged homogenization procedure a volume-weighted average of the respective phases.

The local Cauchy stress tensor $\boldsymbol{\sigma}_I^i$ of the composite inclusion i is given by:

$$\boldsymbol{\sigma}_I^i=f_c^i\boldsymbol{\sigma}_c^i+f_a^i\boldsymbol{\sigma}_a^i \tag{IV.19}$$

in which $\boldsymbol{\sigma}_c^i$ and $\boldsymbol{\sigma}_a^i$ are the local stresses previously defined and, f_c^i and f_a^i are the crystalline and amorphous volume fractions, respectively, expressed as:

$$f_c^i = \frac{f_{c,0}^i J_c}{f_{a,0}^i J_a + f_{c,0}^i J_c} \text{ and } f_a^i = \frac{f_{a,0}^i J_a}{f_{a,0}^i J_a + f_{c,0}^i J_c} \tag{IV.20}$$

where $f_{c,0}^i$ and $f_{a,0}^i$ are the corresponding initial volume fractions.

The macroscopic Cauchy stress tensor $\bar{\boldsymbol{\sigma}}$ in the semi-crystalline polymer is obtained by the volume-averaging of the N_I inclusions in the aggregate:

$$\bar{\boldsymbol{\sigma}} = \sum_{i=1}^{N_I} f_I^i \boldsymbol{\sigma}_I^i, \quad f_I^i = \frac{f_{I,0}^i J_I^i}{\sum_{j=1}^{N_I} f_{I,0}^j J_I^j} = \frac{1}{N_I} \tag{IV.21}$$

The local inclusion-averaged deformation gradient tensor $\mathbf{F}_I^i$ is given by:

$$\mathbf{F}_I^i = f_{c,0}^i \mathbf{F}_c^i + f_{a,0}^i \mathbf{F}_a^i \tag{IV.22}$$

The latter is equal to the imposed macroscopic deformation of the aggregate of the N_I inclusions, i.e. $\bar{\mathbf{F}} = \mathbf{F}_I^i$. In the latter Taylor assumption, compatibility of deformation is satisfied everywhere by considering the local deformation to be related to the global one in an affine sense. It is obvious that the underlying assumptions to relate local and global responses impact the physical consistency and predictability of the model. A realistic modeling allows to propose a framework avoiding (or at least limiting) the arbitrary inclusion of heuristic parameters. Although the Taylor assumption may be questionable, it has the advantage of being easy to implement compared to more sophisticated micromechanical approaches based on an Eshelby formulation (Mesbah et al., 2021), in particular, regarding the complex coupling existing between microstructure, finite-strain, time-dependency, non-linearity and external mechanical loading. Note that the resulting model, applied here to a broad range of crystallinities, involves a relatively low number of parameters with all a physical meaning. The compatibility condition on the deformation gradients is introduced at the amorphous-crystalline interfaces:

$$\mathbf{F}_c^i \cdot \boldsymbol{x}_0^i = \mathbf{F}_a^i \cdot \boldsymbol{x}_0^i = \mathbf{F}_I^i \cdot \boldsymbol{x}_0^i \tag{IV.23}$$

where $\boldsymbol{x}_0^i$ denotes an arbitrary vector in the plane of the interface spanned by the unit vectors $\boldsymbol{e}_{01}^i$ and $\boldsymbol{e}_{02}^i$ of the local orthogonal basis $\left(\boldsymbol{e}_{01}^i, \boldsymbol{e}_{02}^i, \boldsymbol{e}_{03}^i\right)$ in which $\boldsymbol{n}_0^i = \boldsymbol{e}_{03}^i$ denotes the unit normal

vector at the amorphous-crystalline interface in the reference configuration[5]. Additionally, the stress equilibrium condition at the interface between the crystalline lamella and the amorphous layer writes:

$$\boldsymbol{\sigma}_c^i \cdot \boldsymbol{n}^i = \boldsymbol{\sigma}_a^i \cdot \boldsymbol{n}^i = \boldsymbol{\sigma}_I^i \cdot \boldsymbol{n}^i \tag{IV.24}$$

where $\boldsymbol{n}^i$ is the unit normal vector at the amorphous-crystalline interface in the current configuration.

When the crystalline lamella is sheared, the plastic deformation is frozen and the homogeneously plasticized crystals can be then regarded as rigid bodies connecting the amorphous chains and having the possibility to rotate during the stretching of amorphous chains, as conceptually realized in (Guo and Zaïri, 2020) for crystallized rubber systems. The texture evolution is related to the orientation of the amorphous-crystalline interfaces which can be updated at each increment. Considering two independent vectors at time $t=0$, $\delta \boldsymbol{x}_{01}^i$ and $\delta \boldsymbol{x}_{02}^i$, in the crystalline-amorphous interface, they become at time t: $\delta \boldsymbol{x}_1^i = \mathbf{F}^i \delta \boldsymbol{x}_{01}^i$ and $\delta \boldsymbol{x}_2^i = \mathbf{F}^i \delta \boldsymbol{x}_{02}^i$ where $\mathbf{F}^i$ can be either $\mathbf{F}_a^i$, $\mathbf{F}_c^i$ or $\mathbf{F}_I^i$. The normal vector $\boldsymbol{n}^i$ is then obtained by:

$$\boldsymbol{n}^i = \frac{\mathbf{F}^i \delta \boldsymbol{x}_{01}^i \times \mathbf{F}^i \delta \boldsymbol{x}_{02}^i}{\left\| \mathbf{F}^i \delta \boldsymbol{x}_{01}^i \times \mathbf{F}^i \delta \boldsymbol{x}_{02}^i \right\|} = \frac{\mathbf{F}^{i^{-T}} \boldsymbol{n}_0^i}{\left\| \mathbf{F}^{i^{-T}} \boldsymbol{n}_0^i \right\|} \tag{IV.25}$$

with $\mathbf{F}^i \delta \boldsymbol{x}_{01}^i \times \mathbf{F}^i \delta \boldsymbol{x}_{02}^i = \det\left(\mathbf{F}^i\right) \mathbf{F}^{i^{-T}} \boldsymbol{n}_0^i$, the symbol $\times$ meaning the cross product of the vectors.

The model introduces a connection between the polyethylene response, the structure and the physics of the deformation modes of the crystalline and amorphous phases. The combination of amorphous and crystalline stiffness and plastic flow describes the small and moderate-strain response. For the large deformation behavior, two molecular orientation effects that take place as the strain-hardening stage proceeds are taken into account: Amorphous chains network alignment/relaxation and crystallographic orientation. In what follows, the model is applied to

[5] Lamellar surfaces in polyethylene are of the {h0l}-type where the angle between the chain direction and the normal of interface varies between 20° and 40° (Bassett and Hodge, 1981). The initial angle between chain direction and normal of interface is set to be 35°.

the large-plastic deformation of polyethylene materials covering a wide spectrum of the crystallinity.

IV.3. Results and discussion

IV.3.1. Database

IV.3.1.1. Materials

Table IV.2 Molecular characteristics and density of the three polyethylene systems: number-average molar weight M_n; weight-average molar weight M_w; counit content ξ; density ρ.

Material	M_n (kDa)	M_w (kDa)	ξ (mole%) †	ρ (g/cm3) *
UL	75	150	12 (60)	0.870
LL	50	104	5.0 (25)	0.902
HD	14	174	0.1 (0.5)	0.959

† hexene for the HD system; octene for the LL and UL systems; between brackets is the short chain branching per 1000 C atoms in the backbone.

* density of compression-molded sheets.

Three commercial polyethylene systems, differing by their molecular topology and molar masses, were ordered from Total Petrochemicals and DOW Chemicals: a Ziegler-Natta high-density ethylene-hexene copolymer (HD) from Total Petrochemicals, a linear low-density ethylene-octene copolymer (LL) and an ultra-low density ethylene-octene copolymer (UL) from DOW Chemicals, both issued from metallocene catalysis. The molecular characteristics of the polyethylene pellets determined by Gel Permeation Chromatography (GPC) are listed in Table IV.2 (provided by the manufacturers). The high co-unit concentrations for LL and UL interfere with the crystalline lamellae formation, and thus induce lower density and crystal degree than for HD. The crystal morphologies can be observed from the Atomic Force Microscopy (AFM)[6] pictures in Fig. IV.3. Highly regular stacking of crystal lamellae for HD and wide thickness distributions of both the amorphous layers and the crystal lamellae for LL and UL have been evidenced from Small-Angle X-ray Scattering (SAXS) experiments[7]. The

[6] AFM images were obtained on 0.5 mm thick films using a Dimension 3100 apparatus from Digital Instruments operated in Tapping Mode. The films were slowly cooled from the melt with free upper surface in order to generate a natural crystallization-induced morphology.

[7] SAXS experiments were carried out on the BM02 beamline of the European Synchrotron Radiation Facility (Grenoble, France) equipped with a 0.1 mm point-focusing collimation and a CCD camera (Princeton Instruments, Trenton NJ, USA) at a distance of 127 cm from the specimen, using a wavelength of 1.54 Å.

long period $L_p = t_c + t_a$ was extracted from SAXS results and reported in Table IV.3. The term t_c is the mean crystal lamella thickness and t_a is the mean amorphous layer thickness (see Fig. IV.1).

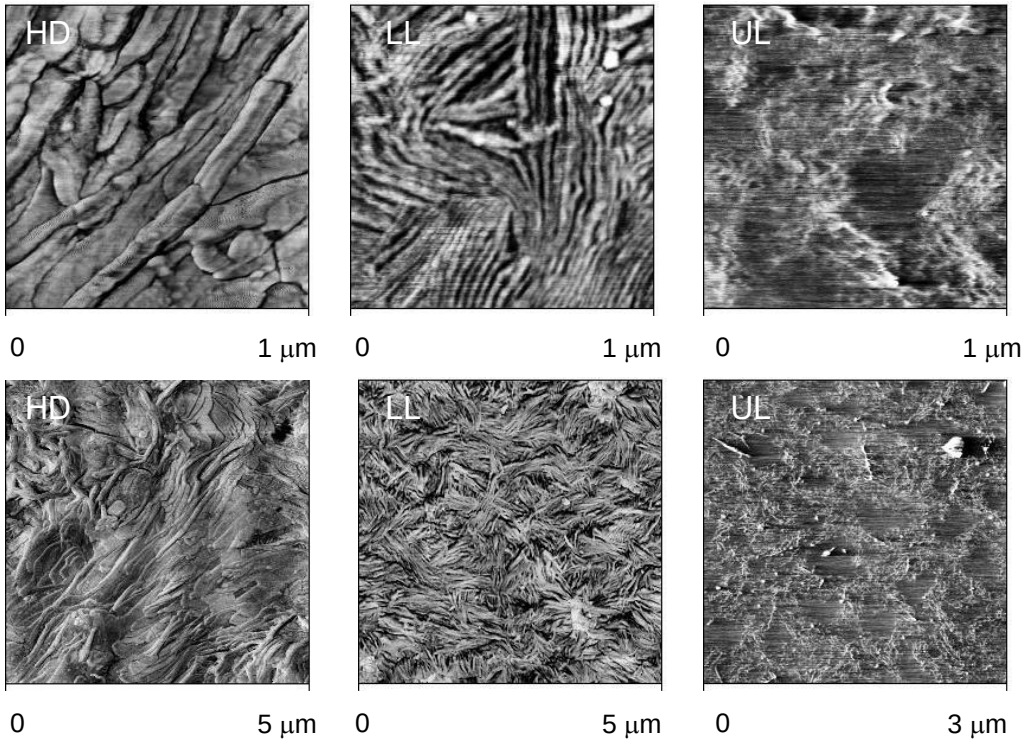

Fig. IV.3. AFM images at different magnifications of the three polyethylene systems showing isotropically distributed stacks of well-defined crystalline lamellae (spherulitic and lamellar morphologies) in the HD and LL systems and fuzzy crystallites akin to fringed micelles (bundle-like crystals embedded in the rubbery amorphous matrix) in the UL system (Ayoub et al., 2010).

The long period L_p was computed thanks to the Bragg relation from the scattering vector q obtained by azimuthal integration of the 2D-patterns:

$$L_p = \frac{2n_d\pi}{q} \tag{IV.26}$$

where n_d is the diffraction order.

The lamellae in HD are the longest and thickest ones as observed in Fig. IV.3. Note that the nearly same long period for LL and UL means distinct t_c values as reported in Table IV.3. The

latter was estimated as follows:

$$t_c = L_p \frac{\rho}{\rho_c} f_{cw} \tag{IV.27}$$

where ρ is the density of the whole material (Table IV.2), ρ_c =1.00 g/cm3 is the density of the crystalline phase and f_{cw} is the crystal weight fraction measured by Differential Scanning Calorimetry (DSC) experiments (Table IV.3).

Table IV.3 Physical characteristics of the three polyethylene systems: long period L_p; mean crystalline thickness t_c; melting enthalpy of a perfect polyethylene crystal $\Delta H_{f,0}$; crystal weight fraction f_{cw}; crystal volume fraction f_c.

Material	L_p (nm)	t_c (nm)	$\Delta H_{f,0}$ (J/g)	f_{cw} (%)	f_c (%)
Experimental method	SAXS	SAXS	DSC	DSC	DSC
UL	13	2	~ 290.3	17.4 ± 0.3	15.1 ± 0.2
LL	14	4.2	~ 299.3	33.3 ± 0.8	30 ± 0.7
HD	26.5	19.2	~ 296.5	75.5 ± 0.8	72.4 ± 0.8

The crystal and amorphous volume fractions, f_c and f_a, requested in the constitutive model can be obtained in terms of the thicknesses:

$$f_c = \frac{t_c}{t_c + t_a} \text{ and } f_a = 1 - \frac{t_c}{t_c + t_a} \tag{IV.28}$$

Table IV.3 provides the crystallinity characteristics at room temperature. The specific melting enthalpy ΔH_f was measured by DSC at a scanning rate of 10°C/min under nitrogen flow with a Q100-apparatus from TA Instruments, which has been indium-calibrated. Melting endotherms and the crystallizing exotherms are provided in Fig. IV.4; The extremums correspond to the melting temperature T_f and the crystallizing temperature T_c. The crystal weight fraction f_{cw} was determined using the following formula:

$$f_{cw} = \frac{\Delta H_f}{\Delta H_{f,0}} \tag{IV.29}$$

in which $\Delta H_{f,0}$ is the melting enthalpy of a theoretically fully crystalline polyethylene

(Wunderlich, 1980) taking into account the melting temperature dependence for every crystal concentration (see Table IV.3).

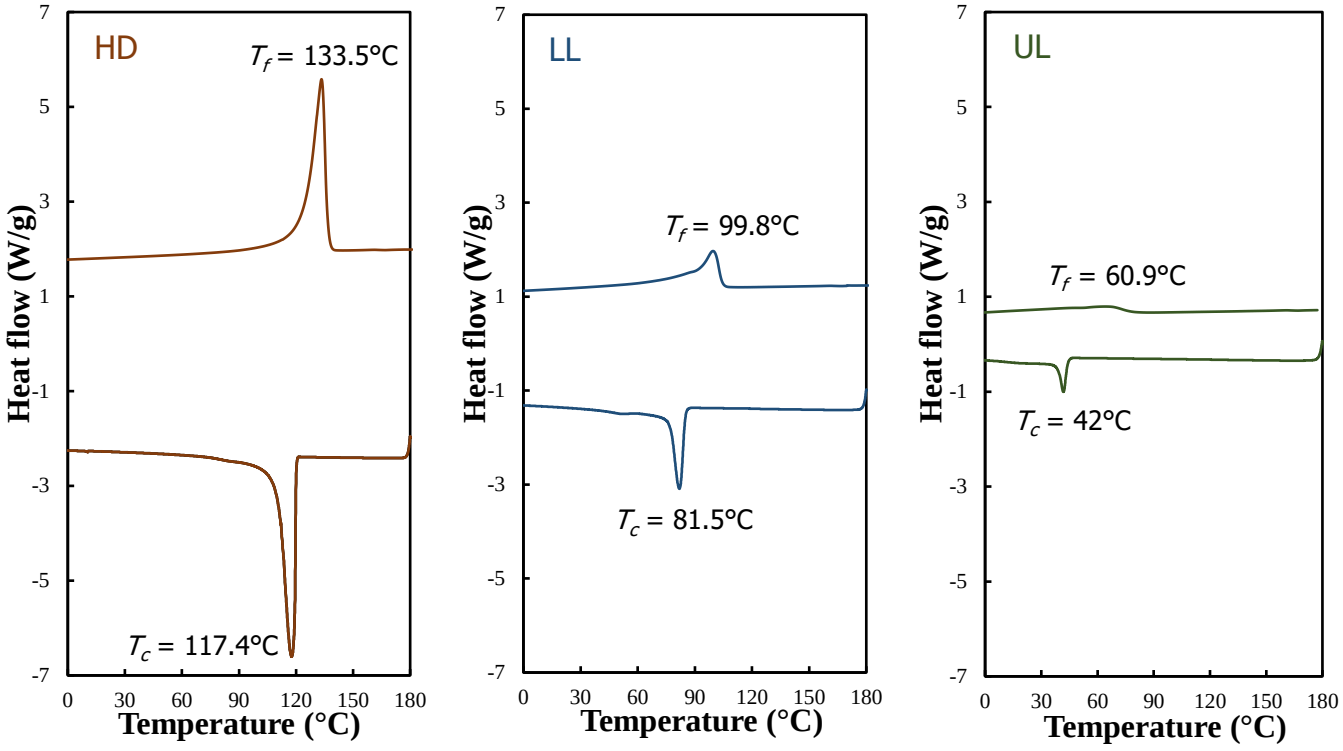

Fig. IV.4. Melting endotherms and cooling exotherms of the three polyethylene systems. The HD heat flow is typical of a high-crystalline polymer. The very broad LL and UL melting endotherms show non-uniform chemical composition distributions due to high co-unit concentrations (Ayoub et al., 2010).

IV.3.1.2. Large-plastic deformation

The intrinsic large-plastic deformation was obtained using video-controlled tensile mechanical tests. They were performed on an electromechanical Instron-5800 universal testing machine interfaced with a non-contact optical extensometer for the local strains measurement on dog bone shaped samples[8] of 28 mm gauge length, 8 mm width and 1 mm thickness; The gauge part presents a curvature radius of about 120 mm in order to localize the necking (if any) while minimize the stress triaxiality effect. The local true axial strain rate was controlled to remain strictly constant throughout the tests in the smallest sample cross-section even after necking by

[8] Although no initial preferential orientation was expected, the samples were cut off in the same direction of 1 mm thick compression-molded sheets; The latter were molded from polyethylene pellets at 180°C for 10 min and slowly cooled to room temperature in order to avoid residual thermal stresses generated during cooling.

regulating the cross-head speed of the testing machine. A series of mechanical tests were carried out to obtain data on the main features of the large-strain plastic deformation at room temperature. Different experiments have been undertaken in the plastic instability:

- Single loading steps up to very large strains for model identification: the sample is stretched to a prescribed strain level of about 1.8 at different constant true strain rates: 0.01 /s, 0.005 /s, 0.001 /s, 0.0005 /s and 0.0001 /s.
- Single loading-unloading steps for model verification: the strain is ramped to a prescribed level at a constant true strain rate of 0.001 /s and then ramped down to zero stress under the same absolute strain rate. Three maximum applied strains are considered: 0.9, 1.2 and 1.5.
- Oligo-cyclic stretching for model verification: The previous sequence is performed repeatedly to determine the progressive stress-softening at maximum applied strain and the accumulation of plastic strain at zero stress with increasing cycle number.

The responses are plotted in the form of true (Cauchy) axial stress versus true (Hencky) axial strain.

IV.3.2. Model identification

The model parameters were identified to fit the constant true strain rate monotonic curves up to very large strains. The values are listed in Tables IV.4 and IV.5 for HD, LL and UL. The three polyethylene systems have been represented by an aggregate of 125 two-phase layered composite inclusions. As the local interaction between the two phases reduces the segmental mobility of the amorphous chains in the vicinity of the crystalline lamella (see Fig. IV.1), the mean stiffness of the amorphous layer is expected to be severely modified from a material system to another. Both initial elastic and hardening moduli vary with the crystal content. Besides, the difference in amorphous network properties is consistent to the difference in molar weights (see Table IV.2) and in chain entanglements that are rejected from crystals to amorphous phase. The higher the crystallinity the more entangled the amorphous phase, showing higher concentration of stress transmitters in the amorphous layers including tie molecules and entanglements (i.e. lesser mean chain length N). The overcoming plastic

resistances in the two phases are assumed to be nearly invariant with the crystal content; Only the interaction coefficient changes to consider the morphology effect.

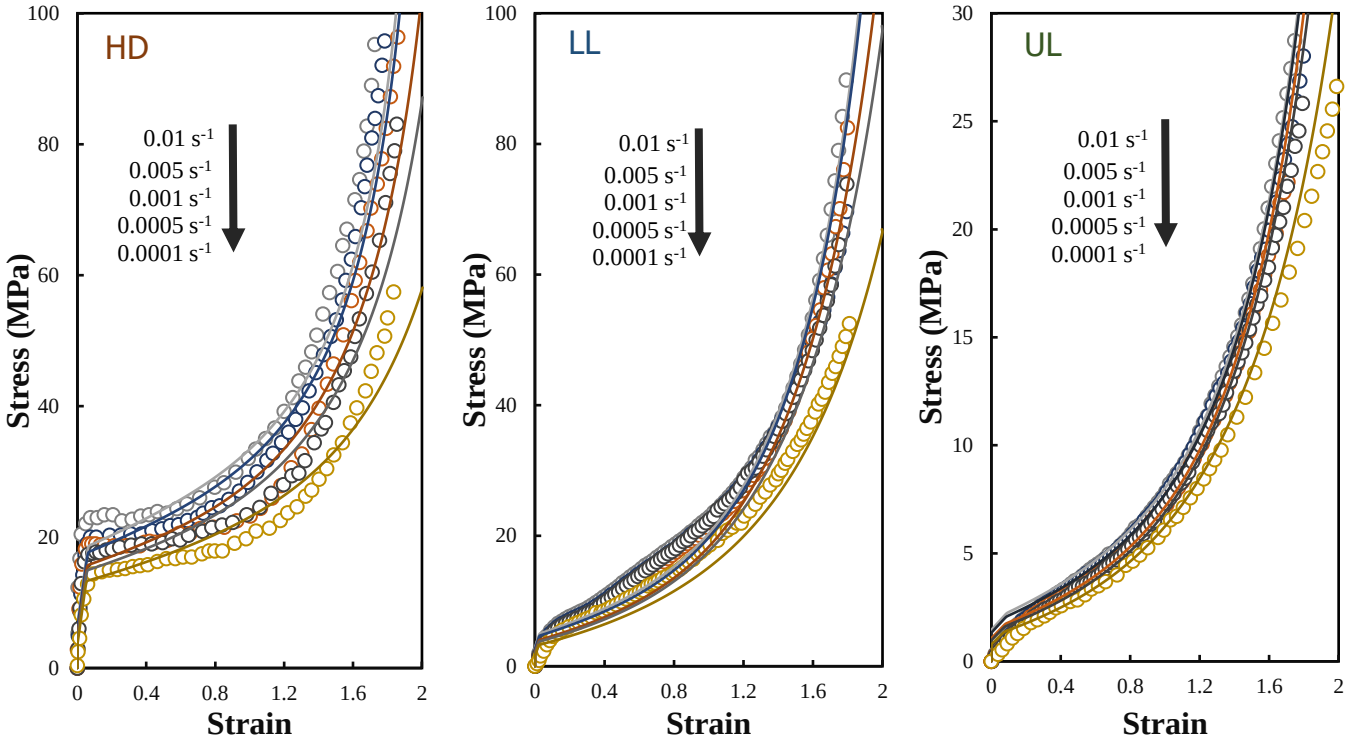

Fig. IV.5. Stress-strain curves of the three polyethylene systems at different true strain rates (symbols: experimental data, solid lines: constitutive model).

Fig. IV.5 presents the identification results for the different local true axial strain rates: 0.01 /s, 0.005 /s, 0.001 /s, 0.0005 /s and 0.0001 /s. The solid lines represent the model simulations while the symbols represent the experimental data. The model appears to be relatively effective to capture the influence of the crystallinity on various features of the nonlinear mechanical response along with the nonlinear rate-dependency. Moreover, it is able to reproduce the crystal content effect on the gradual polyethylene response transition from the thermoplastic-like behavior of the HD system to the elastomeric-like behavior of the UL system. However, the low-strain response is captured rather poorly by the model with a divergence that increases with the crystallinity decrease. That can be mainly the result of the elastic properties of the polyethylene crystal taken from the literature and introduced as direct inputs into the model for the three polyethylene systems. Despite the latter, the model adequately reproduces, as the crystal content decreases, the decrease in plastic features (yield strength and strain-hardening ability) along with the decrease in rate-dependency.

IV.3.3. Model results

IV.3.3.1. Microstructure evolution

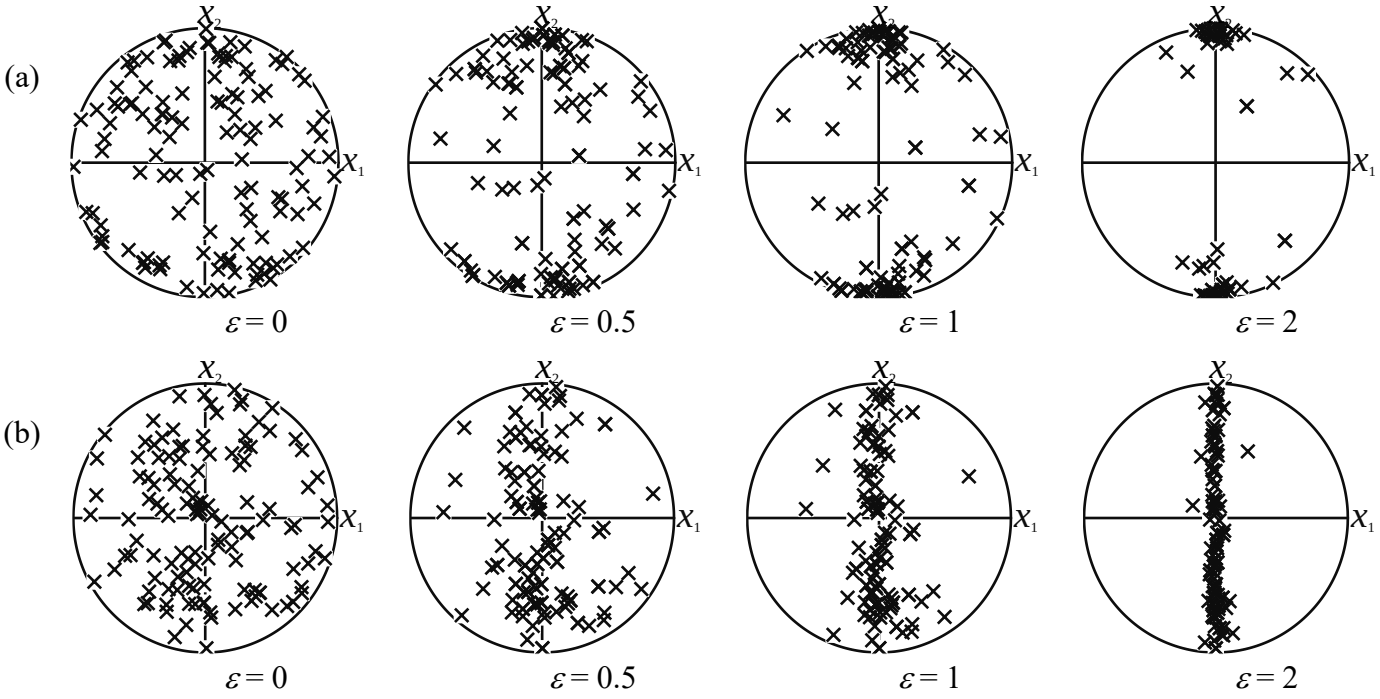

Fig. IV.6. Model predictions of pole figures at different macroscopic strain levels $\varepsilon = \ln(\lambda)$: (a) (010), (b) inclusion normal direction.

Highly anisotropic behavior takes place during the strain-hardening stage[9]. In the model, the orientation-induced strain-hardening region is governed by both crystallographic orientation and molecular orientation/relaxation of the amorphous phase. The predicted results of the crystallographic texture evolution can be evaluated by means of pole figures. Illustrative examples are presented in Fig. IV.6 in the un-deformed state and in three precise deformed states for preferential directions. The initially isotropic material with randomly oriented lamellae transforms into an anisotropic material due to the reorientation mechanism of the

[9] From the earlier studies of Peterlin (1975), the prevailing picture of the microstructure evolution due to tensile straining of a semi-crystalline polymer has been stated (Seguela et al., 1998a, 1998b; Bartczak and Kozanecki, 2005; Bartczak and Galeski, 2010; Rozanski and Galeski, 2013); The tensile yielding results from massive structural modifications accompanied by widely diverse deformation mechanisms in the two constitutive phases. It is determined by the stretching of chains in the amorphous phase occurring in the first place (involving inter-lamellar separation, inter-lamellar shear and lamellar rotation) and by the plastic deformation events in the crystalline lamellae followed by their fragmentation leading to the formation of a fibrillar microstructure at large strains.

crystalline lamellae towards the maximum principal stretch direction. The (010) poles spread around the transverse direction (Fig. IV.6(a)) while the inclusion interface normals are migrating towards the transverse direction (Fig. IV.6(b)).

Table IV.4 HD model parameters.

Crystalline	Reference strain rate	$\dot{\gamma}_{c,0}$	10^{-6} (s^{-1})
	Strain rate sensitivity	m	0.1355
Amorphous	First Lame's constant	λ	100 (GPa)
	Second Lame's constant	μ	200 (MPa)
	Reference strain rate	$\dot{\gamma}_{a,0}$	10^{-6} (s^{-1})
	Activation energy	ΔG	4.03×10^{-20} (J)
	Initial shear strength	s_0	14 (MPa)
	Intermolecular hardening	n	193
	Interaction coefficient	κ	19.6
	Hardening modulus	C_h	1.2 (MPa)
	Chain length	N	26
	Molecular relaxation	D	7.8×10^{28} (MPa^{-1} s^{-1})
	Molecular relaxation	Q/R	25.5×10^{3} (K)

Table IV.5 UL and LL model parameters (all other parameters are listed in Table 4).

Material	λ (GPa)	μ(MPa)	κ	C_h (MPa)	N
UL	1	2	0.28	0.24	42
LL	16.6	33	1.4	0.8	42

The microstructure evolution can be also analyzed using the local axial stresses and stretches plotted in Figs. IV.7 and IV.8, respectively. In the early stage of deformation until yield point, the response is governed by the plastic deformation in the crystalline phase and by the intermolecular interactions in the amorphous phase; Their relative importance depends on the amorphicity. It is worth noticing that the interfacial interactions between crystalline and amorphous domains may form a region in the vicinity of crystalline lamella where the amorphous chain mobility is reduced (see Fig. IV.1). Due to the loss of chain segmental mobility, the glass transition temperature is expected to be severely modified leading to an enhancement of the intermolecular resistance of the amorphous layers. The latter resistance depends on the crystallinity. For the higher crystalline system, the small-strain tensile yielding, manifested by the initial elastic response followed by the rollover to yield, is predominantly associated with the crystallographic shear in the crystalline phase but also, in a certain extent, with the intermolecular barriers to chain-segment rotation in the minor amorphous phase.

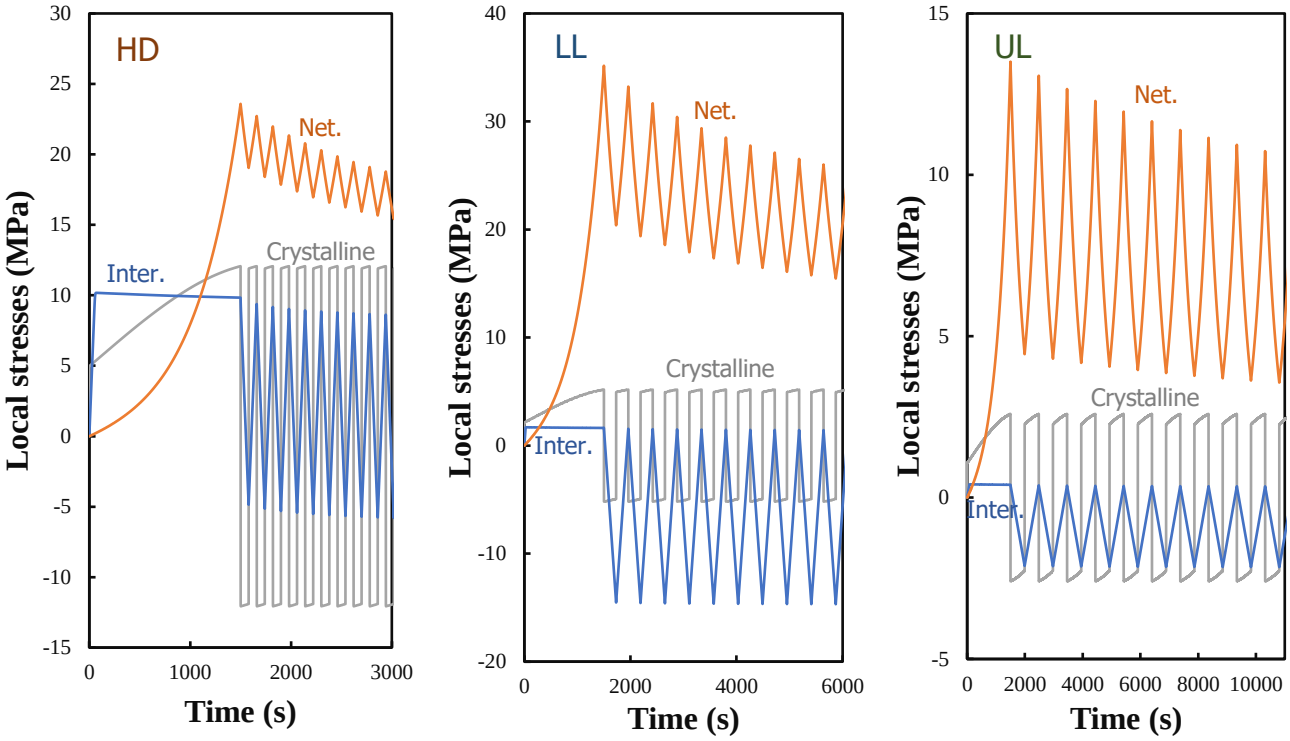

Fig. IV.7. Local axial stresses in the three polyethylene systems upon oligo-cyclic loading at a strain level of 1.5 and at a true strain rate of 0.001 /s.

In the plastic regime, the extension of chains in the amorphous phase progressively governs the response manifested by the progressive strain-hardening and finally the dramatic strain-hardening at very large strains. For low-crystalline systems, the molecular orientation/relaxation of the amorphous phase dominates the material response in all strain range, the contribution of the discrete crystalline lamellae to the overall resistance to deformation being slight and they rather act as junction points in the amorphous matrix.Non-monotonic conditions being one of the most severe tests for the verification of a constitutive model, its predictive capacities are discussed in the two next subsections using the model parameters previously identified in monotonic loading.

IV.3.3.2. Loading-unloading

The model predictions under a loading-unloading path are depicted in Fig. IV.9 by comparing them with the experimental observations of the three polyethylene systems. A global view at these plots shows that the unloading path is strain dependent. A good agreement appears between model simulations and experimental data of the HD system. The plastic strain at zero stress is very well predicted by the model. For the LL system, it is satisfactory to observe that

the model predicts the nonlinearity of the unloading path when the strain level is large. For more moderate strains, the model is unable to capture the nonlinear unloading path which leads

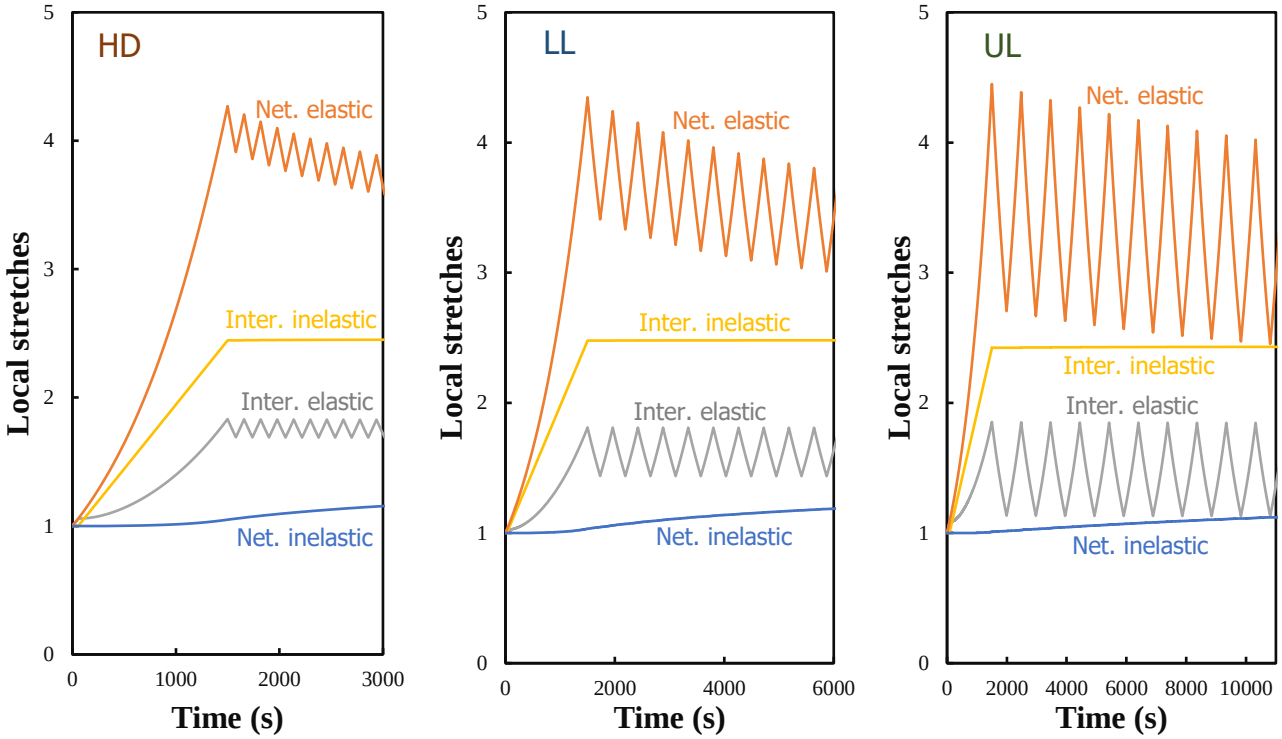

Fig. IV.8. Local axial stretches in the three polyethylene systems upon oligo-cyclic loading at a strain level of 1.5 and at a true strain rate of 0.001 /s.

to an overestimation of the plastic strain at zero stress. Indeed, the stiffness evolves during retraction which leads to a strong nonlinear unloading path. The abrupt initial unloading tangent does not allow to the model to reproduce the unloading response of the UL system. The decrease in crystal content leads to a gradual transition from a linear unloading response dominated by the stiff crystalline lamellae to a drastic recovery upon unloading dominated by the rubbery amorphous layers. It is satisfactory to observe that the model reproduces, as the crystal content decreases, the decrease in residual strain at zero stress. The latter may be associated to the drastic recovery governed by the network elastic stretch during retraction (Fig. IV.8).

IV.3.3.3. Oligo-cyclic loading

In order to check further the predictive capabilities of the constitutive model, the cyclic response is presented and discussed. The predicted results are compared to the cyclic experimental data in Fig. IV.10 for a maximum strain value of 1.5 and ten consecutive cycles. The cyclic response exhibits a Mullins effect common with elastomeric-like materials characterized by a (i)

progressive stress-softening with increasing cycle number, (ii) a hysteresis loop (i.e. a difference between unloading and reloading paths), (iii) an accumulation of plastic strain at zero stress (Drozdov, 2009; Wang et al., 2015; Makki et al., 2017; Guo et al., 2021). Their amounts depend on the amorphous phase fraction. The plastic strain evolution is plotted in Fig. IV.11 until one hundred consecutive cycles. Note that it is divided by the value at the first cycle.

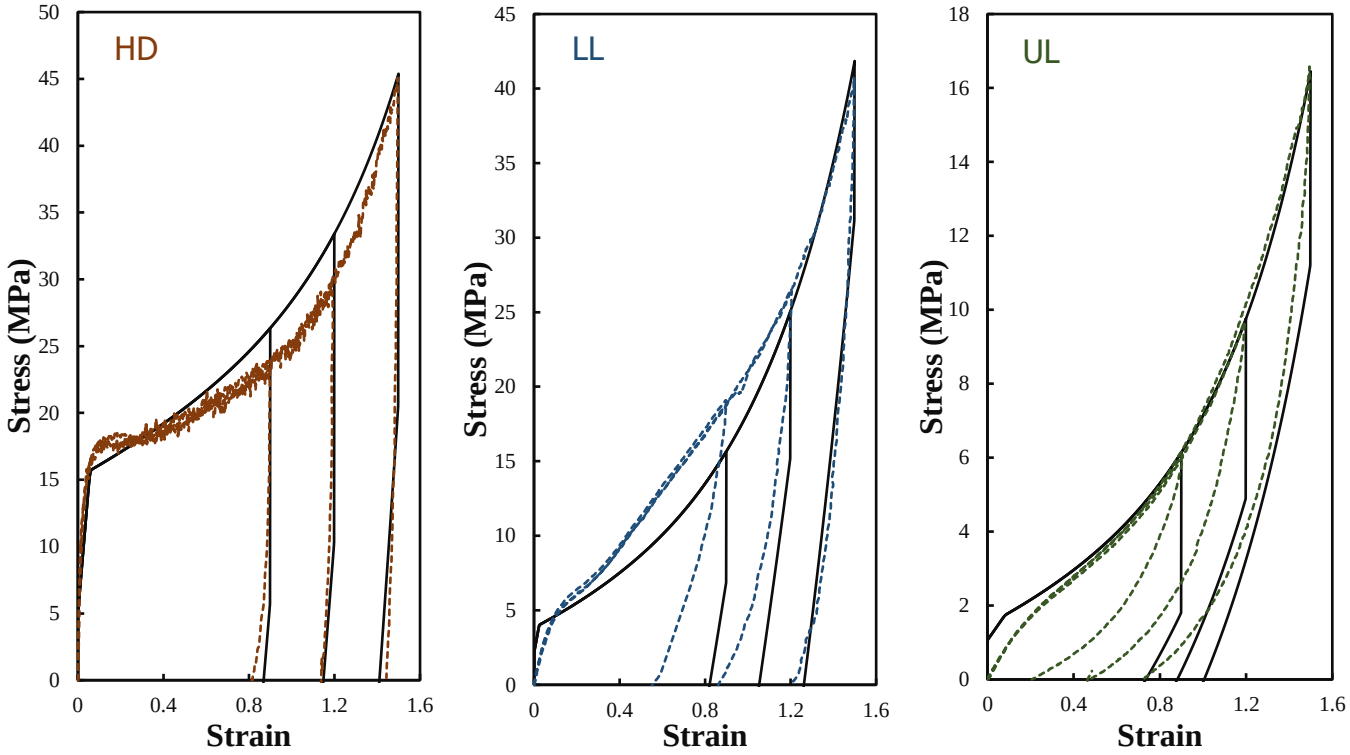

Fig. IV.9. Stress-strain curves of the three polyethylene systems upon loading-unloading at different strain levels and at a true strain rate of 0.001 /s (dashed lines: experimental data, solid lines: constitutive model).

The instantaneous adjustment of the cross-head speed of the testing machine to maintain constant the local strain rate (especially during the necking and post-necking stages if any) induced serrated experimental curves. The observed inflection points on the theoretical evolutions are mainly due to the fact that they are not continuously obtained but are punctually extracted from the cyclic stress-strain curves. The accuracy in the data extraction affects thus the smooth character of the theoretical evolutions. The model ability to capture the plastic strain evolution depends on the amorphous phase fraction. It underestimates the HD and LL data in the first fifty cycles and then overestimates the data, whereas it always underestimates the UL data.

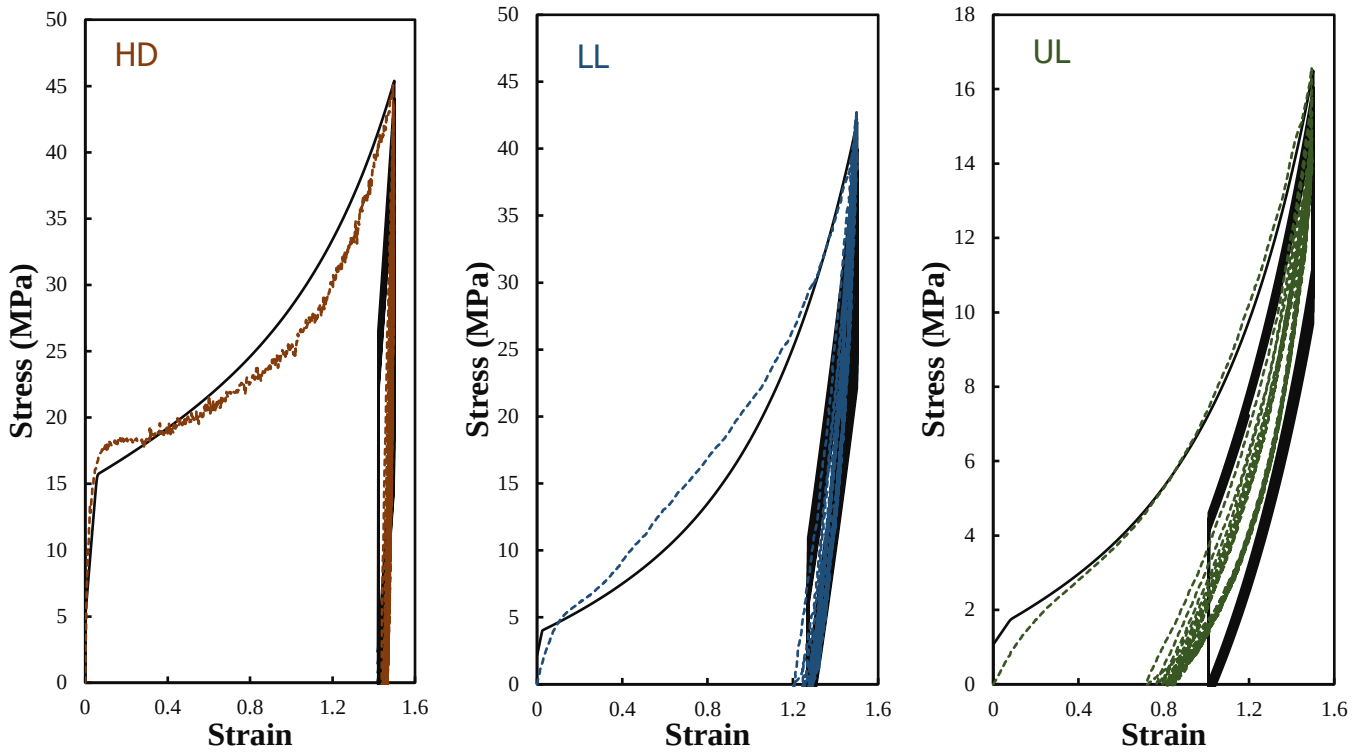

Fig. IV.10. Stress-strain curves of the three polyethylene systems upon oligo-cyclic loading at a strain level of 1.5 and at a true strain rate of 0.001 /s (dashed lines: experimental data, solid lines: constitutive model).

The deformation mechanisms associated to the Mullins effect can be discussed thanks to the plots of Figs. IV.7 and IV.8. When the macroscopic strain is retracted to zero macroscopic stress, the local axial stress in the crystalline lamellae is negative in average whereas the local axial stress in the amorphous phase is positive. The further decomposition of the amorphous stress shows a negative intermolecular stress and a positive network stress. Because the previously sheared crystalline lamellae are in a frozen state, the crystalline stress is seen to be stabilized throughout the consecutive deforming cycles. By contrast, the network stress significantly decreases with increasing cycles whereas the intermolecular stress slightly decreases. The inelastic intermolecular stretch is permanent while the inelastic network stretch slightly increases with increasing cycles. In addition to the crystal texturing, a new molecular network configuration appears in the amorphous linking modifying the previous one at each new cycle of the cyclic loading.

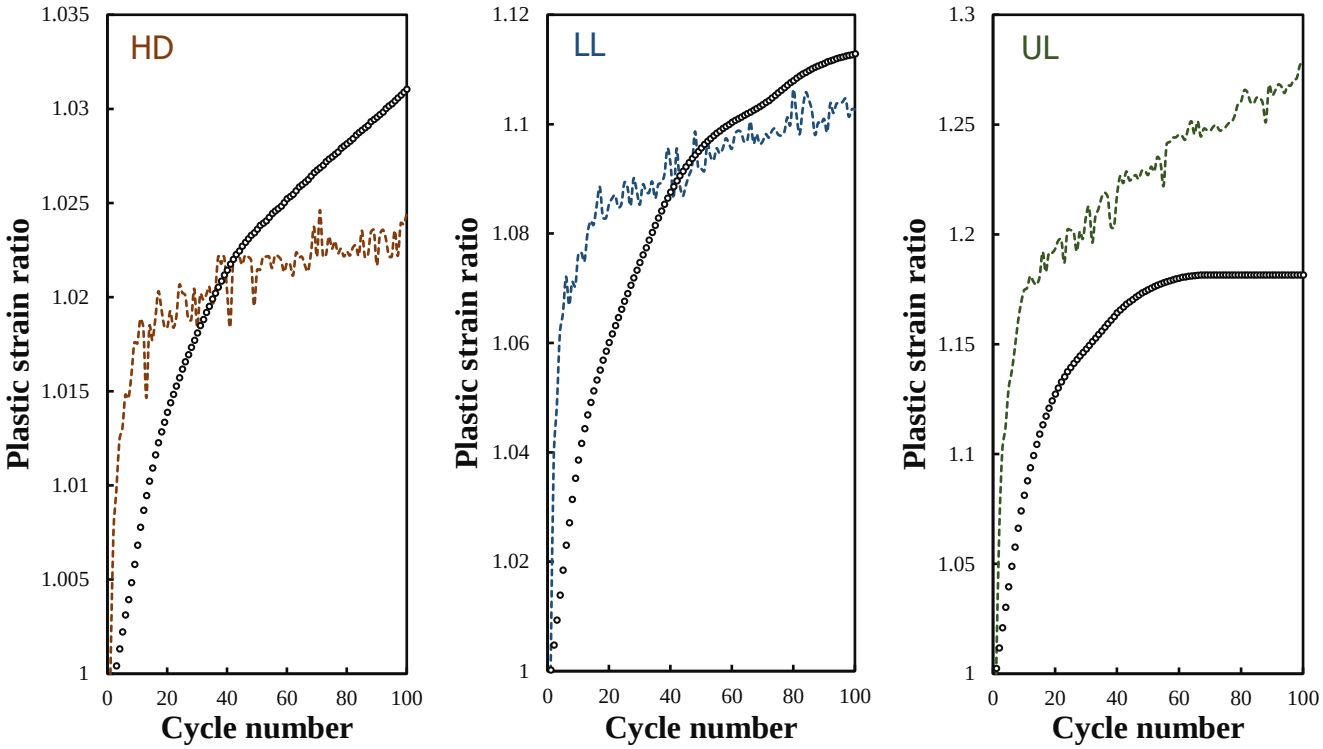

Fig. IV.11. Accumulation of plastic strain at zero stress of the three polyethylene systems upon oligo-cyclic loading at a strain level of 1.5 and at a true strain rate of 0.001 /s (dashed lines: experimental data, symbols: constitutive model).

It can be observed that prediction and experimental data are close to each other for the HD system but the predicted hysteresis loop diverges from the experimental data with the crystallinity increase. Recall that the elastic properties of the polyethylene crystal are introduced as direct inputs into the model which leads to the abrupt reloading. Note that the main goal here is to observe the model limitations rather than propose improvements of modeling capabilities. Disregarding the micromechanical scale transition, the simplest way to improve the model capacities could be done by adapting the crystal stiffness for each fraction and/or by introducing a network alteration upon cyclic loading through an appropriate change of the number of entangled points. As some entanglements will become ineffective with increasing cycle number, $C_h = n_c k\theta$ will decrease and N will increase (the product $n_c N$ remaining constant in order to conserve mass) while the other model parameters would remain unchanged. The evolution equations of n_c and N would require supplementary parameters fitted on the hysteretic response evolution with increasing cycle number (Makki et al., 2017). Nonetheless, our objective here is to limit the number of model parameters and to present the model plots for

predictive purpose only introducing the crystal content as main variable input.

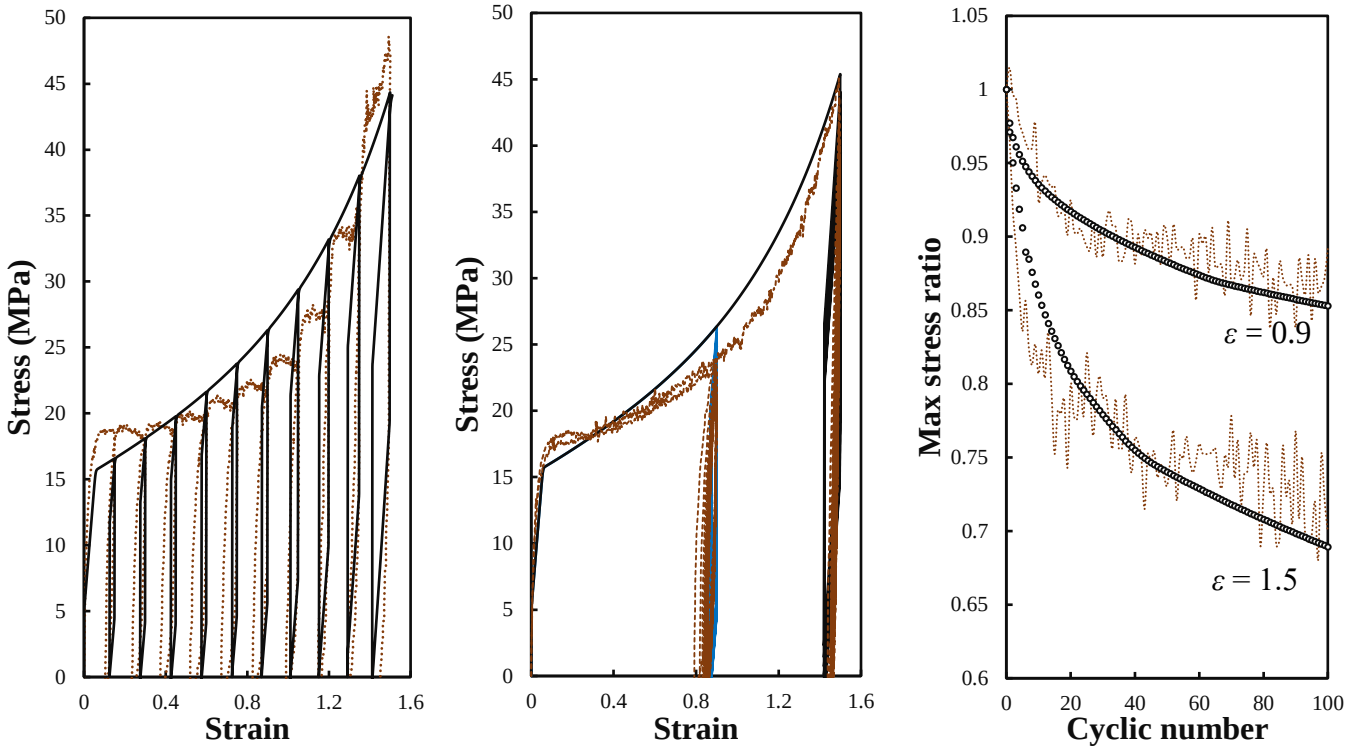

Fig. IV.12. Stress-strain curves of the HD system upon (a) loading-unloading-reloading, (b) oligo-cyclic loading (dashed lines: experimental data, solid lines: constitutive model), (c) stress-softening at different strain levels and at a true strain rate of 0.001 /s (dashed lines: experimental data, symbols: constitutive model).

The quite good agreement with the experimental observations of the HD nonlinear cyclic response confirms the ability of the constitutive representation to describe high crystalline media. Fig. IV.12 compares the predicted and measured curves to present the strain level effect on different aspects of the HD cyclic response considering both one cycle with increasing maximum strain levels and oligo-cyclic loading with two strain levels. It can be observed that the model recaptures the same path as that corresponding to the monotonic one when the strain exceeds the maximum strain previously applied. The general trends of the oligo-cyclic stretching are adequately predicted by the model, in particular the increase in stress-softening magnitude with strain level.

IV.4. Conclusion

In this chapter, the highly nonlinear and rate-dependent mechanical response of semi-crystalline polyethylene systems covering a wide spectrum of the crystallinity was investigated within a

multi-scale homogenization-based approach. The model ability to capture the large-strain response variation with the crystallinity was criticized. The model exhibited weaknesses in small-strain region but it was able to reproduce, within large-strain region, the rate-dependent monotonic response variation with crystallinity. The general trends of the high-crystalline material cyclic response were quantitatively well reproduced by the model while the deviation from experiments increased with amorphicity, which would require to take into account the amorphous network alteration.

In addition to molecular orientation effects that takes place as the deformation proceeds, the cavitation damage associated with progressive nucleation and growth of cavities in the amorphous layers will be presented in the next chapter.

References

Abdul-Hameed, H., Messager, T., Zaïri, F., Naït-Abdelaziz, M., 2014. Large-strain viscoelastic-viscoplastic constitutive modeling of semi-crystalline polymers and model identification by deterministic/evolutionary approach. Computational Materials Science 90, 241-252.

Agoras, M., Ponte Castaneda, P., 2012. Multi-scale homogenization-based modeling of semi-crystalline polymers. Philosophical Magazine 92, 925-958.

Anoukou, K., Zaïri, F., Naït-Abdelaziz, M., Zaoui, A., Qu, Z., Gloaguen, J.M., Lefebvre, J.M., 2014. A micromechanical model taking into account the contribution of □- and □-crystalline phases in the stiffening of polyamide 6-clay nanocomposites: a closed-formulation including the crystal symmetry. Composites Part B 64, 84-96.

Argon, A.S., Galeski, A., Kazmierczak, T., 2005. Rate mechanisms of plasticity in semicrystalline polyethylene. Polymer 46, 11798-11805.

Arruda, E.M., Boyce, M.C., 1993. A three-dimensional constitutive model for the large stretch behavior of rubber elastic materials. Journal of the Mechanics and Physics of Solids 41, 389-412.

Ayoub, G., Zaïri, F., Naït-Abdelaziz, M., Gloaguen, J.M., 2010. Modelling large deformation behaviour under loading-unloading of semicrystalline polymers: application to a high density polyethylene. International Journal of Plasticity 26, 329-347.

Ayoub, G., Zaïri, F., Fréderix, C., Gloaguen, J.M., Naït-Abdelaziz, M., Seguela, R., Lefebvre, J.M., 2011. Effects of crystal content on the mechanical behaviour of polyethylene under finite strains: experiments and constitutive modelling. International Journal of Plasticity 27, 492-511.

Bartczak, Z., Kozanecki, M., 2005. Influence of molecular parameters on high-strain deformation of polyethylene in the plane-strain compression. Part I. Stress-strain behavior. Polymer 46, 8210-8221.

Bartczak, Z., Galeski, A., 2010. Plasticity of semicrystalline polymers. Macromolecular Symposia 294, 67-90.

Bassett, D.C., Hodge, A.M., 1981. On the morphology of melt-crystallized polyethylene I. Lamellar profiles. Proceedings of the Royal Society of London A 377, 25-37.

Bédoui, F., Diani, J., Régnier, G., Seiler, W., 2006. Micromechanical modelling of isotropic elastic behaviour of semicrystalline polymers. Acta Materialia 54, 1513-1523.

Ben Hadj Hamouda, H., Laiarinandrasana, L., Piques, R., 2007. Viscoplastic behaviour of a medium density polyethylene (MDPE): Constitutive equations based on double nonlinear deformation model. International Journal of Plasticity 23, 1307-1327.

Bernard, C.A., Lame, O., Deplancke, T., Cavaillé, J.Y., Ogawa, K., 2020. From rheological to original three-dimensional mechanical modelling of semi-crystalline polymers: Application to a wide strain rate range and large deformation of Ultra-High Molecular Weight PolyEthylene. Mechanics of Materials 151, 103640.

Boyce, M.C., Socrate, S., Llana, P.G., 2000. Constitutive model for the finite deformation stress-strain behavior of poly(ethylene terephthalate) above the glass transition. Polymer 41, 2183-2201.

Chen, K., Kang, G., Yu, C., Jiang, H., 2019. Effect of crystalline content on ratchetting of ultra-high molecular weight polyethylene polymers: Experimental investigation and constitutive model. Mechanics of Materials 133, 37-54.

Colak, O.U., Dusunceli, N., 2006. Modeling viscoelastic and viscoplastic behavior of high density polyethylene (HDPE). Journal of Engineering Materials and Technology 128, 572-578.

Deplancke, T., Fivel, M., Lame, O., 2019. 1D strain rate-dependent constitutive model of UHMWPE: From crystalline network to fibrillar structure behavior. Mechanics of Materials 137, 103129.

Drozdov, A.D., Gupta, R.K., 2003. Constitutive equations of finite viscoplasticity of semicrystalline polymers. International Journal of Solids and Structures 40, 6217-6243.

Drozdov, A.D., 2009. Mullins' effect in semicrystalline polymers. International Journal of Solids and Structures 46, 3336-3345.

Drozdov, A.D., Klitkou, R., Christiansen, J.D., 2013. Multi-cycle deformation of semicrystalline polymers: Observations and constitutive modeling. Mechanics Research Communications 48, 70-75.

Dusunceli N., Colak, O.U., 2008. Modelling effects of degree of crystallinity on mechanical behavior of semicrystalline polymers. International Journal of Plasticity 24, 1224-1242.

Gueguen, O., Ahzi, S., Makradi, A., Belouetta, S., 2010. A new three-phase model to estimate the effective elastic properties of semi-crystalline polymers: Application to PET. Mechanics of Materials 42, 1-10.

Guo, H., Rinaldi, R.G., Tayakout, S., Broudin, M., Lame, O., 2021. Characterization of the spherulitic deformation in equatorial region and cavitation in HDPE materials submitted to mixed-mode oligo-cyclic tensile loading. Polymer Testing 99, 107208.

Guo, Q., Zaïri, F., 2020. A physically-based thermo-mechanical model for stretch-induced crystallizable rubbers: crystallization thermodynamics and chain-network crystallization anisotropy. International Journal of Plasticity 131, 102724.

Hachour, K., Zaïri, F., Naït-Abdelaziz, M., Gloaguen, J.M., Aberkane, M., Lefebvre J.M., 2014. Experiments and modeling of high-crystalline polyethylene yielding under different stress states. International Journal of Plasticity 54, 1-18.

Haward, R.N., Thackray, G., 1968. The use of a mathematical model to describe isothermal stress-strain curves in glassy thermoplastics. Proceedings of the Royal Society of London 302, 453-472.

Hillmansen, S., Hobeika, S., Haward, R.N., Leevers, P.S., 2000. The effect of strain rate, temperature, and molecular mass on the tensile deformation of polyethylene. Polymer Engineering and Science 40, 481-489.

Kazmierczak, T., Galeski, A., Argon, A.S., 2005. Plastic deformation of polyethylene crystals as a function of crystal thickness and compression rate. Polymer 46, 8926-8936.

Khan, F., Krempl, E., 2006. Amorphous and semicrystalline solid polymers: Experimental and modeling studies of their inelastic deformation behaviors. Journal of Engineering Materials and Technology 128, 64-72.

Lee, B.J., Parks, D.M., Ahzi, S., 1993a. Micromechanical modeling of large plastic deformation and texture evolution in semi-crystalline polymers. Journal of the Mechanics and Physics of Solids 41, 1651-1687.

Lee, B.J., Argon, A.S., Parks, D.M., Ahzi, S., Bartczak, Z., 1993b. Simulation of large strain plastic deformation and texture evolution in high density polyethylene. Polymer 34, 3555-3575.

Makki, M., Ayoub, G., Abdul-Hameed, H., Zaïri, F., Mansoor, B., Naït-Abdelaziz, M., Ouederni, M., Zaïri, F., 2017. Mullins effect in polyethylene and its dependency on crystal content: A network alteration model. Journal of the Mechanical Behavior of Biomedical Materials 75, 442-454.

Mesbah, A., Elmeguenni, M., Yan, Z., Zaïri, F., Ding, N., Gloaguen, J.M., 2021. How stress triaxiality affects cavitation damage in high-density polyethylene: experiments and constitutive modeling. Polymer Testing, 107248.

Mirkhalaf, M., van Dommelen, J.A.W., Govaert, L.E., Furmanski, J., Geers, M.G.D., 2019. Micromechanical modeling of anisotropic behavior of oriented semicrystalline polymers. Journal of Polymer Science, Part B: Polymer Physics 57, 378-391.

Nikolov, S., Doghri, I., 2000. A micro/macro constitutive model for the small-deformation behavior of polyethylene. Polymer 41, 1883-1891.

Nikolov, S., Doghri, I., Pierard, O., Zealouk, L., Goldberg, A., 2002. Multi-scale constitutive modeling of the small deformations of semi-crystalline polymers. Journal of the Mechanics and Physics of Solids 50, 2275-2302.

Peacock, AJ., 2000. Handbook of Polyethylene: Structures, Properties, and Applications. Dekker, M. (Eds.), New York.

Peterlin, A., 1975. Plastic deformation of polymers with fibrous structure. Colloid and Polymer Science 253, 809-823.

Qi, Z., Hu, N., Li, G., Zeng, D., 2019. Constitutive modeling for the elastic-viscoplastic behavior of high density polyethylene under cyclic loading. International Journal of Plasticity 113, 125-144.

Rozanski, A., Galeski, A., 2013. Plastic yielding of semicrystalline polymers affected by amorphous phase. International Journal of Plasticity 41, 14-29.

Seguela, R., Gaucher-Miri, V., Elkoun, S., 1998a. Plastic deformation of polyethylene and ethylene copolymers. Part I Homogeneous crystal slip and molecular mobility. Journal of Materials Science 33, 1273-1279.

Seguela, R., Elkoun, S., Gaucher-Miri, V., 1998b. Plastic deformation of polyethylene and ethylene copolymers. Part II Heterogeneous crystal slip and strain-induced phase change. Journal of Materials Science 33, 1801-1807.

Sepiani, H., Polak, M.A., Penlidis, A., 2018. Modeling short- and long-term time-dependent nonlinear behavior of polyethylene. Mechanics of Advanced Materials and Structures 25, 600-610.

Tashiro, K., Kobayashi, M., Tadokoro, H., 1978. Calculation of three-dimensional elastic constants of polymer crystals. 2. Application to orthorhombic polyethylene and poly(vinyl alcohol). Macromolecules 11, 914-918.

Uchida, M., Tada, N., 2013. Micro-, meso- to macroscopic modeling of deformation behavior of semi-crystalline polymer. International Journal of Plasticity 49, 164-184.

van Dommelen, J.A.W., Parks, D.M., Boyce, M.C., Brekelmans, W.A.M., Baaijens, F.P.T., 2003. Micromechanical modeling of the elasto-viscoplastic behavior of semi-crystalline polymers. Journal of the Mechanics and Physics of Solids 51, 519-541.

Wang, M., Shen, J., Li, J., Guo, S., 2015. Network alteration theory on Mullins effect in semicrystalline polymers. Polymer International 64, 105-112.

Wunderlich, B., 1980. Macromolecular Physics, Crystal Melting, Academic Press, New York.

Zaïri, F., Aour, B., Gloaguen, J.M., Naït-Abdelaziz, M., Lefebvre, J.M., 2006. Numerical modelling of elastic-viscoplastic equal channel angular extrusion process of a polymer. Computational Materials Science 38, 202-216.

Zaïri, F., Naït Abdelaziz, M., Gloaguen, J.M., Lefebvre, J.M., 2011. A physically-based constitutive model for anisotropic damage in rubber-toughened glassy polymers during finite deformation. International Journal of Plasticity 27, 25-51.

Zhang, C., Moore, I.D., 1997. Nonlinear mechanical response of high density polyethylene. Part II: Uniaxial constitutive modeling. Polymer Engineering and Science 37, 413-420.

Chapter V

A Multi-Scale Plastic-Damage Model for Strain-Induced Morphological Anisotropy in Semi-Crystalline Polyethylene

Chapter V. A multi-scale plastic-damage model for strain-induced morphological anisotropy in semi-crystalline polyethylene[10]

Abstract

This chapter presents a multi-scale plastic-damage model for strain-induced morphological anisotropy in semi-crystalline polyethylene formulated within a continuum-based micromechanical framework. The crystallographic shear in the crystalline lamellae and the molecular alignment/relaxation of the amorphous phase are two underlying inelastic processes integrated in the constitutive representation. The cavitation damage accumulation related to the progressive nucleation and anisotropic growth of nano-sized cavities in the amorphous phase is also integrated and treated separately for the elastic-viscoplastic intermolecular interactions and for the viscohyperelastic network interactions. The mechanical coupling between the deformation modes in the amorphous and crystalline domains is obtained by considering the crystalline-amorphous interfacial interaction in the micro-macro homogenization procedure. The model output is compared to tensile experimental observations from the literature of high-density polyethylene, in terms of stress-strain response and inelastic volumetric strain, during stretching and stretching-retraction-recovery sequences upon large-strain plastic deformation at different strain rates and temperatures. The effect of strain-induced morphological anisotropy on the internal cavitation damage distributions is analyzed by means of pole figures. The key role of the cavitation damage on the macroscopic and internal responses is studied.

Keywords: Semi-crystalline polyethylene; Multi-scale model; Anisotropic void growth; Crystallographic texturing.

[10] This chapter is based on the following paper: Yan, Z., Guo, Q., Zaïri, F., Zaoui, A., 2022. A multi-scale plastic-damage model for strain-induced morphological anisotropy in semi-crystalline polyethylene. International Journal of Non-Linear Mechanics 147, 104238.

V.1. Introduction

Crystallographic texturing and strain-induced preferred orientation of the amorphous molecular network are the two main inelastic mechanisms at the origin of the finite-strain morphological anisotropy occurring in semi-crystalline polyethylene under in-service or manufacturing processing (Seguela et al., 1998; Argon et al., 2005; Kazmierczak et al., 2005; Bartczak et al., 2010; Rozanski et al., 2013). Due to 3D stress being developed in the thin amorphous layers embedded between broad and wide crystalline lamellae, the local inelastic events may also include nano-sized voids nucleated within the amorphous domain. Over the years, a substantial qualitative understanding of the cavitation damage in semi-crystalline polymers has been brought (Parsons et al., 2005; Pawlak et al., 2005, 2007; Addiego et al., 2006; Castagnet et al., 2007; Boisot et al., 2011; Detrez et al., 2011; Ponçot et al., 2013; Laiarinandrasana et al., 2016; Ovalle et al., 2021; Yan et al., 2021). The reader may also refer to a recent comprehensive review on the literature experimental observations (Zhang et al., 2019). The voiding damage process may experience anisotropic growth during deformation and enter in competition with the plastic shearing of the nano-sized crystalline lamellae. The relative plastic-damage extent depends on complex interactions existing between external loading conditions and features of the two distinguishing phases such as crystal dimensions, crystal degree, crystal form, amorphous strength/consistency and molecular structure.

Continuum-based constitutive modeling of the inelastic deformation behavior of semi-crystalline polyethylene is a prerequisite for advanced engineering use while offering deep understanding of the separate and synergic effects of key microstructural and loading parameters governing the macroscopic response. The model should be as most as physically consistent by considering the above-mentioned microstructure specificities. Although it is a very active subject of research, quantitative modeling of the finite strain anisotropic plastic behavior including cavitation damage in the amorphous phase in connection to the crystallographic shear in the crystalline lamellae is still lacking, and that, for all existing semi-crystalline polymer systems. Addressing this problematic is therefore of prime importance to better understand the interactions between the strain-induced morphological anisotropy and the cavitation damage. The microstructure-based models can be classified according to the approximation of the semi-crystalline polymer microstructure. The overall material response can be constitutively captured in continuum terms by the combination of different rheological resistances invoking mechanical analogs (using combinations of elements, usually linear elastic

springs, viscoplastic dashpots and nonlinear elastic springs) and representing physically distinct sources in the crystalline and amorphous domains (Dusunceli et al., 2008; Ayoub et al., 2010, 2011; Drozdov et al., 2013; Abdul-Hameed et al., 2014; Makki et al., 2017; Sepiani et al., 2018; Chen et al., 2019; Deplancke et al., 2019; Qi et al., 2019; Bernard et al., 2020). These rheological models use a simplified composite-type representation and may integrate the crystalline and amorphous intermolecular micro-mechanisms but neglect both hierarchical semi-crystalline structure and internal interactions. Besides, the crystallographic texturing cannot be predicted because the constitutive representation remains rather macroscopic even if some microstructure ingredients are incorporated such as amorphous chains features and crystal fraction. Proper physically-based constitutive representation requires to take into account the multi-scale inelastic processes while the local interactions are properly considered. In this regard, continuum-based models considered the mesoscopic scale as the starting observation of the constitutive representation by employing multi-scale homogenization-based approaches. Using the Eshelby inclusion theory, some of these models assume a matrix-inclusion microstructure approximation based on a composite-type description (Bédoui et al., 2006; Gueguen et al., 2010; Anoukou et al., 2014; Hachour et al., 2014; Mesbah et al., 2021), the inclusions (individually crystalline lamellae at low crystallinity or amorphous domains at high crystallinity) being randomly dispersed in the matrix material (rubbery amorphous matrix at low crystallinity or percolated crystalline matrix at high crystallinity). The theoretical frameworks are nonetheless restricted to strain levels from the elastic region to the small-strain post-yield region. As an alternative, the semi-crystalline material may be regarded as a mixture of crystalline and amorphous domains organized as an aggregate of two-phase inelastic layered composite inclusions consisting in parallel crystalline lamellae and amorphous layers which are randomly oriented (Lee et al., 1993a, 1993b; Nikolov et al., 2000, 2002; van Dommelen et al., 2003; Agoras et al., 2012; Uchida et al., 2013; Mirkalaf et al., 2019; Yan et al., 2021). These models are used to capture both pre-yielding and post-yielding while taking into account crystal elasto-plasticity, crystallographic texturing and amorphous molecular network preferred orientation during finite plastic deformation. All these deformation mechanisms are purely isochoric. To date, no model takes into account the multi-scale inelastic processes at the origin of the strain-induced anisotropy in semi-crystalline polymers in relation to the inelastic dilatation mechanism occurring in the amorphous phase. The development of such a modeling would bring a more accurate information of the intrinsic mechanical behavior and a deeper understanding of the interactions between the above-mentioned inelastic isochoric mechanisms

and the cavitation damage.

In a previous work (Yan et al., 2021), a multi-scale homogenization-based model was developed and applied to the large-plastic deformation of semi-crystalline polyethylene covering a wide spectrum of the crystallinity allowing to demonstrate the determinant role of the strength and consistency of the amorphous phase on the tensile yielding. The aim of the present chapter is to further develop the model to consider the cavitation damage effects in the material anisotropy during finite plastic deformation of polyethylene. By this way, a more physically consistent description is formulated in continuum terms to describe the complex coupling existing between microstructure (amorphous and crystalline phases), micromechanical deformation processes including cavitation damage and large-strain flow behavior. The efficiency of the proposed plastic-damage model to capture material response in terms of finite deformation stress-strain behavior and inelastic volumetric strain is critically discussed by comparing simulations to experimental results including strain rate and stretching temperature effects. The effects of crystal plasticity and amorphous cavitation damage on the macroscopic and internal responses are observed thanks to the model under stretching and stretching-retraction conditions.

The present chapter is organized as follows. The main elements of the fully three-dimensional model that accounts for the role of cavitation damage are described within the continuum-based micromechanical framework in Section V.2 Section V.3 presents comparisons between model simulations and experimental data as well as microstructure evolution predictions. Concluding remarks are finally given in Section V.4.

The following notation is used throughout the text. Tensors and vectors are denoted by normal boldfaced letters and italicized boldfaced letters, respectively, while scalars and individual components of vectors and tensors are denoted by normal italicized letters. The superposed dot designates the time derivative. The superscript T indicates the transpose quantity. The symbol $\otimes$ denotes tensor product.

V.2. Model formulation

The present modeling satisfies the continuum mechanics rules within the large deformation kinematics and is based on a two-step homogenization process, i.e. microscopic/mesoscopic and then mesoscopic/macroscopic. The two-phase heterogeneous material exhibits a hierarchical organization of the regularly ordered (crystalline) phase from the nano-sized lamellar structure to the well-organized crystalline lamellae, in the form of micro-sized

interconnecting spherulites in the case of high crystallinity polyethylene. The crystalline lamellae are interspaced by a certain amount of randomly oriented entangled chains, namely the amorphous phase. Starting point for the derivation of the multi-scale plastic-damage model is the constitutive representation of the semi-crystalline polymer system. Fig. V.1 shows the representative material element of the lamellar structure that is regarded at the mesoscopic scale as an aggregate of two-phase layered composite inclusions consisting in parallel crystalline lamellae and amorphous layers, involving respectively, crystal plasticity and internal cavitation as main deformation modes.

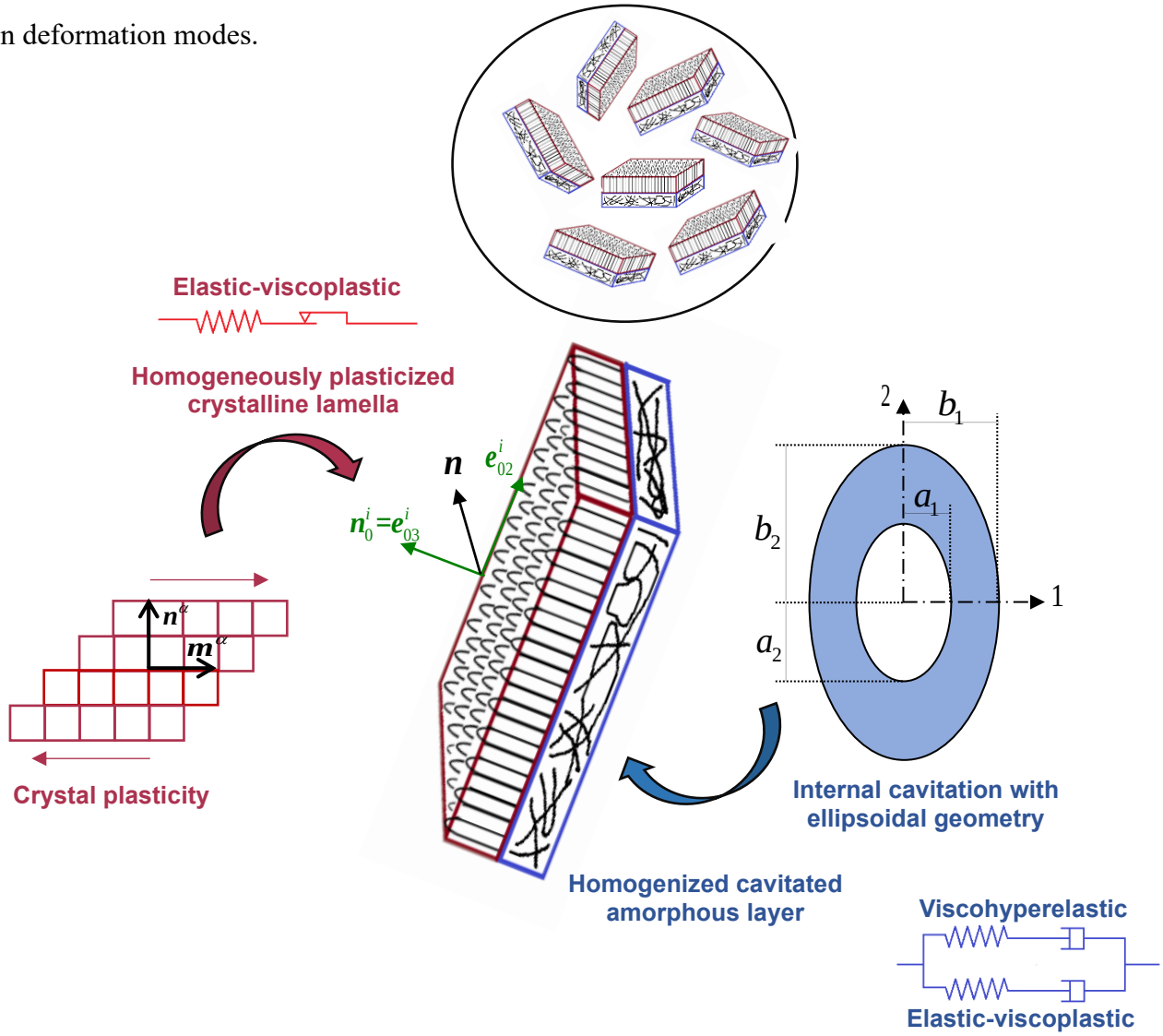

Fig. V.1. Semi-crystalline polymer seen as an aggregate of randomly distributed two-phase layered composite inclusions (stiff crystalline lamella/rubbery amorphous layer) considering crystal plasticity and amorphous cavitation as elementary inelastic mechanisms. The internal cavitation in the amorphous layer is introduced thanks to an ellipsoid unit cell homogenized for both the elastic-viscoplastic intermolecular resistance and the viscohyperelastic network resistance.

V.2.1. Microscopic scale

In a first step of the homogenization process, to achieve the transition from the smallest scale to the mesoscale, the microscopic scale of the material medium must be described by the local stresses in each phase, namely the crystalline Cauchy stress $\boldsymbol{\sigma}_c$ and the amorphous Cauchy stress $\boldsymbol{\sigma}_a$. In accordance with continuum mechanics, both solid phases are considered as homogeneous and continuous media. The physical consistency of their respective constitutive formula depends on the description degree of the deformation modes. In what follows, the crystalline lamellae plasticity and the amorphous phase damage are successively described in connection to features such as finite-strain time-dependency and non-linearity.

V.2.1.1. Plasticity in crystalline lamellae

The elastic-viscoplastic deformation of the crystalline lamellae can be defined via the introduction of an intermediate configuration during a spontaneous elastic unloading allowing the multiplicative decomposition of the crystalline deformation gradient tensor $\mathbf{F}_c$ into an elastic part $\mathbf{F}_c^e$ and an inelastic part $\mathbf{F}_c^{in}$:

$$\mathbf{F}_c = \mathbf{F}_c^e \mathbf{F}_c^{in} \tag{V.1}$$

The crystalline second Piola-Kirchhoff stress tensor $\boldsymbol{\tau}_c$ is constitutively coordinated with the strain as:

$$\boldsymbol{\tau}_c = \mathbf{K}_c : \mathbf{E}_c^e \text{ with } \boldsymbol{\tau}_c = J_c^e \mathbf{F}_c^{e^{-1}} \boldsymbol{\sigma}_c \mathbf{F}_c^{e^{-T}} \tag{V.2}$$

where $\mathbf{K}_c$ is the fourth-order elastic stiffness tensor of the crystalline phase, $\mathbf{E}_c^e = \left(\mathbf{F}_c^{e^T} \mathbf{F}_c^e - \mathbf{I}\right)/2$ is the elastic Green-Lagrange strain tensor and $J_c^e = \det \mathbf{F}_c^e$ is the elastic volume change of the crystalline lamellae.

The elementary inelastic mechanisms operating in the polyethylene crystals are introduced as volume preserving. The inelastic spatial velocity gradient tensor $\mathbf{L}_c^{in}$ introduces the slip deformation for the N_s distinct slip systems:

$$\mathbf{L}_c^{in} = \sum_{\alpha=1}^{N_s} \dot{\gamma}_c^\alpha \mathbf{R}^\alpha \text{ with } \mathbf{R}^\alpha = \frac{1}{2}\left(\boldsymbol{n}^\alpha \otimes \boldsymbol{m}^\alpha + \boldsymbol{m}^\alpha \otimes \boldsymbol{n}^\alpha\right) \tag{V.3}$$

where $\mathbf{R}^\alpha$ is the nonsymmetric Schmid tensor with $\boldsymbol{n}^\alpha$ and $\boldsymbol{m}^\alpha$ are the "slip plane" normal vector and the "slip direction" vector in this plane, respectively (Fig. V.1), and $\dot{\gamma}_c^\alpha$ is the crystalline shear strain rate given by:

$$\dot{\gamma}_c^\alpha = \dot{\gamma}_{c,0} \text{sign}\left(\tau^\alpha\right) \left| \frac{\tau^\alpha}{g^\alpha} \right|^{1/m} \tag{V.4}$$

in which the term $\text{sign}(x)$ denotes the signum function:

$$\text{sign}(x) = \begin{cases} -1 & x < 0 \\ 0 & x = 0 \\ 1 & x > 0 \end{cases} \tag{V.5}$$

The terms $\dot{\gamma}_{c,0}$ is the reference strain rate, m is the strain rate sensitivity parameter, $\tau^\alpha = \boldsymbol{\tau}_c : \mathbf{R}^\alpha$ is the resolved shear stress and g^α is the shear strength of the slip system α.

V.2.1.2. Damage in amorphous layers

Let us now consider the Cauchy stress in the amorphous layers. It may be constitutively represented by considering two additive micro-mechanisms acting in parallel:

$$\boldsymbol{\sigma}_a = \boldsymbol{\sigma}_{a\_\text{inter}} + \boldsymbol{\sigma}_{a\_\text{net}} \tag{V.6}$$

where $\boldsymbol{\sigma}_{a\_\text{inter}}$ is the intermolecular resistance to molecular chain segment rotation in the amorphous layers and $\boldsymbol{\sigma}_{a\_\text{net}}$ is the network resistance to alignment and orientation of the amorphous chains at large strains considering changes in configurational entropy and molecular relaxation process during the strain-hardening stage of the stress-strain response. The two physically distinct sources require different constitutive theories considering the cavitation damage mechanism giving rise to a volume increase. The amorphous phase surrounding the voids is made of an elastic-viscoplastic medium for the intermolecular interactions and of a viscohyperelastic medium for the molecular network alignment and orientation process. The ellipsoid unit cell illustrated in Fig. V.1 introduces the void volume fraction f_{void} and the void aspect ratio w as the basic microstructural features of the voided medium[11]:

$$f_{void} = \frac{a_2 a_1^2}{b_2 b_1^2} \text{ and } w = \frac{a_2}{a_1} \tag{V.7}$$

where a_1 and a_2 are the semi-axes of the void, respectively, along axis 1 and along axis 2. The void is prolate if $a_2 > a_1 = a_3$ and oblate if $a_2 < a_1 = a_3$. The terms b_1 and b_2 are the semi-axes of the volume element in which the ellipsoidal void is included. Note that the representative

[11] The confocality of the ellipsoidal void implies that the semi-axes are related by the following condition: $\sqrt{\left|a_2^2 - a_1^2\right|} = \sqrt{\left|b_2^2 - b_1^2\right|} = c$ where c denotes the focal distance.

material element is considered initially spherical. The initial void volume fraction is denoted $f_{0\_void} = a_0^3/b_0^3 \le f_{void} \le 1$ where a_0 and b_0 are the radii, respectively, of the void and of the volume element in the reference configuration.

V.2.1.2.1. Intermolecular interactions

The intermolecular deformation gradient tensor $\mathbf{F}_{a\_\text{inter}}$ may be obtained using the multiplicative decomposition concept of the deformation:

$$\mathbf{F}_{a\_\text{inter}} = \mathbf{F}^{e}_{a\_\text{inter}}\mathbf{F}^{in}_{a\_\text{inter}} \tag{V.8}$$

where $\mathbf{F}^{e}_{a\_\text{inter}}$ and $\mathbf{F}^{in}_{a\_\text{inter}}$ are the elastic and inelastic intermolecular deformation gradient tensors which can be further decomposed into stretch ($\mathbf{U}$ and $\mathbf{V}$) and rotation $\mathbf{R}$ movements using the polar decomposition:

$$\mathbf{F}^{e}_{a\_\text{inter}} = \mathbf{R}^{e}_{a\_\text{inter}}\mathbf{U}^{e}_{a\_\text{inter}} = \mathbf{V}^{e}_{a\_\text{inter}}\mathbf{R}^{e}_{a\_\text{inter}} \text{ and } \mathbf{F}^{in}_{a\_\text{inter}} = \mathbf{R}^{in}_{a\_\text{inter}}\mathbf{U}^{in}_{a\_\text{inter}} = \mathbf{V}^{in}_{a\_\text{inter}}\mathbf{R}^{in}_{a\_\text{inter}} \tag{V.9}$$

The intermolecular Cauchy stress tensor $\boldsymbol{\sigma}_{a\_\text{inter}}$ is related to the corresponding elastic deformation by the following constitutive relationship:

$$\boldsymbol{\sigma}_{a\_\text{inter}} = \frac{1}{J_{a\_\text{inter}}}\mathbb{K}_a \ln\left(\mathbf{V}^{e}_{a\_\text{inter}}\right) \tag{V.10}$$

where $J_{a\_\text{inter}} = \det \mathbf{F}^{e}_{a\_\text{inter}}$ is the elastic intermolecular volume change of the amorphous phase, $\ln\left(\mathbf{V}^{e}_{a\_\text{inter}}\right)$ is the Hencky elastic strain and $\mathbb{K}_a$ is the fourth-order elastic stiffness tensor of the isotropic amorphous layers whose the components may be expressed using the two Lame's constants λ and μ.

The intermolecular inelastic strain rate tensor $\mathbf{D}^{in}_{a\_\text{inter}}$ at the upper scale (that of the porous amorphous phase) is given by the differentiation of the yield function Φ_{a_inter} with respect to the stress $\boldsymbol{\sigma}_{a\_\text{inter}}$:

$$\mathbf{D}^{in}_{a\_\text{inter}} = \Lambda\frac{\partial \Phi_{a\_\text{inter}}}{\partial \boldsymbol{\sigma}_{a\_\text{inter}}} \tag{V.11}$$

where Λ is a scalar parameter obtained from the necessary condition ensuring a coherence in the definition of the energy dissipation at the two scales involved in the amorphous layer. The equivalence between the inelastic work rate $\boldsymbol{\sigma}_{a\_\text{inter}} : \mathbf{D}^{in}_{a\_\text{inter}}$ of the porous amorphous phase and the local dissipation $(1-f)\left\|\boldsymbol{\sigma}_{a\_\text{inter}}\right\|\dot{\gamma}_{a\_\text{inter}}$ in the amorphous phase surrounding the voids leads

to:

$$\Lambda = (1-f)\left\|\boldsymbol{\sigma}_{a\_\text{inter}}\right\|\dot{\gamma}_{a\_\text{inter}}\left(\boldsymbol{\sigma}_{a\_\text{inter}} : \frac{\partial \Phi_{a\_\text{inter}}}{\partial \boldsymbol{\sigma}_{a\_\text{inter}}}\right)^{-1} \tag{V.12}$$

in which $\left\|\boldsymbol{\sigma}_{a\_\text{inter}}\right\| = \left(\boldsymbol{\sigma}'_{a\_\text{inter}} . \boldsymbol{\sigma}'_{a\_\text{inter}} / 2\right)^{1/2}$ defines the local effective shear stress and $\dot{\gamma}_{a\_\text{inter}}$ is the local intermolecular shear strain rate governing the amorphous phase surrounding the voids that takes the Argon form and is expressed as:

$$\dot{\gamma}_{a\_\text{inter}} = \dot{\gamma}_{a,0} \exp\left[-\frac{\Delta G}{k\theta}\left(1 - \frac{\left\|\boldsymbol{\sigma}_{a\_\text{inter}}\right\|}{s}\right)\right] \tag{V.13}$$

where $\dot{\gamma}_{a,0}$ is the pre-exponential factor, ΔG is the activation energy (which must be overcome for inelasticity begins), k is the Boltzmann's constant, θ is the absolute temperature and s is the shear strength controlling the amorphous chain segment rotation:

$$\dot{s} = h\left(s_{a,s} - s\right)\dot{\gamma}_{a\_\text{inter}} \tag{V.14}$$

where h is the post-yield hardening slope prior to the strain-hardening stage, $s_{a,s}$ is the steady-state shear strength and s_0 is the initial shear strength.

The yield function Φ_{a_inter} may be defined using one of the Gurson-type models proposed to capture the inelastic response of porous polymers (Lazzeri et al., 1995; Steenbrink et al., 1997; Pijnenburg et al., 2001, 2005; Guo et al., 2002, 2008; Jeong et al. 2002; Seeling et al., 2002; Imanaka et al., 2003, 2009; Zaïri et al., 2005, 2008, 2011; Challier at al., 2006; Liarinandrasana et al., 2009; Holopainen et al., 2014). The Gurson model was either used as is or with changes more or less deep in order to; introduce polymer specificities for the solid ligaments between voids such as the matrix yielding pressure dependence (Lazzeri et al., 1995; Jeong et al., 2002), the matrix initial yield strain effects (Sreenbrink et al., 1997; Pijnenbug, 2001) and the matrix plastic anisotropy due to molecular network orientation (Zaïri et al., 2011; Holopainea et al., 2014). Note that the anisotropic damage of material may be formulated within the continuum damage mechanics framework and described by a second-order tensor (Lemaitre et al., 2000; Voyiadjis et al., 2012; Ayadi et al., 2016). In a Gurson-type formulation, a scalar damage variable is conveniently used along with a shape factor making the void growth anisotropic. The anisotropic expression of Gologanu et al. (1997) already employed by Zaïri et al. (2011) for rubber-toughened glassy polymers is here used:

$$\Phi_{a\_\text{inter}} = \frac{C}{\left\|\boldsymbol{\sigma}_{a\_\text{inter}}\right\|^2}\left\|\boldsymbol{\sigma}'_{a\_\text{inter}} + \eta\sigma_{a\_\text{inter\_h}}\mathbf{Y}\right\|^2 + 2f_{void}q_w\cosh\left(\kappa\frac{\sigma_{a\_\text{inter\_h}}}{\left\|\boldsymbol{\sigma}_{a\_\text{inter}}\right\|}\right) - 1 - q_w^2 f_{void}^2 = 0 \quad \text{(V.15)}$$

where $\sigma_{a\_\text{inter\_h}} = \boldsymbol{\sigma}_{a\_\text{inter}} : \mathbf{J}$ is a generalized hydrostatic stress in which the tensors $\mathbf{J}$ and $\mathbf{Y}$ are associated to the void axis:

$$\mathbf{J} = \alpha_2\boldsymbol{e}_1\otimes\boldsymbol{e}_1 + \alpha_2\boldsymbol{e}_3\otimes\boldsymbol{e}_3 + (1-2\alpha_2)\boldsymbol{e}_2\otimes\boldsymbol{e}_2 \text{ and } \mathbf{Y} = \frac{2}{3}\boldsymbol{e}_2\otimes\boldsymbol{e}_2 - \frac{1}{3}\boldsymbol{e}_1\otimes\boldsymbol{e}_1 - \frac{1}{3}\boldsymbol{e}_3\otimes\boldsymbol{e}_3 \quad \text{(V.16)}$$

where $(\boldsymbol{e}_1, \boldsymbol{e}_2, \boldsymbol{e}_3)$ is an orthogonal basis with $\boldsymbol{e}_2$ parallel to the axisymmetric axis of the void. The parameters C, η, κ and α_2 are given in Appendix V.A. The parameter q_w is given by:

$$q_w = 1 + 2(q_0 - 1)\frac{\exp S}{1+\exp(2S)} \quad \text{(V.17)}$$

where q_0 is a material constant that may be related to interaction effects between voids and $S = \ln(w)$ is the void shape parameter with S_0 its initial value.

The intermolecular spatial velocity gradient tensor $\mathbf{L}_{a\_\text{inter}} = \dot{\mathbf{F}}_{a\_\text{inter}}\mathbf{F}^{-1}_{a\_\text{inter}} = \mathbf{L}^{e}_{a\_\text{inter}} + \mathbf{L}^{in}_{a\_\text{inter}}$ may be additively decomposed into an elastic part $\mathbf{L}^{e}_{a\_\text{inter}}$ and an inelastic part $\mathbf{L}^{in}_{a\_\text{inter}}$:

$$\mathbf{L}^{e}_{a\_\text{inter}} = \dot{\mathbf{F}}^{e}_{a\_\text{inter}}\mathbf{F}^{e^{-1}}_{a\_\text{inter}} \text{ and } \mathbf{L}^{in}_{a\_\text{inter}} = \mathbf{F}^{e}_{a\_\text{inter}}\dot{\mathbf{F}}^{in}_{a\_\text{inter}}\mathbf{F}^{in^{-1}}_{a\_\text{inter}}\mathbf{F}^{e^{-1}}_{a\_\text{inter}} \quad \text{(V.18)}$$

The inelastic part $\mathbf{L}^{in}_{a\_\text{inter}} = \mathbf{D}^{in}_{a\_\text{inter}} + \mathbf{W}^{in}_{a\_\text{inter}}$ can be further additively decomposed into a symmetric inelastic rate tensor $\mathbf{D}^{in}_{a\_\text{inter}}$ and an antisymmetric inelastic spin tensor $\mathbf{W}^{in}_{a\_\text{inter}}$:

$$\mathbf{D}^{in}_{a\_\text{inter}} = \frac{1}{2}\left(\mathbf{L}^{in}_{a\_\text{inter}} + \mathbf{L}^{in^T}_{a\_\text{inter}}\right) \text{ and } \mathbf{W}^{in}_{a\_\text{inter}} = \frac{1}{2}\left(\mathbf{L}^{in}_{a\_\text{inter}} - \mathbf{L}^{in^T}_{a\_\text{inter}}\right) \quad \text{(V.19)}$$

The intermolecular inelastic flow is considered irrotational[12], i.e. $\mathbf{W}^{in}_{a\_\text{inter}} = \mathbf{0}$ and the evolution equation of the inelastic deformation gradient $\mathbf{F}^{in}_{a\_\text{inter}}$ is given by:

$$\dot{\mathbf{F}}^{in}_{a\_\text{inter}} = \mathbf{F}^{e^{-1}}_{a\_\text{inter}}\mathbf{D}^{in}_{a\_\text{inter}}\mathbf{F}^{e}_{a\_\text{inter}}\mathbf{F}^{in}_{a\_\text{inter}} \quad \text{(V.20)}$$

The elastic component $\mathbf{F}^{e}_{a\_\text{inter}}$ is then extracted from the multiplicative deformation decomposition: $\mathbf{F}^{e}_{a\_\text{inter}} = \mathbf{F}_{a\_\text{inter}}\mathbf{F}^{in^{-1}}_{a\_\text{inter}}$.

[12] The multiplicative decomposition of the deformation gradient implies that the unloading process (relating the deformed configuration with the relaxed configuration) is not uniquely defined. Indeed, an arbitrary rigid body rotation of the relaxed configuration still leaves the relaxed configuration stress free. One way to make unique the unloaded configuration, with no loss in generality, is to assume the inelastic flow irrotational (Gurtin, et al.,2005).

V.2.1.2.2. Network interactions

The network deformation gradient tensor $\mathbf{F}_{a\_\text{net}}$ may be multiplicatively decomposed into an elastic part $\mathbf{F}^{e}_{a\_\text{net}}$ and an inelastic part $\mathbf{F}^{in}_{a\_\text{net}}$:

$$\mathbf{F}_{a\_\text{net}} = \mathbf{F}^{e}_{a\_\text{net}}\mathbf{F}^{in}_{a\_\text{net}} \tag{V.21}$$

The network Cauchy stress tensor $\boldsymbol{\sigma}_{a\_\text{net}}$ is given by the differentiation of the strain energy density W with respect to the elastic deformation:

$$\left(\boldsymbol{\sigma}_{a\_\text{net}}\right)_i = \frac{\lambda^e_i}{J_{a\_\text{net}}}\frac{\partial W}{\partial \lambda^e_i} \text{ with } i = 1, 2, 3 \tag{V.22}$$

No summation on i is implied in this equation.

With the consideration of a strain energy density W based on the first stretch invariant:

$$\frac{\partial W}{\partial \lambda^e_i} = \frac{1}{V_0}\int_{a_0}^{b_0}\int_0^{2\pi}\int_0^{\pi}\frac{\partial \tilde{W}}{\partial \tilde{I}_1}\frac{\partial \tilde{I}_1}{\partial \lambda^e_i}R^2\sin\Theta d\Theta d\Phi dR \tag{V.23}$$

where the integration is carried out in the standard spherical coordinate system $\left(R, \Theta, \Phi\right)$ with $a_0 \le R \le b_0$, $0 \le \Theta \le \pi$ and $0 \le \Phi \le 2\pi$. The term $\tilde{W}$ is the local strain energy density, $\tilde{I}_1$ is the local first stretch invariant, λ^e_1, λ^e_2 and λ^e_3 are the principal elastic stretches, $V_0 = 4\pi b_0^3/3$ is the initial volume of the representative material element and J_{a_net} is the network volume change:

$$J_{a\_\text{net}} = \frac{1 - f_{0\_void}}{1 - f_{void}} \tag{V.24}$$

The local behavior of the amorphous network is governed by the Arruda and Boyce (Arruda et al., 1993) eight-chain model of rubber elasticity introducing the extensibility limit of amorphous chains as a deformation measure:

$$\tilde{W} = C_h\sqrt{N}\left(\beta\sqrt{\frac{\tilde{I}_1}{3}} + \sqrt{N}\ln\frac{\beta}{\sinh\beta}\right) + \text{cst} \text{ with } \beta = \mathcal{L}^{-1}\left(\sqrt{\frac{\tilde{I}_1}{3N}}\right) \tag{V.25}$$

where two relevant molecular network properties are introduced: the average number of molecular units N between entanglements and the amorphous network hardening modulus $C_h = n_c k\theta$ in which n_c is the average density of amorphous chains per unit volume. The term $\mathcal{L}^{-1}$ is the inverse of the Langevin function $\mathcal{L}(x) = \coth(x) - 1/x$ that may be approximated by

a Padé approximation: $\mathcal{L}^{-1}(x) \approx x\left(3-x^2\right)/\left(1-x^2\right)$. Using the kinematically admissible deformation field defined by Hou and Abeyaratne (1992) for void growth in a hyperelastic solid, the motion of every material point of the representative material element is defined by the components in the deformed configuration:

$$x_i = \frac{\lambda_i^e}{J_{a\_\text{net}}^{1/3}} \psi(R) X_i \text{ with } i = 1, 2, 3 \tag{V.26}$$

No summation on i is implied in this equation. The components X_1, X_2 and X_3 of the reference configuration are given in the standard spherical coordinate system by:

$$X_1 = R\sin\Theta\sin\Phi,\ X_2 = R\sin\Theta\cos\Phi \text{ and } X_3 = R\cos\Theta \tag{V.27}$$

The term ψ is given as a function of the radial distance R from the origin of the representative material element as:

$$\psi(R) = \left(1 + \left(J_{a\_\text{net}} - 1\right)\frac{b_0^3}{R^3}\right)^{1/3} \tag{V.28}$$

The local first stretch invariant $\tilde{I}_1$ may be expressed as (Hou et al., 1992):

$$\tilde{I}_1 = \frac{1}{J_{a\_\text{net}}^{2/3}}\left\{\psi^2 I_1 + \frac{1}{R^2}\left(\lambda_1^{e^2}X_1^2 + \lambda_2^{e^2}X_2^2 + \lambda_3^{e^2}X_3^2\right)\left(\frac{1}{\psi^4} - \psi^2\right)\right\} \tag{V.29}$$

where I_1 is the invariant of the left Cauchy-Green strain tensor $\mathbf{B}_{a\_\text{net}}^e = \mathbf{F}_{a\_\text{net}}^e \mathbf{F}_{a\_\text{net}}^{e^T}$. In the case of an isochoric macroscopic deformation, $\tilde{I}_1$ becomes equal to I_1.

The network inelastic strain rate tensor $\mathbf{D}_{a\_\text{net}}^{in}$ is given by the following flow rule:

$$\mathbf{D}_{a\_\text{net}}^{in} = \dot{\gamma}_{a\_\text{net}} \frac{\boldsymbol{\sigma}'_{a\_\text{net}}}{\sqrt{2}\left\|\boldsymbol{\sigma}_{a\_\text{net}}\right\|} \tag{V.30}$$

in which $\left\|\boldsymbol{\sigma}_{a\_\text{net}}\right\| = \left(\boldsymbol{\sigma}'_{a\_\text{net}} . \boldsymbol{\sigma}'_{a\_\text{net}}/2\right)^{1/2}$ is the effective shear stress, $\boldsymbol{\sigma}'_{a\_\text{net}}$ is the deviatoric part and $\dot{\gamma}_{a\_\text{net}}$ is the network shear strain rate:

$$\dot{\gamma}_{a\_\text{net}} = C_v\left(\frac{1}{\lambda_{a\_\text{net}}^{in} - 1}\right)\left\|\boldsymbol{\sigma}_{a\_\text{net}}\right\| \tag{V.31}$$

with

$$\lambda_{a\_\text{net}}^{in} = \left[\frac{1}{3}\text{tr}\left(\mathbf{F}_{a\_\text{net}}^{in}\left(\mathbf{F}_{a\_\text{net}}^{in}\right)^T\right)\right]^{1/2} + \varsigma \tag{V.32}$$

where $\varsigma = 0.01$ is a small perturbation coefficient ensuring numerical stability of the numerical algorithm at the beginning of the loading process and C_v is the amorphous network viscosity coefficient.

As indicated earlier for the intermolecular interactions, the rate kinematics are described by the network spatial velocity gradient tensor $\mathbf{L}_{a\_\text{net}} = \dot{\mathbf{F}}_{a\_\text{net}}\mathbf{F}_{a\_\text{net}}^{-1} = \mathbf{L}_{a\_\text{net}}^{e} + \mathbf{L}_{a\_\text{net}}^{in}$:

$$\mathbf{L}_{a\_\text{net}}^{e} = \dot{\mathbf{F}}_{a\_\text{net}}^{e}\mathbf{F}_{a\_\text{net}}^{e^{-1}} \text{ and } \mathbf{L}_{a\_\text{net}}^{in} = \mathbf{F}_{a\_\text{net}}^{e}\dot{\mathbf{F}}_{a\_\text{net}}^{in}\mathbf{F}_{a\_\text{net}}^{in^{-1}}\mathbf{F}_{a\_\text{net}}^{e^{-1}} \tag{V.33}$$

The inelastic velocity gradient tensor $\mathbf{L}_{a\_\text{net}}^{in}$ consists of a symmetric inelastic rate tensor $\mathbf{D}_{a\_\text{net}}^{in}$ and an antisymmetric inelastic spin tensor $\mathbf{W}_{a\_\text{net}}^{in}$:

$$\mathbf{L}_{a\_\text{net}}^{in} = \mathbf{F}_{a\_\text{net}}^{e}\dot{\mathbf{F}}_{a\_\text{net}}^{in}\mathbf{F}_{a\_\text{net}}^{in^{-1}}\mathbf{F}_{a\_\text{net}}^{e^{-1}} = \mathbf{D}_{a\_\text{net}}^{in} + \mathbf{W}_{a\_\text{net}}^{in} \tag{V.34}$$

with

$$\mathbf{D}_{a\_\text{net}}^{in} = \frac{1}{2}\left(\mathbf{L}_{a\_\text{net}}^{in} + \mathbf{L}_{a\_\text{net}}^{in^{T}}\right) \text{ and } \mathbf{W}_{a\_\text{net}}^{in} = \frac{1}{2}\left(\mathbf{L}_{a\_\text{net}}^{in} - \mathbf{L}_{a\_\text{net}}^{in^{T}}\right) \tag{V.35}$$

By choosing again the inelastic flow irrotational, i.e. $\mathbf{W}_{a\_\text{net}}^{in} = \mathbf{0}$, the evolution equation of the inelastic deformation gradient $\mathbf{F}_{a\_\text{net}}^{in}$ is given by:

$$\dot{\mathbf{F}}_{a\_\text{net}}^{in} = \mathbf{F}_{a\_\text{net}}^{e^{-1}}\mathbf{D}_{a\_\text{net}}^{in}\mathbf{F}_{a\_\text{net}}^{e}\mathbf{F}_{a\_\text{net}}^{in} \tag{V.36}$$

The elastic component $\mathbf{F}_{a\_\text{net}}^{e}$ is then extracted from the multiplicative deformation decomposition: $\mathbf{F}_{a\_\text{net}}^{e} = \mathbf{F}_{a\_\text{net}}\mathbf{F}_{a\_\text{net}}^{in^{-1}}$.

V.2.2. Mesoscopic scale: Two-phase layered composite inclusions

The homogenized amorphous layer stress is volume-averaged with the crystalline lamella stress to give the local inclusion-averaged stress $\boldsymbol{\sigma}_I^i$ of the composite inclusion *i*:

$$\boldsymbol{\sigma}_I^i = f_a^i\boldsymbol{\sigma}_a^i + f_c^i\boldsymbol{\sigma}_c^i \tag{V.37}$$

in which $\boldsymbol{\sigma}_a^i$ and $\boldsymbol{\sigma}_c^i$ are the local homogenized quantities previously defined and, f_a^i and f_c^i are the amorphous and crystalline volume fractions, respectively, expressed as:

$$f_a^i = \frac{f_{a,0}^i J_c}{f_{a,0}^i J_a + f_{c,0}^i J_c} \text{ and } f_c^i = \frac{f_{c,0}^i J_c}{f_{a,0}^i J_a + f_{c,0}^i J_c} \tag{V.38}$$

where $f_{a,0}^i$ and $f_{c,0}^i$ are the corresponding initial volume fractions and, J_c and J_a are the corresponding volume changes.

The local inclusion-averaged deformation gradient tensor $\mathbf{F}_I^i$ of the composite inclusion *i* is given by[13]:

$$\mathbf{F}_I^i = f_{a,0}^i \mathbf{F}_a^i + f_{c,0}^i \mathbf{F}_c^i \tag{V.39}$$

in which $\mathbf{F}_a^i$ and $\mathbf{F}_c^i$ are the local quantities previously defined.

The stress equilibrium is considered at the amorphous-crystalline interface of the composite inclusion *i* using the following condition:

$$\boldsymbol{\sigma}_c^i \cdot \boldsymbol{n}^i = \boldsymbol{\sigma}_a^i \cdot \boldsymbol{n}^i = \boldsymbol{\sigma}_I^i \cdot \boldsymbol{n}^i \tag{V.40}$$

where $\boldsymbol{n}^i$ is the unit normal vector at the interface in the current configuration.

The compatibility of deformation is also considered:

$$\mathbf{F}_c^i \cdot \boldsymbol{x}_0^i = \mathbf{F}_a^i \cdot \boldsymbol{x}_0^i = \mathbf{F}_I^i \cdot \boldsymbol{x}_0^i \tag{V.41}$$

where $\boldsymbol{x}_0^i$ denotes an arbitrary vector in the plane of the interface spanned by the unit vectors $\boldsymbol{e}_{01}^i$ and $\boldsymbol{e}_{02}^i$ of the local orthogonal basis $\left(\boldsymbol{e}_{01}^i, \boldsymbol{e}_{02}^i, \boldsymbol{e}_{03}^i\right)$ in which $\boldsymbol{n}_0^i = \boldsymbol{e}_{03}^i$ denotes the unit normal vector at the interface in the reference configuration.

V.2.3. Macroscopic scale: Aggregate

In a second step of the homogenization process, the transition to the macroscale is conducted by the volume-averaging of all the inclusions in the aggregate. In the present simulations, the aggregate contains $N_I = 125$ two-phase layered composite inclusions. The macroscopic Cauchy stress tensor $\bar{\boldsymbol{\sigma}}$ is given:

$$\bar{\boldsymbol{\sigma}} = \sum_{i=1}^{N_I} f_I^i \boldsymbol{\sigma}_I^i \quad \text{with} \quad f_I^i = \frac{f_{I,0}^i J_I^i}{\sum_{j=1}^{N_I} f_{I,0}^j J_I^j} \tag{V.42}$$

in which f_I^i is the inclusion volume fraction and J_I^i is the inclusion volume change.

The macroscopic void volume fraction f_{void} is calculated by:

$$f_{void} = \sum_{i=1}^{N_I} f_I^i f_{void}^i \tag{V.43}$$

in which f_{void}^i is the local void volume fraction.

[13] In virtue of the Taylor assumption, the local deformation is related to the global one in an affine sense. In other words, the local inclusion-averaged deformation gradient tensor $\mathbf{F}_I^i$ of the composite inclusion *i* is taken equal to the imposed macroscopic deformation gradient $\bar{\mathbf{F}}$ of the aggregate of the N_I inclusions: $\mathbf{F}_I^i = \bar{\mathbf{F}}$.

V.2.4. Microstructure evolution and model implementation

The present multi-scale homogenization-based approach considers assembled together into the same model, the synergic effects on the material anisotropy of key orientation-induced deformation modes taking place as the large-plastic deformation proceeds, namely crystallographic texture evolution, amorphous molecular chains orientation/relaxation and anisotropic voiding process. This subsection provides specific kinetics of the microstructure evolution along with some numerical aspects concerning the composite inclusions model solving process.

The time domain is subdivided into discrete time steps. For each discrete time level, the set of non-linear equations, comprising the interaction law, the local the interface conditions and the volume-averaging equations, is solved. Thereafter, both interface normals and cavitation damage are explicitly updated.

V.2.4.1. Time-integration of inelastic flow

The inelastic component $\mathbf{F}_c^{in}$ at time $t_{n+1}=t_n+\Delta t$ is calculated incrementally by using the previous one at time t_n (van Dommelen et al., 2003):

$$\mathbf{F}_c^{in}\left(t_{n+1}\right)=\mathbf{F}_{c\_inc}^{in}\mathbf{F}_c^{in}\left(t_n\right) \text{ with } \mathbf{F}_{c\_inc}^{in}\approx\left(\mathbf{I}-\mathbf{L}_c^{in}\left(t_n\right)\Delta t/2\right)^{-1}\left(\mathbf{I}+\mathbf{L}_c^{in}\left(t_n\right)\Delta t/2\right) \tag{V.44}$$

where Δt is the time increment and $\mathbf{I}$ is the identity tensor.

The elastic component $\mathbf{F}_c^e$ is then extracted from the multiplicative deformation decomposition: $\mathbf{F}_c^e=\mathbf{F}_c\mathbf{F}_c^{in^{-1}}$. The time-integration of the amorphous deformation is carried out using the formulae (V.20) and (V.36).

V.2.4.2. Morphological texture evolution

The morphological texture evolution is directly related to the orientation of the amorphous-crystalline interfaces which can be updated at each increment. Considering two independent vectors at time $t=0$, $\delta\boldsymbol{x}_1^i(0)$ and $\delta\boldsymbol{x}_2^i(0)$, in the crystalline-amorphous interface, they become at time t:

$$\delta\boldsymbol{x}_1^i\left(t_n\right)=\mathbf{F}^i\left(t_n\right)\delta\boldsymbol{x}_1^i(0) \text{ and } \delta\boldsymbol{x}_2^i\left(t_n\right)=\mathbf{F}^i\left(t_n\right)\delta\boldsymbol{x}_2^i(0) \tag{V.45}$$

where $\mathbf{F}^i\left(t_n\right)$ can be either $\mathbf{F}_a^i\left(t_n\right)$, $\mathbf{F}_c^i\left(t_n\right)$ or $\mathbf{F}_I^i\left(t_n\right)$.

The normal vector $\boldsymbol{n}^i$ at the amorphous-crystalline interface is then obtained by:

$$\boldsymbol{n}^i(t)=\frac{\mathbf{F}^i(t_n)\delta\boldsymbol{x}_1^i(0)\times\mathbf{F}^i(t_n)\delta\boldsymbol{x}_2^i(0)}{\left\|\mathbf{F}^i(t_n)\delta\boldsymbol{x}_1^i(0)\times\mathbf{F}^i(t_n)\delta\boldsymbol{x}_2^i(0)\right\|}=\frac{\mathbf{F}^{i^{-T}}(t_n)\boldsymbol{n}^i(0)}{\left\|\mathbf{F}^{i^{-T}}(t_n)\boldsymbol{n}^i(0)\right\|} \tag{V.46}$$

with $\mathbf{F}^i(t_n)\delta\boldsymbol{x}_1^i(0)\times\mathbf{F}^i(t_n)\delta\boldsymbol{x}_2^i(0)=\det\left(\mathbf{F}^i(t_n)\right)\mathbf{F}^{i^{-T}}(t_n)\boldsymbol{n}^i(0)$, the symbol $\times$ meaning the cross product of the vectors.

V.2.4.3. Damage evolution

The progressive cavitation damage accumulation gives rise to a volume fraction whose the kinetics $\dot{f}_{void}$ may be expressed as an additive expression of a nucleation part $\dot{f}_n$ and a growth part $\dot{f}_g$:

$$\dot{f}_{void}(t_n)=\dot{f}_n(t_n)+\dot{f}_g(t_n) \tag{V.47}$$

The nucleation phenomenon of voids is difficult to put in equation. In the Gurson-type models, this part introduces the stochastic nature of the process from a statistical form, either strain or stress induced. The mechanism is assumed to be controlled by the local intermolecular shear strain rate:

$$\dot{f}_n(t_{n+1})=\frac{f_a}{s_N\sqrt{2\pi}}\exp\left[-\frac{1}{2}\left(\frac{\gamma_{a\_\text{inter}}(t_n)-\gamma_N}{s_N}\right)^2\right]\dot{\gamma}_{a\_\text{inter}}(t_n) \tag{V.48}$$

where γ_N is the strain at which nucleation takes place, s_N is standard deviation and f_a is the amorphous volume fraction defined above.

Considering the plastic incompressibility of the amorphous solid phase around growing voids, the change in void volume fraction due to void growth is proportional to the macroscopic intermolecular inelastic volumetric strain rate:

$$\dot{f}_g(t_{n+1})=\left(1-f_{void}(t_n)\right)\mathbf{I}:\mathbf{D}^{in}_{a\_\text{inter}}(t_n) \tag{V.49}$$

The void aspect ratio rate $\dot{w}$ is defined by:

$$\dot{w}(t_{n+1})=w(t_n)\alpha_w\left(\boldsymbol{n}_2(t_n)\otimes\boldsymbol{n}_2(t_n)-\boldsymbol{n}_1(t_n)\otimes\boldsymbol{n}_1(t_n)\right):\mathbf{A}:\mathbf{D}^{in}_{a\_\text{inter}}(t_n) \tag{V.50}$$

in which α_w is a parameter and $\mathbb{A}$ is a fourth-order tensor expressed as (Cao et al., 2015):

$$\mathbb{A}=\frac{1}{f_{void}}\left(\mathbb{I}-\frac{3}{2}\mathbb{I}':\mathbb{M}^{-1}\right)\text{ with }\mathbb{M}=\frac{3}{2}\mathbb{I}'+\frac{3f_{void}}{1-f_{void}}\widehat{\mathbb{Q}}^{-1} \tag{V.51}$$

where $\mathbb{I}'$ is the deviatoric part of the fourth-order identify tensor $\mathbb{I}$ and $\widehat{\mathbb{Q}}$ is expressed in Appendix V.B.

V.3. Results and discussion

In what follows, the model is applied to the intrinsic large-plastic deformation of high-density polyethylene represented by the stress-strain behavior along with the inelastic volumetric strain as the most direct indicator of the voiding mechanism nucleated within the amorphous phase. Monotonic data are used to identify the model parameters while non-monotonic (stretching-retraction-recovery) data are used to verify the model predictability. The internal microstructure evolution is then visualized and discussed thanks to the model.

V.3.1. Macroscopic response

V.3.1.1. Model inputs

The crystalline parameters are those used in Chapter IV using the deviatoric version of the constitutive model (Yan et al., 2021). Lamellar surfaces in polyethylene are of the {h0l}-type (i.e. the crystal lamellar growth direction is the crystallographic b-axis) where the angle between the chain direction and the normal of interface varies between 20° and 40° (Bassett et al., 1981). The initial angle between chain direction and normal of interface is set to be 35°. The crystalline phase has therefore an orthorhombic behavior with a high elastic modulus in the chain direction. The values of the elastic stiffness components of the polyethylene crystal are taken from the literature (Tashiro et al., 1978):

$$\left[K_{c\_ij}\right]_{6\times6} = \begin{bmatrix} 7.99 & 3.28 & 1.13 & 0 & 0 & 0 \\ 3.28 & 9.92 & 2.14 & 0 & 0 & 0 \\ 1.13 & 2.14 & 315.92 & 0 & 0 & 0 \\ 0 & 0 & 0 & 3.62 & 0 & 0 \\ 0 & 0 & 0 & 0 & 1.62 & 0 \\ 0 & 0 & 0 & 0 & 0 & 3.19 \end{bmatrix} \text{[GPa]} \qquad \text{(V.52)}$$

The shear strength of the slip system is also taken from the literature (Lee et al.,1993) and reported in Table V.1. They are both introduced as direct inputs into the model. The other model constants are identified using the intrinsic tension data of the high-density polyethylene extracted from the papers of Addiego et al. (2006) and Ponçot et al. (2013). The two key features of the macroscopic material response (true stress-strain and volumetric strain data) reported in Figs. V.2(a) and V.3(a) were experimentally quantified upon monotonic stretching for different true strain rates (0.005 /s, 0.001 /s and 0.0005 /s) at room temperature by Addiego et al. (Addiego et al., 2006) and different stretching temperatures (room temperature, 40°C and 45°C) at a true strain rate of 0.001 /s by Ponçot et al. (2013). In the two papers, the data were measured

for the same material (containing 0.76 of crystals) and the same protocol under well-controlled conditions by means of a video-controlled system able to maintain constant true axial strain rate in the plastic instability of the tested specimen during stretching up to an assigned maximum value. The values of the identified model parameters are listed in Table V.2. The procedure of identification uses a deterministic scheme that consists of successively identifying the different parts of the model. The identification of the cavitation damage parameters was the outcome of a calibration that provides the best fit of the monotonic inelastic volumetric data of Addiego et al. (2006) and Ponçot et al. (2014). Taking as initial values those of the deviatoric version of the constitutive model (Yan et al., 2021), the final values of the amorphous intermolecular and network parameters were then obtained through the adjustment of the best monotonic stress-strain response by means of trial and error.

Table V.1. Slip systems and associated shear strength (Lee et al., 1993a).

Slip system	g^{α} (MPa)
(100)[001]	8
(010)[001]	20
{110}[001]	20
(100)[010]	13.3
(010)[100]	20
{110}<1$\bar{1}$0>	17.6

V.3.1.2. Monotonic stretching

Figs. V.2(b) and V.3(b) show the model-experiments comparison. It can be seen that the model captures in a satisfactory manner the general trends of the elastic-plastic stress-strain response as well as the volumetric strain under increasing tensile strain. The model is able to reproduce well the cavitation damage taking place as the plastic deformation proceeds at room temperature as well as the delay of the damage onset observed with the stretching temperature increase. The significant influence of stretching temperature on the critical strain, beyond which the cavitational behavior takes place, is well captured by the model. Note that the negative volumetric strain experimentally observed below the critical strain is the manifestation of a temperature-dependent material densification phenomenon that may be attributed to the compaction of amorphous polymer chains due to extensive shear yielding delaying the cavitation onset.

The shearing mechanism being assumed to be purely isochoric in our model, the negative volume before the critical strain cannot be captured. Nonetheless, the onset of the cavitation-induced positive inelastic volumetric strain as well as the change in the kinetics of the inelastic

Table V.2. Identified model parameters.

Crystalline	Reference strain rate	$\dot{\gamma}_{c,0}$	(s^{-1})		10^{-6}	
	Strain rate sensitivity	m			0.1355	
Amorphous	First Lame's constant	λ	(MPa)	1938 (25 °C)	1615 (40 °C)	1454 (45 °C)
	Second Lame's constant	μ	(MPa)	425 (25 °C)	354 (40 °C)	319 (45 °C)
	Reference strain rate	$\dot{\gamma}_{a,0}$	(s^{-1})		10^{-6} (s^{-1})	
	Activation energy	ΔG	(J)		7.44×10^{-20}	
	Initial shear strength	s_0	(MPa)	38 (25 °C)	29 (40 °C)	27 (45 °C)
	Intermolecular hardening	s_s	(MPa)	37 (25 °C)	28 (40 °C)	25 (45 °C)
	Interaction coefficient	h		60 (25 °C)	20 (40 °C)	10 (45 °C)
	Network hardening	C_v	($MPa^{-1}s^{-1}$)		2.2×10^{-8}	
	Network viscosity	C_h	(MPa)	2.8 (25 °C)	0.75 (40 °C)	0.7 (45 °C)
	Entanglement density	N			26	
Damage	Initial void volume fraction	f_0			0.001	
	Initial void shape parameter	S_0			0	
	Aspect ratio parameter	α_ω			4	
	Interaction parameter	q_0		4 (25 °C)	1 (40 °C)	0.1 (45 °C)
	Standard deviation	s_N		0.95 (25 °C)	0.35 (40 °C)	0.25 (45 °C)
	Mean nucleating strain	γ_N		0.2(25 °C)	0.65 (40 °C)	0.86 (45 °C)

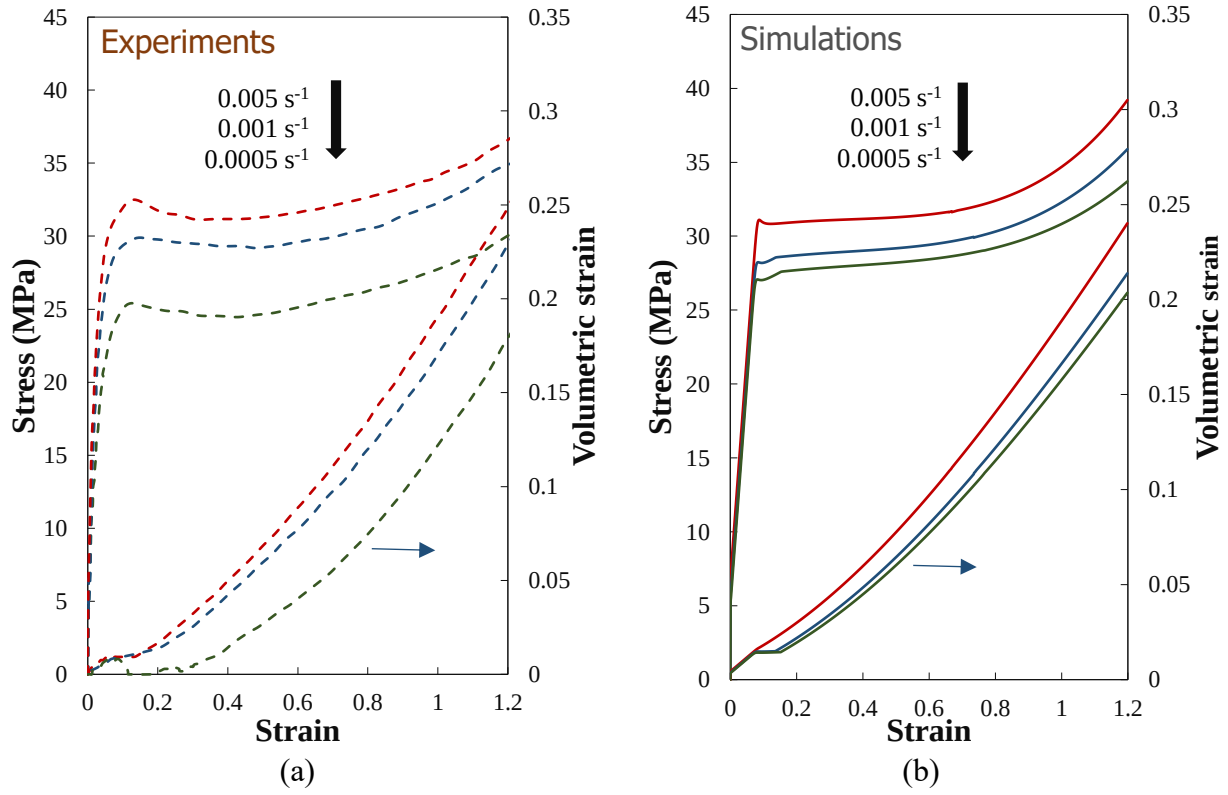

Fig. V.2. Stress and volumetric responses under stretching for different strain rates: (a) experiments taken from Addiego et al. (2006) and (b) model simulations.

volumetric strain are correctly reproduced by the model. In other words, the nucleation and growth process of voids are modeled during plastic deformation. The quite well reproduction of the kinetics of volumetric strain during the course of tensile tests shows that the model can

capture the two competing mechanisms governing the macroscopic response, i.e. the cavitation damage and the shear yielding occurring at constant volume. Although a better agreement could be obtained in terms of nonlinear rate-dependency, the model is able to reproduce the decrease in yield strength and in volumetric strain as the strain rate decreases. The dependence of the material response features, such as yield strength, post-yield nonlinear behavior and shearing facilities, on temperature is quite well captured by the model.

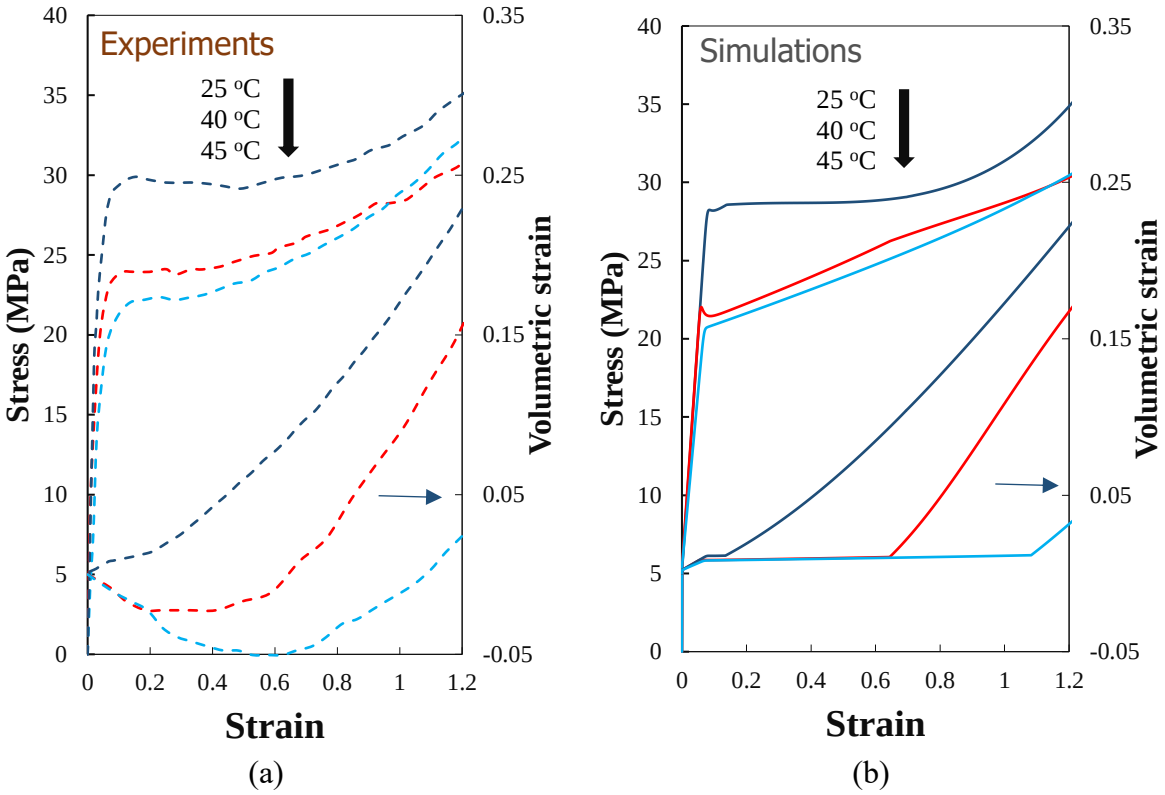

Fig. V.3. Stress and volumetric responses under stretching for different temperatures: (a) experiments taken from Ponçot et al. (2014) and (b) model simulations.

V.3.1.3. Stretching-retraction-recovery

Quantitative comparisons between model simulations and experimental data are now presented under a stretching-retraction-recovery path to verify the model predictability. The experimental observations reported in Fig. V.4(a) are the only data available in the paper of Addiego et al. (2006) and were obtained at room temperature under a true strain rate of 0.001 /s. The experiments were replicated by the model using the constants calibrated under monotonic stretching. The macroscopic strain is ramped to the level of 1 at the constant true strain rate of 0.001 /s, then it is ramped down to zero macroscopic stress under the same absolute strain rate and finally the macroscopic stress was maintained at a zero value to calculate the recovery in strain and in dilatation.

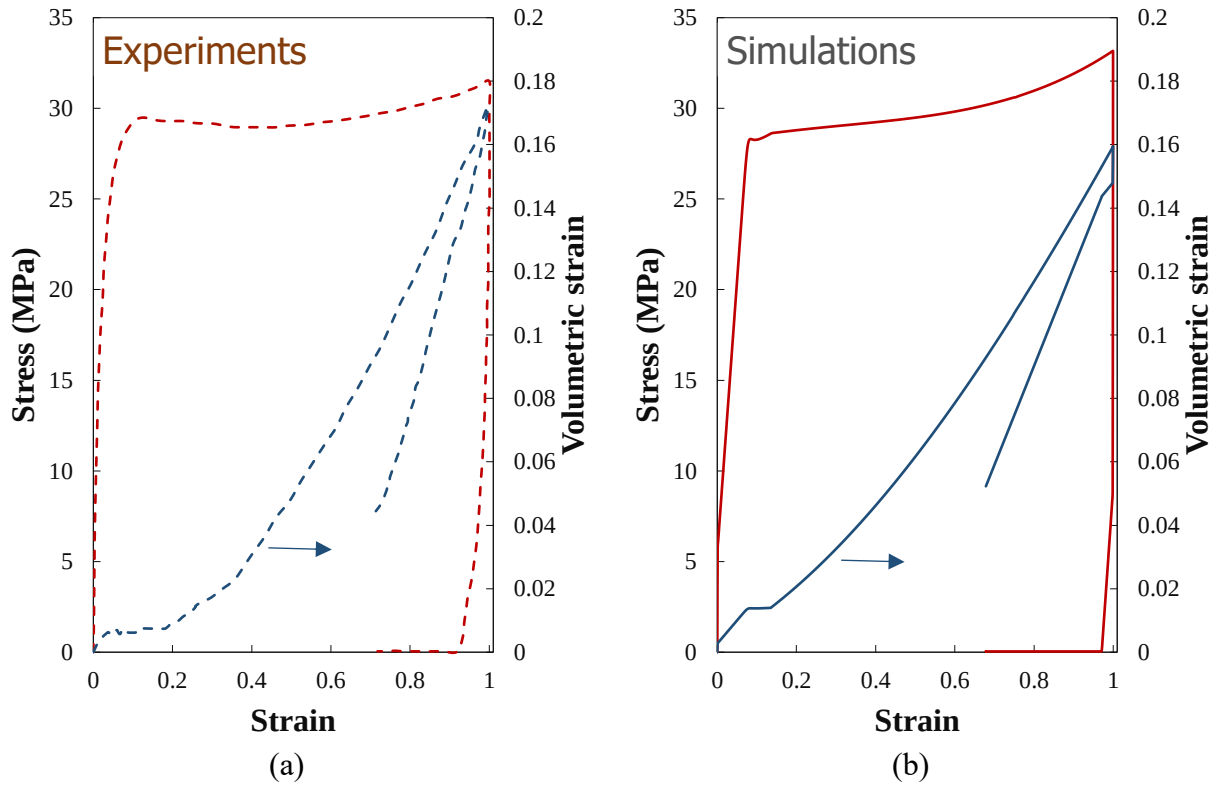

Fig. V.4. Stress and volumetric responses under a stretching-retraction-recovery sequence: (a) experiments taken from Addiego et al. (2006) and (b) model simulations.

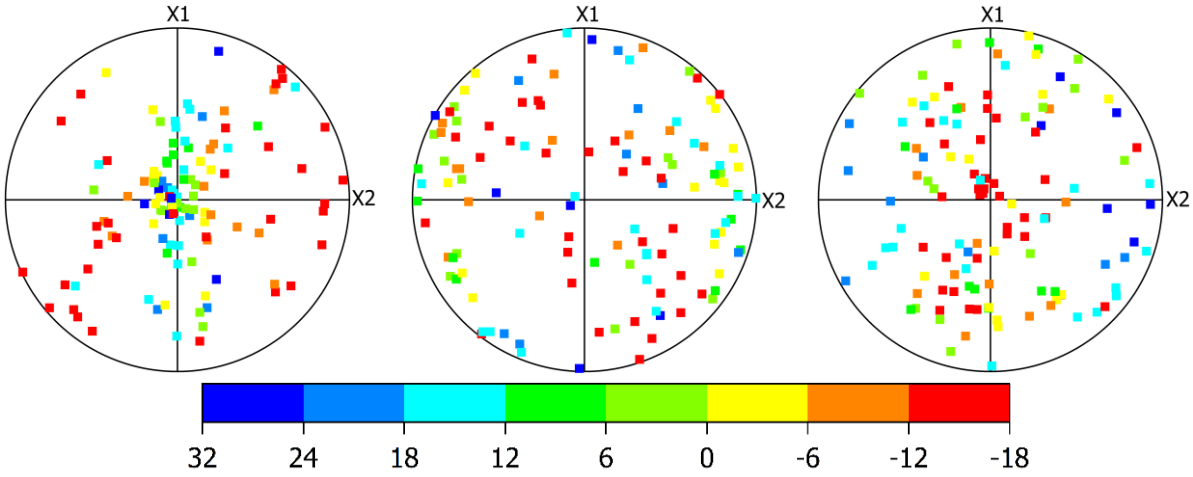

Fig. V.5. Pole figures of the stress at the end of the retraction.

At the end of the retraction, individual crystalline lamellae may be still stressed as observed in the pole figures provided in Fig. V.5 and the recovery process is carried out at zero-stress creep of the volume-averaged stress of all the inclusions in the aggregate. Fig. V.4(b) presents the model predictions of the macroscopic material response under the stretching-retraction-recovery path. It can be observed that the model results are satisfactory when compared with the experimental measurements during both the retraction segment and the zero-stress creep

recovery. The released part upon retraction of the dilatation, corresponding to the elastic Poisson's ratio contribution, is well reproduced by the model.

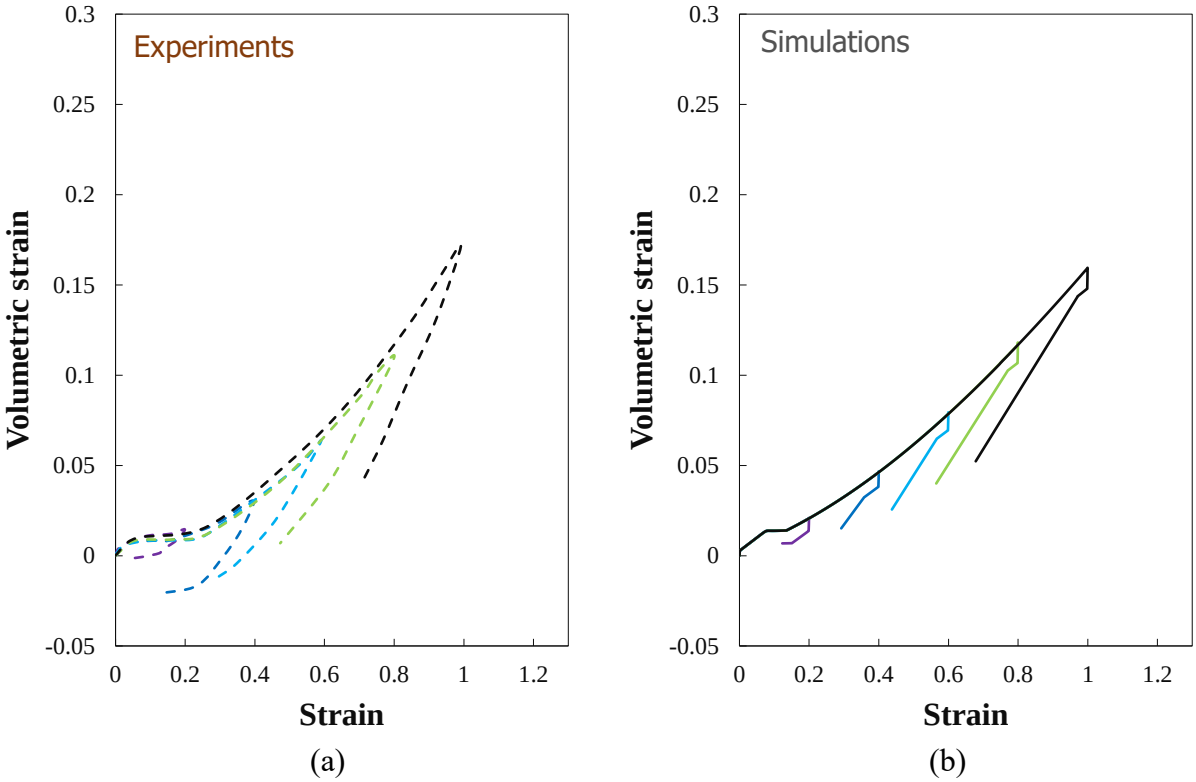

Fig. V.6. Volumetric response under various stretching-retraction-recovery sequences: (a) experiments taken from Addiego et al. (2006) and (b) model simulations.

The partial vanish of the dilatational curve, becoming purely inelastic at zero-stress, is just as well captured by the model during the recovery process. Fig. V.6 shows the model abilities to capture the inelastic volumetric response under various stretching-retraction-recovery sequences.

V.3.1.4. Cyclic stretching

To gain insight into the effect of the cavitation damage, the macroscopic material response is provided in Fig. V.7 under repeated stretching-retraction sequences either assuming incompressibility or taking account the inelastic dilatation. The simulation results are presented for a true strain rate of 0.001 /s and at room temperature. It can be observed that the presence of voids leads to a reduction of the plastic strain-hardening ability, the stress-softening magnitude with increasing cycle number and the accumulated plastic strain at zero stress. The influence of the damage is in line with both the experimental study of Ponçot et al. (2014) and the modeling study of Zaïri et al. (2011) in which the intrinsic monotonic responses of the solid ligaments between voids were extracted and with the cyclic decoupling results of the inelastic-

damage model presented by Guo et al. (2018).

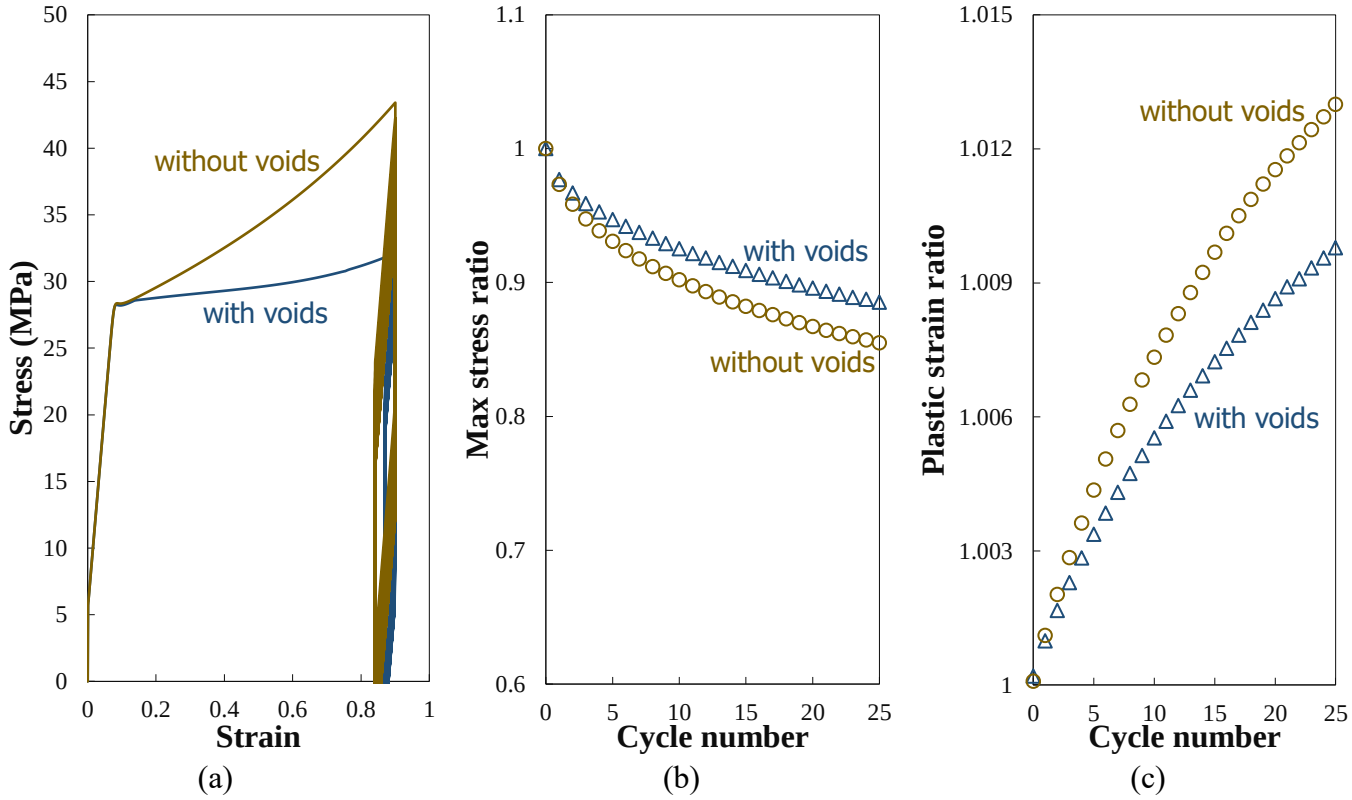

Fig. V.7. Oligo-cyclic response at a strain level of 0.9 and at a true strain rate of 0.001 /s: (a) stress-strain curve, (b) stress-softening evolution (normalized to the initial value), (c) plastic strain accumulation at zero stress (normalized to the initial value).

V.3.2. Microstructure evolution

As a final point, the microstructure evolution in high-density polyethylene is discussed. The quantitative evaluation of the model allows to observe more precisely the mechanisms controlling material deformation by means of pole figures. Figs. V.8, V.9 and V.10 provide them for preferential directions as a function of the applied macroscopic deformation. The goal is to show the importance of accounting for plastic anisotropy in the case of finite deformation and to observe the effect of the deformation-induced reorientation mechanism of the crystalline lamellae on the internal cavitation damage distributions.

Numerical calculations were carried out under tensile deformation at a true strain rate of 0.001 /s and at room temperature. The crystallographic texture evolution illustrated in Fig. V.8 is characterized by the spreading of the (010) poles around the transverse direction and the migrating of the inclusion interface normals towards the transverse direction.

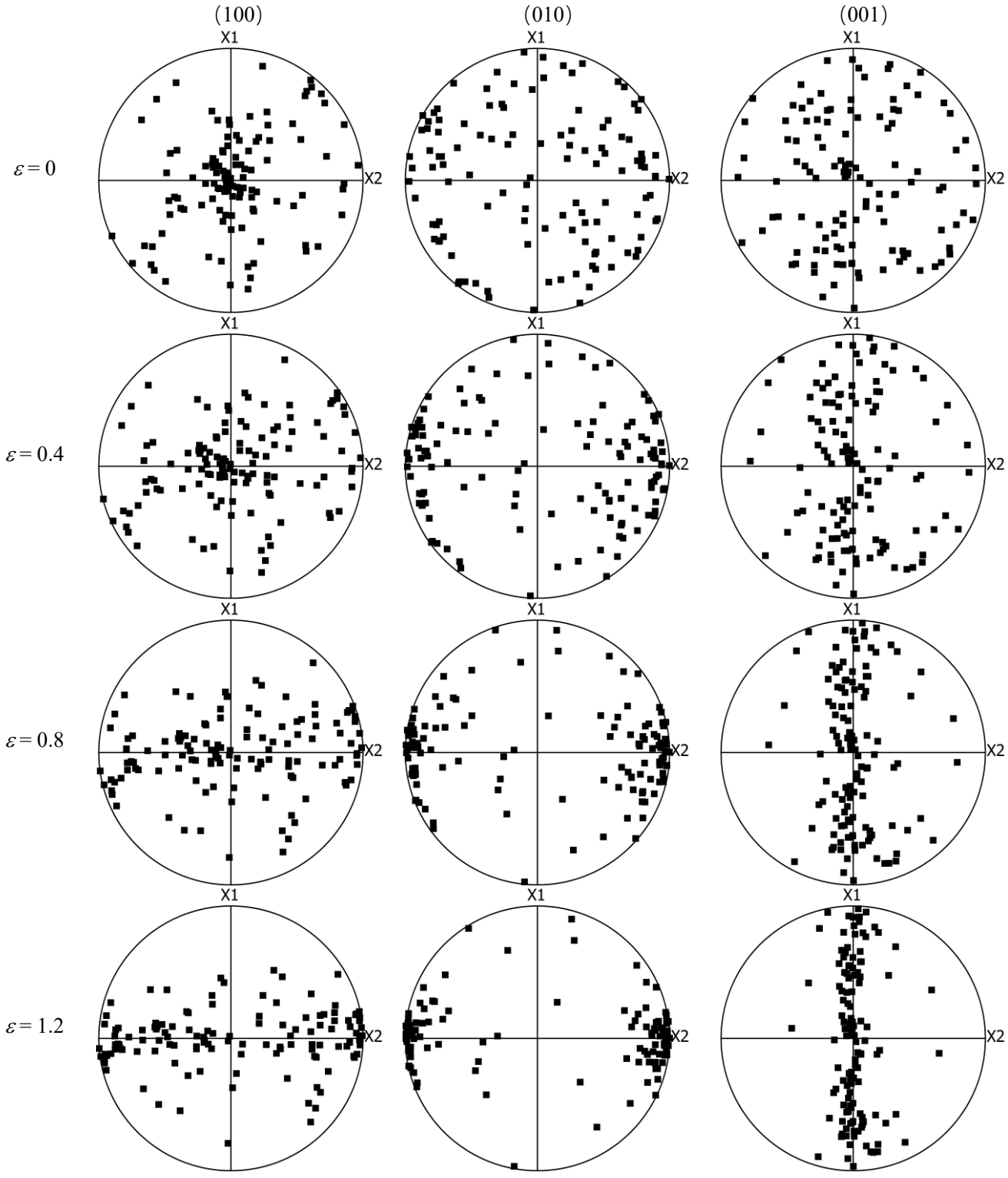

Fig. V.8. Pole figures of the crystal orientation at different macroscopic strain levels.

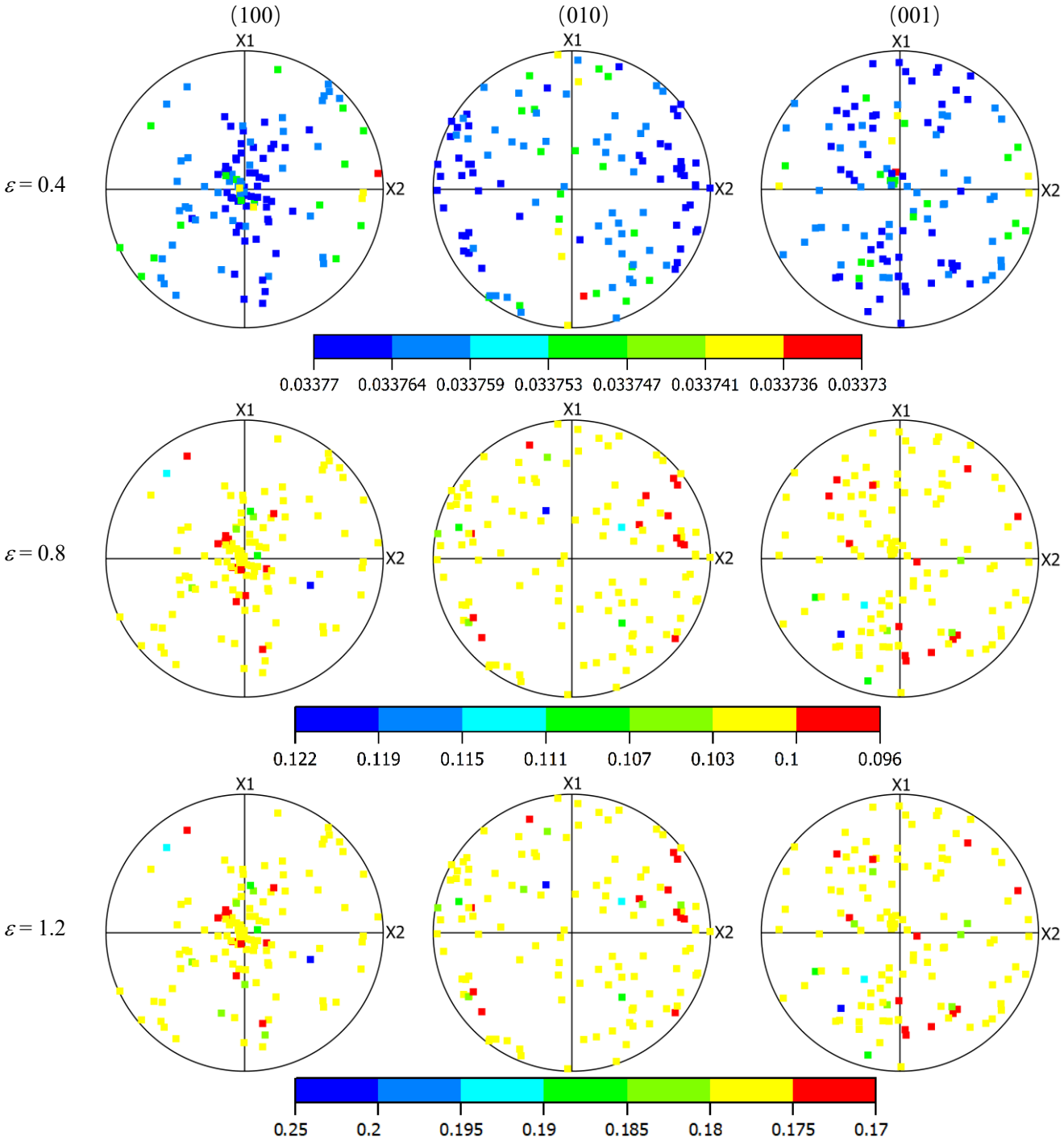

Fig. V.9. Pole figures of the void volume fraction at different macroscopic strain levels.

Figs. V.9 and V.10 show respectively the evolution of void quantity and the anisotropic evolution of void shape. Voids with elongated ellipsoidal shapes can be observed on microstructural images after deformation provided in the papers of Addiego et al. (2006) and Ponçot et al. (2014). Actually, a distribution in voids morphology from circular shapes to elongated ellipsoidal shapes exists as experimentally observed in (Ovalle et al., 2021). The

inhomogeneous distribution and morphology of voids observed in the predictions of Figs. V.9 and V.10 are in line with the anisotropy due to the relative orientation of the crystalline lamellae under increasing tensile strain illustrated by Fig. V.8.

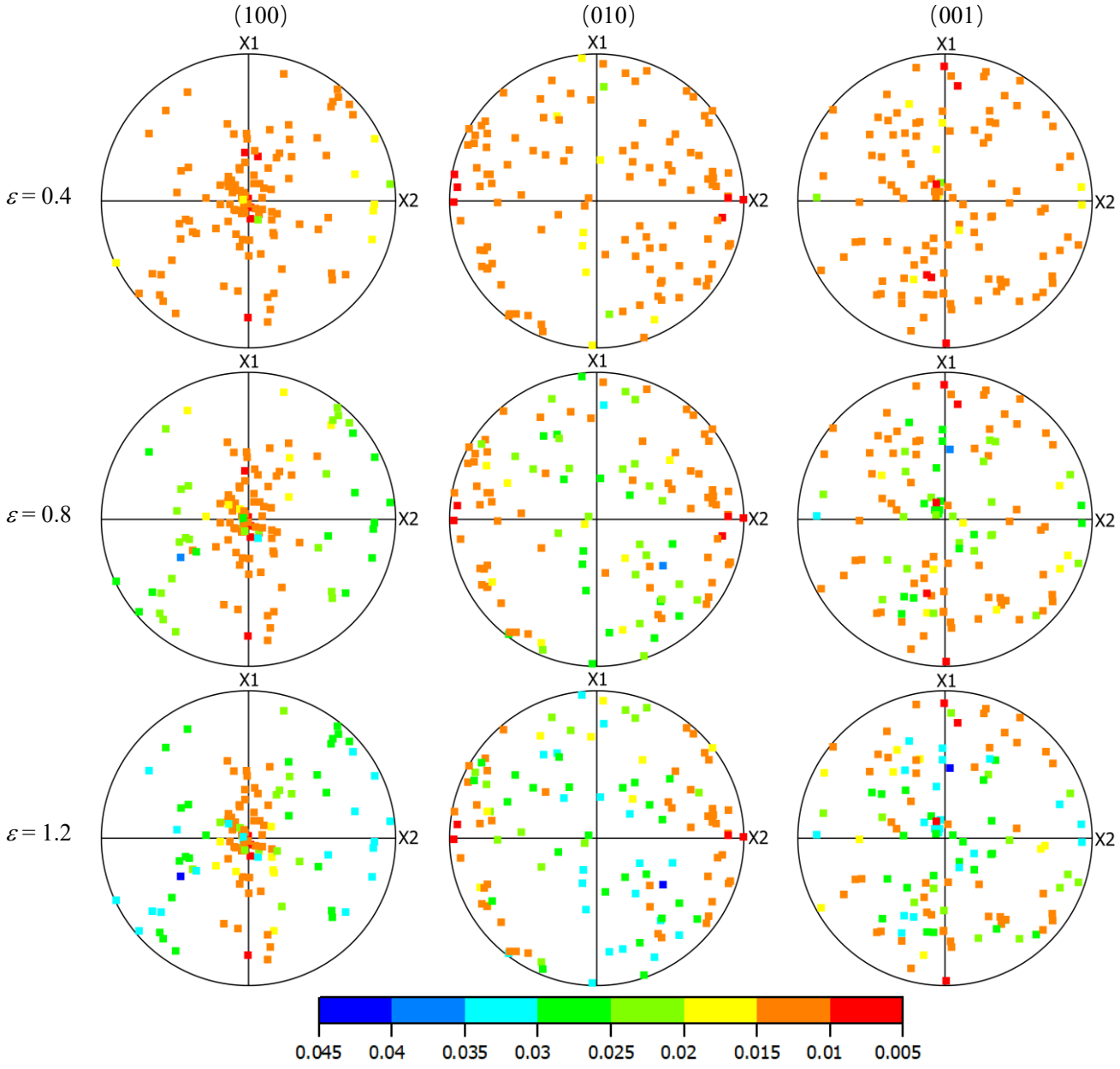

Fig. V.10. Pole figures of the void shape at different macroscopic strain levels.

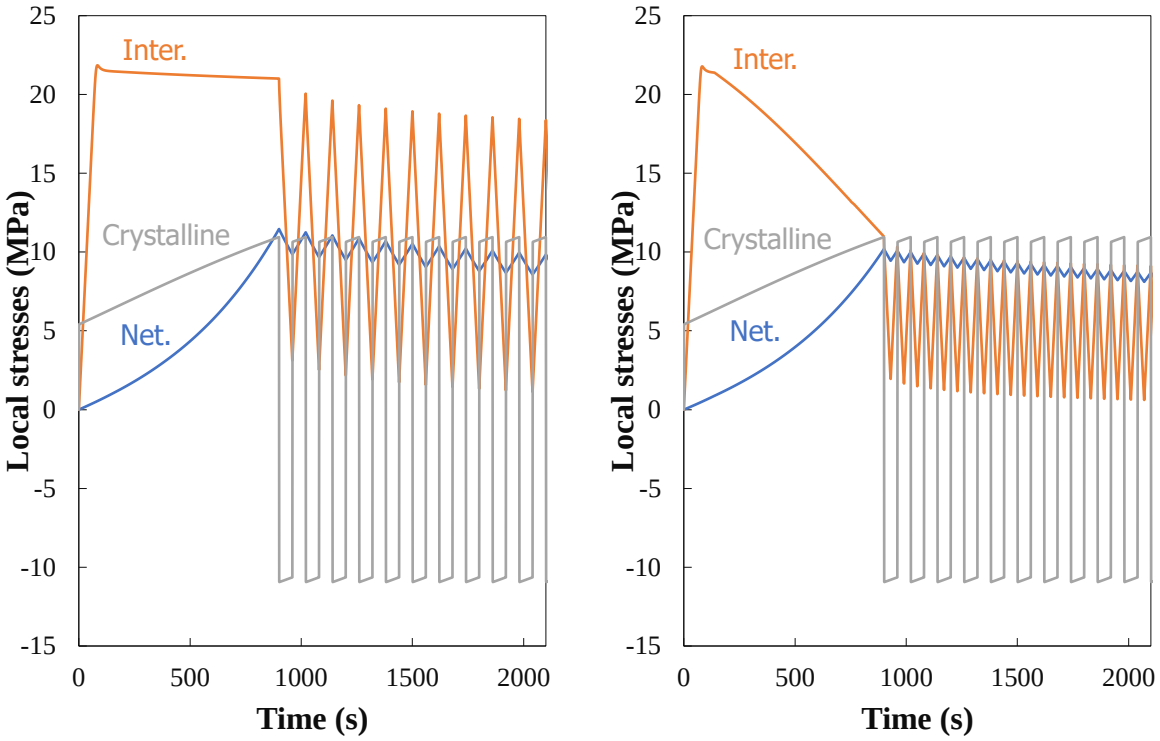

Fig. V.11. Local axial stresses upon oligo-cyclic loading at a strain level of 0.9 and at a true strain rate of 0.001 /s: (a) without voiding process, (b) with voiding process.

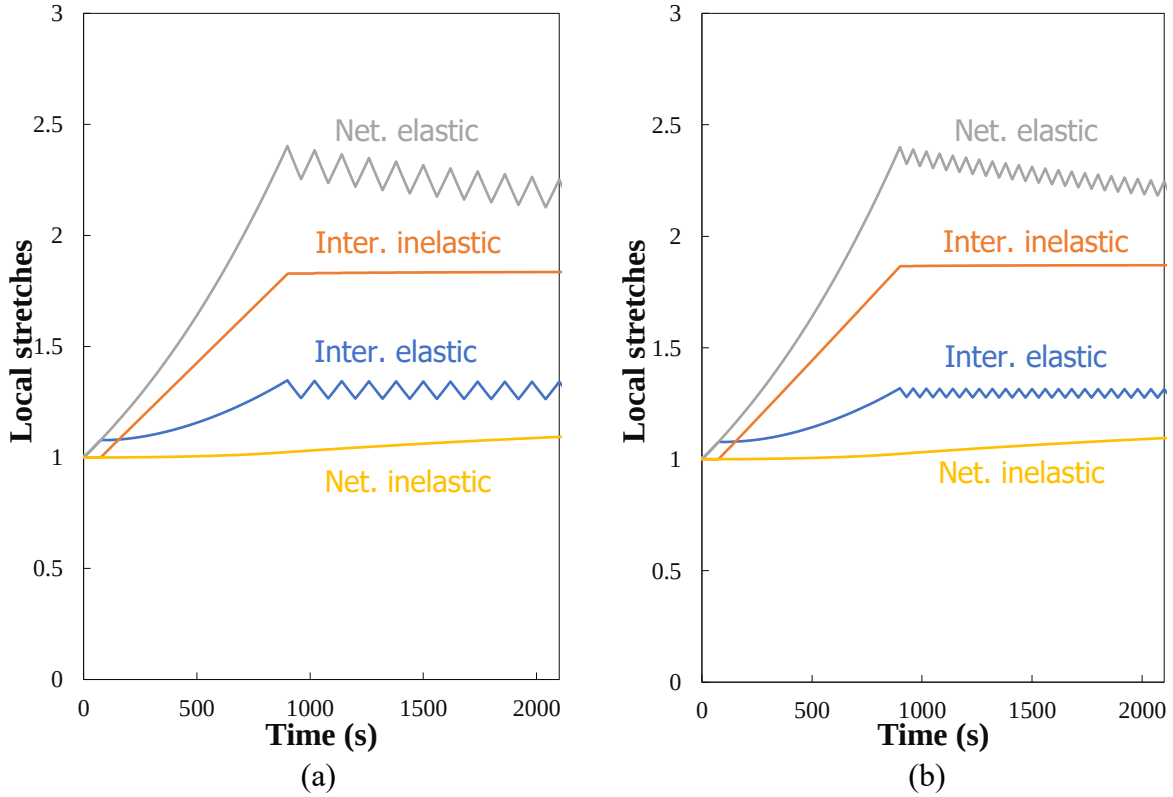

Fig. V.12. Local axial stretches upon oligo-cyclic loading at a strain level of 0.9 and at a true strain rate of 0.001 /s: (a) without voiding process, (b) with voiding process.

The internal mechanics within the spherulitic microstructure of high-density polyethylene is another relevant feature experimentally observed to understand more precisely the mechanisms (Xiong et al., 2018). The shear yielding remains the predominant deformation mechanism and results from both the plastic yielding in the crystalline phase and the intermolecular barriers to chain-segment rotation in the amorphous phase. The role of the cavitation damage on the internal stresses and stretches is pointed out using the model in Figs. V.11 and V.12. Fig. V.11(a) shows the internal stresses considering solely this isochoric plastic mechanism in the simulation while Fig. V.11(b) adds the influence of cavitation damage. The comparison of these two figures highlights the competition between this isochoric plastic mechanism and the voiding mechanism in the amorphous phase. The internal intermolecular and network stresses are accumulated in the amorphous phase in different extents, the former one being the most affected by the presence of voids. As illustrated by Fig. V.12, the progressively accumulated damage modifies also the local stretches, especially upon the non-monotonic sequence.

V.4. Conclusion

As concluding remarks, the synergic effects of crystal texturing and anisotropic cavitation damage on the plastic deformation behavior of high-density polyethylene were integrated into a constitutive model formulated within a multi-scale homogenization-based approach. By comparing simulations and experimental data, the model ability to capture large-strain macroscopic stress and inelastic dilatation was shown. The proposed multi-scale approach provides a good approximation of the intrinsic response of high-density polyethylene and the basic underlying inelastic mechanisms by considering strain rate and stretching temperature effects. Besides, the role of cavitation damage in overall and local responses was observed to better understand its importance under stretching and stretching-retraction conditions.

Although quite sophisticated, the model needs improvements for a fully realistic description of the microstructure evolution through the consideration of the crystal fragmentation.

Appendix V.A

Gologanu et al. (1997) derived analytical relationships for the parameters κ, η, C, α_1, α_2 and α_1' in terms of the variables f and S. The parameters κ, η and C are given by:

$$\begin{aligned}
\kappa &= \left[\frac{1}{\sqrt{3}} + \frac{1}{\ln f}\left(\left(\sqrt{3}-2\right)\ln\frac{e_1}{e_2} - \frac{1}{\sqrt{3}}\ln\frac{3+e_1^2+2\sqrt{3+e_1^4}}{3+e_2^2+2\sqrt{3+e_2^4}} + \ln\frac{\sqrt{3}+\sqrt{3+e_1^4}}{\sqrt{3}+\sqrt{3+e_2^4}}\right)\right]^{-1} \\
\eta &= -\frac{Q\kappa f \sinh(\kappa H)}{1+f+f\left(\kappa H\sinh(\kappa H)-2\cosh(\kappa H)\right)} \\
C &= -\frac{\kappa f \sinh(\kappa H)}{\eta\left(Q+\eta H\right)}
\end{aligned} \tag{V.A1}$$

where

$$\begin{aligned}
Q &= 1-f \\
H &= 2\left(\alpha_1-\alpha_2\right)
\end{aligned} \tag{V.A2}$$

The parameters α_1, α_2 and α_1' are expressed as follows:

$$\begin{aligned}
\alpha_1 &= \frac{1}{2e_1^2} - \frac{1-e_1^2}{2e_1^3}\tanh^{-1}e_1 \\
\alpha_2 &= \frac{1+e_2^2}{3+e_2^4} \\
\alpha_1' &= \frac{1}{3-e_1^2}
\end{aligned} \tag{V.A3}$$

$e_1 = c/a_2$ and $e_2 = c/b_2$ are the eccentricities of the inner and outer ellipsoidal shapes. Since the inner and outer ellipsoids are confocal, these eccentricities are related to f and S by:

$$\begin{aligned}
e_1 &= \left(1-\exp\left(-2|S|\right)\right)^{1/2} \\
\frac{e_2^3}{1-e_2^2} &= f\frac{e_1^3}{1-e_1^2}
\end{aligned} \tag{V.A4}$$

Appendix V.B

The non-zero terms of $\widetilde{\mathbb{Q}}'$ are given in the local ellipsoidal coordinate system by (Cao et al., 2015):

$$\hat{Q}'_{11}=\frac{1}{\pi}\left(4\pi-\frac{I_{a_2}}{2}-\frac{3a_2{}^2 I_{a_2a_2}}{2}\right)\quad \hat{Q}'_{22}=\frac{1}{\pi}\left(4\pi-\frac{I_{a_1}}{2}-\frac{3a_1{}^2 I_{a_1a_1}}{2}\right)$$

$$\hat{Q}'_{33}=\frac{1}{\pi}\left(4\pi-\frac{I_{a_3}}{2}-\frac{3a_3{}^2 I_{a_3a_3}}{2}\right)\quad \hat{Q}'_{44}=1-\frac{1}{4\pi}\left[3\left(a_1{}^2+a_2{}^2\right)I_{a_1a_2}\right]$$

$$\hat{Q}'_{55}=1-\frac{1}{4\pi}\left[3\left(a_2{}^2+a_3{}^2\right)I_{a_2a_3}\right]\quad \hat{Q}'_{66}=1-\frac{1}{4\pi}\left[3\left(a_1{}^2+a_3{}^2\right)I_{a_1a_3}\right] \qquad \text{(V.B1)}$$

$$\hat{Q}'_{12}=\hat{Q}'_{21}=\frac{1}{4\pi}\left[8\pi-\left(I_{a_1}+I_{a_2}\right)-3\left(a_1{}^2+a_2{}^2\right)I_{a_1a_2}\right]$$

$$\hat{Q}'_{13}=\hat{Q}'_{31}=\frac{1}{4\pi}\left[8\pi-\left(I_{a_2}+I_{a_3}\right)-3\left(a_2{}^2+a_3{}^2\right)I_{a_2a_3}\right]$$

$$\hat{Q}'_{23}=\hat{Q}'_{32}=\frac{1}{4\pi}\left[8\pi-\left(I_{a_1}+I_{a_3}\right)-3\left(a_1{}^2+a_3{}^2\right)I_{a_1a_3}\right]$$

with

$$I_{a_1}=I_{a_3}=\frac{2\pi a_2 a_1{}^2}{\left(a_2{}^2-a_1{}^2\right)^{3/2}}\left[\frac{a_2}{a_1}\left(\frac{a_2{}^2}{a_1{}^2}-1\right)^{1/2}-\cosh^{-1}\left(\frac{a_2}{a_1}\right)\right]$$

$$I_{a_2}=4\pi-I_{a_1}-I_{a_3}\quad I_{a_1a_2}=I_{a_2a_3}=\frac{I_{a_1}-I_{a_2}}{3\left(a_2{}^2-a_1{}^2\right)} \qquad \text{(V.B2)}$$

$$I_{a_1a_3}=\frac{\pi}{3a_1{}^2}-\frac{I_{a_2a_3}}{4}\quad I_{a_1a_1}=I_{a_3a_3}=3I_{a_1a_3}\quad I_{a_2a_2}=\frac{4\pi}{3a_2{}^2}-I_{a_1a_2}-I_{a_2a_3}$$

References

Abdul-Hameed, H., Messager, T., Zaïri, F., Naït-Abdelaziz, M., 2014. Large-strain viscoelastic-viscoplastic constitutive modeling of semi-crystalline polymers and model identification by deterministic/evolutionary approach. Computational Materials Science 90, 241-252.

Addiego, F., Dahoun, A., G'Sell, C., Hiver, J.M., 2006. Characterization of volume strain at large deformation under uniaxial tension in high-density polyethylene. Polymer 47, 4387-4399.

Agoras, M., Ponte Castaneda, P., 2012. Multi-scale homogenization-based modeling of semi-crystalline polymers. Philosophical Magazine 92, 925-958.

Anoukou, K., Zaïri, F., Naït-Abdelaziz, M., Zaoui, A., Qu, Z., Gloaguen, J.M., Lefebvre, J.M., 2014. A micromechanical model taking into account the contribution of □- and □-crystalline phases in the stiffening of polyamide 6-clay nanocomposites: a closed-formulation including the crystal symmetry. Composites Part B 64, 84-96.

Argon, A.S., Galeski, A., Kazmierczak, T., 2005. Rate mechanisms of plasticity in semicrystalline polyethylene. Polymer 46, 11798-11805.

Arruda, E.M., Boyce, M.C., 1993. A three-dimensional constitutive model for the large stretch behavior of rubber elastic materials. Journal of the Mechanics and Physics of Solids 41, 389-412.

Ayadi, W., Laiarinandrasana, L., Saï, K., 2016. Anisotropic (continuum damage mechanics)-based multi-mechanism model for semi-crystalline polymer. International Journal of Damage Mechanics 27, 357-386.

Ayoub, G., Zaïri, F., Naït-Abdelaziz, M., Gloaguen, J.M., 2010. Modelling large deformation behaviour under loading-unloading of semicrystalline polymers: Application to a high density polyethylene. International Journal of Plasticity 26, 329-347.

Ayoub, G., Zaïri, F., Fréderix, C., Gloaguen, J.M., Naït-Abdelaziz, M., Seguela, R., Lefebvre, J.M., 2011. Effects of crystal content on the mechanical behaviour of polyethylene under finite strains: Experiments and constitutive modelling. International Journal of Plasticity 27, 492-511.

Bartczak, Z., Galeski, A., 2010. Plasticity of semicrystalline polymers. Macromolecular Symposia 294, 67-90.

Bassett, D.C., Hodge, A.M., 1981. On the morphology of melt-crystallized polyethylene I. Lamellar profiles. Proceedings of the Royal Society of London A 377, 25-37.

Bédoui, F., Diani, J., Régnier, G., Seiler, W., 2006. Micromechanical modelling of isotropic elastic behaviour of semicrystalline polymers. Acta Materialia 54, 1513-1523.

Bernard, C.A., Lame, O., Deplancke, T., Cavaillé, J.Y., Ogawa, K., 2020. From rheological to original three-dimensional mechanical modelling of semi-crystalline polymers: Application to a wide strain rate range and large deformation of Ultra-High Molecular Weight PolyEthylene. Mechanics of Materials 151, 103640.

Boisot, G., Laiarinandrasana, L., Besson, J., Fond, C., Hochstetter, G., 2011. Experimental investigations and modeling of volume change induced by void growth in polyamide 11. International Journal of Solids and Structures 48, 2642-2654.

Cao, T.S., Maziere, M., Danas, K., Besson, J., 2015. A model for ductile damage prediction at low stress triaxialities incorporating void shape change and void rotation. International Journal of Solids and Structures 63, 240-263.

Castagnet, S., Deburck, Y., 2007. Relative influence of microstructure and macroscopic triaxiality on cavitation damage in a semi-crystalline polymer. Materials Science and Engineering A448, 56-66.

Challier, M., Besson, J., Laiarinandrasana, L., Piques, R., 2006. Damage and fracture of polyvinylidene fluoride (PVDF) at 20 °C: Experiments and modelling. Engineering Fracture Mechanics 73, 79-90.

Chen, K., Kang, G., Yu, C., Jiang, H., 2019. Effect of crystalline content on ratchetting of ultra-high molecular weight polyethylene polymers: Experimental investigation and constitutive model. Mechanics of Materials 133, 37-54.

Deplancke, T., Fivel, M., Lame, O., 2019. 1D strain rate-dependent constitutive model of UHMWPE: From crystalline network to fibrillar structure behavior. Mechanics of Materials 137, 103129.

Detrez, F., Cantournet, S., Seguela, R., 2011. Plasticity/damage coupling in semi-crystalline polymers prior to yielding: micromechanisms and damage law identification. Polymer 52, 1998-2008.

Drozdov, A.D., Klitkou, R., Christiansen, J.D., 2013. Multi-cycle deformation of semicrystalline polymers: Observations and constitutive modeling. Mechanics Research Communications 48, 70-75.

Dusunceli N., Colak, O.U., 2008. Modelling effects of degree of crystallinity on mechanical behavior of semicrystalline polymers. International Journal of Plasticity 24, 1224-1242.

Gologanu, M., Leblond, J.B., Perrin, G., Devaux, J., 1997. Recent extensions of Gurson's model for porous ductile metals. In: Suquet, P. Editor, Continuum Micromechanics. Berlin: Springer-Verlag, pp. 61-130.

Gueguen, O., Ahzi, S., Makradi, A., Belouetta, S., 2010. A new three-phase model to estimate the effective elastic properties of semi-crystalline polymers: Application to PET. Mechanics of Materials 42, 1-10.

Guo, T.F., Cheng, L., 2002. Modeling vapor pressure effects on void rupture and crack growth resistance. Acta Materialia 50, 3487-3500.

Guo, T.F., Faleskog, J., Shih, C.F., 2008. Continuum modeling of a porous solid with pressure-sensitive dilatant matrix. Journal of the Mechanics and Physics of Solids 56, 2188-2212.

Guo, Q., Zaïri, F., Guo, X., 2018. A thermo-viscoelastic-damage constitutive model for cyclically loaded rubbers. Part I: Model formulation and numerical examples. International Journal of Plasticity 101, 106-124.

Gurtin, M.E., Anand, L., 2005. The decomposition F=FeFp, material symmetry, and plastic irrotationality for solids that are isotropic-viscoplastic or amorphous. International Journal of Plasticity 21, 1686-1719.

Hachour, K., Zaïri, F., Naït-Abdelaziz, M., Gloaguen, J.M., Aberkane, M., Lefebvre J.M., 2014. Experiments and modeling of high-crystalline polyethylene yielding under different stress states. International Journal of Plasticity 54, 1-18.

Holopainen, S., 2014. Influence of damage on inhomogeneous deformation behavior of amorphous glassy polymers. Modeling and algorithmic implementation in a finite element setting. Engineering Fracture Mechanics 117, 28-50.

Hou, H., Abeyaratne, R., 1992. Cavitation in elastic and elastic-plastic solids. Journal of the Mechanics and Physics of Solids 40, 571-592.

Imanaka, M., Nakamura, Y., Nishimura, A., Iida, T., 2003. Fracture toughness of rubber-modified epoxy adhesives: effect of plastic deformability of the matrix phase. Composites Science and Technology 63, 41-51.

Imanaka, M., Motohashi, S., Nishi, K., Nakamura, Y., Kimoto, M., 2009. Crack-growth behavior of epoxy adhesives modified with liquid rubber and cross-linked rubber particles under mode I loading. International Journal of Adhesion and Adhesives 29, 45-55.

Jeong, H.Y., 2002. A new yield function and a hydrostatic stress-controlled void nucleation model for porous solids with pressure-sensitive matrices. International Journal of Solids and Structures 39, 1385-1403.

Kazmierczak, T., Galeski, A., Argon, A.S., 2005. Plastic deformation of polyethylene crystals as a function of crystal thickness and compression rate. Polymer 46, 8926-8936.

Laiarinandrasana, L., Besson, J., Lafarge, M., Hochstetter, G., 2009. Temperature dependent mechanical behaviour of PVDF: Experiments and numerical modelling. International Journal of Plasticity 25, 1301-1324.

Laiarinandrasana, L., Klinkova, O., Nguyen, F., Proudhon, H., Morgeneyer, T.F., Ludwig, W., 2016. Three dimensional quantification of anisotropic void evolution in deformed semi-crystalline polyamide 6. International Journal of Plasticity 83, 19-36.

Lazzeri, A., Bucknall, C.B., 1995. Applications of a dilatational yielding model to rubber-toughened polymers. Polymer 36, 2895-2902.

Lee, B.J., Parks, D.M., Ahzi, S., 1993. Micromechanical modeling of large plastic deformation and texture evolution in semi-crystalline polymers. Journal of the Mechanics and Physics of Solids 41, 1651-1687.

Lee, B.J., Argon, A.S., Parks, D.M., Ahzi, S., Bartczak, Z., 1993. Simulation of large strain plastic deformation and texture evolution in high density polyethylene. Polymer 34, 3555-3575.

Lemaitre, J., Desmorat, R., Sauzay, M., 2000. Anisotropic damage law of evolution. European Journal of Mechanics - A/Solids 19, 187-120.

Makki, M., Ayoub, G., Abdul-Hameed, H., Zaïri, F., Mansoor, B., Naït-Abdelaziz, M., Ouederni, M., Zaïri, F., 2017. Mullins effect in polyethylene and its dependency on crystal content: A network alteration model. Journal of the Mechanical Behavior of Biomedical Materials 75, 442-454.

Mesbah, A., Elmeguenni, M., Yan, Z., Zaïri, F., Ding, N., Gloaguen, J.M., 2021. How stress triaxiality affects cavitation damage in high-density polyethylene: Experiments and constitutive modeling. Polymer Testing, 107248.

Mirkhalaf, M., van Dommelen, J.A.W., Govaert, L.E., Furmanski, J., Geers, M.G.D., 2019. Micromechanical modeling of anisotropic behavior of oriented semicrystalline polymers. Journal of Polymer Science, Part B: Polymer Physics 57, 378-391.

Nikolov, S., Doghri, I., 2000. A micro/macro constitutive model for the small-deformation behavior of polyethylene. Polymer 41, 1883-1891.

Nikolov, S., Doghri, I., Pierard, O., Zealouk, L., Goldberg, A., 2002. Multi-scale constitutive modeling of the small deformations of semi-crystalline polymers. Journal of the Mechanics and Physics of Solids 50, 2275-2302.

Ovalle, C., Cloetens, P., Proudhon, H., Morgeneyer, T.F., Laiarinandrasana, L., 2021. Nanocavitation mechanisms in deformed High Density PolyEthylene (HDPE) using synchrotron radiation NanoTomography. Polymer 229, 123959.

Parsons, E.M., Boyce, M.C., Parks, D.M., Weinberg, M., 2005. Three-dimensional large-strain tensile deformation of neat and calcium carbonate-filled high-density polyethylene. Polymer 46, 2257-2265.

Pawlak, A., Galeski, A., 2005. Plastic deformation of crystalline polymers: The role of cavitation and crystal plasticity. Macromolecules 38, 9688-9697.

Pawlak, A., 2007. Cavitation during tensile deformation of high-density polyethylene. Polymer 48, 1397-1409.

Pijnenburg, K.G.W., van der Giessen, E., 2001. Macroscopic yield in cavitated polymer blends. International Journal of Solids and Structures 38, 3575-3598.

Pijnenburg, K.G.W., Seelig, T., van der Giessen, E., 2005. Successively refined models for crack tip plasticity in polymer blends. European Journal of Mechanics A/Solids 24, 740-756.

Ponçot, M., Addiego, F., Dahoun, A., 2013. True intrinsic mechanical behaviour of semi-crystalline and amorphous polymers: Influences of volume deformation and cavities shape. International Journal of Plasticity 40, 126-139.

Qi, Z., Hu, N., Li, G., Zeng, D., 2019. Constitutive modeling for the elastic-viscoplastic behavior of high density polyethylene under cyclic loading. International Journal of Plasticity 113, 125-144.

Rozanski, A., Galeski, A., 2013. Plastic yielding of semicrystalline polymers affected by amorphous phase. International Journal of Plasticity 41, 14-29.

Seelig, T., van der Giessen, E., 2002. Localized plastic deformation in ternary polymer blends. International Journal of Solids and Structures 39, 3505-3522.

Seguela, R., Gaucher-Miri, V., Elkoun, S., 1998. Plastic deformation of polyethylene and ethylene copolymers. Part I Homogeneous crystal slip and molecular mobility. Journal of Materials Science 33, 1273-1279.

Seguela, R., Elkoun, S., Gaucher-Miri, V., 1998. Plastic deformation of polyethylene and ethylene copolymers. Part II Heterogeneous crystal slip and strain-induced phase change. Journal of Materials Science 33, 1801-1807.

Sepiani, H., Polak, M.A., Penlidis, A., 2018. Modeling short- and long-term time-dependent nonlinear behavior of polyethylene. Mechanics of Advanced Materials and Structures 25, 600-610.

Steenbrink, A.C., van der Giessen, E., Wu, P.D., 1997. Void growth in glassy polymers. Journal of the Mechanics and Physics of Solids 45, 405-437.

Tashiro, K., Kobayashi, M., Tadokoro, H., 1978. Calculation of three-dimensional elastic constants of polymer crystals. 2. Application to orthorhombic polyethylene and poly(vinyl alcohol). Macromolecules 11, 914-918.

Uchida, M., Tada, N., 2013. Micro-, meso- to macroscopic modeling of deformation behavior of semi-crystalline polymer. International Journal of Plasticity 49, 164-184.

van Dommelen, J.A.W., Parks, D.M., Boyce, M.C., Brekelmans, W.A.M., Baaijens, F.P.T., 2003. Micromechanical modeling of the elasto-viscoplastic behavior of semi-crystalline polymers. Journal of the Mechanics and Physics of Solids 51, 519-541.

Voyiadjis, G.Z., Shojaei, A., Li, G., Kattan, P.I., 2012. A theory of anisotropic healing and damage mechanics of materials. Proceedings of The Royal Society A 468, 163-183.

Xiong, B., Lame, O., Seguela, R., Men, Y., 2018. Micro/macro-stress relationship and local stress distribution in polyethylene spherulites upon uniaxial stretching in the small strain domain. Polymer 140, 215-224.

Yan, Z., Guo, Q., Zaïri, F., Zaoui, A., Jiang, Q., Liu, X., 2021. Continuum-based modeling large-strain plastic deformation of semi-crystalline polyethylene systems: Implication of texturing and amorphicity. Mechanics of Materials 162, 104060.

Yan, Z., Zaoui, A., Zaïri, F., 2021. Crystallization and mechanical behavior of semi-crystalline polyethylene. Physica Scripta 96, 125729.

Zaïri, F., Naït-Abdelaziz, M., Woznica, K., Gloaguen, J.M., 2005. Constitutive equations for the viscoplastic-damage behaviour of a rubber-modified polymer. European Journal of Mechanics A/Solids 24, 169-182.

Zaïri, F., Naït-Abdelaziz, M., Gloaguen, J.M., Lefebvre, J.M., 2008. Modelling of the elasto-viscoplastic damage behaviour of glassy polymers. International Journal of Plasticity 24, 945-965.

Zaïri, F., Naït Abdelaziz, M., Gloaguen, J.M., Lefebvre, J.M., 2011. A physically-based constitutive model for anisotropic damage in rubber-toughened glassy polymers during finite deformation. International Journal of Plasticity 27, 25-51.

Zhang, Y., Ben Jar, P.Y., Xue, S., Li, L., 2019. Quantification of strain-induced damage in semi-crystalline polymers: A review. Journal of Materials Science 54, 62-82.

Chapter VI

Multiscale Modeling of the Strain-Induced α → β Phase Transition in Semi-Crystalline Poly(vinylidene fluoride) over A Large-Strain Range

Chapter VI. Multiscale modeling of the strain-induced α → β phase transition in semi-crystalline poly(vinylidene fluoride) over a large-strain range[14]

Abstract

The present contribution investigates within a hierarchical multi-scale approach the relation between the macroscopic properties of semi-crystalline poly(vinylidene fluoride) (PVDF) and the transition from the α-phase to the β-phase crystalline structure in the course of a mechanical loading. A continuum-based constitutive model is proposed to capture the large-strain material behavior of PVDF, the amorphous molecular network orientation/relaxation process, the strain-induced morphological anisotropy induced by the crystallographic texturing and the strain-induced α → β phase transition; the mechanical coupling between the deformation modes in α-PVDF, β-PVDF and amorphous domains is obtained by considering the interfacial interactions in the micro-macro homogenization procedure. Fundamental parameters from molecular dynamics simulations, such as the amorphous, α crystalline and β crystalline properties along with the onset of α → β phase transition caused by the straining of α-PVDF, are transferred to the continuum scale. By completing the scale bridging method by the identification of the other model parameters, the model outputs are found in good agreement with the existing tensile experiments of a PVDF upon large-strain plastic deformation. The profound influence of the strain-induced α → β phase transition and the crystallographic texturing operated upon large-strain plastic deformation in the piezoelectric activity is finally investigated numerically.

Keywords: Semi-crystalline poly(vinyldene fluoride); Strain-induced α → β phase transition; Elasto-viscoplastic-viscohyperelastic constitutive modeling; Molecular dynamics simulation; Piezoelectric properties.

[14] This chapter is based on the following paper: Yan, Z., Zaïri, F., Zaoui, A., 2023. Multiscale modeling of the strain-induced α → β phase transition in semi-crystalline poly(vinylidene fluoride) over a large-strain range. Mechanics of Materials, accepted.

VI.1. Introduction

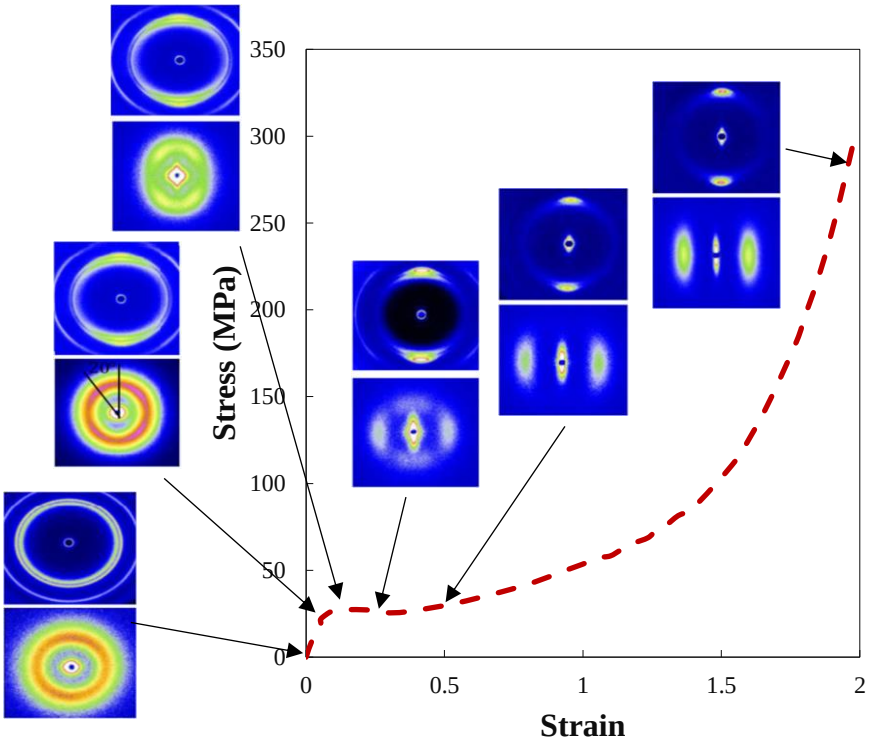

Fig. VI.1. Typical tensile experimental result of a PVDF (containing 0.70 of crystals initially in the α-form) strained up to very large strains in terms of stress as a function of strain along with X-ray plots showing both strain-induced texturing and α → β phase transition; strain rate of 10^{-3} s^{-1} and temperature of 363 K (Defebvin et al., 2016).

Poly(vinylidene fluoride) (PVDF) is a well-known multifunctional piezoelectric semi-crystalline polymer offering flexibility and electro-mechanical conversion capabilities for a wide range of sophisticated engineering applications in modern technologies and industries including tactile sensors, actuators, energy storage, transducers and non-volatile memories (Chang et al., 2012). The piezoelectric properties are highly dependent on polymer crystalline structure. The α-phase and the β-phase are by far the most important crystalline structures (Nalwa, 1995). The α-phase is non-polar, non-piezoelectric, nonpyrroelectric while the β-phase exhibits strong ferroelectric and piezoelectric properties. However, it is not easy to obtain PVDF consisting of entirely β-phase crystalline structure. It has been proved experimentally that the β crystalline form can be obtained by stretching PVDF initially in the α-form, the α → β phase transition benefiting to the electroactive properties (Ye et al., 2013; Sharma et al., 2014). The loading temperature has a significant effect both on the strain-induced α → β phase transition and the elementary plastic deformation mechanisms with a transition, according to the temperature range, from a cavitational behavior to a more roughly homogeneous deformation

governed by shearing mechanisms (Guo et al., 2013; Osaka et al., 2013; Defebvin et al., 2016). Fig. VI.1 provides an illustrative experimental example extracted from the work of Defebvin et al. (2016) of a PVDF stress-strain curve up to very large strains along with the microstructural evolution during straining showed by X-ray plots. The mechanical response is accompanied by the progressive micro-mechanism of α → β phase transition until complete transformation and the internal microstructure ordering in terms of crystallographic texturing and amorphous molecular network orientation.

The advanced use of PVDF in engineering applications requires accurate and flexible predictive tools allowing to tailor and optimize the strain-induced microstructure evolution and its influence on the overall response. That is a challenging task due to the complex multiscale relationship between microstructure features (in terms crystal and amorphous properties, α → β phase transition and morphological anisotropy) and macroscopic response. Concurrent multiscale modeling techniques can be used. In this regard, local interactions and structural properties of PVDF may be investigated using atomistic simulations (Pei and Zeng, 2011; Erdtman et al., 2012; Satyanarayana and Bolton, 2012; Sahihi et al., 2021). Alternatively, quantitative predictive modeling of the structure-property relationship may be constitutively examined in continuum terms. Over the years, continuum-based constitutive models have been proposed for semi-crystalline polymers. Some of them were developed to capture the macroscopic response via rheological elements, combining linear/nonlinear elastic springs and viscoelastic/viscoplastic dashpots, representing the elementary micro-mechanisms and assembled within a simplified composite-type representation of the semi-crystalline material medium (Dusunceli and Colak, 2008; Ayoub et al., 2010, 2011; Drozdov, 2010; Laiarinandrasana et al., 2010; Drozdov and De Christiansen, 2011; Drozdov et al., 2013; Abdul-Hameed et al., 2014; Makki et al., 2017; Sepiani et al., 2018; Chen et al., 2019; Deplancke et al., 2019; Mahjoubi et al., 2019, 2020; Qi et al., 2019; Bernard et al., 2020; Wang et al., 2021; Satouri et al., 2022). In other more physically consistent constitutive models, the macroscopic response is evaluated within a micro-macro homogenization-based approach through Eshelby-type inclusion problems for elastic behavior (Bédoui et al., 2006; Gueguen et al., 2010; Anoukou et al., 2014), yield behavior (Hachour et al., 2014) and small-strain post-yield behavior (Mesbah et al., 2021; Mamache et al., 2022); This theoretical framework uses a composite-type representation in a more suitable. description of the local interactions but the developments are generally limited to small-strain behavior. Other micro-macro homogenization-based models constitutively represent within the finite-strain framework the

organization hierarchy starting from the nano-sized lamellar structure, allowing thus access to the texture evolution in the semi-crystalline material medium and the underlying plastic anisotropy (Lee et al., 1993a, 1993b; Nikolov and Doghri, 2000; Nikolov et al., 2002; van Dommelen et al., 2003; Sedighiamiri et al., 2011; Agoras and Ponte Castaneda, 2012; Poluektov et al., 2013; Uchida and Tada, 2013; Popa et al., 2014; Mirkhalaf et al., 2019; Okereke and Akpoyomare, 2019; Yan et al., 2021). At the mesoscopic scale, the semi-crystalline polymer is regarded as an aggregate of two-phase layered composite inclusions consisting in parallel crystalline lamellae and amorphous layers in which the internal interfacial interaction is explicit. Each distinguishing layer may have each own rheological representation to capture, in addition to the crystallographic texturing, local inelastic events such as intermolecular interactions and orientation/relaxation process of the amorphous molecular network (Yan et al., 2021). In spite of the important number of studies dealing with the development of continuum-based models for semi-crystalline polymers, only a few were proposed for PVDF (Odegard, 2004; Challier et al., 2006; Baudet et al., 2009; Laiarinandrasana et al., 2009; Erol et al., 2019; Garcia-Gonzalez et al., 2019) and, to the best of our knowledge, no one considers the strain-induced structure changes such as α → β phase transition and anisotropy induced by the crystallographic texturing. The formulation of coupled constitutive models would be useful in the design and optimization of multi-functional piezoelectric PVDF-based material media. It would allow a more accurate information of the evolution of the electroactive activity if the α → β phase transition along with the orientation of both the amorphous and crystalline phases are considered.

In the present chapter, a microstructure-based model is developed using a micro-macro transition approach within the continuum mechanics rules to replicate the α → β phase transition caused by the straining in the final aim to clarify the connection between the mesostructural evolution and the benefices on the electroactive response. The strain-induced morphological anisotropy is considered in the continuum-based model while the physics of the deformation modes of the different phases is described by formulating an elasto-viscoplastic-viscohyperelastic coupling. Molecular dynamics simulations are employed to examine the respective mechanical properties of α-PVDF, β-PVDF and amorphous phase. The elastic constants of the distinguishing phases and the onset of α → β phase transition, when α-PVDF is drawn, are then used as direct inputs into the continuum-based model. The intermolecular constants of the amorphous phase are also obtained thanks to molecular dynamics data. The other parameters of the continuum-based model are determined using the stress-strain experimental data of a PVDF deformed over a large-strain range. The effect of the progressive

variation in the mesostructural properties caused by the straining on the piezoelectric properties is finally observed.

The present chapter is organized as follows. The continuum-based constitutive model is formulated in Section VI.2. Section VI.3 provides the model inputs identified using results issued both from molecular dynamics simulation performed for this work and existing experiments. The effect of both material anisotropy and α → β phase transition on the piezoelectric properties is discussed. Concluding remarks are finally given in Section VI.4.

VI.2. Continuum-based model

In this section, a microstructure-based model is formulated in continuum terms to describe the finite-strain deformation processes in the amorphous molecular network and in the crystals while taking into account the strain-induced α → β phase transition. The intrinsic response is described within an elasto-viscoplastic-viscohyperelastic coupling. The superscripts e and in will refer to the elastic (linear elastic and hyperelastic) part and the inelastic (viscoplastic and viscous) part, respectively.

The following notation is used throughout the text. Tensors and vectors are denoted by normal boldfaced letters and italicized boldfaced letters, respectively, while scalars and individual components of vectors and tensors are denoted by normal italicized letters. The superposed dot designates the time derivative. The superscript T indicates the transpose quantity.

VI.2.1. Microstructure-based model

The continuum-based model is formulated within an ensemble-volume averaged homogenization approach in which the interfacial interaction is considered. As illustrated in Fig. VI.2, the semi-crystalline PVDF structure is regarded at the mesoscopic scale as an aggregate of randomly oriented three-phase layered composite inclusions consisting in parallel amorphous layer, α-form lamella and β-form lamella. All the three phases are considered as homogeneous and continuous media in accordance with the continuum mechanics; A key quantity of the finite-strain kinematics framework is the deformation gradient tensor $\mathbf{F} = \partial \boldsymbol{x}/\partial \boldsymbol{X}$ mapping a material point from its initial position $\boldsymbol{X}$ to the current position $\boldsymbol{x}$. The local quantity $\mathbf{F}_I^i$ of the composite inclusion i is obtained by a volume-weighted average of the three phases:

$$\mathbf{F}_I^i = f_{\alpha,0}^i \mathbf{F}_\alpha^i + f_{\beta,0}^i \mathbf{F}_\beta^i + f_{a,0}^i \mathbf{F}_a^i \tag{VI.1}$$

in which the subscripts a, α, β and I refer to the amorphous phase, the α-phase, the β-phase

and the inclusion, respectively.

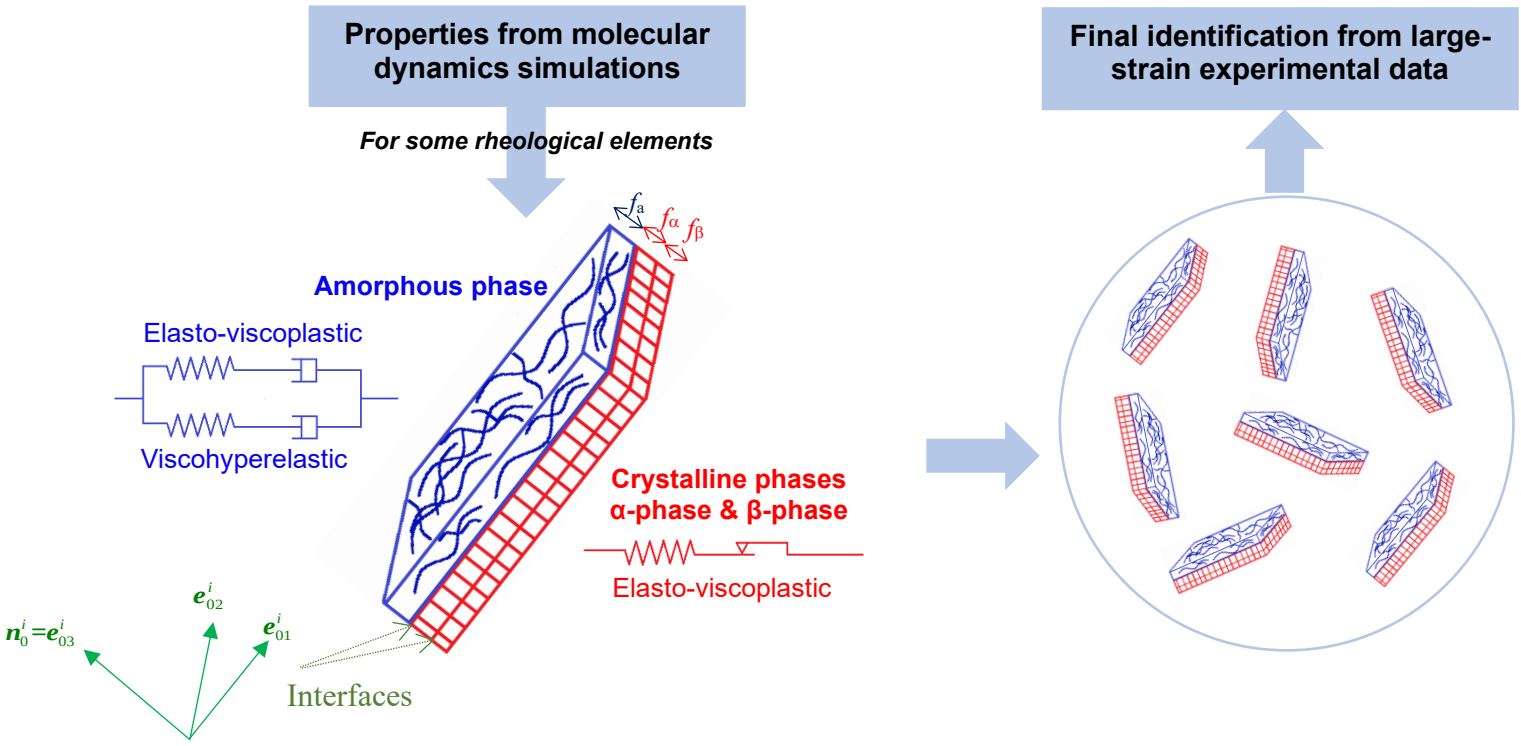

Fig. VI.2. Continuum model of PVDF based on an aggregate of randomly oriented three-phase layered composite inclusions consisting in three parallel layers of amorphous phase, α-phase and β-phase. Two distinct rheological representations are introduced to constitutively represent the amorphous and crystalline layers constructed, respectively, using elasto-viscoplastic-viscohyperelastic and elasto-viscoplastic elements. The material constants of the different rheological elements were identified using a scale bridging method coupling molecular dynamics simulations and experimental data. While the aggregate is subjected to a macrostrain, the α → β phase transition in each individual inclusion is considered by varying the crystal degree with the local strain, f_α varying from its initial value f_{α_0} to 0 and f_β varying from 0 to its maximum value f_{β_∞}.

The terms f_α^i and f_β^i are the α-phase and β-phase volume fractions, $f_{a,0}^i$ is the initial amorphous volume fraction and, $\mathbf{F}_\alpha^i$, $\mathbf{F}_\beta^i$ and $\mathbf{F}_a^i$ are the local deformation gradient tensors respecting the interfacial compatibility condition:

$$\mathbf{F}_\alpha^i \cdot \boldsymbol{x}_0^i = \mathbf{F}_\beta^i \cdot \boldsymbol{x}_0^i = \mathbf{F}_a^i \cdot \boldsymbol{x}_0^i = \mathbf{F}_I^i \cdot \boldsymbol{x}_0^i \tag{VI.2}$$

in which $\boldsymbol{x}_0^i$ is an arbitrary vector in the plane of the interface spanned by the unit vectors $\boldsymbol{e}_{01}^i$ and $\boldsymbol{e}_{02}^i$ of the local orthogonal basis $\left(\boldsymbol{e}_{01}^i, \boldsymbol{e}_{02}^i, \boldsymbol{e}_{03}^i\right)$ with $\boldsymbol{n}_0^i = \boldsymbol{e}_{03}^i$ the unit normal vector at the interface in the reference configuration (Fig. VI.2).

Considering a set of N_I=125 inclusions in the aggregate, the macroscopic Cauchy stress tensor $\bar{\boldsymbol{\sigma}}$ in the semi-crystalline polymer is obtained by the averaging homogenization:

$$\bar{\boldsymbol{\sigma}}=\sum_{i=1}^{N_I} f_I^i \boldsymbol{\sigma}_I^i \text{ with } f_I^i=\frac{f_{I,0}^i J_I^i}{\sum_{j=1}^{N_I} f_{I,0}^j J_I^j}=\frac{1}{N_I} \tag{VI.3}$$

where $\boldsymbol{\sigma}_I^i$ is the local inclusion-averaged Cauchy stress tensor, f_I^i is the inclusion volume fraction, $f_{I,0}^i$ is the initial inclusion volume fraction and J_I^i is the inclusion volume change. While the aggregate is subjected to a macrostrain, the α → β phase transition is considered in each individual inclusion i by varying the α-phase degree f_α^i from its initial value $f_{\alpha\_0}^i$ to 0 and the β -phase degree f_β^i from 0 to its maximum value $f_{\beta\_\infty}^i$. The two volume fractions are expressed here as follows:

$$f_\alpha^i = f_{\alpha\_0}^i - f_\beta^i \text{ and } f_\beta^i = f_{\beta\_\infty}^i \kappa \tag{VI.4}$$

where κ is a parameter capturing the transformation degree (as described in Section VI.2.1.3). The local Cauchy stress tensor $\boldsymbol{\sigma}_I^i$ of the composite inclusion i is obtained by a volume-weighted average of the three phases:

$$\boldsymbol{\sigma}_I^i = f_\alpha^i \boldsymbol{\sigma}_\alpha^i + f_\beta^i \boldsymbol{\sigma}_\beta^i + f_a^i \boldsymbol{\sigma}_a^i \tag{VI.5}$$

where $\boldsymbol{\sigma}_\alpha^i$, $\boldsymbol{\sigma}_\beta^i$ and $\boldsymbol{\sigma}_a^i$ are the local Cauchy stress tensors respecting the interfacial equilibrium condition:

$$\boldsymbol{\sigma}_\beta^i \cdot \boldsymbol{n}^i = \boldsymbol{\sigma}_\alpha^i \cdot \boldsymbol{n}^i = \boldsymbol{\sigma}_a^i \cdot \boldsymbol{n}^i = \boldsymbol{\sigma}_I^i \cdot \boldsymbol{n}^i \tag{VI.6}$$

in which $\boldsymbol{n}^i$ is the unit normal vector in the current configuration given by:

$$\boldsymbol{n}^i = \frac{\mathbf{F}^i \delta \boldsymbol{x}_{01}^i \times \mathbf{F}^i \delta \boldsymbol{x}_{02}^i}{\left\| \mathbf{F}^i \delta \boldsymbol{x}_{01}^i \times \mathbf{F}^i \delta \boldsymbol{x}_{02}^i \right\|} = \frac{\mathbf{F}^{i^{-T}} \boldsymbol{n}_0^i}{\left\| \mathbf{F}^{i^{-T}} \boldsymbol{n}_0^i \right\|} \tag{VI.7}$$

where $\delta \boldsymbol{x}_1^i = \mathbf{F}^i \delta \boldsymbol{x}_{01}^i$ and $\delta \boldsymbol{x}_2^i = \mathbf{F}^i \delta \boldsymbol{x}_{02}^i$ are two independent vectors in the plane of the interface, $\delta \boldsymbol{x}_{01}^i$ and $\delta \boldsymbol{x}_{02}^i$ being the vectors in the reference configuration. $\mathbf{F}^i$ can be either $\mathbf{F}_\alpha^i$, $\mathbf{F}_\beta^i$, $\mathbf{F}_a^i$ or $\mathbf{F}_I^i$. The symbol × means the cross product of the vectors.

The monitoring of the orientation of the interfaces allows simulating the texture evolution and thus the strain-induced anisotropy. In what follows, the constitutive equations are specified in order to describe the different micro-mechanisms governing the macroscopic response. Fig.

VI.2 provides a rheological representation for each phase, analog of their resistance to deformation. Both α-form and β-form crystals are described by a linear elastic spring in series with a viscoplastic slider. The amorphous phase is described by a hyperelastic spring in series with a nonlinear viscous damper, all in parallel with a linear elastic spring in series with a viscoplastic damper.

VI.2.2. Elasto-viscoplasticity in α-PVDF and in β-PVDF

Elasto-viscoplastic deformation occurs both in α-form and β-form crystals. The general elastic stress-strain relationship in α-PVDF and in β-PVDF is given, respectively, by:

$$\boldsymbol{\tau}_\alpha = \mathbf{C}_\alpha : \mathbf{E}^e_\alpha \text{ and } \boldsymbol{\tau}_\beta = \mathbf{C}_\beta : \mathbf{E}^e_\beta \tag{VI.8}$$

in which $\mathbf{C}_\alpha$ and $\mathbf{C}_\beta$ are the fourth-order elastic stiffness tensors, $\boldsymbol{\tau}_\alpha$ and $\boldsymbol{\tau}_\beta$ are the second Piola-Kirchhoff stress tensors and, $\mathbf{E}^e_\alpha$ and $\mathbf{E}^e_\beta$ are the elastic Green-Lagrange strain tensors. The stress tensors $\boldsymbol{\tau}_\alpha$ and $\boldsymbol{\tau}_\beta$ are related to their corresponding Cauchy stress tensors $\boldsymbol{\sigma}_\alpha$ and $\boldsymbol{\sigma}_\beta$ by:

$$\boldsymbol{\tau}_\alpha = J^e_\alpha \mathbf{F}^{e^{-1}}_\alpha \boldsymbol{\sigma}_\alpha \mathbf{F}^{e^{-T}}_\alpha \text{ and } \boldsymbol{\tau}_\beta = J^e_\beta \mathbf{F}^{e^{-1}}_\beta \boldsymbol{\sigma}_\beta \mathbf{F}^{e^{-T}}_\beta \tag{VI.9}$$

where $J^e_\beta = \det \mathbf{F}^e_\beta$ and $J^e_\beta = \det \mathbf{F}^e_\beta$ are the elastic volume changes and, $\mathbf{F}^e_\alpha$ and $\mathbf{F}^e_\beta$ are the elastic deformation gradient tensors coming from the multiplicative decomposition: $\mathbf{F}^e_\alpha = \mathbf{F}_\alpha \mathbf{F}^{in^{-1}}_\alpha$ and $\mathbf{F}^e_\beta = \mathbf{F}_\beta \mathbf{F}^{in^{-1}}_\beta$ in which $\mathbf{F}_\alpha$ and $\mathbf{F}_\beta$ are the deformation gradients and, $\mathbf{F}^{in}_\alpha$ and $\mathbf{F}^{in}_\beta$ are the inelastic parts. The time derivative of the latter are $\dot{\mathbf{F}}^{in}_\alpha = \mathbf{L}^{in}_\alpha \mathbf{F}^{in}_\alpha$ and $\dot{\mathbf{F}}^{in}_\beta = \mathbf{L}^{in}_\beta \mathbf{F}^{in}_\beta$ with $\mathbf{L}^{in}_\alpha$ and $\mathbf{L}^{in}_\beta$ the inelastic spatial velocity gradients describing the crystallographic slip:

$$\mathbf{L}^{in}_\alpha = \sum_{s=1}^{N_s} \dot{\gamma}^s_\alpha \mathbf{R}^s \text{ and } \mathbf{L}^{in}_\beta = \sum_{s=1}^{N_s} \dot{\gamma}^s_\beta \mathbf{R}^s \tag{VI.10}$$

in which N_s denotes the slip systems, $\mathbf{R}^s = \left(\boldsymbol{n}^s \otimes \boldsymbol{m}^s + \boldsymbol{m}^s \otimes \boldsymbol{n}^s\right)/2$ is the nonsymmetric Schmid tensor with $\boldsymbol{n}^s$ and $\boldsymbol{m}^s$ the "slip plane" normal vector and the "slip direction" vector in this plane, respectively, and, $\dot{\gamma}^s_\alpha$ and $\dot{\gamma}^s_\beta$ are the shear strain rates given by:

$$\dot{\gamma}^s_\alpha = \dot{\gamma}_{\alpha,0} \operatorname{sign}\left(\tau^s_\alpha\right) \left| \frac{\tau^s_\alpha}{g^s_\alpha} \right|^{1/m_\alpha} \text{ and } \dot{\gamma}^s_\beta = \dot{\gamma}_{\beta,0} \operatorname{sign}\left(\tau^s_\beta\right) \left| \frac{\tau^s_\beta}{g^s_\beta} \right|^{1/m_\beta} \tag{VI.11}$$

where $\dot{\gamma}_{\alpha,0}$ and $\dot{\gamma}_{\beta,0}$ are the reference strain rates, m_α and m_β are the strain rate sensitivity

parameters, $\tau_\alpha^s = \boldsymbol{\tau}_\alpha : \mathbf{R}^s$ and $\tau_\beta^s = \boldsymbol{\tau}_\beta : \mathbf{R}^s$ are the resolved shear stresses and, g_α^s and g_β^s are the shear strengths of the slip system s. The term $\text{sign}(x)$ signifies -1 for $x<0$, 1 for $x>0$ and 0 for $x=0$.

VI.2.3. Elasto-viscoplastic-viscohyperelasticity in amorphous PVDF

The intermolecular interactions and the molecular orientation/relaxation process occurring in the PVDF amorphous domain is captured by considering the elasto-viscoplastic-viscohyperelastic deformation. The amorphous stress $\boldsymbol{\sigma}_a$ is additively decomposed into an elasto-viscoplastic intermolecular stress and an Arruda-Boyce eight-chain viscohyperelastic network stress: $\boldsymbol{\sigma}_a = \boldsymbol{\sigma}_{a\_\text{inter}} + \boldsymbol{\sigma}_{a\_\text{net}}$, that are constitutively given, respectively, by:

$$\boldsymbol{\sigma}_{a\_\text{inter}} = \frac{1}{J_{a\_\text{inter}}} \mathbf{C}_a \ln\left(\mathbf{V}^e_{a\_\text{inter}}\right) \text{ and } \boldsymbol{\sigma}_{a\_\text{net}} = \frac{1}{J_{a\_\text{net}}} \frac{C_h}{3} \frac{\sqrt{N}}{\lambda^e_{a\_\text{net}}} \mathcal{L}^{-1}\left(\frac{\lambda^e_{a\_\text{net}}}{\sqrt{N}}\right)\left(\mathbf{B}^e_{a\_\text{net}} - \lambda^{e^2}_{a\_\text{net}} \mathbf{I}\right) \quad \text{(VI.12)}$$

where $\mathbf{C}_a$ is the fourth-order elastic stiffness tensor (whose the components may be expressed using the Young's modulus E_a and the Poisson's ratio ν_a), N is the average number of molecular units between entanglements, C_h is the hardening modulus, $J_{a\_\text{inter}} = \det \mathbf{F}^e_{a\_\text{inter}}$ and $J_{a\_\text{net}} = \det \mathbf{F}^e_{a\_\text{net}}$ are the elastic volume changes, $\mathbf{V}^e_{a\_\text{inter}}$ is the elastic stretch movement part coming from the polar decomposition of the elastic deformation gradient $\mathbf{F}^e_{a\_\text{inter}} = \mathbf{V}^e_{a\_\text{inter}} \mathbf{R}^e_{a\_\text{inter}}$ with $\mathbf{R}^e_{a\_\text{inter}}$ the elastic rotation movement part, $\lambda^e_{a\_\text{net}} = \left[\text{trace}\left(\mathbf{B}^e_{a\_\text{net}}\right)/3\right]^{1/2}$ is the elastic stretch on each molecular chain in the amorphous network in which $\mathbf{B}^e_{a\_\text{net}} = J^{-2/3}_{a\_\text{net}} \mathbf{F}^e_{a\_\text{net}} \mathbf{F}^{e^T}_{a\_\text{net}}$ is the isochoric elastic left Cauchy-Green tensor, $\mathbf{I}$ is the identity tensor and $\mathcal{L}^{-1}$ is the inverse Langevin function which can be treated by a Padé approximation: $\mathcal{L}^{-1}(x) \approx x\left(3-x^2\right)/\left(1-x^2\right)$. The elastic deformation gradients $\mathbf{F}^e_{a\_\text{inter}}$ and $\mathbf{F}^e_{a\_\text{net}}$ are obtained via the multiplicative forms using the conceptual sequence of configurations proposed by Lee (1969): $\mathbf{F}^e_{a\_\text{inter}} = \mathbf{F}_{a\_\text{inter}} \mathbf{F}^{in^{-1}}_{a\_\text{inter}}$ and $\mathbf{F}^e_{a\_\text{net}} = \mathbf{F}_{a\_\text{net}} \mathbf{F}^{in^{-1}}_{a\_\text{net}}$ in which $\mathbf{F}_{a\_\text{inter}}$ and $\mathbf{F}_{a\_\text{net}}$ are the deformation gradients and, $\mathbf{F}^{in}_{a\_\text{inter}}$ and $\mathbf{F}^{in}_{a\_\text{net}}$ are the inelastic parts. The time derivative of the latter are $\dot{\mathbf{F}}^{in}_{a\_\text{inter}} = \mathbf{L}^{in}_{a\_\text{inter}} \mathbf{F}^{in}_{a\_\text{inter}}$ and $\dot{\mathbf{F}}^{in}_{a\_\text{net}} = \mathbf{L}^{in}_{a\_\text{net}} \mathbf{F}^{in}_{a\_\text{net}}$ with $\mathbf{L}^{in}_{a\_\text{inter}}$ and $\mathbf{L}^{in}_{a\_\text{net}}$ the inelastic spatial velocity gradients given by:

$$\mathbf{L}^{in}_{a\_\text{inter}} = \mathbf{F}^e_{a\_\text{inter}} \dot{\mathbf{F}}^{in}_{a\_\text{inter}} \mathbf{F}^{in^{-1}}_{a\_\text{inter}} \mathbf{F}^{e^{-1}}_{a\_\text{inter}} \text{ and } \mathbf{L}^{in}_{a\_\text{net}} = \mathbf{F}^e_{a\_\text{net}} \dot{\mathbf{F}}^{in}_{a\_\text{net}} \mathbf{F}^{in^{-1}}_{a\_\text{net}} \mathbf{F}^{e^{-1}}_{a\_\text{net}} \quad \text{(VI.13)}$$

With no loss in generality (Gurtin and Anand, 2005), irrotationality for inelastic flow both in the intermolecular resistance and the network resistance gives the evolution equation of the inelastic deformation gradients:

$$\dot{\mathbf{F}}^{in}_{a\_\text{inter}} = \mathbf{F}^{e^{-1}}_{a\_\text{inter}}\mathbf{D}^{in}_{a\_\text{inter}}\mathbf{F}^{e}_{a\_\text{inter}}\mathbf{F}^{in}_{a\_\text{inter}} \text{ and } \dot{\mathbf{F}}^{in}_{a\_\text{net}} = \mathbf{F}^{e^{-1}}_{a\_\text{net}}\mathbf{D}^{in}_{a\_\text{net}}\mathbf{F}^{e}_{a\_\text{net}}\mathbf{F}^{in}_{a\_\text{net}} \quad \text{(VI.14)}$$

where the tensors $\mathbf{D}^{in}_{a\_\text{inter}}$ and $\mathbf{D}^{in}_{a\_\text{net}}$ provide the specificity of the intermolecular and network inelastic strain rates. They are defined by the following general flow rules:

$$\mathbf{D}^{in}_{a\_\text{inter}} = \dot{\gamma}_{a\_\text{inter}}\frac{\boldsymbol{\sigma}'_{a\_\text{inter}}}{\sqrt{2}\left\|\boldsymbol{\sigma}_{a\_\text{inter}}\right\|} \text{ and } \mathbf{D}^{in}_{a\_\text{net}} = \dot{\gamma}_{a\_\text{net}}\frac{\boldsymbol{\sigma}'_{a\_\text{net}}}{\sqrt{2}\left\|\boldsymbol{\sigma}_{a\_\text{net}}\right\|} \quad \text{(VI.15)}$$

where $\left\|\boldsymbol{\sigma}_{a\_\text{inter}}\right\| = \left(\boldsymbol{\sigma}'_{a\_\text{inter}}.\boldsymbol{\sigma}'_{a\_\text{inter}}/2\right)^{1/2}$ and $\left\|\boldsymbol{\sigma}_{a\_\text{net}}\right\| = \left(\boldsymbol{\sigma}'_{a\_\text{net}}.\boldsymbol{\sigma}'_{a\_\text{net}}/2\right)^{1/2}$ are the effective shear stresses, $\boldsymbol{\sigma}'_{a\_\text{inter}}$ and $\boldsymbol{\sigma}'_{a\_\text{net}}$ are the deviatoric parts and, $\dot{\gamma}_{a\_\text{inter}}$ and $\dot{\gamma}_{a\_\text{net}}$ are the inelastic shear strain rates given, respectively, by the Argon (1973) expression for the thermally activated process (Boyce et al., 2000) and the Bergstrom-Boyce (1998) expression for the thermal-induced relaxation process of the amorphous layers:

$$\dot{\gamma}_{a\_\text{inter}} = \dot{\gamma}_{a,0}\exp\left[-\frac{\Delta G}{k\theta}\left(1-\frac{\left\|\boldsymbol{\sigma}_{a\_\text{inter}}\right\|}{s}\right)\right] \text{ and } \dot{\gamma}_{a\_\text{net}} = C_v\left|\lambda^{in}_{a\_\text{net}} - 1\right|^{-1}\left\|\boldsymbol{\sigma}_{a\_\text{net}}\right\| \quad \text{(VI.16)}$$

The left formula of Eq. (VI.16) captures barriers to molecular chain segment rotation in the amorphous layers. The term $\dot{\gamma}_{a,0}$ is the pre-exponential constant, ΔG is the activation energy barrier to molecular mobility, k is the Boltzmann's constant, θ is the absolute temperature and s is the shear strength controlling the amorphous chain segment rotation: $\dot{s} = h\dot{\gamma}_{a\_\text{inter}}$ in which h is the hardening rate given by the following power-law: $h = \left(s_0/s\right)^n s/n$ where s_0 is the initial shear strength and n is the intermolecular hardening coefficient. The right formula of Eq. (VI.16) captures molecular relaxation process in the amorphous layers. The term C_v is the chain relaxation parameter and $\lambda^{in}_{a\_\text{net}} = \left[\text{trace}\left(\mathbf{B}^{in}_{a\_\text{net}}\right)/3\right]^{1/2} + \varsigma$ is the inelastic stretch on each molecular chain in the amorphous network in which $\mathbf{B}^{in}_{a\_\text{net}} = \mathbf{F}^{in}_{a\_\text{net}}\mathbf{F}^{in^T}_{a\_\text{net}}$ is the inelastic left Cauchy-Green tensor and $\varsigma = 0.01$ is an added perturbation coefficient avoiding singularity of the right formula at the beginning of loading process.

VI.2.4. Strain-induced α → β phase transition

The random orientation of the inclusions in the aggregate before straining, along with the tilting

towards the maximum principal strain of the normal to the surface of the crystalline lamellae during plastic deformation, implies a non-uniform distribution of the α → β phase transition mechanism at the scale of the inclusions. The degrees of α-phase f_α^i and β-phase f_β^i in each inclusion i are governed by the following conditions on the α-phase micro-strain ε_α^i:

$$f_\alpha^i = \begin{cases} f_{\alpha\_0} & 0 \le \varepsilon_\alpha^i < \varepsilon_c \\ f_\alpha & \varepsilon_\alpha^i \ge \varepsilon_c \end{cases} \text{ and } f_\beta^i = \begin{cases} 0 & 0 \le \varepsilon_\alpha^i < \varepsilon_c \\ f_\beta & \varepsilon_\alpha^i \ge \varepsilon_c \end{cases} \tag{VI.17}$$

where ε_c is the critical strain for the onset of α → β phase transition when α-PVDF is drawn, $f_\alpha \in [0,1]$ and $f_\beta \in [0,1]$ are the macro-variables of α-phase and β-phase amounts and f_{α_0} is the initial α-phase amount.

The α-phase degree f_α decreases progressively with the increase of the β-phase degree f_β upon straining according to the following formulae:

$$f_\alpha = f_{\alpha\_0} - f_\beta \text{ and } f_\beta = f_{\beta\_\infty}\kappa \tag{VI.18}$$

where f_{β_∞} is the maximum β-phase amount (taken equal to f_{α_0} for a full transformation) and κ is the total degree of transformation given by the following Avrami-type kinetics (Doufas et al., 2000):

$$\dot{\kappa} = \frac{\dot{\varepsilon}}{\dot{\varepsilon}_{ref}} \alpha_{av} K_{av} \left(-\ln\left(1-\kappa\right)\right)^{\frac{\alpha_{av}-1}{\alpha_{av}}} \left(1-\kappa\right) \tag{VI.19}$$

in which $\dot{\varepsilon}$ is the applied strain rate, $\dot{\varepsilon}_{ref}$ is the reference strain rate, α_{av} is the Avrami exponent and K_{av} is the phase transformation rate given here in the case of PVDF by the empirical form defined as follows:

$$K_{av} = 0.75\times10^{-3}\left(\frac{4\pi Nu}{3f_{\beta\_\infty}}\right)^{1/3} \exp\left(-\left(\frac{\theta-206}{47.33}\right)^2\right) \tag{VI.20}$$

in which Nu represents the number density of nuclei.

Eq. (VI.20) is an empirical formula emerged for the study of spherulitic growth in thermally-induced crystallization. It was employed in previous studies of the literature in the context of strain-induced crystallization of poly(ethylene terephthalate) (Ahzi et al., 2003; Makradi et al., 2005) and poly(lactic acid) (Mahjoubi et al., 2019, 2020) as a phenomenological description of the evolution of newly formed phase. The involved constants are here slightly modified in order to fit the observations in the PVDF model application. The Avrami-type kinetics is probably not

an optimal choice for the description of the micro-mechanism of α → β phase transition which requires more work to propose an expression through a thermodynamic reasoning, see e.g. (Guo and Zaïri, 2020).

The continuum-based model provides the necessary framework for the analysis of the relation between mesostructural characteristic and overall mechanical response. In what follows, an identification procedure of the model parameters using a hierarchical multi-scale strategy is developed. At the atomic scale, the mechanical properties of the different phases (α-PVDF, β-PVDF and amorphous PVDF), which are difficult to characterize experimentally, are derived through molecular dynamics simulations (Fig. VI.2). Subsequently, based on the properties calculated from molecular dynamics simulations, the other model parameters are identified by matching simulation outputs of the macroscale aggregate of inclusions and existing tensile experiments of a PVDF upon large-strain plastic deformation.

VI.3. Identification and simulations

VI.3.1. Molecular dynamics analysis of α-PVDF and β-PVDF

Molecular dynamics simulations are employed to examine the physical properties of α-PVDF and β-PVDF and to extract their elastic properties along with the onset of α → β phase transition caused by the straining.

VI.3.1.1. Simulation details and structural properties

Fig. VI.3(a) displays packing structure in a unit cell of the two crystalline structures. The optimized cell parameters are listed in Table VI.1. The ReaxFF reactive force field was used. Note that the traditional force fields for polymers, such as AMBER, CHARMM, CVFF, UFF, CFF, COMPASS, and so on, are not adaptive here because the bond breaking/formation are not taken into account. Indeed, ReaxFF eschews explicit bonds in favor of bond orders calculated from interatomic distances that are updated every molecular dynamics simulation step, which allows for continuous bond breaking/formation during the simulation.

Table VI.1. Optimized cell parameters of nine crystalline forms of PVDF. The α, β and γ are angles between cell vectors a and b, b and c and, a and c, respectively.

	a (Å)	b (Å)	c (Å)	α (°)	β (°)	γ (°)
α-phase	4.45868	8.44829	4.54098	90	90	90
β-phase	7.85031	4.94145	1.92177	90	90	90

After preparing all the structures, the molecular dynamics simulations were performed. Each

simulation involves three steps. In the first step, a geometry optimization was performed on the model to obtain an energy minimized structure. In the second step, a NPT dynamic equilibration was running for 10000 steps at 298 K. The evolution in total energy and density during the equilibrium process was analyzed (see Appendix VI.A) for both crystal forms. In the equilibrium phase, both energy and density have been equilibrated. The β-PVDF density is found to be slightly higher than the α-PVDF density, which is similar to the 1.92 g/cm^3 for pure α-PVDF and 1.97 g/cm^3 for pure β-PVDF (Hasegawa et al., 1972; Ameduri, 2009). Based on the information provided by the atoms contributions to radial distribution function (RDF), the partial RDF of bonded atom for both crystal forms was analyzed (see Appendix VI.A) and it was confirmed that the behavior is found close to that found in earlier studies (Hasegawa et al., 1972; Wang et al., 2006; Zhu et al., 2009; Li et al., 2019).

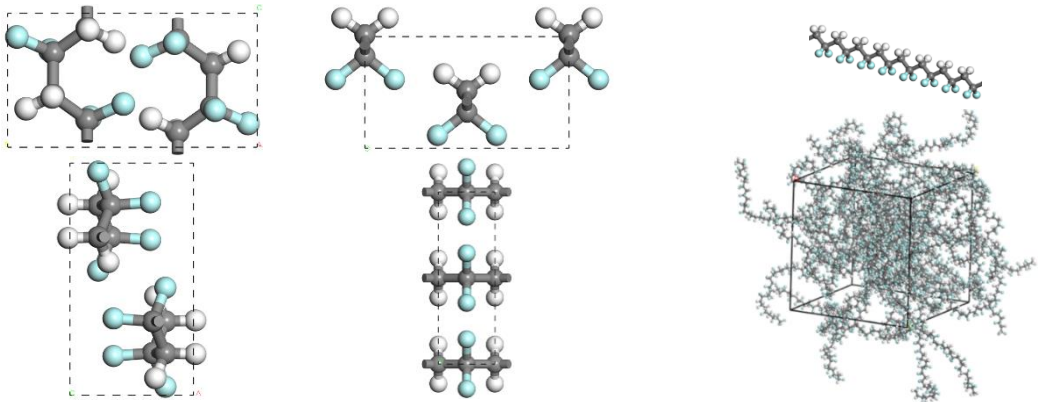

Fig. VI.3. Molecular dynamics model of the three constitutive phases in PVDF: (a) Side and top view of packing crystalline structure in a unit cell for α-phase and β-phase, (b) Single chain and supercell of the amorphous phase structure (Gray, white, and blue spheres represent carbon, hydrogen and fluorine atoms, respectively).

VI.3.1.2. Elastic constants

Multi-directional uniaxial stretching and multi-plane shearing tests were performed on the equilibrium structure with engineering strain rate 10^{10} s^{-1} in the NVT ensemble at the temperature of 298 K and stress-strain curves were obtained. The normal stress σ_{11}, σ_{22} and σ_{33} of each uniaxial stretch for α-PVDF and β-PVDF are shown in Fig. VI.4. The normal stress σ_{33} is found much higher than the two other normal stresses σ_{11} and σ_{22}. This is because the Z-axis direction is the direction of chain elongation, and the energy required to break C-C is much greater than the energy required to break non-bonded bonds. The linear part of the stress-strain

response enables to calculate the elastic constants C_{α_ij} and C_{β_ij} of α-PVDF and β-PVDF. They are reported in Table VI.2 and VI.3, respectively, and compared to theoretical results of the literature (Pei and Zeng, 2011) obtained by density-functional theory. We only retained the 9 most important components of the elastic stiffness tensors:

$$C_{\alpha\_11}, C_{\alpha\_22}, C_{\alpha\_33}, C_{\alpha\_44}, C_{\alpha\_55}, C_{\alpha\_66}, C_{\alpha\_12}, C_{\alpha\_13}, C_{\alpha\_23} \quad \text{(VI.21)}$$

for α-PVDF and

$$C_{\beta\_11}, C_{\beta\_22}, C_{\beta\_33}, C_{\beta\_44}, C_{\beta\_55}, C_{\beta\_66}, C_{\beta\_12}, C_{\beta\_13}, C_{\beta\_23} \quad \text{(VI.22)}$$

for β-PVDF since the remaining elastic coefficients are very weak and can be neglected.

Table VI.2. Elastic constants of α-PVDF calculated in this work by molecular dynamics simulation in comparison with other theoretical results of the literature obtained by density-functional theory (values in GPa).

	C_{α_11}	C_{α_22}	C_{α_33}	C_{α_44}	C_{α_55}	C_{α_66}	C_{α_12}	C_{α_13}	C_{α_23}
This work	17.169	15.916	145.25	1.34	3.877	3.47	10.203	3.003	1.14
Pei and Zeng (2011)	16.10	15.70	148.1	0.5	3.9	6.5	6.2	8	0.8

Table VI.3. Elastic constants of β-PVDF calculated in this work by molecular dynamics simulation in comparison with other theoretical results of the literature obtained by density-functional theory (values in GPa).

	C_{β_11}	C_{β_22}	C_{β_33}	C_{β_44}	C_{β_55}	C_{β_66}	C_{β_12}	C_{β_13}	C_{β_23}
This work	16.089	20.554	304.64	3.41	5.078	6.778	11.486	11.766	21.266
Pei and Zeng (2011)	19.83	24.50	287.33	1.17	0.33	1.67	4.33	0.83	3.33

VI.3.1.3. Onset of α → β phase transition

As the manifestation of the α → β phase transition caused by the straining, the α-PVDF exhibits a stress drop followed by a resumption in Fig. VI.4(a). That results in two distinct processes of linear elasticity, one from 0 to a strain level of 0.05, and a second one from a strain level of 0.08. The elastic constant C_{α_33} calculated in the second stage is found to be 310 GPa which is very close to the β-PVDF elastic constant C_{β_33}. The structure of α-PVDF in the second stage becomes the same than the β-PVDF structure. The screenshots of the stretching process inserted in Fig. VI.4(a) show a twisting of the bond angle of α-PVDF leading to a conversion to β-PVDF structure as compared with the screenshots of β-PVDF inserted in Fig. VI.4(b). The bond angle opening of β-PVDF progresses until final breaking leading to the observable dramatic stress drop in Fig. VI.4(b). The α-PVDF response along with the mechanism of phase transition are influenced by the straining temperature as shown in Fig. VI.5(a). The critical strain in α-PVDF for α → β phase transition is plotted against the inverse absolute temperature in Fig. VI.5(b)

such that a straight line is obtained which can be thus described by a simple linear formula:

$$\varepsilon_c = \frac{3.25}{\theta} + 0.047 \qquad \text{(VI.23)}$$

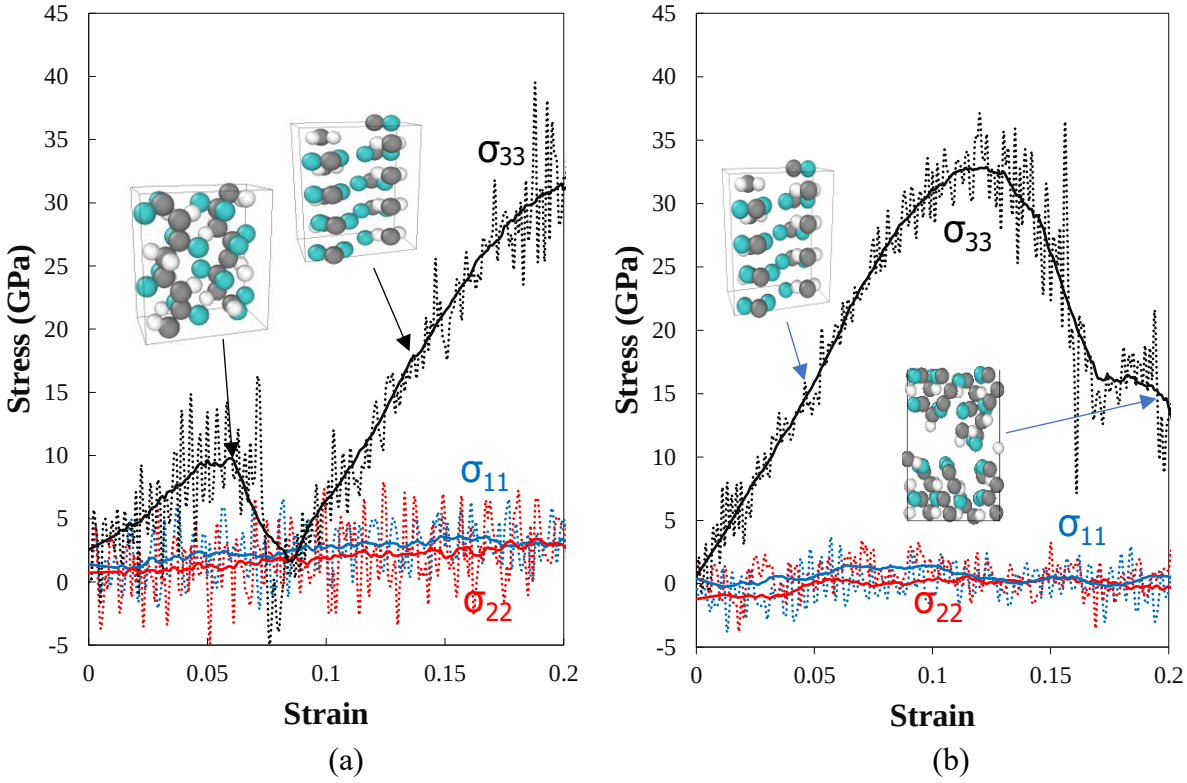

Fig. VI.4. Stress as a function of strain issued from molecular dynamics simulation at the temperature of 298 K for (a) α-PVDF and (b) β-PVDF.

VI.3.2. Molecular dynamics analysis of the amorphous phase

Molecular dynamics simulations are employed to examine the properties of the amorphous PVDF phase. It is modeled using the explicit atom model (Kang et al., 2019; Sharma and Roy, 2020; Zhang et al., 2021). The monomer atomic formula of amorphous PVDF is $C_2H_2F_2$ as shown in Fig. VI.3(b). Each single chain is represented by 50 monomers. Twenty chains are then heated and melted to form a PVDF melt.

VI.3.2.1. Simulation details and structural properties

The polymer consistent force field (PCFF) is adapted as the basis of the potential function (Sun et al., 1994). The PCFF force-field is one member of the ab initio consistent force-field family (composed of CFF91, CFF, pcff, and COMPASS force-field) with the same functional form. It involves a Lennard-Jones 9-6 potential for the intermolecular and intramolecular dispersion - repulsion interactions. Specific stretching, bending and torsion terms describe 1-2, 1-3 and 1-4

interactions, respectively. Electrostatic charges are determined from pair contributions. In this force field, the carbon atoms in the PVDF can be classified into three types according to the way the atoms are grouped, as shown by the different colors in Fig. VI.3(b). The parameter of these interactions are described in details in (Sun et al., 1994; Li et al., 2016) and skipped here for brevity.

The initial structure is studied for four relaxation steps to relax any high-energy configurations. Initially, the simulation ran for 2×10^5 timesteps (Δt=1 fs) using NVT ensemble at 600 K, then the structure is relaxed for 5×10^5 timesteps (Δt=1 fs) using NPT ensemble at 600 K. The next relaxation cooled the structure down to the desired temperature at 1 K/ps cooling rate (Δt=1 fs) followed by further relaxation of 3×10^6 timesteps (Δt=1 fs) at the desired temperature. The energy history of the models was monitored through this process to ensure that final structure was stable. (see Appendix VI.A).

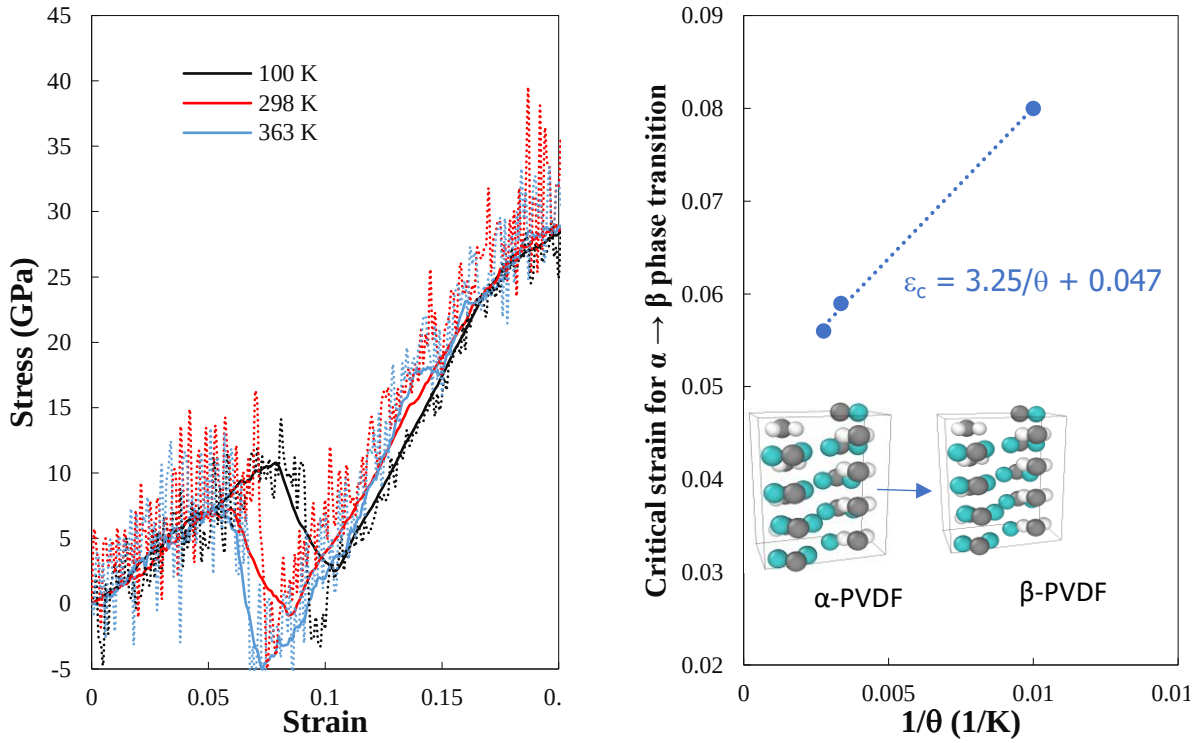

Fig. VI.5. Temperature effect of the α-PVDF response along with onset of α → β phase transition issued from molecular dynamics simulation: (a) Stress as a function of strain and (b) critical strain for α → β phase transition.

VI.3.2.2. Elastic and yield constants

After the stable structure was obtained, uniaxial tension was performed at different straining temperatures and strain rates and, the stress-strain curves are plotted in Fig. VI.6. Note that the

fluctuations in the response are due to the small size of the simulated cell as also observed in other studies for different systems (Yazdani et al., 2018; Payal et al., 2019; Zhang et al., 2021) and they were smoothed via the Savitzky-Golay filter (Larive and Sweedler, 2013) to obtain the stress trends. It can be seen that the latter trends exhibit a clear dependence on the loading parameters; The lower the strain rate (the higher the loading temperature), the lowest the stiffness and the yield stress.

In order to identify the equilibrium response, the system was uniaxially stretched at a constant strain rate of 10^9 s^{-1} for 10000 steps (ε=0.1) followed by equilibration for 200000 steps (Δt=1 fs) with the axial dimension kept fixed to stabilize the energy in the system and to provoke the stress relaxation. This process is iterated until the desired strain is obtained. The relaxed stress-strain response is plotted in Fig. VI.6(b).

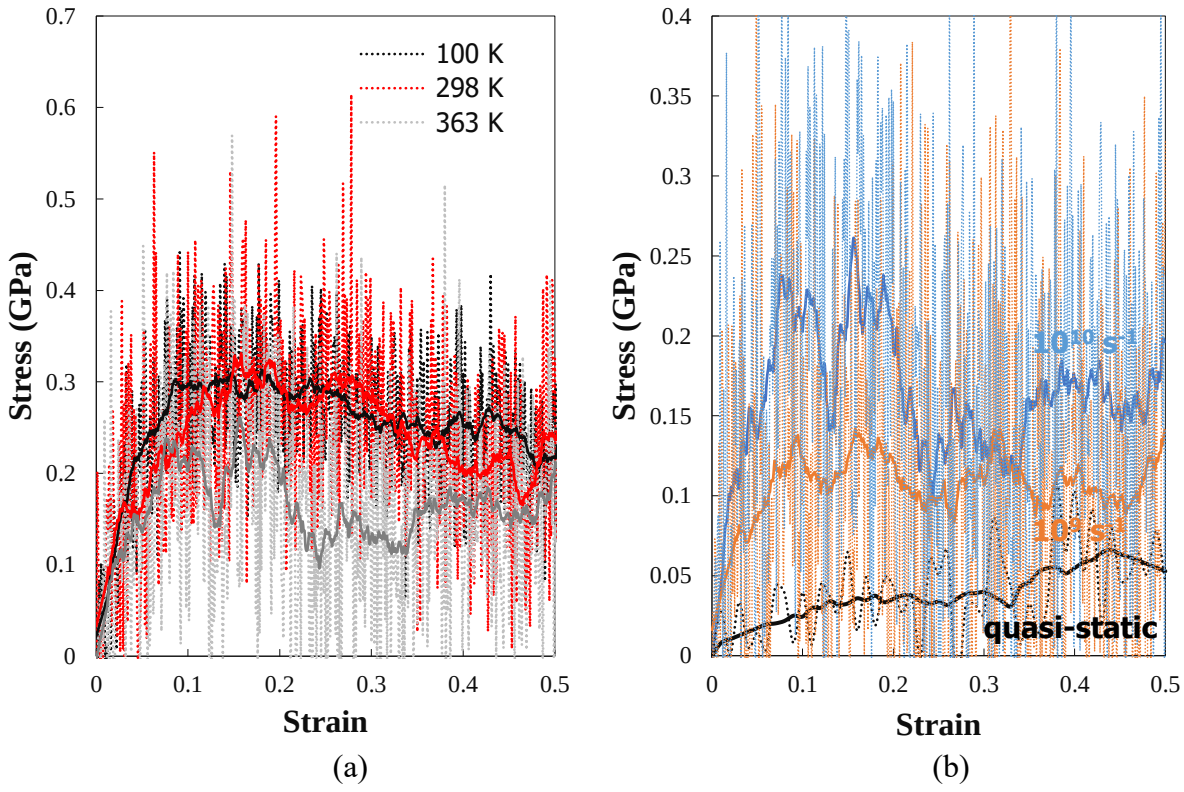

Fig. VI.6. Stress as a function of strain issued from molecular dynamics simulation for the amorphous PVDF: (a) Temperature effect (at the strain rate of 10^{10} s^{-1}) and (b) strain rate effect (at the temperature of 363 K).

The amorphous stiffness modulus can be obtained from the initial slope of stress-strain curve. The small-strain region of the relaxed response was also used to evaluate the amorphous yield strength as shown in Fig. VI.7(a). Different graphical methods may be utilized to identify the stress at yield onset from a monotonic stress-strain curve according to its shape (Ward and

Sweeney, 2004): i) deviation point of the linear elastic domain of the stress-strain curve, ii) intersection of a line with an offset strain from the origin and parallel to the linear elastic domain, iii) local maximum if a yield drop is present or iv) Considère construction defined by a tangency point of a line with a negative offset strain from the origin.

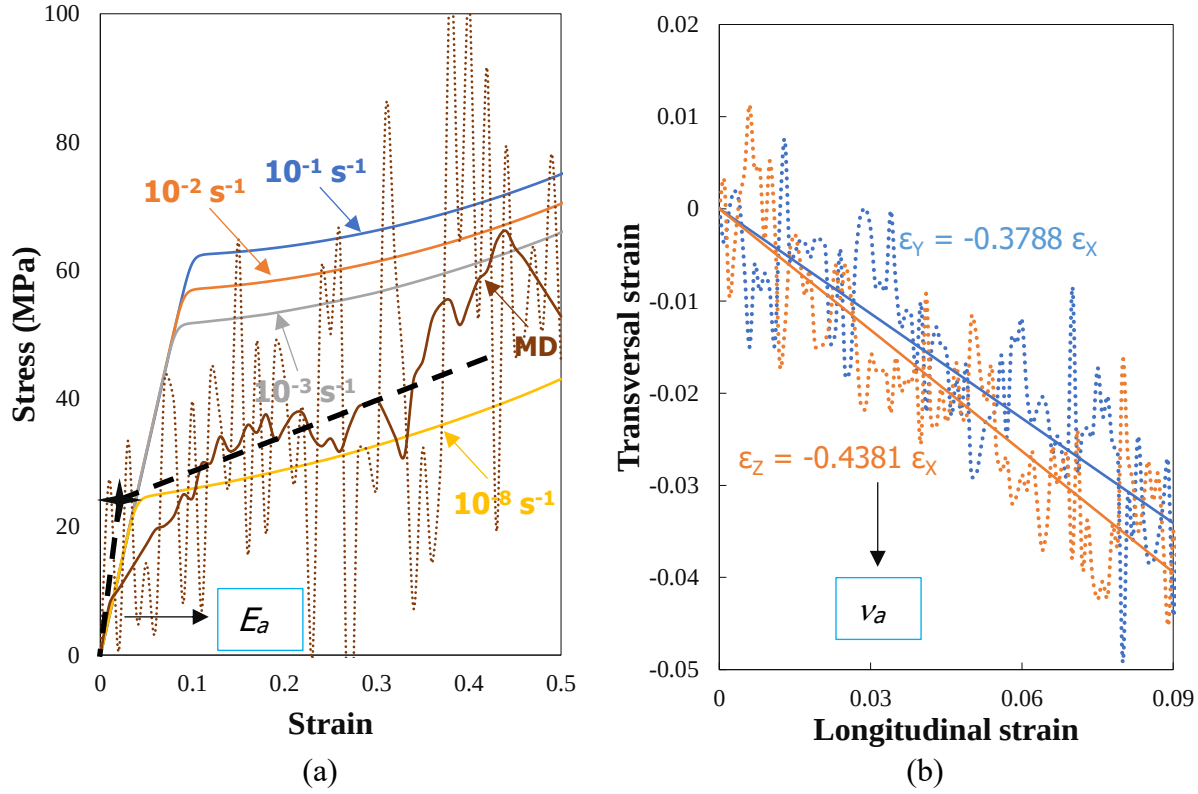

Fig. VI.7. Amorphous PVDF response at the temperature of 363 K: (a) Stress as a function of strain at different strain rates issued from continuum-based simulation in comparison to the relaxed result issued from molecular dynamics (MD) calculations and (b) transversal strain as a function of longitudinal strain issued from MD calculations.

Due to the presence of fluctuations, the yield point determination follows the criterion presented in Fig. VI.7(a); it was obtained as the intersecting point of two lines (shown in dashed lines in Fig. VI.7(a)), one follows the linear elastic domain and the other one corresponds to the slope of the post-yield hardening domain. To complete the characterization of the elastic response of the amorphous phase (assumed to be isotropic), the amorphous Poisson's ratio was obtained from the slope of the transversal strain-longitudinal strain curve issued from molecular dynamics calculations as shown in Fig. VI.7(b).

VI.3.3. Continuum-based simulation

The continuum-based model was entirely coded in Fortran language and compared to the homogeneous material data taken from the work of Defebvin et al. (2016) (see also Defebvin

(2015)) of a semi-crystalline PVDF strained up to very large strains. The authors examined the temperature-dependent tensile deformation and the strain-induced α → β phase transition in PVDF (containing 0.70 of crystals initially in the α-form) by means of in situ SAXS/WAXS experiments. The phase transformation occurred in the whole temperature range between glass transition temperature and melting temperature. Nonetheless, brittle or non-homogeneous ductile behaviors were not exploited and only homogeneous material data were employed for the model identification. The data were obtained at the strain rate of 10^{-3} s^{-1} and the temperature of 360 K over a large-strain range. The experimental data are reported in Fig. VI.1 in which are also reported X-ray plots at different strain levels showing a complete α → β phase transition at the maximum strain reached.

In the following subsection, a robust hybrid deterministic calibration procedure of the continuum-based model is detailed by using molecular dynamics and experimental data.

VI.3.3.1. Model parameters

The elastic constants of the α phase, the β phase and the amorphous phase obtained separately by molecular dynamics are introduced as direct inputs into the continuum-based model. The identification of the inelastic and α → β phase transition mechanism parameters of the model was carried out using the large tensile deformation data of Defebvin et al. (2016). The values of the identified parameters for each part of the model are listed in Table VI.4.

In accordance with the actual material, the initial microstructure is modeled with composite inclusions including fully α-form crystals. The critical strain for α → β phase transition taken from the molecular dynamics results (Fig. VI.5(b)) are directly used as constraints at the scale of the inclusions. That constitutes a fundamental aspect of this scale bridging method transferring molecular dynamics results to constitutive modeling. The moment when the maximum β-phase degree is reached being known from the X-ray plots (see Fig. VI.1), the kinetics of the α → β phase transition is designed using the experimental stress-strain data of Defebvin et al. (2016). The crystallographic shear parameters are assumed identical for the α-form and the β-form. The pre-exponential factors are taken identical for all the phases, $\dot{\gamma}_{\alpha,0} = \dot{\gamma}_{\beta,0} = \dot{\gamma}_{a,0}$. Inherent to the structure of the constitutive representation of the amorphous layers, a deterministic scheme is used to identify separately the parameters of the viscoplastic intermolecular part and the viscohyperelastic molecular network part.

Table VI.4. Continuum-based model parameters.

Crystalline	Initial α-phase amount	f_{α_0}	0.7
	Reference strain rate	$\dot{\gamma}_{\alpha,0}=\dot{\gamma}_{\beta,0}$	10^{-6} (s^{-1})
	Strain rate sensitivity	$m_\alpha=m_\beta$	0.1355
Amorphous	Young's modulus	E_a	600 (MPa)
	Poisson's ratio	ν_a	0.4
	Reference strain rate	$\dot{\gamma}_{a,0}$	10^{-6} (s^{-1})
	Activation energy	ΔG	7.44×10^{-20} (J)
	Initial shear strength	s_0	19 (MPa)
	Intermolecular hardening	n	2.8
	Hardening modulus	C_h	2.6 (MPa)
	Chain length	N	25
	Viscosity coefficient	C_v	2.42×10^{-6} (MPa^{-1} s^{-1})
Phase transformation	Reference strain rate	$\dot{\varepsilon}_{ref}$	0.001 (s^{-1})
	Maximum β-phase amount	f_{β_∞}	0.7
	Avrami exponent	α_{av}	2.2
	Number density of nuclei	Nu	3.88×10^{9}

The intermolecular yield parameters of the amorphous phase are obtained by using simultaneously the yield point extracted from the molecular dynamics results and an inverse identification of the experimental yield point at 10^{-3} s^{-1}. A very low strain rate of 10^{-8} s^{-1} is used to plot the quasi-static yield stress computed from the molecular dynamics simulations. The amorphous yield stress is plotted against the logarithmic strain rate in Fig. VI.8(a) such that a straight line is obtained. Fixing the pre-exponential factor $\dot{\gamma}_{a,0}$ to a prescribed value, the amorphous initial shear strength s_0 and the amorphous activation energy ΔG may be simultaneously determined by a linear regression of data of Fig. VI.8(a) by reformulating the left formula of Eq. (VI.16) at yield onset:

$$\left\|\boldsymbol{\sigma}_{a\_\text{inter}}\right\|_{\text{yield}}=\frac{s_0 k\theta}{\Delta G}\ln\left(\frac{\dot{\gamma}_{a\_\text{inter}}}{\dot{\gamma}_{a,0}}\right)+s_0 \tag{VI.24}$$

in which $\dot{\gamma}_{a\_\text{inter}}$ and $\left\|\boldsymbol{\sigma}_{a\_\text{inter}}\right\|_{\text{yield}}$ were approximated as $\sqrt{3}\dot{\varepsilon}$ and $\sigma_{\text{yield}}/\sqrt{3}$, respectively, $\dot{\varepsilon}$ being the applied strain rate and σ_{yield} the yield stress.

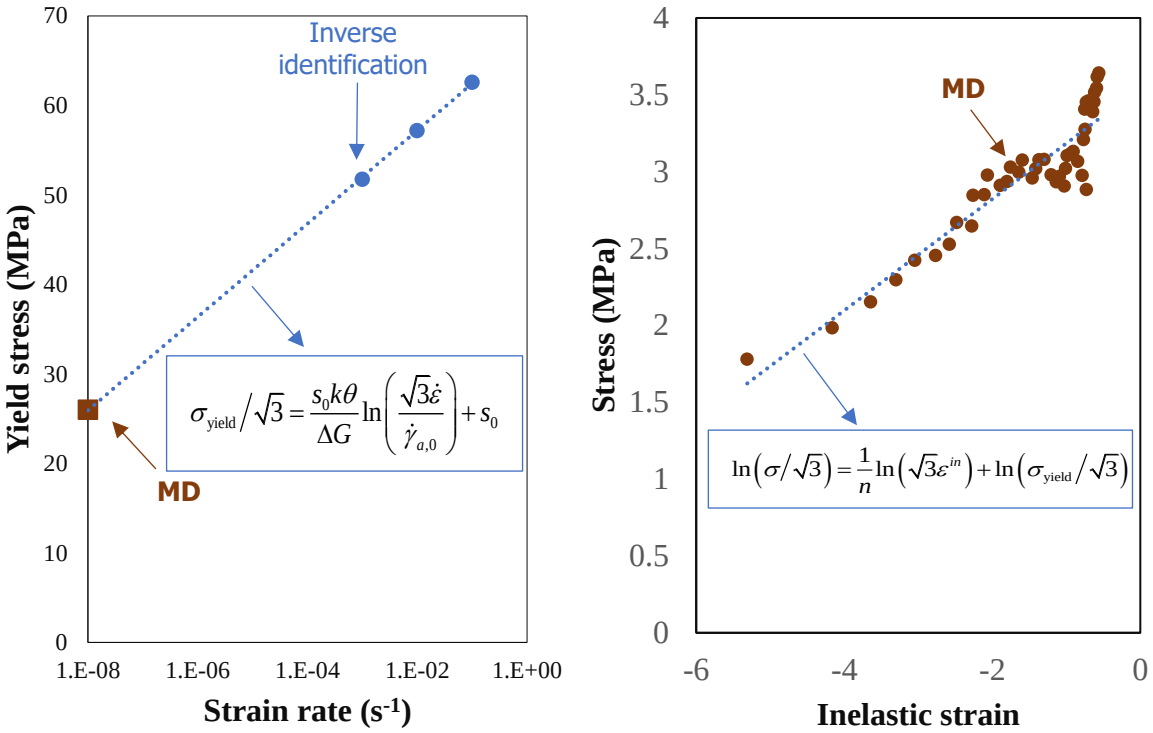

Fig. VI.8. Identification of the amorphous viscoplastic intermolecular features using molecular dynamics (MD) data: (a) identification of the initial shear strength s_0 and the activation energy ΔG using the yield stress evolution with strain rate (constructed by taking the quasi-static data (at 10^{-8} s^{-1}) from the MD curve and the data at 10^{-3} s^{-1} by inverse identification using the experimental curve) and (b) identification of the hardening coefficient n using the MD data in terms of logarithmic stress vs. logarithmic inelastic strain.

To complete the identification of the viscoplastic intermolecular features of the amorphous layers, the hardening coefficient n was determined from the slope of the molecular dynamics data of Fig. VI.8(b) in terms of logarithmic stress-logarithmic inelastic strain by reformulating the left formula of Eq. (VI.16) as follows:

$$\ln\left(\left\|\boldsymbol{\sigma}_{a\_inter}\right\|\right) = \frac{1}{n}\ln\left(\gamma_{a\_inter}\right) + \ln\left(\left\|\boldsymbol{\sigma}_{a\_inter}\right\|_{yield}\right) \tag{VI.25}$$

in which $\gamma_{a\_inter} = \sqrt{3}\varepsilon^{in}$ with ε^{in} the inelastic strain and $\left\|\boldsymbol{\sigma}_{a\_inter}\right\| = \sigma/\sqrt{3}$ with σ the stress in the post-yield region at small/moderate strains.

The parameter identification exercise ends with the viscohyperelastic molecular network parameters of the amorphous phase, C_h, N and C_v, which were identified using a standard optimization procedure providing the best fit of the strain-hardening level at large strains. Fig. VI.7(a) provides the strain rate effect on the individual amorphous post-yield response computed from the continuum-based simulations. Interestingly, a reasonable agreement

between the two kinds of simulations is obtained when the continuum-based model is computed at a strain rate of 10^{-8} s^{-1}. This shows that the elaborated hybrid molecular dynamics/experiments identification procedure ensures that the model parameters are determined appropriately.

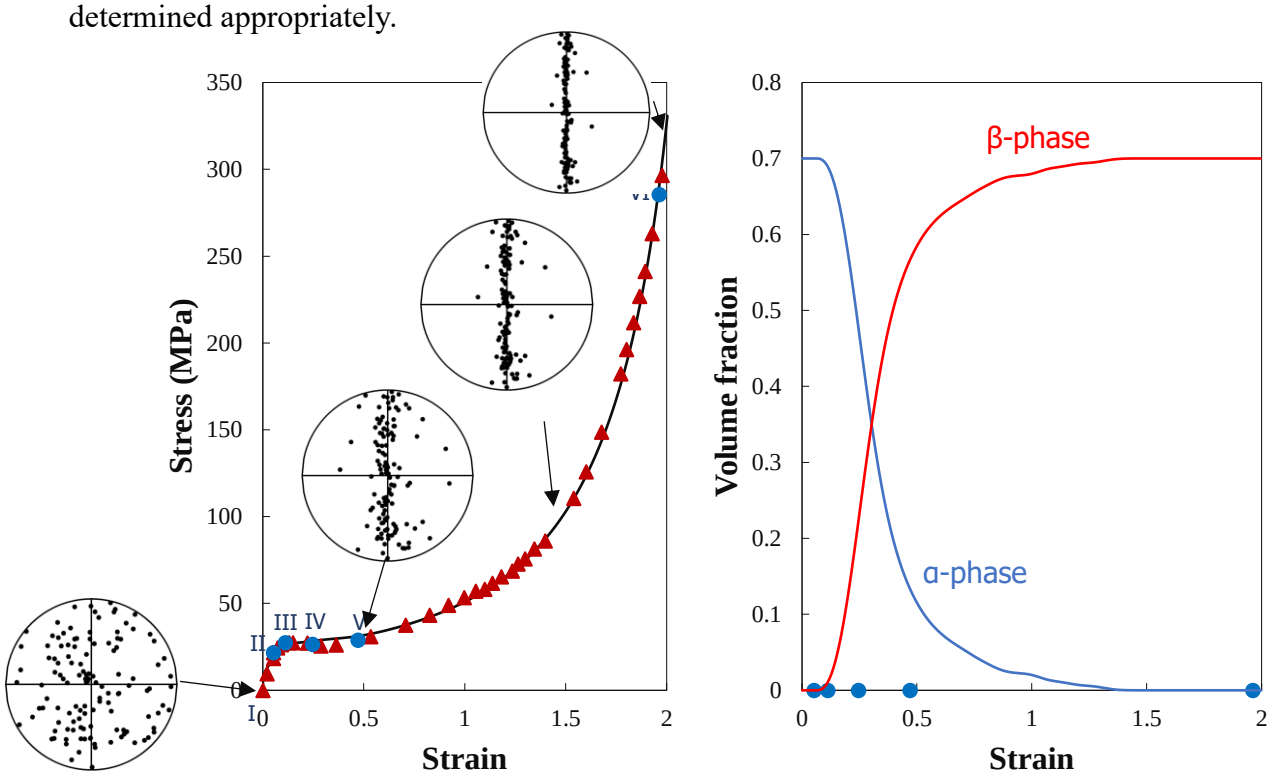

Fig. VI. 9. Continuum-based simulation of the PVDF response (containing 0.70 of crystals initially in the α-form): (a) Stress as a function of strain (solid line: model result, triangular symbols: experimental data) and (b) strain-induced α → β phase transition; strain rate of 10^{-3} s^{-1} and temperature of 363 K.

VI.3.3.2. Simulations vs. experiments

The continuum-based model output is plotted in Fig. VI.9(a) in the form of a solid line while the experimental data are plotted in the form of symbols. The simulation consists in an isothermal straining at the temperature of 360 K under a constant strain rate of 10^{-3} s^{-1}. It can be observed that the model adequately reproduces the finite-strain macroscopic stress including the elastic region, the yield strength, the progressive strain-hardening and the dramatic strain-hardening at very large strains. While providing a good approximation of the intrinsic mechanical response, the model takes into account the changes in mesostructural properties. Predicted pole figures are also provided in Fig. VI.9(a) showing the crystallographic texturing at the origin of the morphological anisotropy under increasing tensile strain.

VI.3.3.3. Phase transition evolution

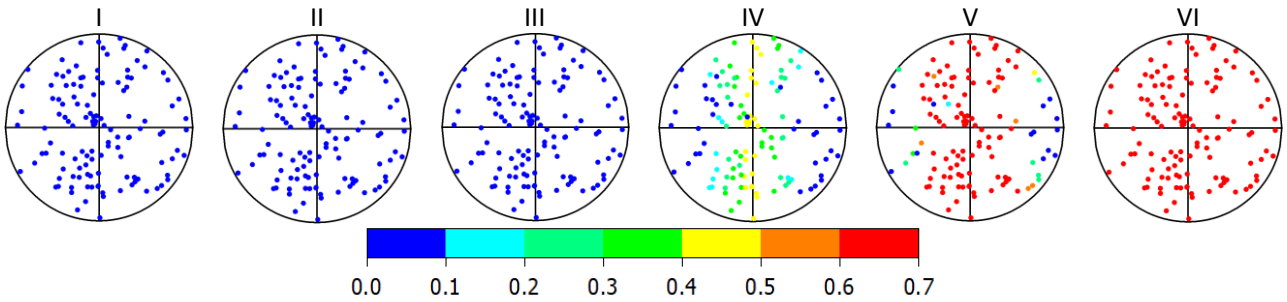

Fig. VI.10. Continuum-based simulation of the local β-phase content in PVDF (containing 0.70 of crystals initially in the α-form) at different strain levels indicated by the circular symbol in Fig. VI.9.

As a relevant feature monitored by the model, Fig. VI.9(b) presents the microstructure evolution passing from the α-form before straining to the β-form at the end of the maximum strain reached following a sigmoid kinetics; between these two strain levels the two crystal forms co-exist. The local α → β phase transition caused by the straining can be observed by means of pole figures provided in Fig. VI.10 at different applied macroscopic deformation levels. It can be observed that some inclusions in the aggregate may contain the two crystalline forms while others may continue to contain only the α-phase according to the strain level reached. The heterogeneity of the internal phase transformation is due to the material anisotropic effects caused by the deformation-induced internal ordering coming from the reorientation mechanism of the crystalline lamellae during the progressive strain-hardening response while taking into consideration the thermal-induced relaxation of the amorphous layers.

VI.3.3.4. Piezoelectric activity evolution

As a final point of discussion, the effect of strain-induced structural evolution on the piezoelectric activity of PVDF can be numerically examined by the model in connection to the changes in mesostructural properties due to the α → β phase transition. Because they are not polarized, the piezoelectric strain coefficients of both the amorphous phase and the α-phase are null, i.e. $d_{a\_ij}=0$ and $d_{\alpha\_ij}=0$. The piezoelectric strain coefficient of the β-phase d_{β_ij} is defined as:

$$d_{\beta\_ij}=e_{i1}C_{\beta\_1j}+e_{i2}C_{\beta\_2j}+e_{i3}C_{\beta\_3j}+e_{i4}C_{\beta\_4j}+e_{i5}C_{\beta\_5j}+e_{i6}C_{\beta\_6j} \quad \text{(VI.26)}$$

in which C_{β_ij} are the elastic constants obtained by molecular dynamics simulations and e_{β_imn} are the piezoelectric constants.

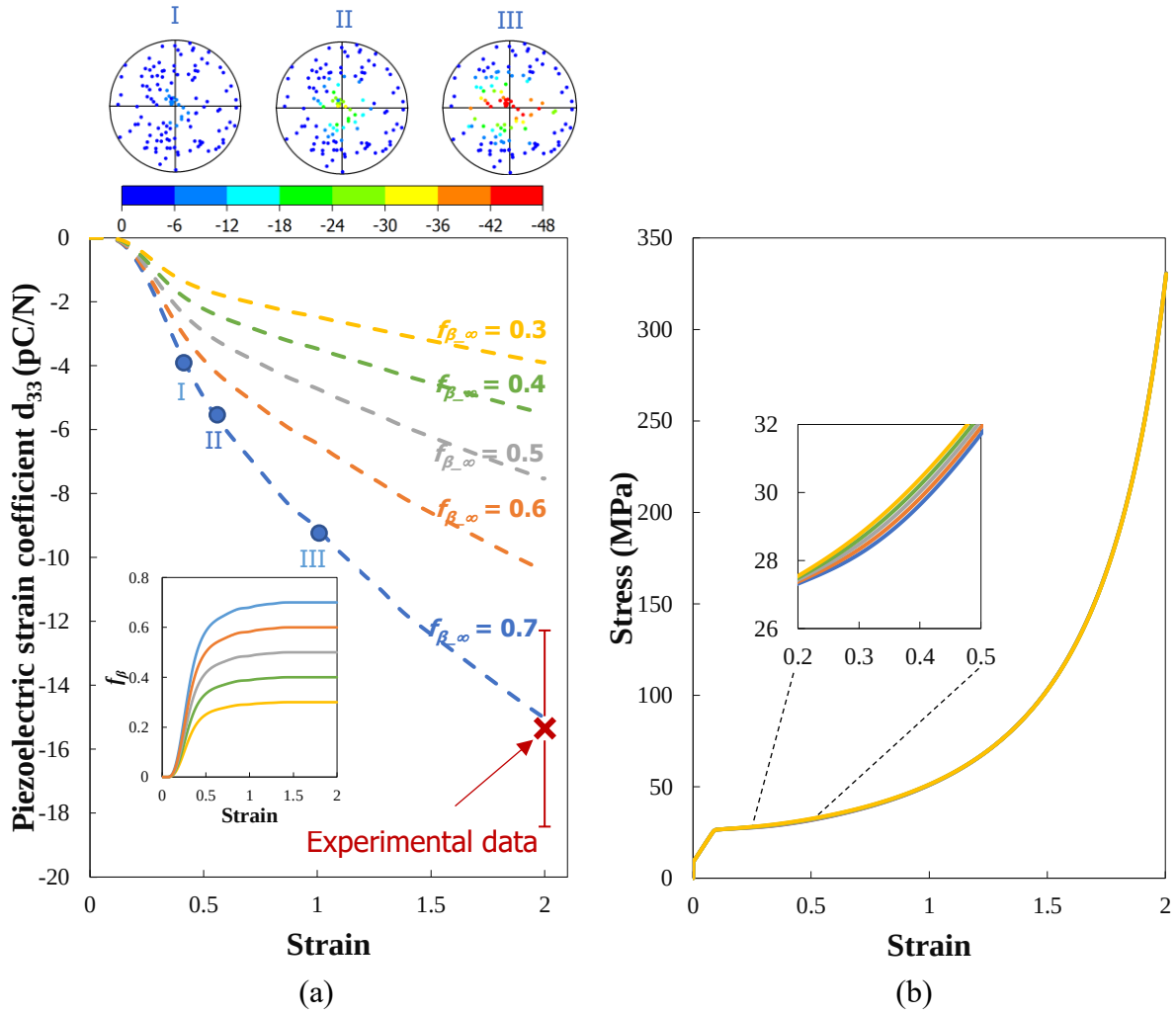

Fig. VI.11. Continuum-based simulation of the effect of the strain-induced evolution of the β-phase content on (a) room-temperature piezoelectric strain coefficient d_{33} and (b) mechanical response.

The overall piezoelectric strain coefficient d_{33} can be defined as an evolution function of the β-phase volume fraction and $d_{\beta\_33}=e_{31}C_{\beta\_13}+e_{32}C_{\beta\_23}+e_{33}C_{\beta\_33}$. The values of the piezoelectric constants are taken from the paper of Moleiro et al. (2015): e_{β_31}= -0.13 C/m^2, e_{β_32}=-0.14 C/m^2 and e_{β_33}=-0.28 C/m^2. The overall piezoelectric strain coefficient is plotted as a function of the applied strain in Fig. VI.11(a). The simulation consists to an isothermal straining at the temperature of 360 K up to a pre-determined strain level under a constant strain rate of 10^{-3} s^{-1} and to extract at this strain level the values of the electroelastic moduli at room temperature. As soon as the α → β phase transition begins, the piezoelectric strain coefficient increases with the increasing applied strain following a gradual rate decrease until a maximum strain level showing a good correlation with the experimental data of Defebvin et al. (2016) (see also

Defebvin, 2015). The internal values are strongly connected to the strain-induced anisotropy effects, as illustrated by the heterogeneous distribution in the predicted pole figures provided in Fig. VI.11(a). The evolution of the piezoelectric strain coefficient interacts closely with the micro-mechanism of α → β phase transition as highlighted by the effect of the maximum β-phase amount whereas slight effects are found on the overall mechanical response (Fig. VI.11(b)). This clarifies the relation between large-strain mesostructural properties and piezoelectric activity evolution. An illustrative example of the coupled electromechanical behavior is provided in Fig. VI.12(a). The simulations are performed under different applied electric fields while stretching-retraction sequences are applied at two pre-determined strain levels. Although only the β-phase is polarized, the internal stresses of the two other phases are also affected by the external electric loading as illustrated in Fig. VI.12(b) in reason of the mechanical coupling between the different phases.

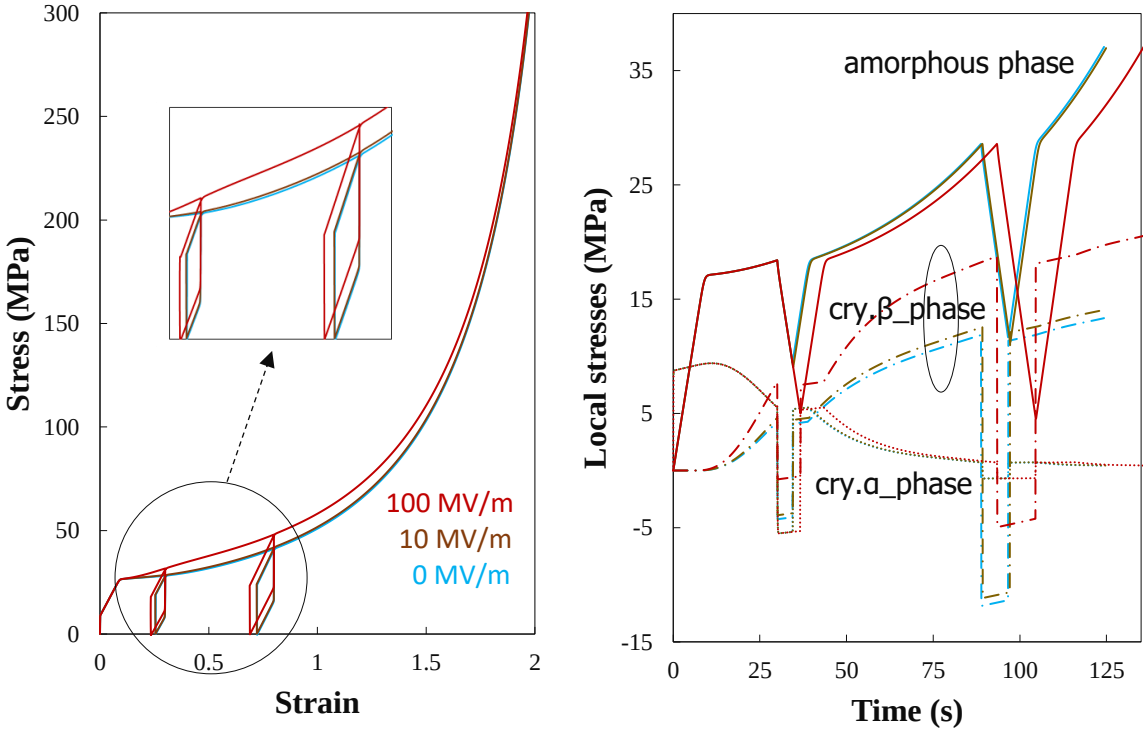

(a) (b)

Fig. VI.12. Continuum-based simulation of the coupled electromechanical behavior: (a) Stress as a function of strain and (b) internal stresses as a funtion of time.

VI.4. Conclusion

As concluding remarks, in this study, we have investigated the α → β phase transition in semi-crystalline PVDF within a hierarchical multi-scale analysis coupling molecular dynamics simulations in atomistic and microstructure-based modeling in a continuum term. We have

presented a continuum-based model formulated within a micromechanical framework to connect the PVDF elastic-viscoplastic-viscohyperelastic deformation behavior to the α → β phase transition caused by the straining. The identification of the developed micromechanics model was performed thanks to a rigorous deterministic scheme using relevant results issued from molecular dynamics simulations performed in this work and available experiments. Quantitative comparisons showed that the model was able to correctly capture the large-strain stress-strain response of a PVDF under uniaxial straining accounting for the strain-induced α → β phase transition. Besides, the model was used to clarify the influence of the microstructure evolution, in terms of α → β phase transition and internal ordering, on the piezoelectric activity.

The continuum-based model contains very few parameters and allows to better understand the relation between key PVDF microstructure features (strain-induced crystallographic texturing and α → β phase transition) and mechanical response. Although it appears as a valuable tool for the reliable design and optimization of multi-functional piezoelectric PVDF-based material media, a complete verification of the model capabilities under more complex mechanical loading conditions remains an important issue for further investigations.

Appendix VI.A. Supplementary information

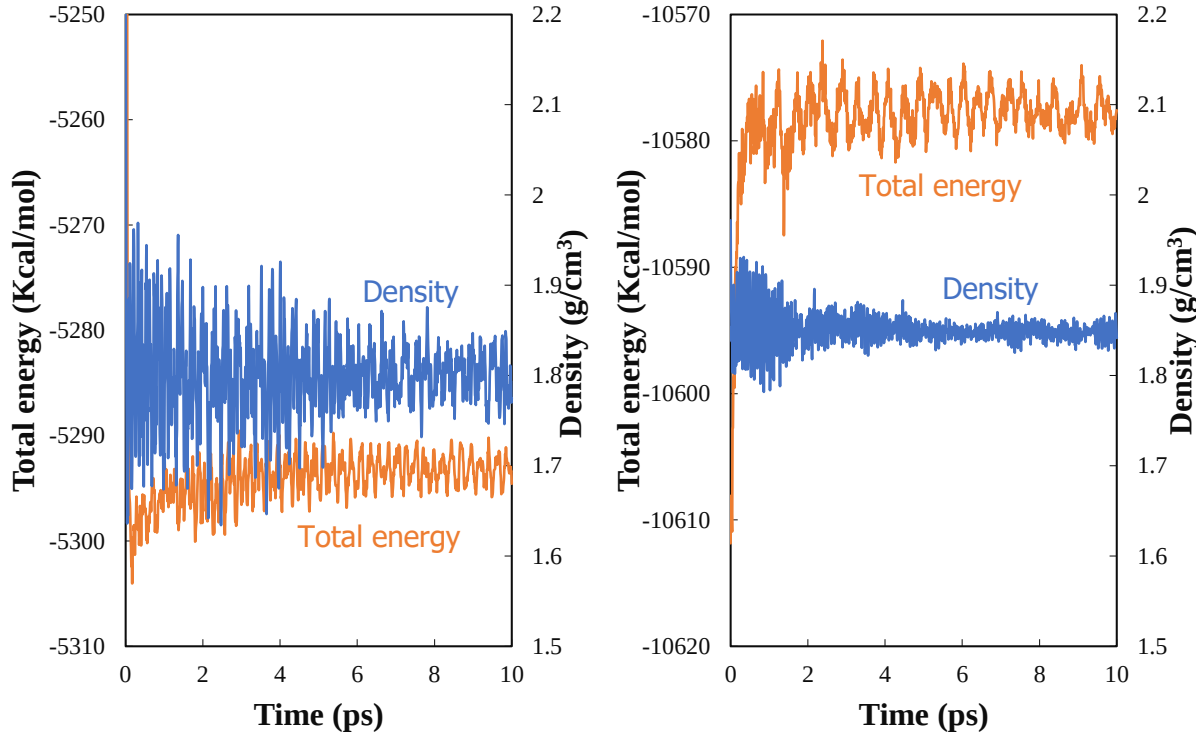

Fig. VI.A1. Total energy and density evolution during the equilibrium process for (a) α-PVDF and (b) β-PVDF.

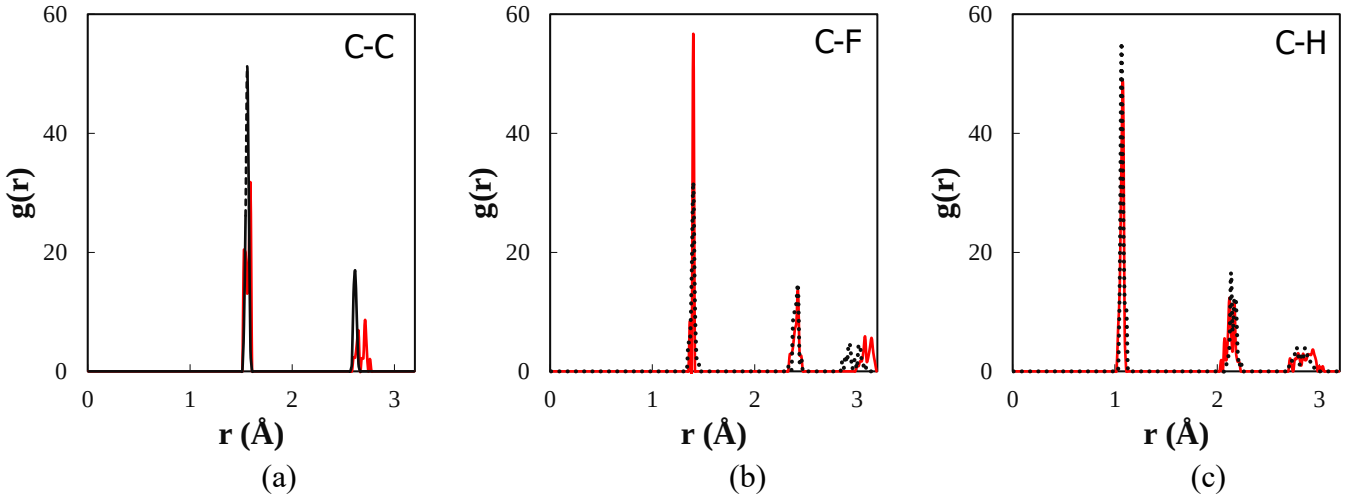

Fig. VI. A2. Partial radial distribution function for (a) C-C, (b) C-F, (c) C-H (red solid line: α-PVDF, black dashed line: β-PVDF). The first peak in each curve represents the bond length of the corresponding atomic pair; Mean bond of C-C is 1.553 Å for α-PVDF and 1.542 Å for β-PVDF; Mean bond of C-F is 1.39 Å for α-PVDF and 1.38 Å for β-PVDF; Mean bond of C-F is 1.08 Å for α-PVDF and 1.1 Å for β-PVDF.

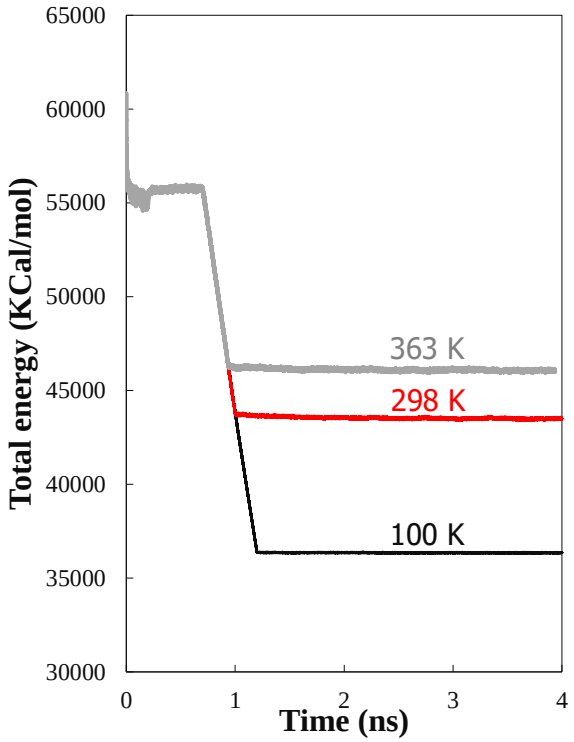

Fig. VI. A3. Total energy evolution during the equilibrium process for the amorphous PVDF at different temperatures.

References

Abdul-Hameed, H., Messager, T., Zaïri, F., Naït-Abdelaziz, M., 2014. Large-strain viscoelastic-viscoplastic constitutive modeling of semi-crystalline polymers and model identification by deterministic/evolutionary approach. Computational Materials Science 90, 241-252.

Agoras, M., Ponte Castaneda, P., 2012. Multi-scale homogenization-based modeling of semi-crystalline polymers. Philosophical Magazine 92, 925-958.

Ahzi, S., Makradi, A., Gregory, R.V., Edie, D.D., 2003. Modeling of deformation behavior and strain-induced crystallization in poly(ethylene terephthalate) above the glass transition temperature. Mechanics of Materials 35, 1139-1148.

Ameduri, B., 2009. From vinylidene fluoride (VDF) to the applications of VDF-containing polymers and copolymers: Recent developments and future trends. Chemical Reviews 109, 6632-6686.

Anoukou, K., Zaïri, F., Naït-Abdelaziz, M., Zaoui, A., Qu, Z., Gloaguen, J.M., Lefebvre, J.M., 2014. A micromechanical model taking into account the contribution of □- and □-crystalline phases in the stiffening of polyamide 6-clay nanocomposites: A closed-formulation including the crystal symmetry. Composites Part B 64, 84-96.

Argon, A.S., 1973. A theory for the low temperature plastic deformation of glassy polymers. Philosophical Magazine 28, 839-865.

Ayoub, G., Zaïri, F., Naït-Abdelaziz, M., Gloaguen, J.M., 2010. Modelling large deformation behaviour under loading-unloading of semicrystalline polymers: Application to a high density polyethylene. International Journal of Plasticity 26, 329-347.

Ayoub, G., Zaïri, F., Fréderix, C., Gloaguen, J.M., Naït-Abdelaziz, M., Seguela, R., Lefebvre, J.M., 2011. Effects of crystal content on the mechanical behaviour of polyethylene under finite strains: Experiments and constitutive modelling. International Journal of Plasticity 27, 492-511.

Baudet, C., Grandidier, J.-C., Cangémi, L., 2009. A two-phase model for the diffuso-mechanical behaviour of semicrystalline polymers in gaseous environment. International Journal of Solids and Structures 46, 1389-1401.

Bédoui, F., Diani, J., Régnier, G., Seiler, W., 2006. Micromechanical modelling of isotropic elastic behaviour of semicrystalline polymers. Acta Materialia 54, 1513-1523.

Bergstrom, J.S, Boyce, M.C., 1998. Constitutive modeling of the large strain time-dependent behavior of elastomers. Journal of the Mechanics and Physics of Solids 46, 931-954.

Bernard, C.A., Lame, O., Deplancke, T., Cavaillé, J.Y., Ogawa, K., 2020. From rheological to original three-dimensional mechanical modelling of semi-crystalline polymers: Application to a wide strain rate range and large deformation of Ultra-High Molecular Weight PolyEthylene. Mechanics of Materials 151, 103640.

Boyce, M.C., Socrate, S., Llana, P.G., 2000. Constitutive model for the finite deformation stress-strain behavior of poly(ethylene terephthalate) above the glass transition. Polymer 41, 2183-2201.

Challier, M., Besson, J., Laiarinandrasana, L., Piques, R., 2006. Damage and fracture of polyvinylidene fluoride (PVDF) at 20 °C: Experiments and modelling. Engineering Fracture Mechanics 73, 79-90.

Chang, J., Dommer, M., Chang, C., Lin, L., 2012. Piezoelectric nanofibers for energy scavenging applications. Nano Energy 1, 356-371.

Chen, K., Kang, G., Yu, C., Jiang, H., 2019. Effect of crystalline content on ratchetting of ultra-high molecular weight polyethylene polymers: Experimental investigation and constitutive model. Mechanics of Materials 133, 37-54.

Defebvin, J., 2015. Étude des relations structure-propriétés de matériaux hybrides piézoélectriques à base PVDF. PhD Thesis, Lille University.

Defebvin, J., Barrau, S., Stoclet, G., Rochas, C., Lefebvre, J.M., 2016. In situ SAXS/WAXS investigation of the structural evolution of poly(vinylidene fluoride) upon uniaxial stretching. Polymer 84, 148-157.

Deplancke, T., Fivel, M., Lame, O., 2019. 1D strain rate-dependent constitutive model of UHMWPE: From crystalline network to fibrillar structure behavior. Mechanics of Materials 137, 103129.

Doufas, A.K., McHugh, A.J., Miller, C., 2000. Simulation of melt spinning including flow-induced crystallization: Part I. Model development and predictions. Journal of Non-Newtonian Fluid Mechanics 92, 27-66.

Drozdov, A.D., 2010. Effect of temperature on the viscoelastic and viscoplastic behavior of polypropylene. Mechanics of Time-Dependent Materials 14, 411-434.

Drozdov, A.D., De Christiansen, J.C., 2011. Mullins' effect in semicrystalline polymers: Experiments and modeling. Meccanica 46, 359-370.

Drozdov, A.D., Klitkou, R., Christiansen, J.D., 2013. Multi-cycle deformation of semicrystalline polymers: Observations and constitutive modeling. Mechanics Research Communications 48, 70-75.

Dusunceli N., Colak, O.U., 2008. Modelling effects of degree of crystallinity on mechanical behavior of semicrystalline polymers. International Journal of Plasticity 24, 1224-1242.

Erdtman, E., Satyanarayana, K.C., Bolton, K., 2012. Simulation of α- and β-PVDF melting mechanisms. Polymer 53, 2919-2926.

Erol, A., Ahmed, S., Ounaies, Z., von Lockette, P., 2019. A microstructure-based approach to modeling electrostriction that accounts for variability in spatial locations of domains. Journal of the Mechanics and Physics of Solids 124, 35-62.

Garcia-Gonzalez, D., Garzon-Hernandez, S., Rusinek, A., Bernier, R., Arias, A., 2019. Low temperature mechanical behaviour of PVDF: Cryogenic pre-treatment, quasi-static, cyclic and dynamic experimental testing and modelling. Mechanics of Materials 147, 103436.

Gueguen, O., Ahzi, S., Makradi, A., Belouetta, S., 2010. A new three-phase model to estimate the effective elastic properties of semi-crystalline polymers: Application to PET. Mechanics of Materials 42, 1-10.

Guo, H., Zhang, Y., Xue, F., Cai, Z., Shang, Y., Li, J., Chen, Y., Wu, Z., Jiang, S., 2013. In-situ synchrotron SAXS and WAXS investigations on deformation and α-β transformation of uniaxial stretched poly(vinylidene fluoride). CrystEngComm 15, 1597-1606.

Guo, Q., Zaïri, F., 2020. A physically-based thermo-mechanical model for stretch-induced crystallizable rubbers: Crystallization thermodynamics and chain-network crystallization anisotropy. International Journal of Plasticity 131, 102724.

Gurtin, M.E., Anand, L., 2005. The decomposition F= Fe Fp, material symmetry, and plastic irrotationality for solids that are isotropic-viscoplastic or amorphous. International Journal of Plasticity 21, 1686-1719.

Hachour, K., Zaïri, F., Naït-Abdelaziz, M., Gloaguen, J.M., Aberkane, M., Lefebvre J.M., 2014. Experiments and modeling of high-crystalline polyethylene yielding under different stress states. International Journal of Plasticity 54, 1-18.

Hasegawa, R., Takahashi, Y., Chatani, Y., Tadokoro, H., 1972. Crystal structures of three crystalline forms of poly(vinylidene fluoride). Polymer Journal 3, 600-610.

Kang, Y., Zhou, D., Wu, Q., Duan, F., Yao, R., Cai, K., 2019. Fully atomistic molecular dynamics computation of physico-mechanical properties of PB, PS, and SBS. Nanomaterials 9, 1088.

Laiarinandrasana, L., Besson, J., Lafarge, M., Hochstetter, G., 2009. Temperature dependent mechanical behaviour of PVDF: Experiments and numerical modelling. International Journal of Plasticity 25, 1301-1324.

Laiarinandrasana, L., Morgeneyer, T.F., Proudhon, H., Regrain, C., 2010. Damage of semicrystalline polyamide 6 assessed by 3D X-ray tomography: From microstructural evolution to constitutive modeling. Journal of Polymer Science, Part B: Polymer Physics 48, 1516-1525.

Larive, C.K., Sweedler, J.V., 2013. Celebrating the 75th anniversary of the ACS division of analytical chemistry: A special collection of the most highly cited analytical chemistry papers published between 1938 and 2012. Analytical Chemistry 85, 4201-4202.

Lee, B.J., Parks, D.M., Ahzi, S., 1993a. Micromechanical modeling of large plastic deformation and texture evolution in semi-crystalline polymers. Journal of the Mechanics and Physics of Solids 41, 1651-1687.

Lee, B.J., Argon, A.S., Parks, D.M., Ahzi, S., Bartczak, Z., 1993b. Simulation of large strain plastic deformation and texture evolution in high density polyethylene. Polymer 34, 3555-3575.

Lee, E.H., 1969. Elastic-plastic deformation at finite strains. Journal of Applied Mechanics 36, 1-6.

Li, X., Murthy, N.S., Becker, M.L., Latour, R.A., 2016. Multiscale approach for the construction of equilibrated all-atom models of a poly(ethylene glycol)-based hydrogel. Biointerphases 11, 021002.

Li, Y., Ma, X., Ding, Y., Li, X., Li, Z., 2019. Density functional theory simulation of PVDF transition in electric field polarization. Advances in Computer Science Research 93, 21-25.

Mahjoubi, H., Zaïri, F., Tourki, Z., 2019. A micro-macro constitutive model for strain induced molecular ordering in biopolymers: Application to polylactide over a wide range of temperatures. International Journal of Plasticity 123, 38-55.

Mahjoubi, H., Zaïri, F., Tourki, Z., 2020. Strain-induced phase transformation in poly(lactic acid) across the glass transition: Constitutive model and identification. International Journal of Non-Linear Mechanics 118, 103241.

Makki, M., Ayoub, G., Abdul-Hameed, H., Zaïri, F., Mansoor, B., Naït-Abdelaziz, M., Ouederni, M., Zaïri, F., 2017. Mullins effect in polyethylene and its dependency on crystal content: A network alteration model. Journal of the Mechanical Behavior of Biomedical Materials 75, 442-454.

Makradi, A., Ahzi, S., Gregory, R.V., Edie, D.D., 2005. A two-phase self-consistent model for the deformation and phase transformation behavior of polymers above the glass transition temperature: application to PET. International Journal of Plasticity 21, 741-758.

Mamache, F.E., Mesbah, A., Bian, H., Zaïri, F., 2022. Micromechanical modeling of the biaxial behavior of strain-induced crystallizable polyethylene terephthalate-clay nanocomposites. Archive of Applied Mechanics, in press.

Mesbah, A., Elmeguenni, M., Yan, Z., Zaïri, F., Ding, N., Gloaguen, J.M., 2021. How stress triaxiality affects cavitation damage in high-density polyethylene: Experiments and constitutive modeling. Polymer Testing, 107248.

Mirkhalaf, M., van Dommelen, J.A.W., Govaert, L.E., Furmanski, J., Geers, M.G.D., 2019. Micromechanical modeling of anisotropic behavior of oriented semicrystalline polymers. Journal of Polymer Science, Part B: Polymer Physics 57, 378-391.

Moleiro, F., Mota Soares, C.M., Mota Soares, C.A., Reddy, J.N., 2015. Layerwise mixed models for analysis of multilayered piezoelectric composite plates using least-squares formulation. Composites Structures 119, 134-149.

Nalwa, H.S., 1995. Ferroelectric Polymers: Chemistry, Physics and Applications. Marcel Dekker, New York.

Nikolov, S., Doghri, I., 2000. A micro/macro constitutive model for the small-deformation behavior of polyethylene. Polymer 41, 1883-1891.

Nikolov, S., Doghri, I., Pierard, O., Zealouk, L., Goldberg, A., 2002. Multi-scale constitutive modeling of the small deformations of semi-crystalline polymers. Journal of the Mechanics and Physics of Solids 50, 2275-2302.

Odegard, G.M., 2004. Constitutive modeling of piezoelectric polymer composites. Acta Materialia 52, 5315-5330.

Okereke, M.I., Akpoyomare, A.I., 2019. Two-process constitutive model for semicrystalline polymers across a wide range of strain rates. Polymer 183, 121818.

Osaka, N., Yanagi, K., Saito, H., 2013. The optical transparency and structural change of quenched poly(vinylidene fluoride) caused by cold-drawing. Polymer Journal 45, 1033-1040.

Payal, R.S., Fujimoto, K., Jang, C., Shinoda, W., Takei, Y., Shima, H., Tsunoda, K., Okazaki, S., 2019. Molecular mechanism of material deformation and failure in butadiene rubber: Insight from all-atom molecular dynamics simulation using a bond breaking potential model. Polymer 170, 113-119.

Pei, Y., Zeng, X.C., 2011. Elastic properties of poly(vinyldene fluoride) (PVDF) crystals: A density functional theory study. Journal of Applied Physics 109, 093514.

Poluektov, M., van Dommelen, J.A.W., Govaert, L.E., Yakimets, I., Geers, M.G.D., 2013. Micromechanical modelling of short-term and long-term large-strain behaviour of polyethylene terephthalate. Modelling and Simulation in Materials Science and Engineering 21, 085015.

Popa, C.M., Fleischhauer, R., Schneider, K., Kaliske, M., 2014. Formulation and implementation of a constitutive model for semicrystalline polymers. International Journal of Plasticity 61, 128-156.

Qi, Z., Hu, N., Li, G., Zeng, D., 2019. Constitutive modeling for the elastic-viscoplastic behavior of high density polyethylene under cyclic loading. International Journal of Plasticity 113, 125-144.

Sahihi, M., Jaramillo-Botero, A., Goddard III, W.A., Bedoui, F., 2021. Interfacial interactions in a model composite material: Insights into α → β phase transition of the magnetite reinforced poly(vinylidene fluoride) systems by all-atom molecular dynamics simulation. The Journal of Physical Chemistry C 125, 21635-21644.

Satouri, S., Chatzigeorgiou, G., Benaarbia, A., Meraghni, F., 2022. A gradient enhanced constitutive framework for the investigation of ductile damage localization within semicrystalline polymers. International Journal of Damage Mechanics, in press.

Satyanarayana, K.C., Bolton, K., 2012. Molecular dynamics simulations of α- to β-poly(vinylidene fluoride) phase change by stretching and poling. Polymer 53, 2927-2934.

Sedighiamiri, A., Govaert, L.E., van Dommelen, J.A.W., 2011. Micromechanical modeling of the deformation kinetics of semicrystalline polymers. Journal of Polymer Science, Part B: Polymer Physics 49, 1297-1310.

Sepiani, H., Polak, M.A., Penlidis, A., 2018. Modeling short- and long-term time-dependent nonlinear behavior of polyethylene. Mechanics of Advanced Materials and Structures 25, 600-610.

Sharma, M., Madras, G., Bose, S., 2014. Process induced electroactive β-polymorph in PVDF: Effect on dielectric and ferroelectric properties. Physical Chemistry Chemical Physics 16, 14792-14799.

Sharma, P., Roy, S., 2020. Glass transition temperature of polybutadiene and polyisoprene from high temperature segmental relaxation correlation using molecular dynamics. Soft Materials 18, 290-296.

Sun, H., Mumby, S.J., Maple, J.R., Hagler, A.T., 1994. An ab initio CFF93 all-atom force field for polycarbonates. Journal of the American Chemical Society 116, 2978-2987.

Uchida, M., Tada, N., 2013. Micro-, meso- to macroscopic modeling of deformation behavior of semi-crystalline polymer. International Journal of Plasticity 49, 164-184.

van Dommelen, J.A.W., Parks, D.M., Boyce, M.C., Brekelmans, W.A.M., Baaijens, F.P.T., 2003. Micromechanical modeling of the elasto-viscoplastic behavior of semi-crystalline polymers. Journal of the Mechanics and Physics of Solids 51, 519-541.

Wang, Z.Y., Fan, H.Q., Su, K.H., Wen, Z.Y., 2006. Structure and piezoelectric properties of poly(vinylidene fluoride) studied by density functional theory. Polymer 47, 7988-7996.

Wang, H., Liu, H., Ding, Z., Li, N., 2021. Experimental and constitutive modelling studies of semicrystalline thermoplastics under solid-state stamp forming conditions. Polymer 228,123939.

Ward, I., Sweeney, J., 2004. An introduction to the mechanical properties of solid polymers. 2nd Edition, Wiley.

Yan, Z., Guo, Q., Zaïri, F., Zaoui, A., Jiang, Q., Liu, X., 2021. Continuum-based modeling large-strain plastic deformation of semi-crystalline polyethylene systems: Implication of texturing and amorphicity. Mechanics of Materials 162, 104060.

Yazdani, H., Ghasemi, H., Wallace, C., Hatami, K., 2018. Mechanical properties of carbon nanotube-filled polyethylene composites: A molecular dynamics simulation study. Polymer Composites 40, 1850-1861.

Ye, H.J., Yang, L., Shao, W.Z., Sun, S.B., Zhen, L., 2013. Effect of electroactive phase transformation on electron structure and dielectric properties of uniaxial stretching poly(vinylidene fluoride) films. RSC Advances 3, 23730-23736.

Zhang, Z., Wang, Y., Liu, P., Chen, T., Hou, G., Xu, L., Wang, X., Hu, Z., Liu, J., Zhang, L., 2021. Quantitatively predicting the mechanical behavior of elastomers via fully atomistic molecular dynamics simulation. Polymer 223, 123704.

Zhu, G.D., Zhang, J.H., Luo, X.Y., Yan, X.J., 2009. Microscopic characterization of polarization fatigue in ferroelectric vinylidene fluoride and trifluoroethylene copolymer films. Organic Electronics 10, 753-760.

Chapter VII

Kroon Network Theory Verification for Rubber Biaxial Mechanics via A Multi-scale Modeling

Chapter VII. Kroon network theory verification for rubber biaxial mechanics via a multi-scale modeling[15]

Abstract

In this chapter, we address the problem of the multiscale prediction of the multiaxial hyperelastic behavior of rubbers. We attempt to verify the predictive abilities of a hyperelastic constitutive model based on the theoretical framework of continuum mechanics while connecting the continuum-level mechanics to the molecular-level description. In the constitutive model, the behavior at a macroscopic level is the consequence of the non-affine deformation of the molecular network and the topological constraint effects. Molecular dynamics method is used to quantify the mechanical behavior of a rubber network structure for different modes of deformation. The energy contribution during the straining process was analyzed to further highlight the underlying deformation mechanisms at the molecular level. After analyzing how the total network stress of the designed molecular structure is governed by the biaxial strain ratio, the capacities of the hyperelastic constitutive model are evaluated.

Keywords: Rubber network; Biaxial deformation; Multiscale approach; Molecular dynamics; Continuum mechanics.

[15] This chapter is based on the following paper: Yan, Z., Zaïri, F., Zaoui, A.. Kroon network theory verification for rubber biaxial mechanics via a multi-scale modeling. Under review.

VII.1. Introduction

A reliable design of rubber systems can only be achieved by proposing accurate structure-mechanics relationships accounting for the multiaxial character of the mechanical loading. The prediction problem of the mechanical behavior for this class of materials may be approached using two ways of investigation, namely, molecular dynamics and continuum-based modeling. Molecular dynamics is a very interesting tool to analyze and predict the mechanics of polymers under biaxial monotonic loading. Indeed, if constitutive modeling has attracted attention of many researchers, connecting the molecular-level description to the continuum-level mechanics under monotonic and multiaxial loading is less documented (Uddin and Ju, 2016, 2017; Chaube et al., 2019; Chen et al., 2021; Yuan et al., 2022).

The hyperelastic model proposed by Arruda and Boyce (1993) constitutively represents the rubber network by eight long-chain molecules. This so-called eight-chain model has found many applications. It was for example combined to viscous and plastic components to describe the inelastic features of a wide range of polymer systems such as unfilled rubbers and filled rubbers, amorphous and semi-crystalline thermoplastics; the reader may refer to the literature background in the following references (Yan et al., 2021, 2022). Although the eight-chain model has several advantages, especially a flexible and explicit formulation, its main weakness relies in its incapacities to predict rubber biaxial mechanics (Boyce and Arruda, 2000). Indeed, several studies showed that models based solely on the first strain invariant have poor multiaxial predictive capacities whatever the mathematical expression (Horgan and Saccomandi, 1999; Wineman, A., 2005; Horgan, C.O., Smayda, M.G., 2012; Puglisi and Saccomandi, 2016; Destrade et al., 2017), the presence of the second strain invariant appearing as necessary. Several extensions of the eight-chain model were proposed in order to enhance its predictive capacities under biaxial loading (Boyce and Arruda, 2000; Meissner and Matejka, 2003, 2004; Miroshnychenko and Green, 2009; Bechir et al., 2010; Kroon, M., 2011; Dal et al., 2020; Anssari-Benam and Bucchi, 2021). Among these extensions, Kroon (2011) proposed modifications using a reasoning from the micromechanics of the chain molecules by considering the chain deforms non-affinely while the interactions with neighboring chains are accounted for through the adding of the topological constraint effects imposed on the lateral motions. The Kroon model contains three supplementary parameters.

Our purpose in this chapter is to examine the validity of the Kroon network theory by connecting the continuum-level mechanics to the molecular-level description. The latter

description is carried out by means of molecular dynamics simulations on a rubber network structure treated as a collection of chains using the coarse-grained molecular model and deformed under different biaxial strain ratios. The constants of the Kroon continuum-based model are identified on the basis of molecular dynamics data under tensile deformation as illustrated in Fig. VII.1. The predictive ability is then critically discussed for different biaxial strain ratios.The chapter is organized as follows. Section VII.2 introduces details on the continuum-based model. The molecular dynamics details are presented in Section VII.3. Results and discussion are given in Section VII.4. In Section VII.5, concluding remarks are provided.

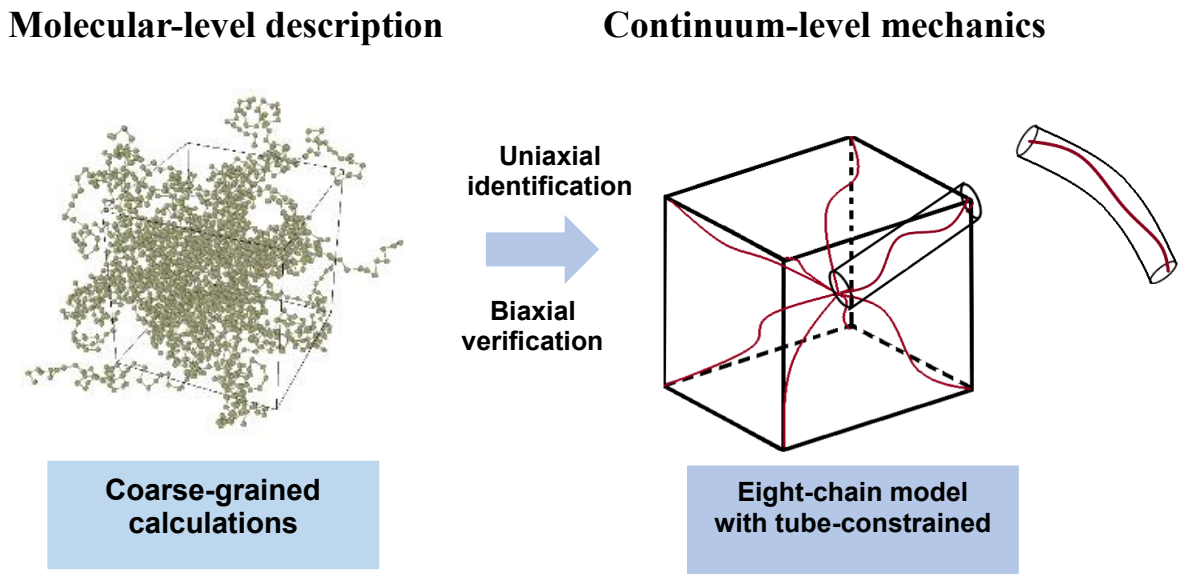

Fig. VII.1. Multiscale modeling rubber network connecting the molecular-level description and the continuum-level mechanics using a rubber network theory adapted from Kroon (2011) including non-affine deformation of the molecular network and topological constraint effects.

VII.2. Kroon model for rubber biaxial mechanics

In the continuum mechanics context, the deformation gradient $\mathbf{F}=\partial \boldsymbol{x}/\partial \boldsymbol{X}$ describes the transformation of a material point of the continuum medium from the initial position $\boldsymbol{X}$ to the current position $\boldsymbol{x}$. The Jacobian of the transformation is noted $J=\det(\mathbf{F})>0$. The stretch invariants of the right Cauchy-Green deformation $\mathbf{C}=\mathbf{F}^T\mathbf{F}$ are:

$$I_1=\mathrm{trace}(\mathbf{C}),\ I_2=\left(\mathrm{trace}(\mathbf{C})^2-\mathrm{trace}(\mathbf{C}^2)\right)/2 \text{ and } I_3=\det(\mathbf{C})=J^2 \qquad \text{(VII.1)}$$

The stress state is obtained from the differentiation of strain energy with respect to deformation. The Kroon strain energy can be expressed at the macro-scale as a function of the three stretch invariants:

$$\Psi = c_c n\left(\frac{\lambda_c}{\sqrt{n}}\beta + \ln\frac{\beta}{\sinh\beta}\right) + c_{nc}\left(\lambda_{nc}^2 - 1\right)^{\alpha} + c_{con} n\nu - p(J-1) \tag{VII.2}$$

with

$$\nu = I_3^{-1}\left(I_2/3\right)^{1/2} \text{ and } \lambda_m = \left(I_1/3\right)^{1/2} \tag{VII.3}$$

The term β is defined by the Langevin function:

$$\coth\beta - \frac{1}{\beta} = \frac{\lambda_c}{\sqrt{n}} \tag{VII.4}$$

The constrained and non-constrained stretches λ_c and λ_{nc} are related to the macroscopic stretch λ_m via a multiplicative decomposition:

$$\lambda_m = \lambda_c \lambda_{nc} \tag{VII.5}$$

The first term in Eq. (VII.2) describes the molecular network stretching process while the last term corresponds to the volumetric part in which p is the Lagrange multiplier. The two other terms were added by Kroon (2011). The power-law term originates from the consideration of the non-affine polymer chain deformation and the third term introduces the I_2-dependence coming from the tube-constraints. The model contains five material constants to be identified: n, c_c, c_{nc}, α and c_{con}. The three last material constants are the supplementary ones compared to the original Arruda-Boyce eight-chain strain energy (Arruda and Boyce, 1993). In the limit case $c_{nc} \to \infty$, $\alpha > 1$ and $c_{con} = 0$, the interactions between polymer chains are ignored and the Kroon strain energy becomes the original Arruda-Boyce form based on an affine description of the deformation. Moreover, it degenerates to the more classical Neo-Hookean model for extremely long-chain molecules, i.e. $n \to \infty$. A fully affine deformation is obtained when $\lambda_{nc} = 1$, otherwise it is an unknown in Eq. (VII.2) and can be determined via a Newton method from the following condition:

$$\left.\frac{\partial\Psi\left(\lambda_m, \lambda_{nc}, \nu\right)}{\partial\lambda_{nc}}\right|_{\lambda_{m,\nu}} = -c_c\sqrt{n}\beta\frac{\lambda_m}{\lambda_{nc}^2} + 2c_{nc}\alpha\left(\lambda_{nc}^2 - 1\right)^{\alpha-1} = 0 \tag{VII.6}$$

The deformation gradient tensor $\mathbf{F}$ can be written on the form of the principal directions:

$$\mathbf{F} = \lambda_1\mathbf{e}_1 \otimes \mathbf{e}_1 + \lambda_2\mathbf{e}_2 \otimes \mathbf{e}_2 + \lambda_3\mathbf{e}_3 \otimes \mathbf{e}_3 \tag{VII.7}$$

in which $\mathbf{e}_i$ denote basis vectors in a Cartesian coordinate system.

Generally, to simplify the calculation, material incompressibility is assumed (i.e. $I_3 = J^2 = 1$) and the deformation gradient tensor $\mathbf{F}$ may take the following form:

$$\mathbf{F} = \lambda \mathbf{e}_1 \otimes \mathbf{e}_1 + \lambda^n \mathbf{e}_2 \otimes \mathbf{e}_2 + \lambda^{-(n+1)} \mathbf{e}_3 \otimes \mathbf{e}_3 \quad \text{(VII.8)}$$

where λ is the applied stretch and $n \in [-0.5, 1.0]$ is a biaxiality exponent varying from -0.5 for uniaxial tension to 1.0 for equibiaxial tension.

VII.3. Molecular dynamics simulations

VII.3.1. Construction of model systems

The rubber network structure is treated as a collection of chains using the coarse-grained model considering each methyl group (i.e. the C_5H_8 monomer, Fig. VII.2(a)) as single beads with a force field that determines the interactions between beads. A single polymer chain consists of beads connected by potential energy determined as the sum of energies for bonded and non-bonded interactions:

$$U_{total} = U_{bonded} + U_{non\text{-}bonded} \quad \text{(VII.9)}$$

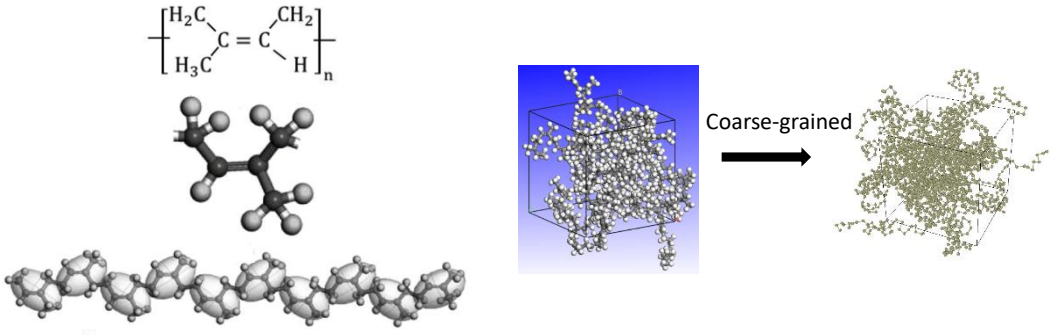

(a) (b)

Fig. VII.2. Construction of molecular-level model systems: (a) Chemical structure (monomers) and (b) a full-atomic model and coarse-grained model.

The term U_{bonded} includes specific stretching and bending terms to describe 1-2 and 1-3 interactions, respectively:

$$U_{bonded} = U_{bond}(r) + U_{angle}(\theta) \quad \text{(VII.10)}$$

in which the bond and angle potentials are given by:

$$U_{bond} = K_b (r - r_0)^2 \text{ and } U_{angle} = K_\theta (\theta - \theta_0)^2 \quad \text{(VII.11)}$$

where K_b and K_θ are spring constants for bond stretching and angular motion and, r_0 and θ_0 are the equilibrium bond length and angle, respectively.

The non-bonded (van der Walls) interactions are approximated by a Lennard-Jones-12-6 potential:

$$U_{non\text{-}bonded} = 4\varepsilon\left[\left(\frac{\sigma}{r}\right)^{12} - \left(\frac{\sigma}{r}\right)^{6}\right] \quad \text{(VII.12)}$$

where ε is the depth of potential well, σ is the finite distance at which the inter-particle potential is zero, and r is the distance between the particles for Lennard-Jones potentials. The parameter of these interactions are described in Table VII.1.

Table VII.1. Potential parameters used for coarse-grained calculations.

Interaction	Parameters
Bond Length	$K_b = 3.2\,\text{kcal/mol}/A^2, r_0 = 4.6\text{Å}$
Bond Angle	$K_\theta = 1.53\,\text{kcal/mol/rad}^2, \theta_0 = 121.5°$
Non-bonded	$\sigma = 4.89\text{Å}, \varepsilon = 0.38\,\text{kcal/mol}$

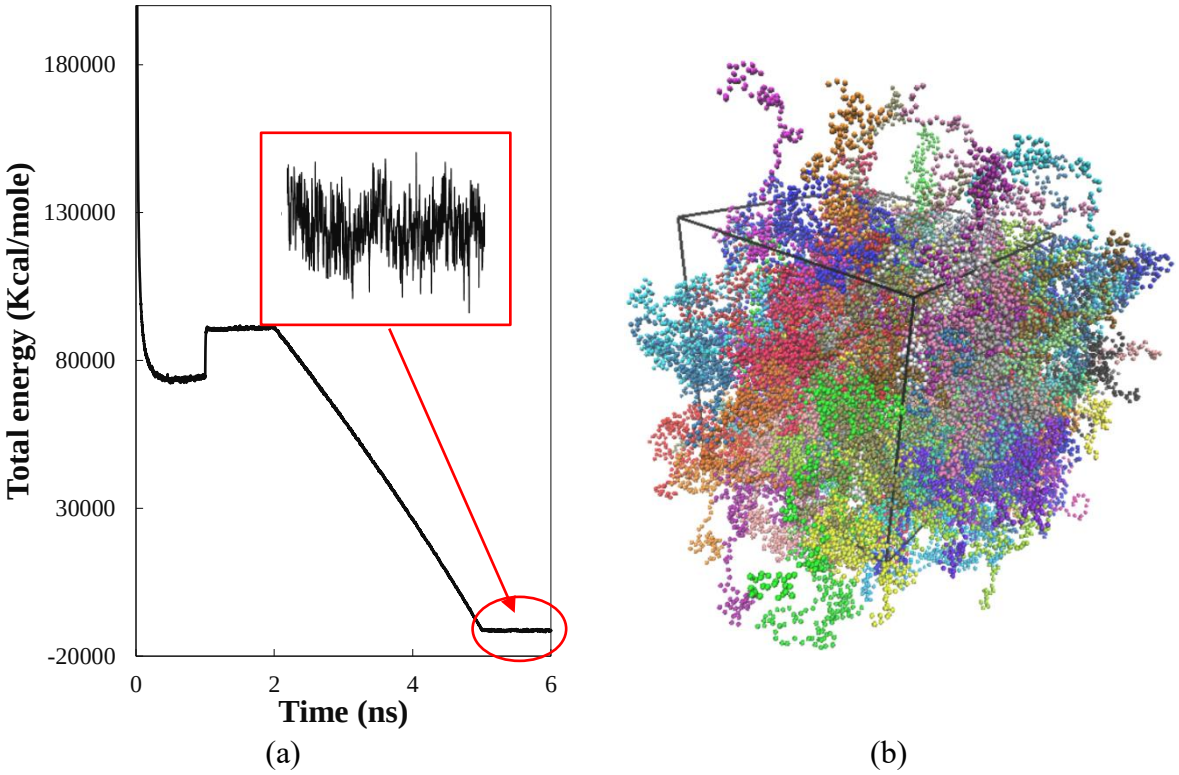

Fig. VII.3. Relaxation of the molecular structure: (a) Total energy evolution during the equilibrium process and (b) screenshot of equilibrated structure in VMD.

The model consists of 120 chains with a long chain length of 400 beads (48000 beads in total) to simulate the entangled chain structure (Fig. VII.2(b)). The relaxation of the molecular structure involves four different steps. Initially, the simulation ran for 10^6 timesteps (Δt = 1 fs) using NVT (constant number of atoms, volume, and temperature) dynamics at 600 K followed by relaxation for different timesteps (Δt = 1 fs) for getting enough relax structures at 600 K. The next relaxation relaxes the new molecular structure at 600 K, NPT (constant number of

atoms, pressure, and temperature) ensembles for 2×10^6 timesteps ($\Delta t = 1$ fs). The structure was then cooled to 298 K and followed by another equilibrium step at 298 K with NPT. The energy evolution during the whole process is displayed in Fig. VII.3(a). In last equilibrium step, the energy has reach the equilibrium state. A screenshot of equilibrated structure in VMD is provided in Fig. VII.3(b). The total response of the network is trivially dependent on the response of the individual chains experiencing different extent of deformation. To illustrate this feature, the probability distribution of the end-to-end distance of the whole system and the end-to-end distance of each chain extracted using the script in VMD are shown in Fig. VII.4. The shortest end to end distance is 13.718 Å and the longest distance is 222 Å. Since the equilibrium bond length is 5.3 Å and each chain contains 400 beads, the chain is 2114.7 Å when fully elongated, and if the equilibrium angle is considered to be 121°, the complete orientation length when the single chain is equilibrated is 1151.8 Å.

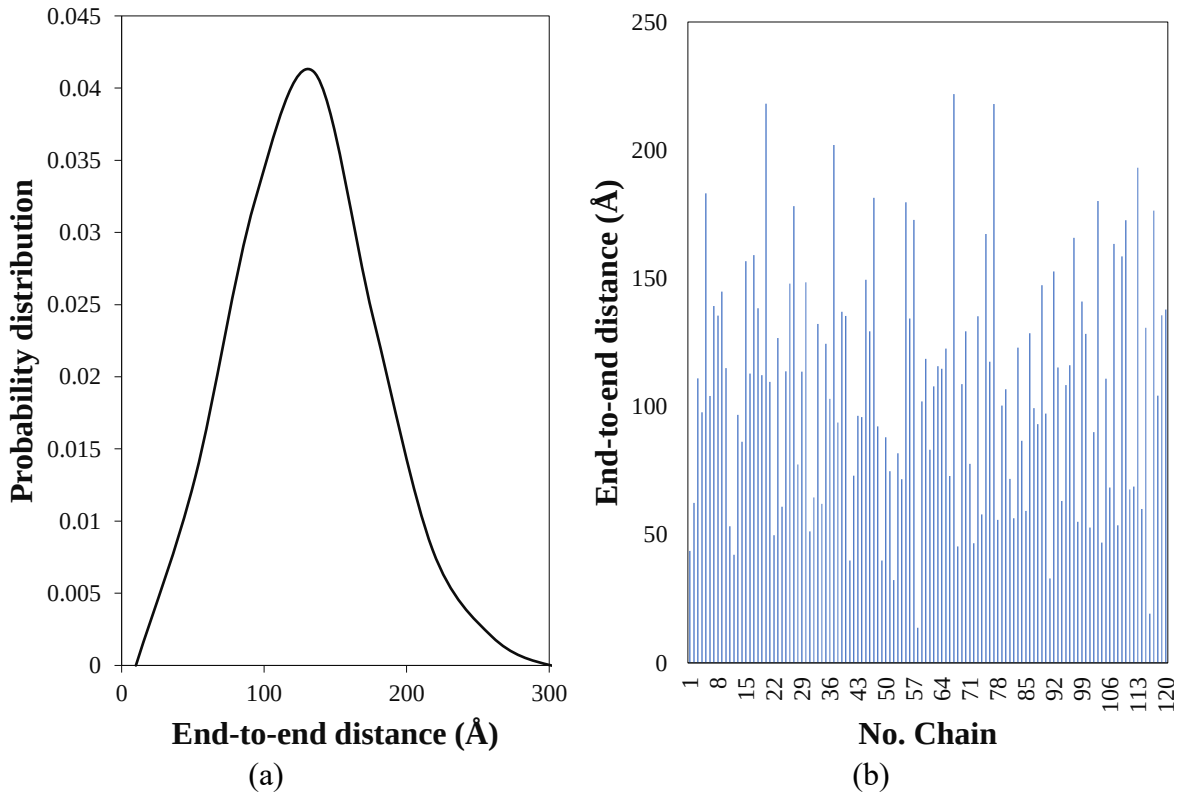

Fig. VII.4. Molecular-level chain response: (a) Probability distribution of end-to-end distance of the whole system and (b) end-to-end distance for individual chains.

VII.3.2. Mechanical response

The model system was then deformed under a uniaxial tensile loading at a constant strain rate of 10^{10} s^{-1}. This deformation condition was implemented in LAMMPS by decoupling the boundary in the loading direction from the NPT equations of motion.

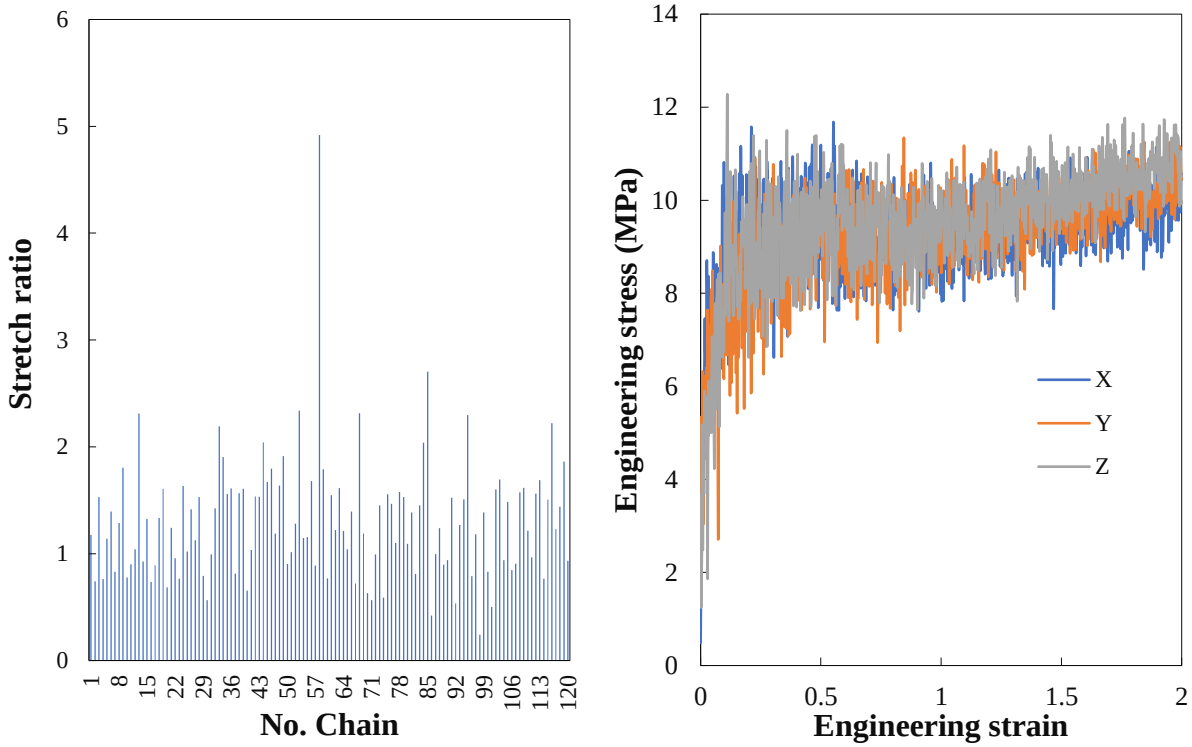

Fig. VII.5. Local and global responses of the molecular model under uniaxial stretching: (a) Stretch ratio of individual chains at a stretch ratio of 1 and (b) stress-strain curves along the three main directions.

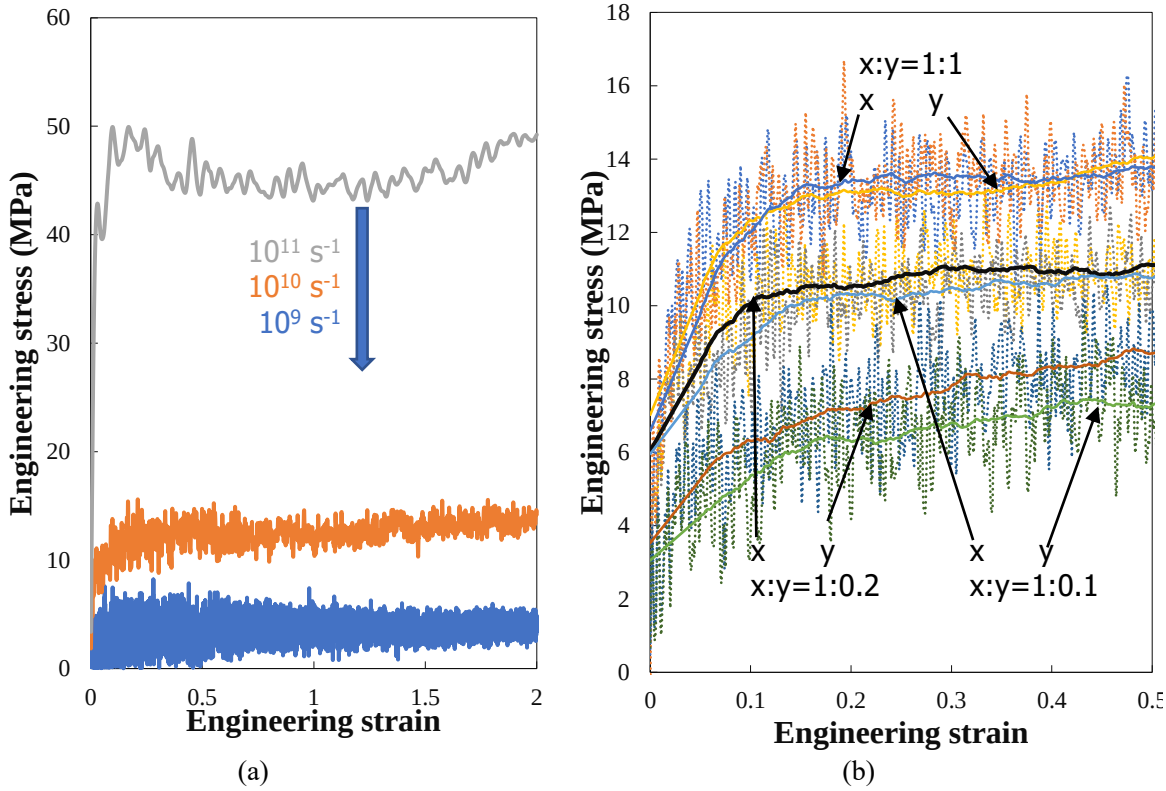

Fig. VII.6. Overall response of the molecular structure: (a) Uniaxial stress-strain curves at different strain rates and (b) biaxial stress-strain response at different biaxial strain ratios.

The stretch contribution of each individual chain defined as the ratio of end-to-end vectors after and before deformation is plotted in Fig. VII.5(a). Fig. VII.5(b) presents stress-strain curves in the three main directions. It can be observed that the material response exhibits no preferential direction. The rate-dependency of the uniaxial stress-strain response is illustrated in Fig. VII.6(a) by considering three decades of strain rates of 10^9 s^{-1}, 10^{10} s^{-1} and 10^{11} s^{-1}. The material response exhibits a clear rate dependence. The overall response of the network is dependent on the loading path since the chains experience different extent of deformation. The system was biaxially stretch at different strain ratios 1:1, 1:0.2 and 1:0.1 at a strain rate of 10^{10} s^{-1} and the results are reported in Fig. VII.6(b).

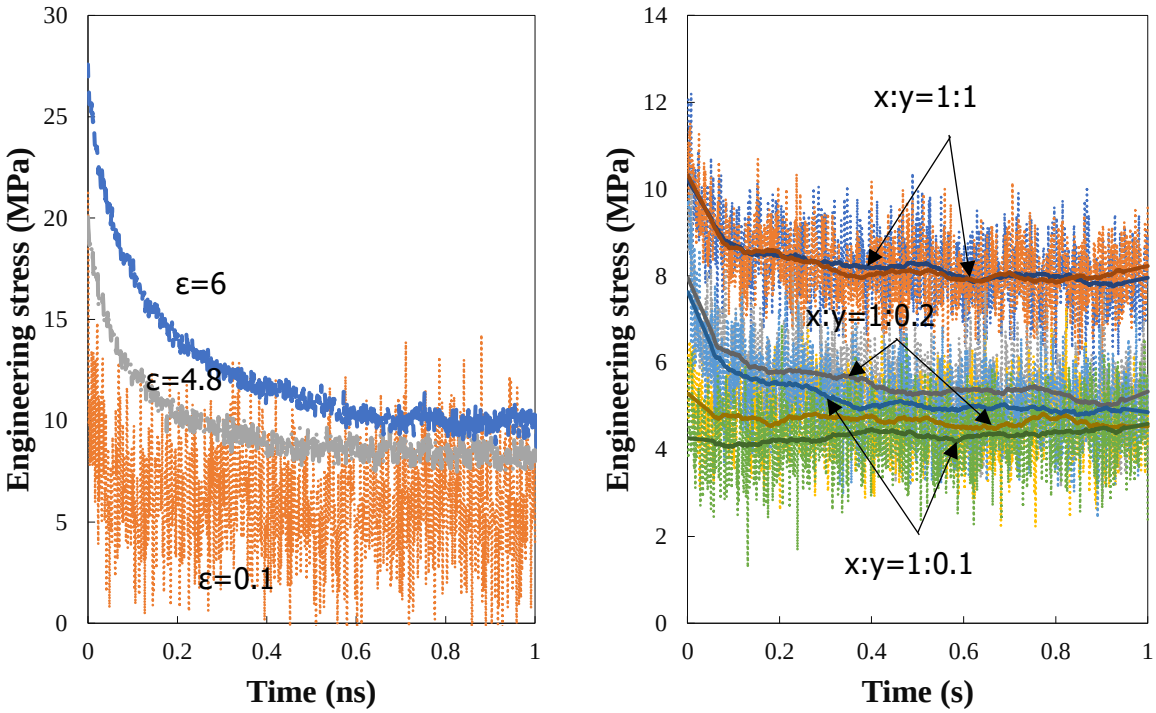

(a) (b)

Fig. VII.7. Stress relaxation after (a) uniaxial stretching at different strain levels and (b) biaxial stretching at different biaxial strain ratios.

In order to identify the equilibrium response of the molecular model, the boxes were maintained in the deformed state for different prescribed strain levels in order to provoke the stress relaxation. A sufficient holding time was used to reach the stabilized relaxed-response. At each relaxation, all information about the extended polymer in the box were recorded such as velocity, position and virial stress of every atom. The uniaxial relaxed-stress is plotted in Fig. VII.7(a). The relaxed-stress was quantified for different biaxial strain ratios and the results are reported in Fig. VII.7(b).

VII.4. Kroon model predictions

Our purpose now is to examine the validity of the Kroon model discussed above to predict the biaxial behavior. The model parameters were calibrated using the uniaxial response. Fig. VII.8(a) presents the comparison between the simulated curve of the continuum-based modeling and the molecular dynamics data. Fig. VII.8(b) allows to appreciate the predictive capacities of the continuum-based modeling. The Kroon model is in relatively acceptable agreement with the collected molecular dynamics data during biaxial loading, especially by comparing with the Arruda-Boyce model. That can be understood as a better description of the deformation mechanisms provided by the Kroon model.

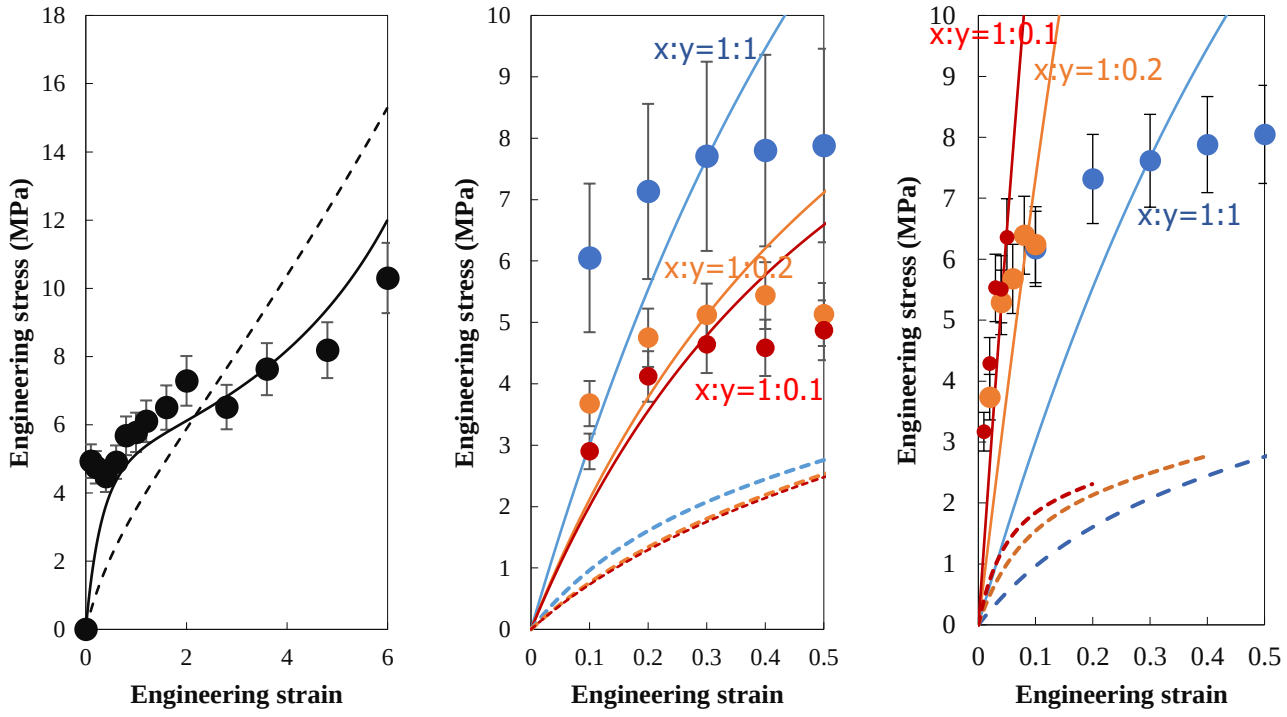

Fig. VII.8. Molecular dynamics data vs. continuum-based model: (a) Uniaxial stress-strain response, (b) biaxial stress-strain curve in x-direction, (c) biaxial stress-strain curve in y-direction for different biaxial strain ratios; Symbols with standard deviation: dynamics molecular data, Solid lines: Kroon continuum-based model (n=13, c_c=2.2, c_{nc}=0.15, α=8 and c_{con}=1), Dashed lines: Arruda-Boyce continuum-based model (n =13, c_c=2, $c_{nc}\rightarrow\infty$, α =2.2 and c_{con}=0).

VII.5. Conclusion

A series of model systems were constructed by molecular dynamics simulation method. The relaxed-stress was quantified under different biaxial strain ratios. Checking the validity of the Kroon model for the model system, we have found that it gives good estimates of the behavior

for different biaxial loading paths. Nonetheless, the molecular dynamics data requires a deepener analysis by extending the variety of model systems for pure elastomers (i.e. no additive fillers) as well as filled elastomeric systems.

References

Anssari-Benam, A., Bucchi, A., 2021. A generalised neo-Hookean strain energy function for application to the finite deformation of elastomers. International Journal of Non-Linear Mechanics, 103626.

Arruda, E.M., Boyce, M.C., 1993. A three-dimensional constitutive model for the large stretch behavior of rubber elastic materials. Journal of the Mechanics and Physics of Solids 41, 389-412.

Bechir, H., Chevalier, L., Idjeri, M., 2010. A three-dimensional network model for rubber elasticity: The effect of local entanglements constraints. International Journal of Engineering Science 48, 265-274.

Boyce, M.C., Arruda, E.M., 2000. Constitutive models of rubber elasticity: A review. Rubber Chemistry and Technology 73, 504-523.

Chaube, S., Mishra, S., Maiti, S., Rai, B., 2019. Multiscale analysis of large-strain deformation behaviour of random cross-linked elastomers. Molecular Simulation 45, 111-119.

Chen, G., Xian, W., Wang, Q., Li, Y. 2021. Molecular simulation-guided and physics-informed mechanistic modeling of multifunctional polymers. Acta Mechanica Sinica 37, 725-745.

Dal, H., Gültekin, O., Açıkgöz, K., 2020. An extended eight-chain model for hyperelastic and finite viscoelastic response of rubberlike materials: Theory, experiments and numerical aspects. Journal of the Mechanics and Physics of Solids 145, 104159.

Destrade, M., Saccomandi, G., Sgura, I., 2017. Methodical fitting for mathematical models of rubber-like materials. Proceedings of the Royal Society A: Mathematical, Physical and Engineering Sciences 473, 20160811.

Horgan, C.O., Saccomandi, G., 1999. Simple torsion of isotropic, hyperelastic, incompressible materials with limiting chain extensibility. Journal of Elasticity 56, 159-170.

Horgan, C.O., Smayda, M.G., 2012. The importance of the second strain invariant in the constitutive modeling of elastomers and soft biomaterials. Mechanics of Materials 51, 43-52.

Kroon, M., 2011. An 8-chain model for rubber-like materials accounting for non-affine chain deformations and topological constraints. Journal of Elasticity 102, 99-116.

Meissner, B., Matejka, L., 2003. A Langevin-elasticity-theory-based constitutive equation for rubberlike networks and its comparison with biaxial stress–strain data. Part I. Polymer 44, 4599-4610.

Meissner, B., Matejka, L., 2004. A Langevin-elasticity-theory-based constitutive equation for rubberlike networks and its comparison with biaxial stress–strain data. Part II. Polymer 45, 7247-7260.

Miroshnychenko, D., Green, W.A., 2009. Heuristic search for a predictive strain-energy function in nonlinear elasticity. International Journal of Solids and Structures 46, 271-286.

Puglisi, G., Saccomandi, G., 2016. Multi-scale modelling of rubber-like materials and soft tissues: An appraisal. Proceedings of the Royal Society A: Mathematical, Physical and Engineering Sciences 472, 20160060.

Uddin, M.S., Ju, J., 2016. Multiscale modeling of a natural rubber: Bridging a coarse-grained molecular model to the rubber network theory. Polymer 101, 34-47.

Uddin, M.S., Ju, J., 2017. Enhanced coarse-graining of thermoplastic polyurethane elastomer for multiscale modeling. Journal of Engineering Materials and Technology 139, 011001.

Wineman, A., 2005. Some results for generalized neo-Hookean elastic materials. International Journal of Non-Linear Mechanics 40, 271-279.

Yan, Z., Guo, Q., Zaïri, F., Zaoui, A., Jiang, Q., Liu, X., 2021. Continuum-based modeling large-strain plastic deformation of semi-crystalline polyethylene systems: Implication of texturing and amorphicity. Mechanics of Materials 162, 104060.

Yan, Z., Guo, Q., Zaïri, F., Zaoui, A., 2022. A multi-scale plastic-damage model for strain-induced morphological anisotropy in semi-crystalline polyethylene. International Journal of Non-Linear Mechanics 147, 104238.

Yuan, B., Zeng, F., Cui, J., Wang, Y., 2022. Molecular simulation guided constitutive modeling of filled rubber: Bridging structural parameters to constitutive equations. Polymer 254, 125090.

General conclusions and perspectives

This PhD dissertation concerned the multiscale modeling of the large-strain mechanical behavior of various polymer systems using two different, but complementary, approaches, namely molecular dynamics simulations and constitutive modeling within the continuum mechanics rules. The first approach provides the molecular-level description whereas the second approach provides the continuum-level mechanics.

Molecular dynamics simulations were firstly carried out to investigate the structure-property relation of semi-crystalline polyethylene (PE) systems. The simulations were conducted for different material systems under various loading temperatures representing different states (100 K: glassy state, 250 K and 300 K: transition state and 400 K: rubbery state). When side lengths change independently, polymer crystallinity in each direction was different. It was found that structure composition and temperature have a great effect on the crystallinity parameters (i.e. crystallinity based on bond orientation and global order parameters). The higher the temperature, the lower the crystallinity and the longer the chain length, the lower the crystallinity. The stress-strain curves obtained during the course of the uniaxial stretching showed four distinct regimes before failure with a strong effect of both the structure composition and the stretching temperature. Besides, the strain decomposition concept allowed to clearly highlight the main deformation mechanisms split into shear yielding and dilatational mechanisms. A directional effect was pointed out both on the uniaxial response and the underlying deformation micro-mechanisms. A significant effect of the biaxial strain ratio was pointed out on the different mechanical properties, especially the yield strength and the strain-hardening ability. Data were collected to construct yield and failure envelopes under a wide range of biaxial strain ratios and temperatures. The response of the memory behavior indicated that PE with low crystallinity can restore the original shape well, the lower the temperature, the higher the recovery rate. In addition, it was evidenced that the material through the shape memory behavior has better mechanical properties. Then, we investigated the structure-property relation of carbon-black filled vulcanized *cis*-polyisoprene (*cis*-PI) systems. The latter were vulcanized by adding element sulphur to *cis*-PI and vulcanizing at high temperatures to obtain vulcanized rubber, and then adding different amounts of fullerenes (C_{60}) to the vulcanized rubber at high temperatures to obtain carbon-black (CB) filled vulcanized rubber. The macroscopic physical and thermodynamic properties of vulcanized rubber and CB filled vulcanized rubber were studied to obtain the effect of vulcanization and nanofiller on natural

rubber. The higher the degree of vulcanization, the formation of a network between the molecular chains, resulting in higher density, lower thermal expansion and higher specific heat capacity. It was pointed out that vulcanization leads to an increased ability of the rubber to withstand stress at large strains. Moreover, it was showed that fillers have the same effect on density and specific heat capacity as vulcanization, but there is no clear trend towards an effect on the coefficient of thermal expansion. The reinforcement mechanisms were studied at the macroscale through the mechanical behavior and at the nanoscale by analyzing the local interactions. The attraction of fullerenes to *cis*-PI atoms and the aggregation configuration of *cis*-PI atoms around fullerenes were analyzed by radial distribution function, introducing local number density and potential mean force.

Besides, the finite-strain mechanical response and deformation processes of various polymer systems were analyzed by means of microstructure-based models formulated in continuum terms. The highly nonlinear and rate-dependent mechanical response of semi-crystalline polyethylene systems covering a wide spectrum of the crystallinity was firstly investigated within a multi-scale homogenization-based approach. The model ability to capture the large-strain response variation with the crystallinity was criticized. The model exhibited weaknesses in small-strain region but it was able to reproduce, within large-strain region, the rate-dependent monotonic response variation with crystallinity. The general trends of the high-crystalline material cyclic response were quantitatively well reproduced by the model while the deviation from experiments increased with amorphicity, which would require to take into account the amorphous network alteration. In addition to molecular orientation effects that takes place as the deformation proceeds, the cavitation damage associated with progressive nucleation and growth of cavities in the amorphous layers was presented. The synergic effects of crystal texturing and anisotropic cavitation damage on the plastic deformation behavior of high-density polyethylene were integrated into a constitutive model formulated within a multi-scale homogenization-based approach. By comparing simulations and experimental data, the model ability to capture large-strain macroscopic stress and inelastic dilatation was shown. The proposed multi-scale approach provides a good approximation of the intrinsic response of high-density polyethylene and the basic underlying inelastic mechanisms by considering strain rate and stretching temperature effects. Besides, the role of cavitation damage in overall and local responses was observed to better understand its importance under stretching and stretching-retraction conditions. We have then investigated the $\alpha \rightarrow \beta$ phase transition in semi-crystalline polyvinylidene fluoride (PVDF) within a hierarchical multi-scale analysis coupling molecular

dynamics simulations in atomistic and microstructure-based modeling in a continuum term. We have presented a continuum-based model formulated within a micromechanical framework to connect the PVDF elastic-viscoplastic-viscohyperelastic deformation behavior to the α → β phase transition caused by the straining. The identification of the developed micromechanics model was performed thanks to a rigorous deterministic scheme using relevant results issued from molecular dynamics simulations performed in this work and available experiments. Quantitative comparisons showed that the model was able to correctly capture the large-strain stress-strain response of a PVDF under uniaxial straining accounting for the strain-induced α → β phase transition. Besides, the model was used to clarify the influence of the microstructure evolution, in terms of α → β phase transition and internal ordering, on the piezoelectric activity.

The continuum-based model contains very few parameters and allows to better understand the relation between key PVDF microstructure features (strain-induced crystallographic texturing and α → β phase transition) and mechanical response. Although it appears as a valuable tool for the reliable design and optimization of multi-functional piezoelectric PVDF-based material media, a complete verification of the model capabilities under more complex mechanical loading conditions remains an important issue for further investigations. Finally, we check the validity of a hyperelastic model to provide good estimates of the behavior of a rubber model system under different biaxial loading paths by means of the molecular dynamics simulation method.

This work led to several aspects that can be treated in the future for both sides concerning the molecular dynamics simulations and the development of continuum-based models. We need to deepen the understanding of the reinforcement mechanisms of different polymer systems using a wider range of nanofillers (nanotube, graphene, …). On the continuum terms side, although quite sophisticated, the constitutive model needs improvements for a fully realistic description of the microstructure evolution and the underlying large-strain-induced anisotropy. In particular, the fragmentation mechanism operating in the crystalline lamellae and leading to the formation of a fibrillar microstructure deserves to be included.

Abstract

As a meaningful prerequisite of advanced applications of polymer systems, predictive multiscale modeling is needed. This thesis deals with the multiscale modeling of the large-strain mechanical behavior of polymer systems using both molecular dynamics and continuum-level mechanics. The key role of the structural factors (length and number of chains, crystallinity, cavitation damage, phase transformation, vulcanization and nanofiller reinforcement) and the loading conditions (strain rate, temperature, non-monotonicity and biaxiality) on the large-strain mechanical behavior is highlighted for various polymers, including semi-crystalline polyethylene, semi-crystalline polyvinylidene fluoride and carbon-black filled vulcanized *cis*-polyisoprene.

Keywords: Polymer systems; Molecular dynamics; Continuum mechanics; Mechanical properties; Interface; Strain-induced mechanisms.

Résumé

En vue de leurs applications toujours plus innovantes, la modélisation multi-échelle prédictive des systèmes polymères est un prérequis nécessaire. Cette thèse porte sur la modélisation multi-échelle du comportement mécanique en grandes déformations de cette classe de matériaux en utilisant la description au niveau moléculaire via la dynamique moléculaire et à l'échelle du continuum via la mécanique des milieux continus. Le rôle clé des facteurs structuraux (tels que longueur et nombre de chaînes, cristallinité, endommagement par cavitation, transformation de phase, vulcanisation et renforcement des nanocharges) et des conditions de chargement (telles que vitesse de déformation, température, non monotonicité et biaxialité) sur le comportement mécanique en grandes déformations est mis en évidence pour divers polymères, notamment le polyéthylène semi-cristallin, le fluorure de polyvinylidène semi-cristallin et le *cis*-polyisoprène vulcanisé et chargé en noir de carbone.

Mots clés : Systèmes polymères ; Dynamique moléculaire ; Mécanique des milieux continus ; Propriétés mécaniques; Interface ; Mécanismes de déformation.